HERIOT WATT UNIVERSITY

Visualisation of Shielding Gas Flows during High-Value Manufacture

Ioannis Bitharas

Institute of Photonics and Quantum Sciences

March 2018

A thesis presented in the fulfilment of the requirements for the degree of

Doctor of Engineering

Abstract

This thesis is a collection of experimental and theoretical analyses of the behaviour of inert gases during material processing. The approach taken is the use of a combination of schlieren imaging and numerical simulations to understand the physical mechanisms associated with the gas flows in each process. The visualisations carried out experimentally were used to validate the models, while the models aided in the interpretation of the imaged refractive index gradients.

For gas metal arc welding (GMAW), the variation of Ar input flowrate with varying torch angle, standoff and joint type was investigated. Magnetohydrodynamic (MHD) models of the arc and electrodes showed that air entrainment was determined by the interplay between the momentum in the shielding gas stream and the inwards pull of Lorentz forces which develop within the plasma jet. Good agreement was found between the images and model, showing that gas coverage decreased at values below 9 l/min. Torch angle and standoff were shown to not significantly influence coverage. Similar coverage was found to occur in bead on plate and fillet welds under the same conditions. Further experiments using flux-cored, gas shielded arc welding (FCAW-G) and 80% Ar / 20% CO_2 gas allowed good quality welds to be deposited with flowrates as low as 3 l/min. These results supported the use of flow controllers in production welding units at BAE systems Govan, leading to cost savings and reduced environmental impact by locking the gas flowrate to 12 l/min.

A study of gas tungsten arc welding (GTAW) using alternating Ar and He shielding gases as a method of arc pulsing was also investigated. The effects of pulsing frequency and input flowrate were investigated. When pulsing, it was found that alternating the gases resulted in He constriction close to the arc region due to the preceding Ar pulse. Comparison of weld macrographs showed that He can be used more efficiently through alternating technique compared to a premixed gas with the same He content.

The schlieren system was used to analyse the flow of Ar from a trailing shield device and plasma arc welding (PAW) torch in the context of wire-arc additive manufacture (WAAM). Flow characterisation with changes in standoff and welding configuration showed that air entrainment can be minimised when using a trailing shield. However, increasingly tall parts were insufficiently covered due to interactions between fast jets from the torch and shielding gas streams. MHD modelling of the torch allowed the characterisation of heat transfer and O_2 levels with varying input current or over different geometrical features.

The final study in this thesis concerns the fluid-particle interactions in laser powder-bed fusion (LPBF). High-speed direct and schlieren imaging showed that differences in laser plume orientation arise from different process settings, even under the same energy input. It was shown that the denudation of the powder bed was caused by drag forces acting on particles, due to atmospheric gas flow induced by the plume. Numerical modelling was in good agreement with the experiments, indicating that evaporative phenomena are an integral part of the heat and mass transfer in LPBF.

Acknowledgements

This thesis is the culmination of 4 years of learning, researching and experimenting. During this period, the constant support from a few individuals has been critical for me to be productive, creative and positive. In no particular order, I wish to extend my sincerest gratitude for their involvement in this project.

To my supervisor Andrew, without whom this work wouldn't have been possible. Thank you for introducing me into the world of academia, and your shrewd guidance on how to best navigate it. Most importantly, thank you for your trust; it gave me space to grow, learn and meet expectations on my own terms.

To my supervisor Norrie, without whom this project wouldn't even exist! Thank you for the stimulating conversations on welding metallurgy, for always asking the right questions to guide our work and for encouraging me to go even further.

To the guys from BAE systems in Govan, Billy and Douglas, for taking the time to be involved with the project and for securing all the resources needed to make it a success.

To Prveen, Jonathan, Stuart, Anthony, Sergio and Mark, with whom I had the pleasure of conducting experiments. Thank you for all the good moments in the lab, for the effort and long hours you put into the experiments and for putting up with me and my setups!

To my fellow research engineers Luke and Iain, who helped me survive and ultimately enjoy four months at St. Andrews. Thanks for keeping alive the spirit of competition, which made me strive to exceed expectations and for the sense of camaraderie during these four years.

To my friend and fellow modeller Emmanouel for long discussions into maths, physics, simulations, convergence and the reason of it all!

To my family Giorgos, Irene, Dimitris, Chrysa and my companion Alice, for their unwavering love, support and patronage during all my years of studying. Thank you for shaping me into who I am. Finally, thank you for your understanding when spending countless hours with COMSOL took priority over you.

Contents

List of research outputs arising from this work 7

1. INTRODUCTION 8

1.1. Motivation 8

1.2. Outline of thesis 9

2. LITERATURE SURVEY 11

2.1. Physics of plasma arcs 11

2.1.1. Fluid flow 12

2.1.2. Species transport 14

2.1.3. Heat transfer 15

2.1.4. Electric and Magnetic Fields 17

2.1.5. Thermophysical properties 18

2.2. Overview of numerical modelling in arc welding 19

2.2.1. Arc Models 20

2.2.2. Arc and Electrode Models 21

2.2.3. Influence of evaporated Fe in plasma mixture 24

2.2.4. Unified Arc, Electrode and Weld Pool Models 24

2.3. Optical Flow Diagnostics 28

2.3.1. Shadowgraphy 28

2.3.2. Schlieren Photography 32

2.3.3. Particle Imaging Velocimetry 36

2.3.4. Plasma Optical Emission Spectroscopy 38

2.4. Summary 40

3. OPTIMISATION OF GAS SHIELDING DURING GMAW 42

3.1. Experimental setup 43

3.2. MHD Model 46

3.2.1. Geometry and meshing 46

3.2.2. Governing equations and boundary conditions 48

3.3. Results 50

3.3.1. Variation of shielding gas flowrate 50

3.3.2. Torch standoff variation 55

3.3.3. Variation in torch angle 57

3.3.4. Metallurgical analysis of welded samples 59

3.4. Discussion 61

3.4.1. Schlieren imaging of FCAW-G 62

3.4.2. Arc length variation 63

3.5. Conclusions 65

4. ANALYSES ON THE EFFICIENT USE OF SHIELDING GAS DURING WELDING 67

4.1. IMAGING AND 3D SIMULATION OF GAS FLOWS IN MIG FILLET WELDS 67

4.1.1. Experimental setup 67

4.1.2. Numerical model setup 69

4.1.3. Flowrate variation during fillet GMAW 71

4.1.4. Flowrate variation during fillet FCAW-G 78

4.1.5. Discussion 81

4.2. TIG WELDING USING AN ALTERNATING GAS SUPPLY AS A PULSING METHOD 83

4.2.1. Experimental setup 84

4.2.2. GTAW visualisation using pure Ar 86

4.2.3. GTAW visualisation using pure He 88

4.2.4. GTAW visualisation using alternating Ar and He gases 89

4.2.5. Discussion 94

4.3. CONCLUSIONS 96

5. LOCAL SHIELDING DIAGNOSTICS DURING WAAM 98

5.1. INTRODUCTION 98

5.2. FLOW VISUALISATION FROM WAAM COMPONENTS 100

5.2.1. Investigation of trailing shield effectiveness 100

5.2.2. Analysis of flow patterns from plasma arc welding torch 103

5.2.3. Schlieren imaging of shielding conditions during WAAM 107

5.3. NUMERICAL MODELLING OF PAW DURING WAAM 110

5.3.1. Numerical PAW arc models: a brief literature survey 110

5.3.2. Model setup: geometry, mesh, material properties and physics 111

5.3.3. Flow during the 1st layer 113

5.3.4. Flow during the nth layer 116

5.4. CONCLUSIONS 119

6. GAS FLOWS DURING METALLIC LASER-POWDER BED FUSION AM 121

6.1. INTRODUCTION 121

6.2. EXPERIMENTAL RIG AND IMAGING SETUP 123

6.3. DIRECT AND SCHLIEREN IMAGING OF FLUID AND PARTICLE DYNAMICS IN LPBF 124

6.3.1. High speed imaging of the 1st powder layer: laser line scans 125

6.3.2. Visualisation of LPBF plumes, including the effect of cross-flows 127

6.4. NUMERICAL MODELLING OF LASER-INDUCED GAS FLOWS DURING LPBF 129

6.4.1. Model geometry, materials and mesh 130

6.4.2. Governing equations and boundary conditions 131

6.4.3. Results 133

6.5. DISCUSSION 136

6.5.1. Species ionisation 137

6.5.2. Plume hydrodynamics and effect on particles 139

6.6. CONCLUSIONS 141

7. CONCLUDING SUMMARY AND REMARKS 142

7.1. FURTHER WORK 146

7.1.1. GMAW and FCAW-G 146

7.1.2. GTAW, PAW and WAAM 147

7.1.3. LPBF 147

7.1.4. Schlieren imaging system 147

REFERENCES 149

List of research outputs arising from this work

Journal articles

I. Bitharas, S. W. Campbell, A. M. Galloway, N. A. McPherson, and A. J. Moore, "Visualisation of alternating shielding gas flow in GTAW," Mater. Des. 91, 424–431 (2016).

I. Bitharas, N. A. McPherson, W. McGhie, D. Roy, and A. J. Moore, "Visualisation and optimisation of shielding gas coverage during gas metal arc welding," J. Mater. Process. Technol. 255, 451–462 (2018).

P. Bidare, I. Bitharas, R. M. Ward, M. M. Attallah, and A. J. Moore, "Fluid and particle dynamics in laser powder bed fusion," Acta Mater. 142, 107–120 (2018).

Conference proceedings

I. Bitharas, N.A. McPherson, W.McGhie, D. Roy, A. Moore, "Imaging and simulation of shielding gas flows during GMAW", Proceedings of the 10th Trends In Welding Research conference, Tokyo (2016)

Conference presentations & posters

I. Bitharas, N. McPherson, and A. J. Moore, “Visualisation of shielding gas flows during high value manufacture”, poster in Manufacturing the Future conference, Glasgow (2014)

I. Bitharas, N. McPherson, and A. J. Moore, “Visualisation of shielding gas flows during high value manufacture”, poster in Optics and Photonics conference, Edinburgh (2014)

I. Bitharas, N. McPherson, D. Roy, W. McGhie and A. J. Moore, “Visualisation of shielding gas flows during high value manufacture,” presented at IDC Optics and Photonics Conference, Edinburgh (2015)

I. Bitharas, A. McAnthony, R. Cortese, J. Ding, S. Williams, A. J. Moore, “Schlieren imaging and numerical simulation of Ar-air flows in wire-arc additive manufacture”, presented at WAAMmat industry day, Cranfield (2017)

I. Bitharas, P. Bidare, A. J. Moore, “Optical diagnostics of metal powder 3D printing: laser explosions?” presented at CDT applied photonics conference, Edinburgh (2017)

1. Introduction

1.1. Motivation

When the temperature of a solid metallic surface increases above melting (~1700 K for steel), the atoms comprising it are dislocated from their geometric lattice and are free to interact with any elements present in their surroundings. In the case of steel, air reacts with iron (Fe), carbon (C) and other molten alloying elements, creating unwanted by-products. When the system cools and eventually reaches ambient temperature, these formed non-metallic compounds will have altered the resulting microstructure, deteriorating the structural properties of the re-solidified metal. It is therefore necessary to limit such reactions when processing metals. To that end, inert gases such as argon (Ar), helium (He) or carbon dioxide (CO_2) are typically channelled through a nozzle or provided in an ambient state.

This situation is encountered during welding, where typically a directed gas flow prevents contamination of the solidifying weld metal and heat affected zone from environmental elements by locally controlling the surface reaction rates. If shielding conditions are poor, air impingement on the weld pool may lead to the formation of excess oxides or nitrides. The effect these may have on the weld varies with base and filler material but can include excess porosity, reduced toughness and ductility or internal cracking for some alloys [1]. Most importantly, such defects are sometimes not detectable through visual inspection, so if any process variables change adversely to the gas shield, then the weldment's quality might be compromised. Porosity defects could have catastrophic results for high-value components in critical, load bearing applications, where the standards for weld properties can be stringent.

Although its main function is to counter contamination, the gas used plays another important role in arc-based processes; its thermophysical properties, which vary with flow regimes, directly influence the overall heat and mass transfer. Consequently, the mechanical properties of the weldment are strongly dependent on the shielding gas flow [2], making process optimisation crucial for the economical and efficient operation of manufacturing sites. This is particularly true during the manufacture of large structures, where operating costs can be a significant part of the total cost. However, the plasma jet formed due to the arc is governed by complex magneto-hydrodynamic (MHD) phenomena, presenting a challenge for process optimisation [3].

Apart from traditional joining, large volumes of shielding gases are also needed for metal additive manufacturing (AM) processes. In wire-arc additive manufacturing (WAAM), parts are made by depositing several layers of melting wire on a metallic substrate. Materials used with this method are commonly titanium (Ti), nickel (Ni) or aluminium (Al) alloys, which are very susceptible to contamination. The high temperatures in a part due to repeated heating cycles from the plasma jet increase the surface oxidation rates. Through diagnostics, the mechanisms that govern entrainment can be visualised, identifying local shielding requirements. The successful deposition of large-scale parts with minimal defects and standardised microstructures can be therefore be facilitated.

Finally, laser-powder bed fusion (LPBF) or selective laser melting (SLM) AM, regarded as one of the most prevalent contemporary 3D printing technologies for metal components, also requires the solidifying metal to be protected from air. To achieve that, this process is carried out within a chamber and under an inert atmosphere. However, the gas flows incurred through material-laser interactions have so far been overlooked. High-speed visualisations of phenomena such as laser plume generation or particle ejection offer unprecedented insight into aspects of the process such as powder dynamics and consolidation, melt pool formation or laser de-focusing and scintillation.

The motivation therefore arises to develop understanding of shielding gas flows at a fundamental level. The systematic visualisation of these processes through optical diagnostics can reveal a plethora of information about the physical phenomena that comprise them. The insight gained experimentally can be used to provide reference to multiphysics modelling, forming a framework to characterise the flow under a given set of conditions. In addition, analysis and comparison of the samples produced during imaging serves as a source of validation. The work presented throughout this thesis employs this approach to identify the most critical influencing factors and determine optimal flow conditions for the process discussed in each section.

1.2. Outline of thesis

Beyond this introduction, chapter 2 attempts to summarise the research carried out to date about plasma arcs and their interaction with gas flows. An account of the physics governing each process are given, and progress in the numerical solution of its mathematics is discussed. Additionally, optical techniques employed to validate and improve the state-of-the-art in arc models are presented, along with the relevant experimental results.

Chapter 3 is a study of metal inert gas (MIG) welding, also known as gas metal arc welding (GMAW). The aim of the chapter is to understand and characterise how gas coverage is affected by the input gas flow under typical welding conditions. The minimum input flow required to achieve acceptable weld quality with Ar is discussed and extended to a range of gas mixtures but also for the case of flux cored wire welding (FCAW-G). Macrographs and x-ray measurements are utilised to determine porosity levels, validating the diagnostics.

In the first part of chapter 4, the same framework as in chapter 3 is used to study MIG fillet welds, where flow effects are entirely non-symmetric. In the second part, a method of efficiently utilising He in gas tungsten arc welding (GTAW) or tungsten inert gas (TIG) is investigated. The conditions under which the pulsed supply of Ar and He results in deeper penetration are examined through high speed visualisation.

In Chapter 5, numerical modelling of plasma arc welding (PAW) is used to analyse the local shielding in the context of Ti-6Al-4V deposition during WAAM. Visualisations of a gas trailing shield, as used during such processing, are reported with and without the influence of a torch. In addition, the effect process settings have on the coverage is determined for different part geometries.

High-speed, long distance microscopy and flow visualisations of SLM under various operating conditions are found in chapter 6. The effect of an Ar or He atmosphere is analysed through imaging but also theoretically through a finite element model of the process which includes the gas flow incurred due to the laser-material interaction.

2. Literature Survey

2.1. Physics of plasma arcs

During arc welding, electrical current is channelled between two electrodes, one at the end of the welding torch, and the other comprised of the workpiece itself. The gas between the electrodes then becomes ionised though various means and a plasma state is reached and sustained by high temperatures, a consequence of Joule heating. In addition, as dictated by the Maxwell-Faraday law, the electric field induces a magnetic field, and both contribute to Lorentz forces accelerating the gas. This gas plasma jet therefore conducts the current, enabling the transfer of energy to the workpiece. Therefore, the shielding gas strongly affects the mass, momentum and heat transfer regimes that take place between the welding electrode and workpiece [3]–[5], as well as various aspects of the process, as shown in Fig. 1. Consequently, the gas flow affects the process in the most fundamental way, with direct impact to the weld's physical properties due to the change in heat input.

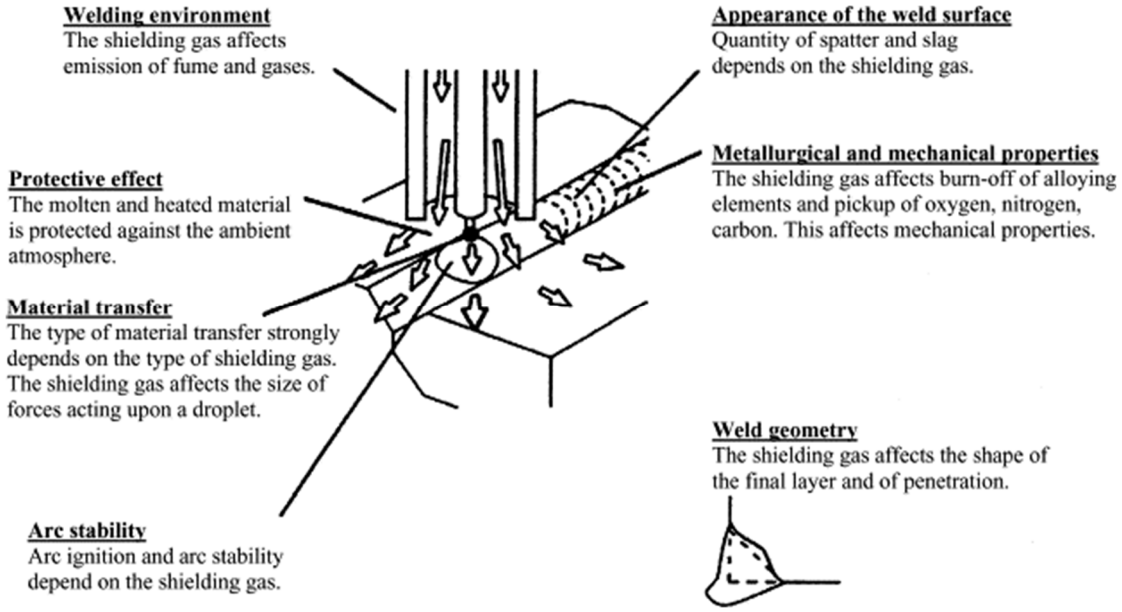

Fig. 1 Shielding gas functions in arc welding [5].

To macroscopically analyse the process, one must first describe the system's thermodynamics and fluid dynamics, along with their interaction with the electromagnetic effects due to the current flow. Using a continuum mechanics approach, this "coupling" of the physics can be achieved explicitly, by simultaneously solving the conservation equations for momentum, mass, heat and current along with the self-induced magnetic field [6]. Additionally, the convection and diffusion between the shielding gas and ambient atmosphere can be determined through conservation of the mass fraction. This mathematical treatment of plasma flows in this manner is termed magneto-

hydrodynamics (MHD). The governing equations are also coupled implicitly, by considering the thermophysical properties as a function of the temperature and mass fraction, reflecting the state of the plasma.

Due to the complexity of the partial differential equations (PDE) involved, no analytical solutions exist for the fully coupled problem, but these governing equations may be solved numerically. The resulting problem is a non-linear system of PDEs. By using techniques such as finite element modelling (FEM), or the finite difference (FDM) or finite volume (FVM) methods, the system can be linearised and solved through an iterative process.

Within the next sub-sections, the PDEs commonly used to describe the arc processes in this manner are presented along with their associated physical phenomena. Focus is given on time-independent formulations, as a steady-state approach has been employed throughout this thesis (this is discussed further in section 2.3.3 and in the model setup section of each chapter). The equations are given in vector form, to avoid reference to a particular dimensional frame. Characters in bold represent vectors while for scalars, normal characters are used.

2.1.1. *Fluid flow*

The equations commonly utilised to describe the fluid's convective motion are well established for arc models [4], [7]–[9]. These are the Navier-Stokes equations, derived from considering momentum and mass conservation and given in their differential, stationary form for a compressible flow by

$$\rho(\mathbf{u} \cdot \nabla \mathbf{u}) = \nabla \cdot [-p + \mu(\nabla \mathbf{u} + (\nabla \mathbf{u})^{\mathbf{T}})] + \mathbf{F} \quad (1)$$

$$\nabla \cdot (\rho \mathbf{u}) = 0 \quad (2)$$

where ρ is the fluid's density, μ is the viscosity, **u** is the velocity vector, p is the pressure and F are other body forces applied to the fluid. From the solution of these equations, the velocity and pressure of the plasma may be determined. Analytical solutions of equations (1) and (2) alone, for a cylindrical column of gas exiting a welding nozzle are available [3], [10]. However, with the assumption of an incompressible isothermal flow, the effect of Joule heating as well as the MHD effects of the jet are poorly portrayed. Nevertheless, in the early 80's, results were obtained in this manner by Chang [10], where he showed that near the flow's symmetry axis the velocity of the plasma jet is of the order of 10^3

m/s, and that maximum velocity may reach several hundred meters per second for currents of around 300 A.

Due to the flow of plasma between the electrodes where current is also flowing, a magnetic field is induced. This self-induced magnetic field in combination with the electric field between the electrodes can exert forces on the charge-carrying fluid. The interaction between these fields and the charged particles in the fluid is termed the Lorentz force. The net momentum imparted to the fluid can be included as a body force term in (1) and is given by:

$$\mathbf{F}_L = \mathbf{B} \times \mathbf{J} \tag{3}$$

where **B** is the magnetic flux density and **J** is the current density. Moreover, the effect of gravity acting on the fluid can be included, although sensitivity studies have shown that its contribution to the arc's momentum becomes negligible for currents above 20 A [8].

For the compressible formulation of the Navier - Stokes equations, the term

$$\mathbf{F}_g = -\rho g \tag{4}$$

can be used directly, as the density is variable. In this manner, effects such as buoyancy are, in theory reproduced numerically through the computed density gradient. With incompressible flows, the density remains constant or varies linearly, through the so-called Boussinesq approximation [11].

A simplification that has been employed in part of the literature is that the flow is laminar, an assumption that contradicts experimental observations of turbulence in the shielding gas flow, using the schlieren method [12]–[14]. In order to more adequately describe the velocity distributions that develop near walls and within MHD jet's structure, various turbulence models have therefore been proposed.

A comparison between Reynolds-averaged Navier-Stokes (RANS), large eddy simulation (LES) and Reynolds stress (RS) turbulence models is presented for arc welding by Schnick et al. [13]. It was shown that while the calculated mass fractions for all models were in general agreement with measurements, neither was entirely successful in reproducing measurements carried out under cold flow conditions. Williamson et al. [15] used the RANS k-ε model to simulate the MHD Ar flow in a non-transferred arc plasma torch, and the results were compared to optical and enthalpy probe measurements, presented by Fincke et al. [16]. A good agreement was noted in the computed temperature

and velocity fields, however the authors concluded that the dependence of turbulence intensity on the prescribed initial conditions limited the model's predictive capability. An 'enhanced' version of the same turbulence model was presented in [17], where turbulent mixing was taken into account through the use of an additional term in the species transport equation (see section 2.1.2).

In his 2016 review article [18], Shigeta discussed the state of the art for modelling turbulence in thermal plasma flows. The review pointed out that despite their usefulness in engineering applications, the large deviations in energy dissipation at different length scales are not adequately portrayed through RANS simulations, due to their limited capacity in resolving large variations in viscosity. Representative large-eddy simulations (LES) showed that the Kelvin-Helmholtz instability at the fringes of plasma torch jets, an effect responsible for the generation of large eddies in the slower and cooler part of the flow, can be modelled using this more sophisticated approach. Also, a small grid scale (SGS) method was used, where the governing equations are filtered according to the size of the eddies they are describing and solved using multiscale discretisation techniques. Sadly, the high computational costs associated with LES techniques renders them largely unavailable in commercial FE software.

2.1.2. *Species transport*

In order to evaluate the quality of gas coverage, the mixing and de-mixing of the shielding gas with the air must be included so as to estimate the concentration of environmental contaminants entrained in the plasma jet and beyond. Alternatively, the same treatment can be applied to include the effect of Fe vapour transport within an Ar environment (section 2.2.3). Regardless of application, an additional set of conservation equations must be solved, accounting for the convective and diffusive modes of transport of the species present during the process [4]. For a gas mixture, the total mass fraction of the i-th constituent ω_i is given by

$$-\nabla \cdot \left(\rho D_i^o \nabla \omega_i + \rho \omega_i D_i^o \frac{\nabla M_n}{M_n} + D_i^T \frac{\nabla T}{T} \right) + \rho (\mathbf{u} \cdot \nabla) \omega_i = 0, \tag{5}$$

where D_i^o is the ordinary diffusion coefficient and D_i^T is the thermal diffusion coefficient [19] while M_n is the sum of the molar masses of all the constituents. In (5), the first three terms represent diffusion due to concentration and temperature gradients, while the fourth term represents convective transport. An additional contribution to the diffusion

coefficient of each species can be added to account for turbulent mixing of small eddies, as discussed for the plasma spray process in Cheng et al. [17]:

$$D_{iT} = \frac{\mu_T}{Sc_T} \tag{6}$$

Here, μ_T is the Reynolds-averaged turbulent kinematic viscosity and Sc_T is the turbulent Schmidt number.

2.1.3. *Heat transfer*

During the welding process, heat is transferred from the top electrode towards the plasma, and from the plasma towards the workpiece. To model the thermodynamic effects occurring in the flow, an energy balance considering conduction and radiation is used in the solid domains, while convection is also considered in the fluid domain. The convective term couples the velocity and temperature fields. The velocity can either represent the calculated flow values or it can be a translational velocity of a solid component. The convection-diffusion equation thus takes the following general form:

$$-\nabla \cdot (k\nabla T) + \rho c_p(\mathbf{u} \cdot \nabla T) = S \tag{7}$$

Where k is the thermal conductivity (W m^{-3}), T is the temperature (K), c_p is the specific heat at constant pressure (J kg^{-1} K^{-1}) and S is a source term, which contains domain-specific terms.

The most significant heat source term is electromagnetic (Joule) heating due to current flow within the conductive medium. This is commonly given by

$$\mathbf{Q_{joule}} = \frac{\sum j_x^2}{\sigma} \tag{8}$$

where j_x are the components of the current density in the appropriate coordinate reference frame and σ is the electrical conductivity within the domain. However, since the electrical conductivity of the shielding gases is almost zero at atmospheric pressure and temperature, this formulation introduces numerical instability. Alternatively, Joule heating may be expressed in terms of the electric field **E** and the current density **J** as follows:

$$S_{joule} = \mathbf{J} \cdot \mathbf{E} \tag{9}$$

Although the conductivity term is not present in equation (9), it is considered equally valid and is generally preferable to use in FEM.

Due to presence of both thermal gradients and electrical currents in the conducting domains, the thermoelectric effect also occurs. Hence within such domains there is flow of thermal current, being "dragged along" by the flow of electric current. The magnitude of this secondary current depends on the Seebeck coefficient, a material-dependent constant that determines how strong the thermoelectric coupling is. Since the material properties are temperature-dependent, heat may be generated or lost where the Seebeck coefficient changes. This is called the Thomson effect, given by

$$S_{\mathrm{Thomson}} = \mathrm{K}\,\mathbf{J}\cdot\nabla\mathrm{T} \tag{10}$$

where $K = 5k_b/2e$ is the Thomson coefficient, a special case of the Seebeck coefficient. In this relation, k_b is the Boltzmann constant and e is electron charge.

Moreover, a significant portion of the energy supplied in the arc is lost through radiation. Each atom is electrically excited to a higher level, with de-excitation resulting with the emission of the respective photon. As there are different species within the plasma at various levels of ionisation [20], numerous spectral lines are detectable. The added complication comes when a part of the radiation emitted from some species is reabsorbed by others, making it hard to predict theoretically. In order to implement this in the model without the input of extensive experimental data, the net radiative emission coefficient method is utilised. This is an approximate statistical spectroscopic analysis of plasma radiation, representing the line spectrum of different species in terms of atomic properties as a function of temperature, first utilised by Cram for Ar plasma and Argon contaminated with Iron [21], and later by Menart and Malick [22]. Hence the radiation losses can be treated as a negative, temperature-dependent heat flux given by

$$S_{rad} = -4\pi\varepsilon_N(\mathrm{T}) \tag{11}$$

where $\varepsilon_N(T)$ is the net radiative emission coefficient, as shown in Fig. 2.

Inserting equations (1.6)-(1.8) into (1.4) yields the complete energy balance for the plasma domain, with each part accounting respectively for conduction, convection, Joule heating, thermoelectric heating and radiation losses, given below:

$$-\nabla\cdot(\mathrm{k}\nabla\mathrm{T}) + \rho c_p(\mathbf{u}\cdot\nabla\mathrm{T}) = \mathbf{J}\cdot\mathbf{E} + \frac{5k_b}{2e}\mathbf{J}\cdot\nabla\mathrm{T} - 4\pi\varepsilon_N \tag{12}$$

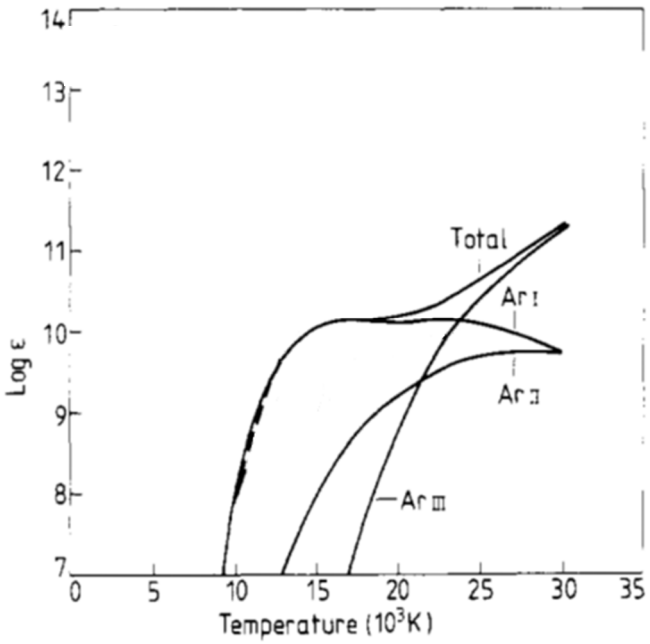

Fig. 2 Radiative emission coefficients ε (logarithmic scale, in W m^{-3} sr^{-1}) as a function of temperature (10^3 K). The contribution from the Ar, Ar^+ and Ar^{++} species is summed up to comprise the total coefficient, ε_N [21].

2.1.4. *Electric and Magnetic Fields*

In order to calculate the energy transfer to the plasma through the thermoelectric effects, the current and magnetic flux densities have to be determined by solving the electromagnetic problem. With these known, the calculation of the Lorentz force (eqn. 3) is also possible. Initially, current continuity may be applied in terms of the electric potential V, given by

$$\nabla \cdot \sigma \nabla V = 0, \tag{13}$$

where σ is the electrical conductivity of the material. Additionally, the magnetic potential vector may be described using the Ampere-Maxwell law,

$$\nabla \times \left(\frac{1}{\mu_0} \nabla \times \mathbf{A} \right) + \sigma \nabla V = 0 \tag{14}$$

The current density is then given by Ohm's law, while the magnetic flux density **B** and electric field **E** must be defined in terms of their respective potential:

$$\mathbf{J} = -\sigma \nabla V \tag{15}$$

$$E = -\nabla V \tag{16}$$

$$\mathbf{B} = \nabla \times \mathbf{A} \tag{17}$$

Finally, the constitutive relations for the electric field and magnetic field **H** can be defined, forming a comprehensive, time independent description of the electromagnetic phenomena than occur during MIG, TIG and PAW. Although slight variations in the formulations of these equations and their numerical analysis differ when implemented in different studies [4], [8], [9], the results from either may be considered equally valid [23].

2.1.5. *Thermophysical properties*

Simplifications may be made on the portrayal of the complex state of plasma, so that the problem can be formulated efficiently. According to the degree of ionisation in a plasma (which increases with its total energy), a population of free electrons flows alongside ions and neutral particles in the gas. Firstly, we can treat the plasma as quasi-neutral, implying that, on average, the total charge between particles cancels out and therefore the system remains neutral. Further, it may be assumed that this plasma "soup" is one continuous fluid in local thermodynamic equilibrium (LTE), where electrons also have the same temperature with heavy particles. This is a widely used and experimentally validated assumption [24] which, for welding applications, yields similar results with the non-equilibrium case. Assuming a plasma is in LTE allows the use of a single temperature variable for the calculation of its properties.

The thermal plasma's transport properties, namely density, heat capacity, viscosity, thermal, electrical conductivity and diffusion coefficients must therefore be defined as a function of the local temperature. Additionally, as the composition of the plasma varies, or indeed when the gas itself is treated as an ideal mixture, the properties must reflect this by being dependent to the mass fraction of its constituents. It therefore becomes necessary to use the gas-kinetic equation to derive the equilibrium values.

The particle-level interactions within gases change dramatically with heat input, as the atoms dissociate to higher degrees. Broadly, the sum of these microscopic interactions for all species present determines how the plasma behaves macroscopically. To derive the macroscopic properties, first the number density of each species for a given temperature, pressure and molar concentration must be established by minimising the Gibbs free energy of the system. Following that, the Boltzmann equation must be solved for each property; this is carried out by polynomial expansion using the Chapman-Enskog or Grad methods [25]. Regardless, both methods utilise an average of the Maxwellian kinetic cross-section for a given interaction between two species, termed a collision integral. The main information required for their calculation in each case concerns the

characteristic intermolecular potential, obtained directly through experiment or through calculations of the electronic structure coupled with simpler, accurate measurements [26].

Boulos et al. [20] made a set of tables with transport coefficients calculated from several experimental and theoretical values for common ideal gases. Properties for Ar, He, N, O_2, H_2, air and Ar/H_2 were given for temperature ranges of 500 – 25000 K, that have since been adopted by several authors. Crucial to studies of entrainment in air plasmas, Murphy et al. [26] calculated properties for mixtures of Ar-air. More recently, the accuracy of these properties has been enhanced by updated collision integrals for Ar and N species, as presented in [27], [28].

2.2. Overview of numerical modelling in arc welding

Many theoretical models have been developed to model the physics of arc welding, involving the arc, the electrodes, the weld pool or the mechanics of the solidified macrostructure. The numerical study of MHD plasma processing is a mature field and several review articles [4], [29], [30] and textbooks [3], [20], [31] have been written, detailing the progress that has been made. A complete account of the bibliography would therefore be impossible to contain within this literature survey. Instead, attention is given to results from studies focusing on the gas flows in MIG, TIG and PAW, especially when solved using FEM (employed in the following chapters in this thesis).

For the MIG process, Eagar's group [32] categorised models based on how many partial problems were solved and coupled in the computation. For clarity, the scientific literature of this section will be presented following this classification, as per the structure of Fig. 3 (right). For TIG and PAW, a similar set of partial problems would need to be considered, with reversed polarity and metal transfer instead taking place between a separate filler wire and the weld pool. The models presented in this thesis conceptually belong to the second generation, including the physics of the arc and simple expressions for the electrodes.

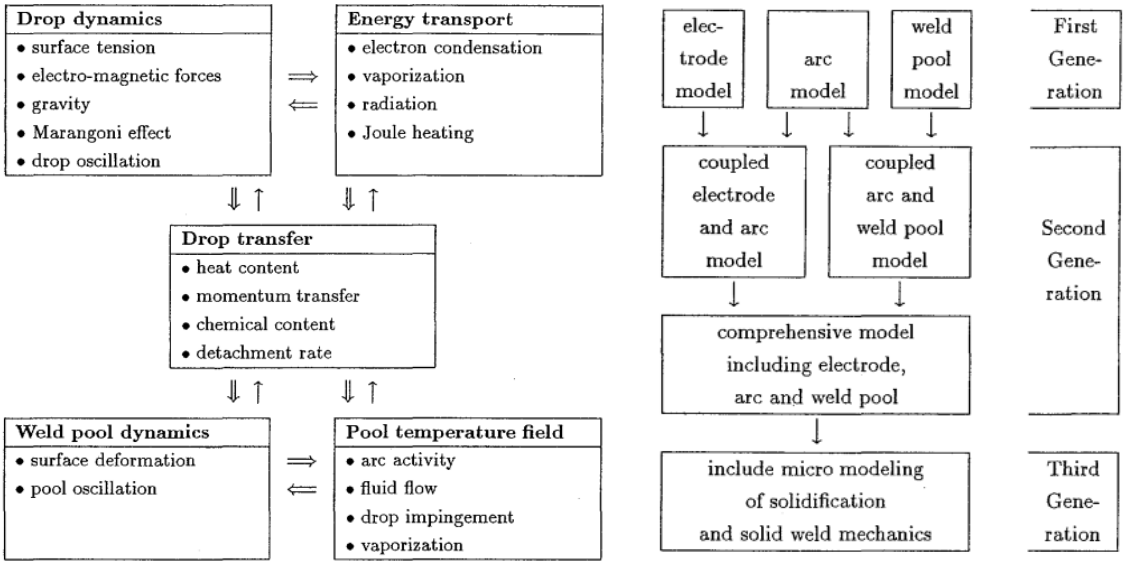

Fig. 3 Partial problem interdependence (left) and model classification (right) in GMAW [32]**.**

2.2.1. *Arc Models*

In the early 80's, Hsu et al. presented a free-burning arc model, using the MHD equations in a unified formalism, by way of the finite difference method [6]. To assess the cross-sectional area that the input current is applied to, they imaged the tip of the thoriated electrode, allowing the conversion to current density. The estimated current density was used as a boundary condition to solve the electromagnetic problem. In conjunction with spectroscopic measurements of the arc temperature profiles, he carried out sensitivity analyses on the flow's input characteristics. The results showed that the applied current influences the output temperature, pressure and velocity fields greatly, while other parameters were less sensitive to variation under currents of 100 – 300 A.

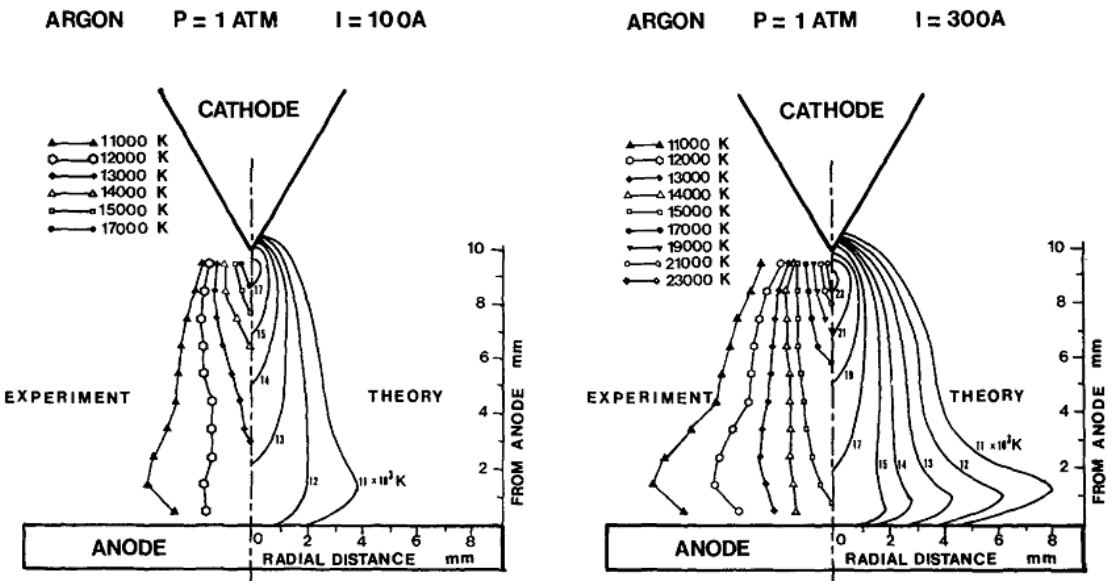

Fig. 4 Theoretical and experimental temperature profiles for 100 and 300A free-burning arcs [6].

A few authors have since used FEM to develop similar models, only with minor changes in the initial conditions. In Bauchire et al. [33], the arc model was coupled with ray tracing equations to account for an optical mirage effect occurring at the plasma tip, previously observed experimentally. Savaş et al. [34] examined the variations in GTAW flow fields under the effect of Ar, He, and N_2 shielding gases or mixtures thereof by using different sets of material properties, as given in [20].

The biggest shortcoming of these models is the failure to account for the non-LTE zones that occur at the electrode plasma sheaths and the significant physical phenomena taking place therein. By not including these, the simulation is made more unreliable, since the initial boundary conditions are posed at the electrode-plasma interface, resulting in inaccurate fluxes due to the high sensitivity of the results on the selected current density. Finally, an initial temperature of ~10,000 K must be imposed on the whole domain to reflect the ionisation temperature of the plasma [33], [34]. This is necessary for 1st generation models to achieve numerical convergence, replicating the increased thermal and electrical conductivity due to ionisation. While these simplifications may be reasonable for the area around the arc, they introduce error in the calculations in addition to being more numerically unstable [35].

2.2.2. *Arc and Electrode Models*

In order to address this issue, a unified treatment of the arc-electrode interface was developed [36]–[38]. In these models the non-LTE plasma sheath was treated separately, accounting for the one-dimensional ambipolar diffusion of charged particles. Electron density was determined at the edge of the electrodes by locally conserving charge in addition to the other MHD equations. Based on this, an expression for the effective electrical conductivity was used, further linking the physics and allowing stable solutions. Comparison with experimental data showed better agreement in the magnitudes and distributions of the flow variables compared to the free burning arc case. A simplified method by Lowke et al. [39], [40], suggested that the plasma sheath phenomena can be well represented by omitting ambipolar diffusion calculations and instead using a mesh size comparable to the sheath's diffusion length (~0.1 – 0.3 mm) around the electrode.

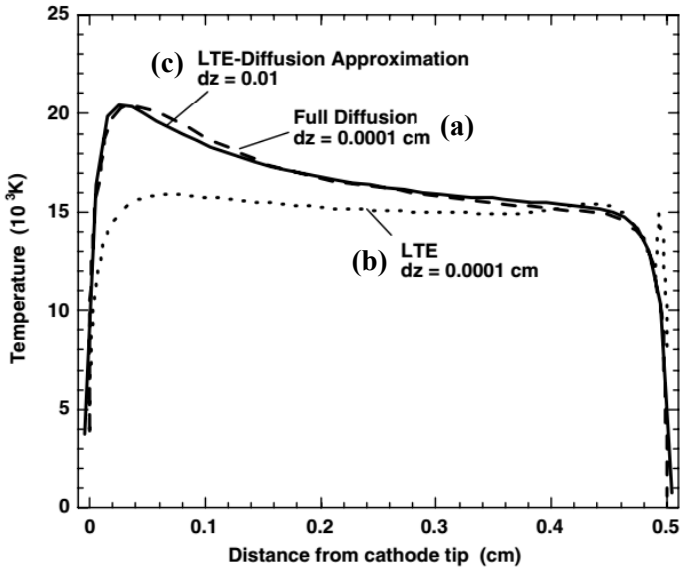

Fig. 5 Temperature distribution in the arc, (a) with explicit electron density calculations and (b-c) without calculating electron density. A very fine boundary mesh was used in (b) and diffusion length-scaled elements were used in (c) [40]**.**

Beyond modelling of the sheath, the heating or cooling due to the currents which develop at the surface of the electrodes must be accounted for. Generally, for a solid surface the thermionic current is given by Richardson's equation:

$$|\mathbf{j_r}| = A\mathrm{T}^2 \exp\left(\frac{-\varphi \mathrm{e}}{\mathrm{k_B T}}\right) \tag{18}$$

Where A is a material dependent constant ($A \sim 6{\cdot}10^5$ A m^{-2} K^{-2} is commonly for Fe-based material), φ is the work function of the surface material, e is the electron charge and k_B is Boltzmann's constant. The electron current j_e can be thought of as leaving the cathode (a cooling term) and becoming absorbed by the anode, heating it up. At the same time, some ionic current $\mathbf{j_i}$ develops due to the electron flow, also affecting the thermodynamics at the electrodes. It can be assumed that

$$|\mathbf{j_i}| = |\mathbf{J}| - |\mathbf{j_r}|, \qquad |\mathbf{j_i}| \geq 0 \tag{19}$$

$$|\mathbf{J}| = |\mathbf{j_e}| - |\mathbf{j_i}| \tag{20}$$

Consequently, at the anode and cathode interfaces, the extra fluxes in the energy balance are respectively given by

$$\mathbf{q_a} = \mathbf{j_e}\varphi_a \tag{21}$$

$$\mathbf{q_c} = \mathbf{j_i}V_i - \mathbf{j_e}\varphi_c \tag{22}$$

The full ionisation potential V_i is in this case considered to be delivered to the cathode with negligible voltage drop. Thermionic effects treated in this manner for the higher temperature tungsten cathodes encountered in TIG and PAW portrays the arc's

characteristics consistently with experiments [4]. However, a distinction is made between thermionic and non-thermionic cathodes [41], such as those encountered during MIG welding. To account for measurements of reduced electric potentials of Fe cathodes [42], the following equations are commonly used instead [41], [43].

$$\mathbf{q_a} = \mathbf{J}\varphi_a \tag{23}$$

$$\mathbf{q_c} = \mathbf{J}(V_i - \varphi_c) \tag{24}$$

Second generation models have been widely employed to explore and optimise aspects of various arc welding processes theoretically. Dreher et al. and Schnick et al. investigated the effect of torch design and process settings on the oxygen concentrations near the electrodes [13], [44]–[46]. Dreher et al. [46] numerically examined a large set of variables, including aspects of torch geometry, as well as standoff and angle. The model confirmed the profound influence of Lorentz forces on the bulk flow, as coverage quality deteriorated with an increase in current. Additionally, it was proven that diffusion plays an increasingly important role in gas dynamics due to the increased temperatures at higher currents. Finally, they showed using a transient model of pulsed GMAW that an increase in standoff distance of the order of 10 mm required flow compensation of up to 60% to maintain the same coverage. Discrepancies between measurements and numerical results were found and attributed to the radiation model utilised in the study. The criterion for adequate coverage was set as a maximum of 50 ppm oxygen over a 16 mm diameter area on top of the workpiece. While the 50 ppm limit might be sensible for Al or Ti welds, mild steel has a higher absorptive capacity, partly due to the comparatively large number of alloying elements [47].

In a review article, Murphy et al. [48] investigated the effect changes in gas thermodynamic and transport properties have on the calculated temperature distributions. To do so, they created “imaginary ideal gases”, where one property would change and the others would remain the same. Each gas property is an averaged macroscopic representation of a larger ensemble of complex particle interactions, which vary strongly with the degree of ionisation. Therefore, examination of each thermophysical property independently enabled more detailed understanding on plasma behaviour compared to simpler approaches such as comparison of ionisation potentials. The coupled arc-electrode model was used to make calculations of the flow variables in which Ar would have the electrical conductivity of He, etc. Using this analysis, they showed that the heat flux and current density towards the workpiece was maximised with better conducting gasses such as He, N or H_2, while the properties of N and H_2 incurred less shear stresses,

thus less turbulence. They concluded that a deeper weld pool may be achieved through the usage of welding gases with high specific heat, thermal conductivity and viscosity. Additionally, it was highlighted that three-dimensional models that also took into account the deformation of the electrodes were required before realistic predictions about the weld bead may be made purely by means of theoretical computation.

2.2.3. *Influence of evaporated Fe in plasma mixture*

More recently, MIG arc predictions were improved by including the influence of iron vapour from the electrodes on the arc temperature distribution, [4], [49]–[52], as spectroscopic measurements reported that axial temperatures peaked at 13,000 K [24], [53] (as detailed in section 2.3.4). It was shown that by correctly accounting for Fe mixing within the gas flow, the computed temperature profiles were in better agreement with the experiments. To add experimental verification to the theoretical temperature distribution, images of the arc were interposed with computed radiated fluxes in Schnick et al. [52], showing qualitative agreement under similar conditions.

In order to produce a model consistent with the measurements of [53], Haidar simulated the dynamics of the GMAW process under the effect of metallic vapours [49]. His results showed that a loss in conductivity due to increased iron vapour concentration induces the cooling effect on the central plasma column, also suggested by [50]. He thus concluded that the properties of the plasma are significantly impacted by Fe evaporation, a major drawback of previous models.

2.2.4. *Unified Arc, Electrode and Weld Pool Models*

Prior to second generation welding models, Fig. 3, the heat input of the arc was approximated in calculations by directly applying a Gaussian-distributed flux to the workpiece. To improve the predictive ability, in a 2002 paper Tanaka et al. [54] used the physical description of TIG but also included the flow of metal within the anode domain, the first work to present a unified model. To model the weld pool, the Marangoni stresses at the plasma-anode interface were given by using a temperature-dependent surface tension coefficient. The model gave results for the whole computational domain, with values in approximate agreement with experiments in determining the weld shape based on the input arc parameters.

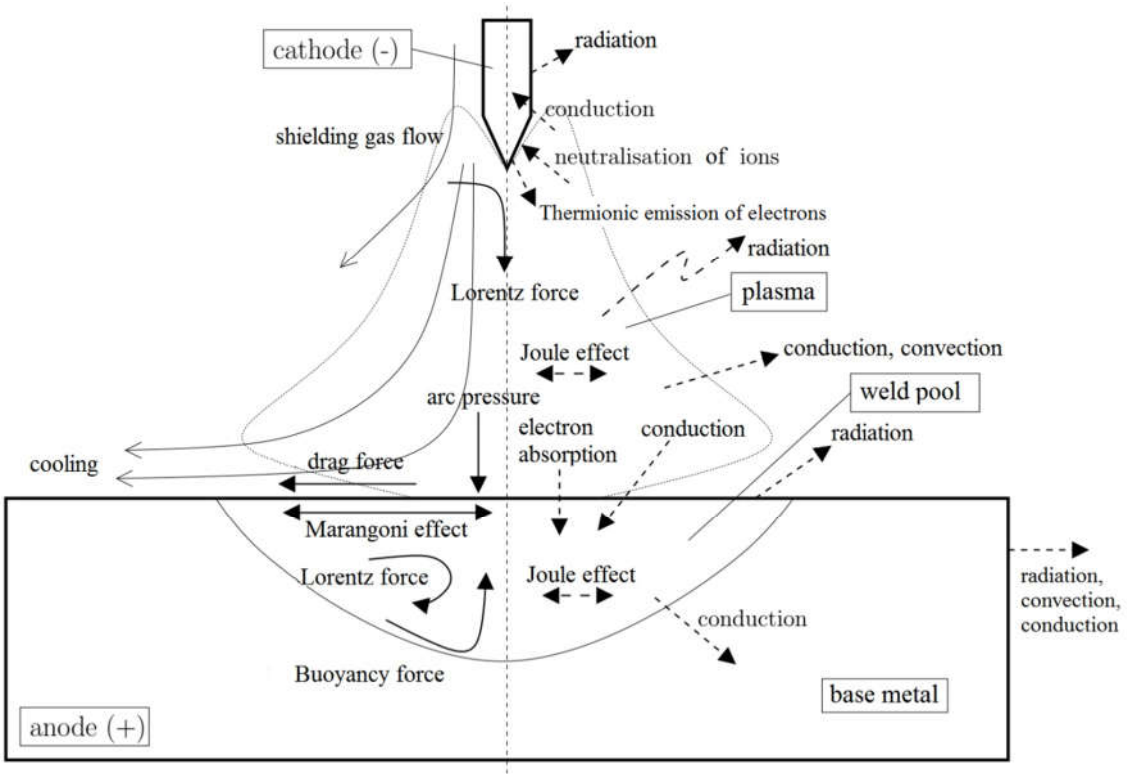

Fig. 6 Summary of physical phenomena in TIG welding, translated to English from [55]**.**

Following from earlier work studying the partial problems in MIG independently, Zhu et al. introduced a comprehensive mathematical description of the continuum mechanics, including the formation of metal droplets and their interaction with the weld pool [56] in 2004. In their model, the phase change in the wire and workpiece was included, allowing solutions for the liquid metal flow in both electrodes. The interface between the liquid and solid interfaces, driven by surface tension, arc pressure/drag and thermocapillary convection was tracked using the volume of fluid (VOF) method.

Using the same model, Hu and Tsai [57], [58] calculated the contribution of arc variables to the droplet formation and the resulting weld shape. They showed that, compared to simpler treatments of the heat transfer which omit the arc [59], the predicted weld pool shapes resulted in better agreement with real welds. Additionally, their theoretical results suggested that the shape of the weld pool influences the current distribution in the MIG arc due to strong cathodic fluxes, as has been widely reported for the tungsten electrode in TIG [60]. Despite this, the model showed rather high temperature distributions of around 20,000 K, because the influence of metallic vapours had not been taken into account.

In his 2009 PhD thesis, Brochard [55] used FEM instead of the FVM as a numerical procedure. To aid in convergence, he used the Galerkin method [61] to find weak solutions to the equations presented in 2.1. In addition to providing a mathematically

rigorous account of the governing mathematics, he showed that despite the large inter-electrode gradients in the thermophysical properties of the plasma, the highly-coupled problem may be solved and numerical convergence may be achieved if appropriate test functions are used. By comparing with the models of previous authors, such as [54], he showed that his computed weld profile agreed better with the actual weld profile made using the same inputs. He attributed the improvement to a difference in the treatment of the surface tension coefficient to vary with temperature and sulphur content and possibly differences in the sets of material properties used. To draw conclusions about certain operating parameters during TIG, he carried out temperature measurements of the workpiece by using several thermocouples as well as weld sections. His results showed that the applied current is the most sensitive parameter of the process, accounting for: 70% of the radiation, 95% of the weld penetration and 67% of the total size. Additionally, the arc's height contributed around 20 - 35% to all of these factors, while the electrode taper angle only marginally so (0 – 5%).

In 2012, a similar FE model was employed to determine the optimal wire feed speed with which droplet melting occurs in a stable manner [62]. By optimising the melting rate in terms of the size of the electrode and the current input, the metal transfer to the weld pool resulted in the weld profile that agreed best with real welds, consistently with [58]. Murphy [43] introduced a self-consistent 3D model to analyse steady-state MIG welding of Al. It was shown that while it is possible to predict weld geometries through a time independent model, by treating volumetric mass transfer per unit time as a constraint to the moving boundary equations. Further, plots of the heat input into the workpiece under realistic geometries encountered in welding suggested that its distribution significantly deviates from Gaussian.

Traidia et al. [8], [11] implemented a unified model in COMSOL multiphysics, with a few changes to better suit the FEM approach, such as using thin resistive layers with greater conductivities as the electrode sheaths. He carried out a study for the effects of pulsed current on spot welds. He showed that due to a change in the sign of the surface tension gradient with different temperatures, there are two vortices that alternate in "dominating" the weld pool, thus positively affecting weld size. He suggested that through pulsing, welds of similar sizes and penetration can be made using a lower energy input, reducing residual stresses or energy costs. Moreover, to verify these findings, he cross-correlated qualitative IR imaging data with the predicted weld pool size distributions, reporting good agreement over the same time intervals. The predicted melt

pool shape was also shown to match the cross section of spot welds shown through macrographs. However, no information was given about the structural properties of the respective workpieces.

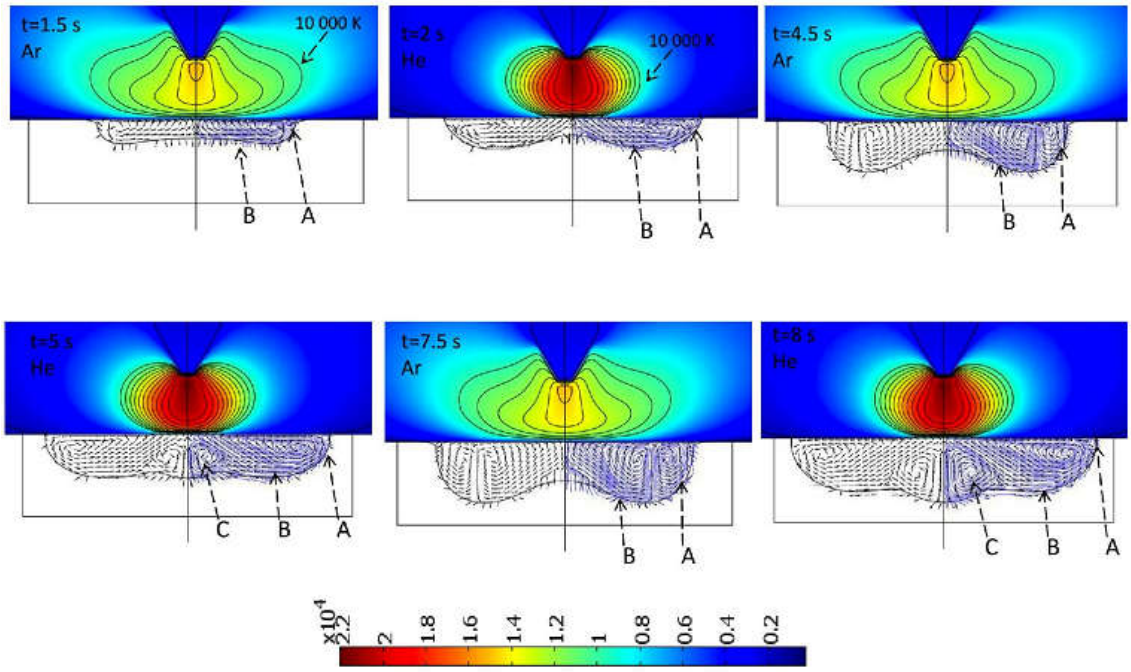

Fig. 7 Temperature profiles and weld pool evolution after 8 s of Ar - He pulsed shield gas flow, where an additional vortex C is formed.

Furthermore, he analysed the behaviour of the arc plasma, weld pool and electrodes under the flow of pure Ar, He and mixtures thereof, compared to a method where a combination of gases is supplied to the torch in an alternating manner, at a frequency of 1 Hz. His analysis indicated that when the gas supply is pulsed, improvements in terms of width and penetration may be seen in comparison with mixtures the same mass fraction, even for a total of 10% He. From observation of the predicted flow vectors in the weld pool time evolution, he implied that if enough He is utilised, an additional vortex may be formed, as indicated by C in Fig. 7, increasing the weld size by a factor of 3, thus underlining the importance of the Marangoni effect on weld pool dynamics.

More recently, Ogino et al. [63], [64] presented a model of MIG which also takes into account the effect of Fe vapours on the heat and mass transfer. Comparison of the process using pure Ar and Ar mixed with 18% CO_2 suggested that the mode of mass transfer is different in each case for the same heat input. This effect was attributed to greater interelectrode pressures developing in the plasma containing CO_2.

2.3. Optical Flow Diagnostics

Due to the extreme temperatures and high currents in the arc region, experimental measurement of the exact magnitudes of the phenomena therein is difficult and expensive. Unsurprisingly, a plethora of optical techniques have been employed for the study of various aspects of arc welding. For imaging, a camera in conjunction with a neutral density filter [65] may produce good quality photographs of an arc's radiation profile. Phenomena such as droplet transfer can be recorded clearly with a well-chosen interference filter [53], [66]. The resulting images cannot however visualise the flow, since shielding gasses are transparent.

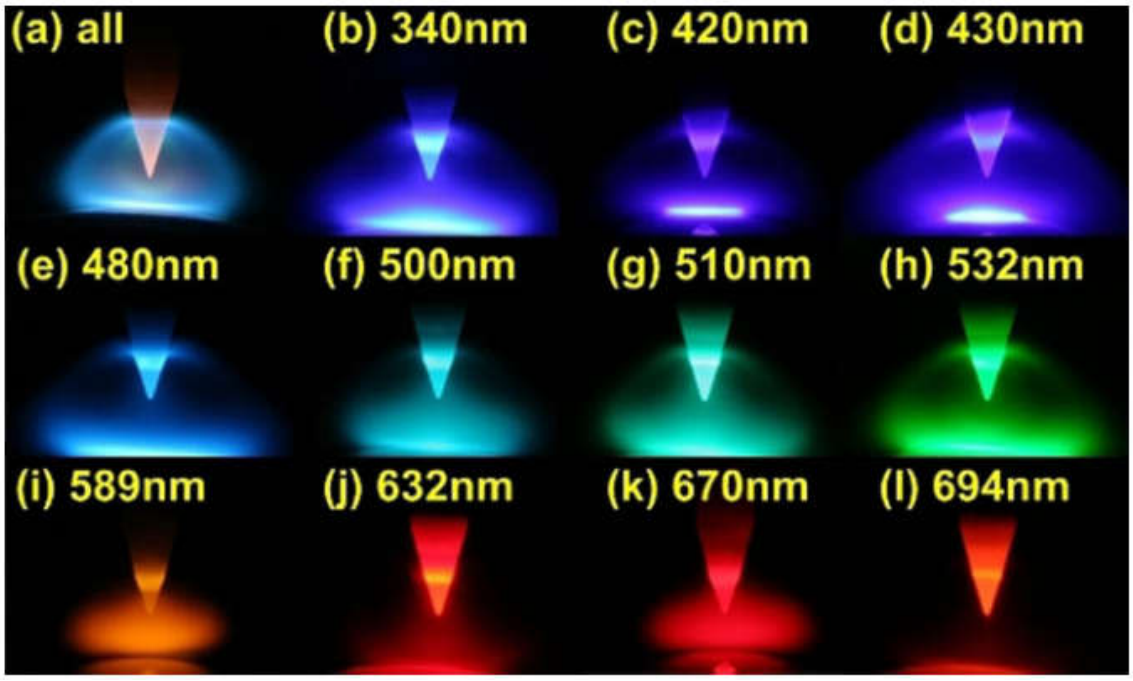

Fig. 8 Images of TIG He arc radiation using different 10 nm FWHM band pass filters [65]**.**

As refractive index gradients are in place within the flow due to the gradients in gas density, it is possible to use the refraction of the light to image the gas and its interaction with the plasma column optically. Schlieren and shadowgraphy techniques have been used previously to visualise gas flow under a variety of conditions [67], [68] and will thus be discussed in greater detail below. Additionally, optical measurement techniques that have been applied to validate arc models within a welding context will be reviewed.

2.3.1. *Shadowgraphy*

When a light beam refracts through a transparent medium, the incoming rays' trajectories will be bent towards some direction when a spatial variation in refractive index is present. During the MHD flow, large temperature and pressure gradients arise. Additionally, there

is a change in bulk density due to the argon plasma mixing with the environment. All three of these result in density gradients in some region of the flow, based on their field distribution [12], [69]. These in turn translate to refractive index gradients, making shadowgraph and schlieren methods useful for imaging the shielding gas flow. These techniques provide a means of imaging the resulting change in ray trajectories.

The simplest method is through a shadowgraph, which is essentially a visualisation of the unilluminated regions the rays create when they are refracted. In the simplest form of shadowgraphy, an object *O* with uneven refractive index may be inserted between a point light source and a screen, as shown in Fig. 9 (left). In terms of light intensity, the bright and dark regions on the projected image are shaped to portray positive or negative gradients of the displacement **ε**. In this manner, variation in the refractive index *n* is visualised through the shadow *S* cast on the screen as

$$|\nabla\varepsilon| \propto \nabla^2 n \tag{25}$$

Change in the distance *g* between the object and the screen results in smaller or larger displacement **ε** of the diverging rays, enhancing or diminishing the effect.

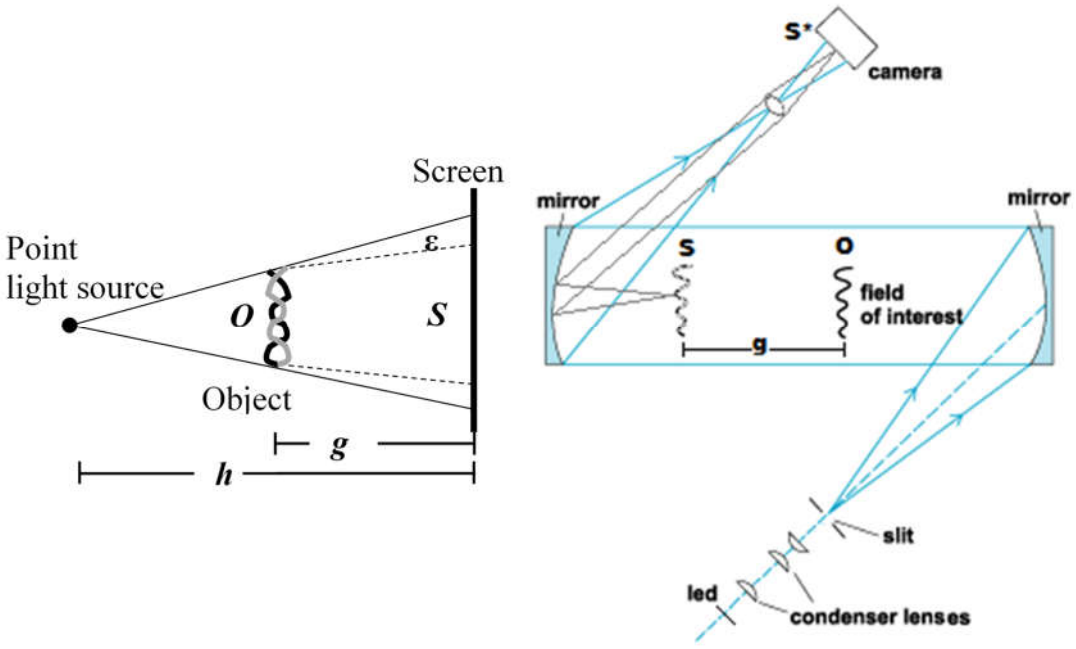

Fig. 9 (Left) Direct shadowgraph layout: An ideal source projects a shadow S of object O onto a screen. (Right) Focused Shadowgraph system, implemented with a Z-type layout. It is comprised of a composite source, long focal length parabolic mirrors, macro lens and camera.

To achieve the best possible image quality through a shadowgraph system, the light must be collimated and not diverging [70], which can be accomplished through the use of a lens or parabolic mirror. To capture the image of the formed shadow *S*, a second element

must focus that image onto the surface of a camera chip or photographic paper, shown in Fig. 9 (Right). The source can be either composite, comprised of a lamp and lens system, or alternatively collimated light such as that of a laser may be expanded through a biconcave lens to achieve a greater imaging cross-section.

In reality, any light source cannot be infinitely small thus the conceptual point source would in practice be an extended one (a superposition of several point sources along a characteristic length)[71]. Since its light rays assume slightly different trajectories, this planar source introduces a "circle of confusion" around the object's projection, which may essentially be regarded as the cause of geometric blur. This distortion becomes more evident with an increase in the source's diameter, requiring a small light-emitting surface area. However, if the source diameter becomes too small (as is the case with lasers), diffraction effects are evident on the captured images, especially in the presence of sharp objects. Apart from the fact that diffraction can be significant in such an arrangement, highly coherent sources cause interference effects in the illuminated cross section, which are the two main reasons that lasers are not preferable for high quality imaging [70].

Despite their limitations, several authors have used lasers to image arc welding processes, mainly due to the intensity attainable through a laser beam and ease to implement. Allemand et al. used a He-Ne laser as a source to produce "focused" shadowgraphs of metal transfer in MIG welding, however no information regarding the flow were visible as the backlight from the laser was very intense and the camera became saturated [72]. In order to block the majority of the arc's light while keeping the intensity of the laser source high in comparison, Okada et al. utilised a band pass filter at 632.8 nm, full width half maximum 6.3 nm in their setup [73]. Since the GTAW spectrum peaks in the 300 – 600 nm region, the details captured in the shadowgraphs showed the flow characteristics clearly, despite the increased back illumination.

This visualisation of the flow showed that the gas flow was affected by variations in the arc current, showing the contribution of the Lorentz force, as shown in Fig. 10. Additionally, the images produced were supplemented with Ar concentration measurements carried out through gas chromatography. This procedure revealed that the boundaries shown in the shadowgraphs may be closely correlated with strong concentration gradients in the gas, thereby determining the coverage capabilities for a given nozzle, a result which assists in the correct interpretation of similar images from subsequent studies.

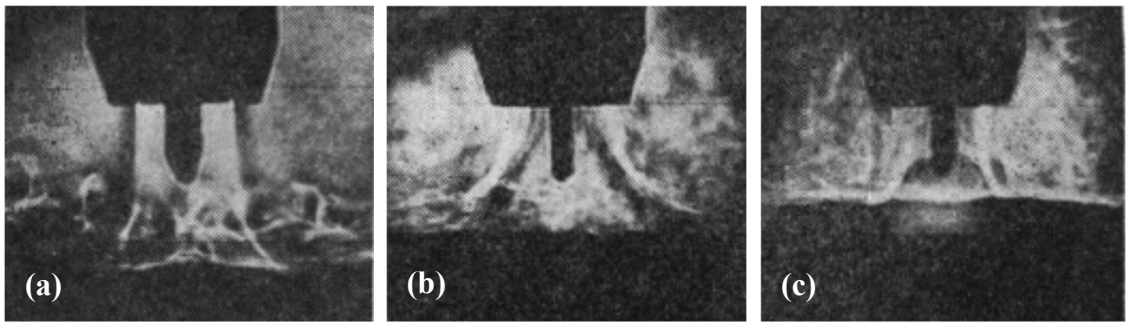

Fig. 10 Argon flow visualisation in GTAW. a) "cold flow", i.e. no arc is struck, b) arc with a welding current of 20 A, c) arc with a current of 300 A. Images taken from [73]**.**

Hou et al. showed that for variable polarity plasma arc (VPPA) welding of Aluminium, the shielding gas flow may influence the heat transfer regimes by influencing the cooling rate of the workpiece and heat affected zone [74]. Analysis of the flow showed that a tilt on the nozzle might introduce undercut in the weld, due to impingement cooling on the weld pool where the jet becomes parallel with the workpiece. He concluded that even with nozzle tilts of up to 4^{o}, the convective heat fluxes and pressure profiles on the weld pool are uneven, affecting the weld's microstructure in addition to compromising the coverage quality, and possibly contaminating the pool with unacceptable levels of nitrogen.

Beyer et al. considered the minimum amount of shielding gas required in order to achieve high quality GMAW welds under realistic conditions [68]. The shadowgraphy technique was employed to visualise the coverage with gas flow rates of 5 to 18 L min^{-1} for nozzles of different diameters under cross-drafts of 1 to 5 mph. The qualitative assessment from the flow's shadowgrams was cross-correlated with quantitative data produced by x-ray radiography. Their analysis suggested that a 12 L min^{-1} flow rate produced acceptable quality welds under most tested conditions. The optical flow visualization established the minimum flow rates at which weld coverage was lost at different levels of side-draft. It was possible to predict the weld quality based on the ratio of the side-draft speed to the shield gas flow rate. Specifically, it was observed that there was no degradation in the weld quality at shield gas flow rates of 10 L min^{-1} and above, for the worst side-draft conditions in a typical shipyard building hall. Shield gas flow reductions were identified as a consequence of the study, producing a more economical and environmentally-friendly welding process with no compromise to the final weld quality.

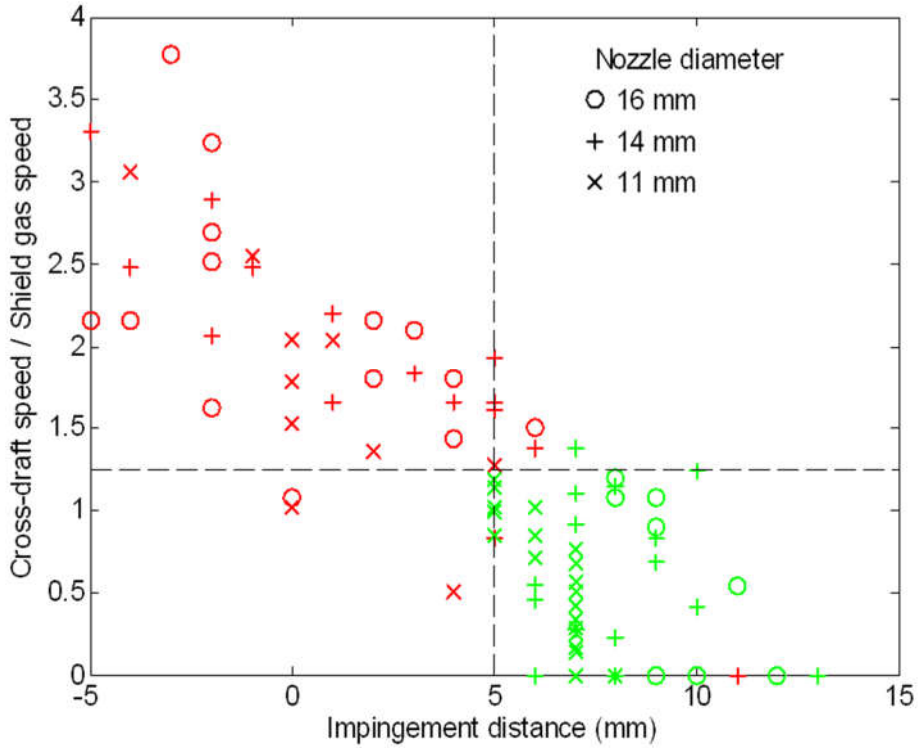

Fig. 11 Comparison of impingement distance, cross-draft speed to shield gas speed ratio, and radiography measurements [75]**.**

Apart from imaging the shielding gas, laser shadowgraphy imaging has been used for several studies in a welding context, such as to image the mass transfer regimes achieved for droplets [66], [76], [77]. Usually the flow visibility on such images is poor at best, because apart from the source problems, the torch is usually completely in focus in order to capture the phenomenon in question. With the torch in perfect focus, the distance **g** shown in Fig. 9 would be close to zero, thus the refractive index gradients would not be visualised. Finally, as shadowgraphy is seldom used as a secondary method of image acquisition in conjunction with another experiment, ease of implementation outweighs the benefits of a precision imaging system.

2.3.2. *Schlieren Photography*

Another commonly used method of imaging refractive index gradients is through the use of a schlieren apparatus, a technique very similar to shadowgraphy but promising a clearer representation of the phenomena under scrutiny. This imaging method has been used to visualise a variety of phenomena, such as supersonic flows around airfoils or jet streams in wind tunnels, flame dynamics or bacterial dispersion [70], [78].

The physics governing this technique may be explained either in terms of geometric or Fourier optics [71]. Either way, one must first consider the refraction of a beam passing

through a gas flow under the nozzle, as shown in Fig. 12. It has been shown that the use of long focal length parabolic mirrors at L1 and L2 in a Z-type arrangement, first described by A. Toepler, minimises aberrations (apart from astigmatism), and offers increased sensitivity compared to simpler layouts [69]–[71], [79], [80], thus this optical arrangement will be used as a reference to briefly describe its operating principles, although comprehensive accounts and practical implementation guides may be found in [69], [70], [79].

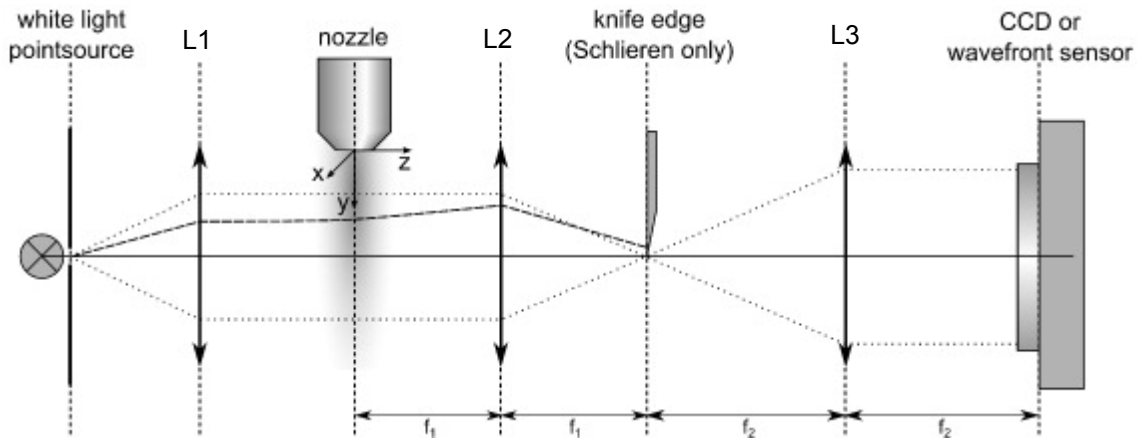

Fig. 12 Basic collimated schlieren/shadowgraphy system. Although collimation is not required, it is preferable to achieve better sensitivity. Image from [81]

Firstly, the source light must be collected and spatially filtered to achieve uniform intensity and shape. Using the Fourier optics interpretation, after collimation at L1, the imaged source light passes through the test area, with the resulting composite image being filtered through a 4-f optical correlator. This optical arrangement can be implemented by arranging the parabolic mirrors (noted L2 and L3) two focal lengths apart [71], thus the object is analysed into spatial frequency components at the Fourier plane from L2 and imaged back into a conjugate plane at the CCD by L3. Introducing a physical cut-off such as a knife edge allows the filtering of a portion of the frequency content contained in the composite image. To achieve an even measuring range, half of the light should be blocked, allowing positive and negative refractive index gradients to be imaged equally on the far field as bright or dark regions. Finally, L3 brings the far field in focus right at the surface of the camera, where the images may be recorded. The difference in focal length between L2 and L3 results in image resizing. Usually a high-speed camera is utilised for flow visualisation, since highly transient phenomena may be analysed in this manner.

The Gladstone-Dale relation, used to relate refractive index with density, can be summarised as [82]

$$\frac{n-1}{\rho} = K \tag{26}$$

Unfortunately, such a simple, linear relation is difficult to apply for a non-isothermal, non-isobaric gas mixture flow, because the molar refractivity K of weakly ionised gases is not constant. Generally, the density variation in the fluid during an MHD flow can be expressed as:

$$\mathrm{d}\rho = \frac{\partial \rho}{\partial \mathrm{T}}\mathrm{dT} + \frac{\partial \rho}{\partial \mathrm{p}}\mathrm{dp} + \frac{\partial \rho}{\partial \mathrm{c}}\mathrm{dc} \tag{27}$$

The fact that temperature T, pressure p and concentration c significantly vary in the flow renders the quantitative evaluation of schlieren images unfeasible as the observed intensity in the detector cannot be attributed to a single source of refraction. Finally, intense light from the plasma arc can locally change the intensity if not completely filtered out (which is very hard), adding to the uncertainty. Thus in the literature, the imaging technique has always been complemented with another experimental method to assess weld quality or with theoretical predictions.

During the 50's, Gibson et al. published two studies detailing the effects of nozzle standoff, diameter and flow rate on gas coverage, which they defined as *"the area on the surface of the workpiece from which air is excluded by the shielding gas"* [12], [83]. schlieren images were utilised to show the Helium (He) or Ar flow under which sufficient coverage was generated on the workpiece. Additionally, to investigate optimal coverage, imaging of the gas flow without a workpiece or arc was carried out. With this experimental layout, a modified wind tunnel was used to channel a side draft onto the weld, deflecting the jet under various flow rates. Aluminium and Titanium spot welds performed under the imaged parameters were used to support the qualitative evaluation from the schlieren.

Results showed that a smaller standoff distance improves the shielding quality and that while nozzle size affected the coverage, no simple relation between the two was evident. Furthermore, by observing the flow under the side currents, they showed that air drafts have profound effects on gas coverage, specifying a wind velocity of 0.5 m/s as the maximum acceptable for a side draft. Also, comparison of the two gases revealed that generally half as much Ar than He was required to achieve the same coverage. Finally, he observed that the flow of Argon is turbulent under flow rates higher than 2 l/min while of that of He is laminar even at 16 l/min, with a 80% Ar 20% He mixture behaving midway between the two.

More recently, Dreher et al. employed a number of optical systems on GMAW and GTAW [9], [13], [46], [67]; amongst them, a Z-type schlieren system was used in order to visualise spatial density gradients of the plasma jet and surrounding area, using these as a validation mechanism for a numerical model. In order to avoid light saturation in the images, apart from a band pass filter, they used a GTAW arc emitting strongly at 750 nm to image GMAW and vice versa. After matching source slit with the cut-off, the refractive index gradient highlighted in the visualisation would be perpendicular to the orientation of the knife edge [70]. And since

$$\frac{\partial \rho}{\partial y} \propto \frac{\partial n}{\partial y}, \tag{28}$$

the images were compared with artificial schlieren, produced by an MHD analysis carried out using ANSYS CFX [45]. The authors proceeded to show a visualisation of the predicted density spatial gradient, a consequence of the computed process variables. Interposing the two images showed qualitative agreement in the results, suggesting that the computed variable fields were naturally distributed.

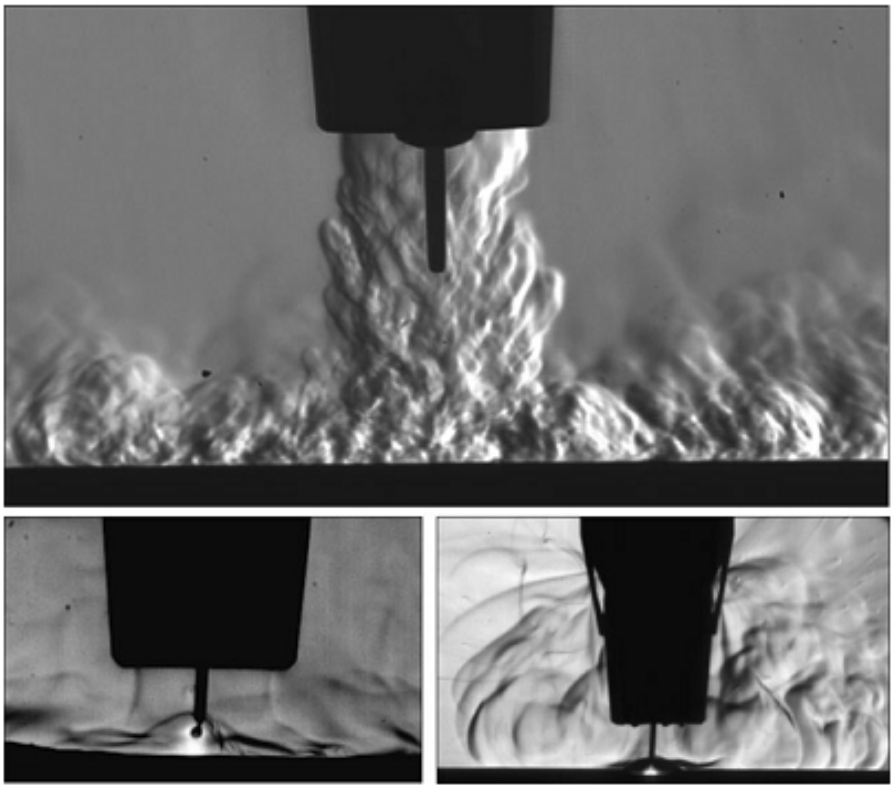

Fig. 13 High speed schlieren of a gas free jet (top), a MIG spray arc (bottom left) and flow profile of a fume extraction torch (bottom right) [46].

Dreher at al. [46] utilised the schlieren system to investigate the influence of different nozzle and contact tip geometries on the turbulence developing in the arc region. Firstly, it was shown from the model that if the flow of gas at the inlet is constricted from narrow boreholes, turbulence may occur within the nozzle due to higher stagnation pressure at the top of the contact tip. Additionally, oxygen measurements were carried out by attaching a lambda sensor to a copper cooled anode for flow rates of 2-18 L/min and for three different bore sizes. These were cross-correlated with schlieren images of the coverage under the same conditions. It was found that to avoid turbulence build-up, relatively large, symmetrical flow cross sections should be maintained within the nozzle. Furthermore, the nozzle should be covering the contact tip entirely, since otherwise turbulence develops rapidly at the exit, as shown in Fig. 13 (top). Schnick et al. [13] concluded that current, torch design and positioning, welding speed and the wire/workpiece materials used may influence the gas flow.

An article containing practical advice on the implementation and applicability of such a system for imaging welding processes was published by Siewert et al. of the same group in early 2014 [67]. The well-established methods and optics behind the technique were discussed within an arc welding context. Thus, four light sources of 50 – 250 W power inputs were compared in terms of the resulting image quality. Still, all images contained identical information although no details were given stating the exposure times, arc current or band pass filter used. Due to the large amounts of radiation emanating from the arc, the camera was heavily saturated at the centre of the plasma column in all instances. To increase the luminous flux channelled to the test area, the light of a GTAW arc was used instead of a conventional lamp, achieving an approximate 1000 W flux. Used in conjunction with a band pass filter at 750 nm where the GTAW arc peaks [84], imaging of the complete inter-electrode region was achieved and it was reported that exposure times were successfully reduced. The work confirmed that regardless of the actual source, matching the source slit with the cut-off type and orientation is important to properly highlight the gradients.

2.3.3. *Particle Imaging Velocimetry*

Although no original particle imaging velocimetry (PIV) or spectroscopy work is presented in this thesis, some points that have important consequences to modelling shielding gas flows in welding are discussed in this and the following sections. PIV can be utilised to measure velocity flow fields, allowing transient flow characterisation [13], [46], [85]. Results can easily be cross correlated with numerical predictions to give more

theoretical weight to measurements and vice versa. The main disadvantage of this method is the requirement of the gas to be seeded with tracing particles, which cannot withstand the temperatures encoundered during processing. Conversely, the benefit of this approach is that contactless measurement of various parameters under 'cold flow' conditions may be achieved, in an environment where physical instrumentation is difficult to setup and operate. Finally, even though the equipment required to implement such techniques is mobile and can be used in industry, it is non-trivial to do so. As such, the usage of PIV for experimental studies in welding processes has been limited.

PIV analysis of a pulsed MIG process was reported in Dreher et al. [46]. Tracking of fine magnesium oxide particles showed that the low velocity shielding gas flow (up to 5 m/s) is accelerated towards the arc during the high and low current phase. As shown in Fig. 14, rotational flow fields were observed during peak currents, promoting air entrainment. This result confirms the notion that the maximum body forces exerted on the fluid, and therefore the highest O_2 entrainment, occur when current is highest. This idea is also supported by MHD theory, where as per eqn. 14, the self-induced magnetic field scales proportionally to the applied current, and according to eqn. 3, the resulting Lorentz forces increase accordingly. The time-independent approach taken in the modelling presented in this thesis can therefore be considered a valid method of predicting the maximum possible O_2 levels for the given inputs over long processing periods.

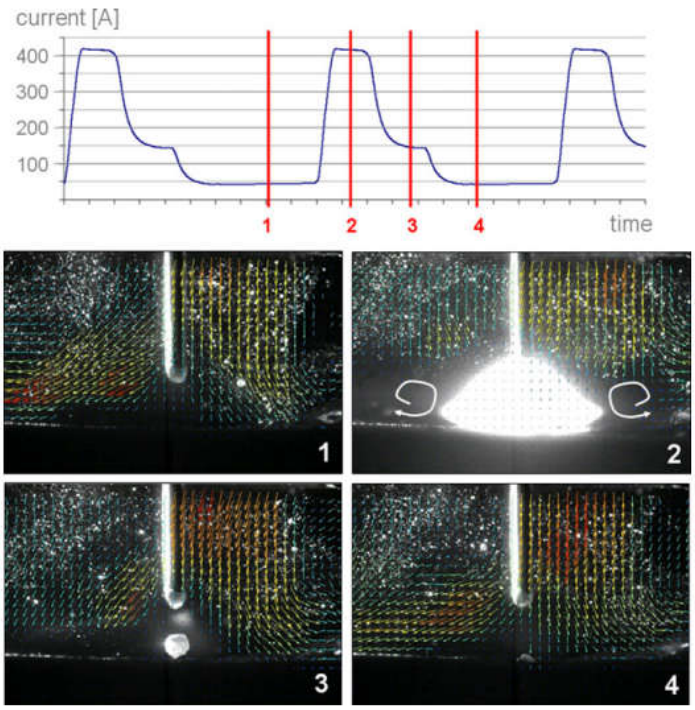

Fig. 14 PIV measurement of pulsed GMAW. Fluid acceleration towards arc peaks during high current phase due to stronger Lorentz forces, suggesting highest O_2 entrainment levels occur during that period.

With regards to torch positioning, it was observed that when the nozzle was tilted at angles greater than 25^{o}, the molten droplets might be transported through areas of higher than acceptable O_2 concentration levels, being contaminated before impinging on the weld pool. The authors recommended the use of a trailing shield to compensate for the loss of coverage under such conditions.

2.3.4. *Plasma Optical Emission Spectroscopy*

Plasma optical emission is a variant of spectroscopy where information about the radiating species is gained by measuring the absolute brightness of their characteristic lines. In equilibrium plasmas, the electron and heavy particle temperature may be determined, while for those not in equilibrium, the "excitation temperature" is measured instead [86]. Experimental temperature measurements have informed arc models since the earliest free burning arc models were implemented. Key results from the use of this technique are briefly presented here, to provide context for the modelling work presented in the following chapters.

In 1976, after earlier investigations, Glickstein used Kodak spectral analysis plates to capture the spectrum emitted through the GTAW arc [87]. He used a lens and slit setup to magnify and image the spectrum onto the plates. The intensity information of the 370 – 490 nm spectra was recorded and translated into temperatures by assuming the plasma was in LTE and using the Boltzmann plot method. Results showed that for a 2 mm long, 100 A arc the temperature peaked at 12,000 ± 2,000 K, at a distance 0.5 mm away from the cathode.

Almost a decade later, Haddad and Farmer introduced a monochromator, photomultiplier tubes and digital acquisition system to the lens – slit arrangement described previously, with the arc emission signal being recorded for 25 μm intervals [88]. They reported LTE temperatures of over 20,000 K for higher current free-burning arcs in air, showing a discrepancy with the previous class of results, like those of [87]. This was attributed to ambiguities associated with the Boltzmann plot method, such as deviations from Planck's law for the emitted light, as well as uncertainty in the measurement of the required constants. The temperature values from the latter experiments generally agreed with numerical predictions of models using the MHD physics presented earlier, as well as measurements of arc temperatures in an inert atmosphere (without flow).

Using a novel, less ambiguous technique, the Stark Broadening of typical emission lines of Ar and Fe was measured simultaneously to diagnose the plasma flow [53]. The measurement was carried out by using correlations of the number densities and temperatures of electrons in terms of the Stark length of each line, established through numerous experimental studies since the early 90's [89]. The arc of a GMAW torch was used, shielded by a 20 L min^{-1} flow rate of either pure, 5% or 20% CO_2 enriched Argon under a 326 A DC current and 20 mm standoff. In addition, high-speed imaging was used to show the intensity distribution of the Ar I and Fe I lines under the resulting mass transfer regime (spray transfer for the pure and 5% case and globular transfer for the 20%).

The resulting temperature measurements showed a maximum temperature of 13,000 K, as shown in Fig. 15; the discrepancies with previous numerical models predicting 20,000 K were attributed to the neglect of the contribution of the evaporated Fe. In terms of the shielding gases, they showed the plasma became hotter with the addition of CO_2, thus affecting the mass transfer mode. Later studies by the same group confirmed the temperature distributions and reported that there is evidence to suggest that LTE is in place [24].

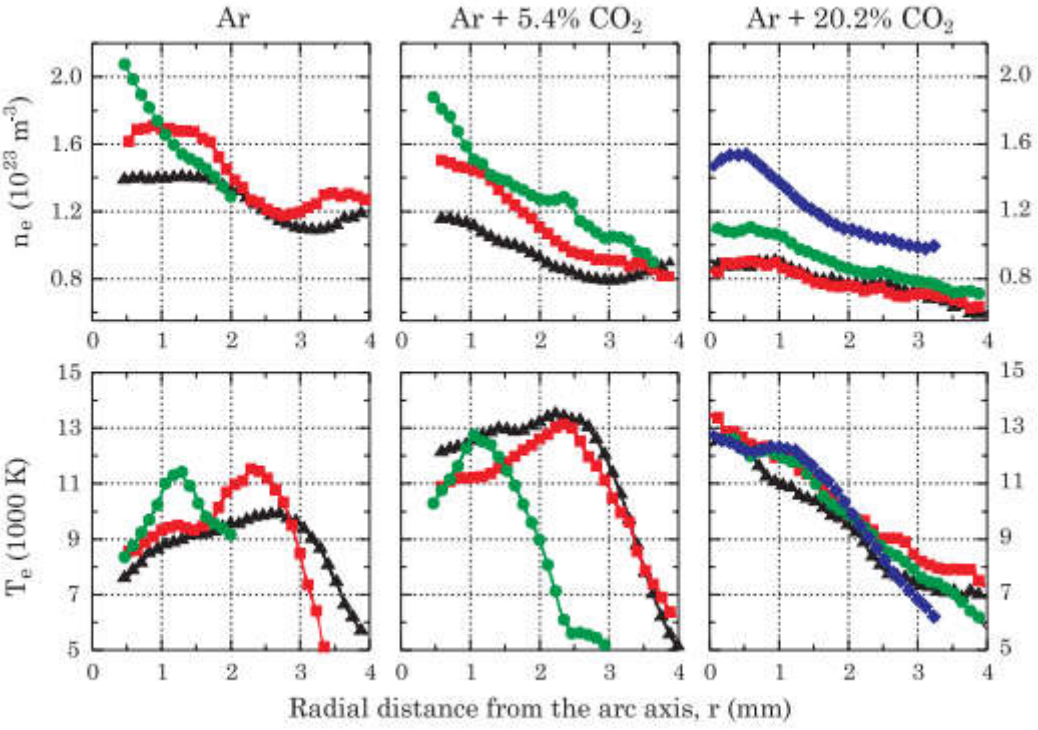

Fig. 15 Radial distribution of electron density and temperature at (black) 3 mm, (red) 4.5 mm, (green) 6 mm and (blue) 7.5 mm above the cathode [53].

Tanaka et al. carried out spectroscopic measurements of the work functions of three different electrodes: pure tungsten (W), 2% thoriated (Th) or 2% lanthanated (La). The measurements were made by utilising the photoelectric effect, through excitation of the GTAW cathode using an Nd:YAG and a Dye laser. They used Ar shielding gas, for 100 and 200 A free burning arcs. They showed that for 200 A, the work functions of the electrodes would be in the 2.8 – 4.6 eV range, similar to the values given for pure W, as well as Th and La oxides. For the 100 A, the work functions were reported to be as low as 2 – 2.9 eV, suggesting reduced benefit from enriched electrodes for low power arc processes.

In 2008, using a simplified spectroscopy setup, Mirapeix et al. developed a system for real-time monitoring of defect appearance during arc welding [90]. Through an approach called the line-to-continuum method, intensity information of a specific line (preferably one not affected by self-absorption) is compared with its own background signal. By introducing signal filtering and smoothing procedures and carrying out test welds, it was shown that when seams were introduced in the weld, strong correlation could be detected as peaks in the characteristic intensity ratio introduced by the technique. It was concluded that the threshold for error detection would depend on the allowed deviation of the monitored line, suggesting that high value component welds should show signals like those under experimentally validated "good weld" conditions. Moreover, this approach could be combined with an iterative method for the calculation of electron temperatures from the spectroscopic data [4], allowing even more control over the process.

2.4. Summary

The literature survey presented in this chapter identified that the study of arc welding is a mature field, with decades of rigorous numerical modelling underpinned by measurements and accumulated practical knowledge. Although questions about various aspects of welding arcs and the underlying physics remain unanswered, experiments have by and large established the macroscopic validity of MHD arc models. The main application of such models has been the calculation of heat and mass transfer to the melt pool, and the self-consistent prediction of weld profiles. Several numerical studies have been carried out concerning shielding gases for both GMAW and GTAW, focusing mainly on heat, momentum and mass transfer as well as process dynamics associated with the use of different gases or mixtures.

Only a small number of studies are available regarding coverage and local shielding in arc welding. Oxygen measurements under "cold" conditions, as well as process simulation and visualisation have been reported for GMAW and GTAW torches. Despite this, no studies were identified which utilised these methods systematically to relate in situ flow conditions under different process settings with the quality of weld samples produced experimentally. Limited work has been carried out specifically for steel in this context, which has a higher tolerance for contamination compared to more reactive metals such as Al or Ti.

The objective of this thesis is therefore to use optical diagnostics to visualise gas behaviour for processes which have not been systematically analysed in this manner previously. The fields of application covered in the following chapters range from joining processes, where limited work has been published, to areas such as AM of metals, where no such studies have been reported. In addition, the underpinning science introduced in this chapter is utilised in the construction of numerical models allowing deeper understanding of the observed phenomena. Whilst the use of MHD modelling is well established for bead on plate welds, no such models have been published for fillet welds. Finally, the combination of modelling and visualisation is applied to understand and potentially improve novel AM processes in which hydrodynamic phenomena have not yet been characterised fully such as AM and LPBF.

3. Optimisation of gas shielding during GMAW

As discussed in the previous chapter, GMAW uses a flow of argon (Ar), carbon dioxide (CO_2), or a mixture thereof, to limit chemical reactions of the molten metal with the surrounding air. If shielding conditions are poor, then air entrainment on the arc jet leads to weld pool or droplet contamination: unwanted reactions occur between O_2 and N from the air and the liquid metal including any alloying elements it contains, leading to increased spatter and large variability in the properties of welded joints [47], [91]. For steels, excess CO is released after solidification of the metal, forming pores [1]. Such discontinuities in welded joints reduce the effective cross section and accumulate stresses, constituting potential crack initiation or propagation sites.

The volumetric flow-rate of the gas supply should therefore be set sufficiently high to achieve the required weld quality. A shield gas flow-rate of 15 to 20 litres per minute (l/min) is often used in GMAW, but in practice welders sometimes use as much 36 l/min. Such overuse of shield gas is wasteful, impacts negatively on the environment and can lead to turbulence induced porosity in the weld. Similarly, reducing shield gas usage is also important in the additive manufacture of metals via directed energy deposition processes based on welding, where localized trailing shield units use flow-rates as high as 195 l/min [92]. Although many models of welding are reported in the literature, and shield gas coverage has been visualized by experimental techniques, there has been no systematic study reported that specifically aims to optimize the shield gas usage.

The majority of the models outlined in chapter 2.1 focus on the behaviour of the arc core, high velocity plasma jet or droplet/weld pool dynamics: the low velocity nozzle flow and thus optimum coverage during welding have not been thoroughly examined. Furthermore, the equations of species transport are commonly applied to the mixing and de-mixing of metal vapour with Ar [48], [49] rather that to model an Ar-air plasma in a GMAW context. The key features of the model in this chapter are therefore the interaction of the plasma jet with the low velocity nozzle flow, and the introduction of the transport of air into the plasma as introduced for plasma spray processes in to a GMAW context.

This chapter presents a systematic study on the minimum flow conditions with which to adequately shield an acceptable bead-on-plate weld using a combined experimental and modelling approach. An advantage of the combined experimental and modelling approach is that the sensitivity of the shield gas coverage to variations in these process

parameters can also be determined in order to identify their relative importance in maintaining weld integrity.

Section 3.1 describes the schlieren setup that we used to visualise GMAW under typical workshop conditions. Pure Ar shield gas was used in this set of experiments, to enable direct comparison with the model. Section 3.2 gives details of the MHD finite element model used to simulate the process, based on solid core filler wire and pure Ar shield gas. In section 3.3, the model is used to examine temperature, pressure and Ar concentration in the weld region and thus understand the refractive index gradients observed optically. Using a combination of experiment and simulation, parameters that influence the shield gas coverage (such as shield gas flow-rate, nozzle stand-off and angle) were varied systematically in order to determine the minimum shield gas input for which weld quality was not compromised. The final weld quality was validated with x-ray radiography in order to determine a pragmatic limit of O_2 concentration for mild steel. A microstructural analysis of the welded samples was performed to understand the metallurgical changes incurred and correlate with the diagnostics. In section 3.4, the process understanding gained from solid wire and pure Ar is used to perform schlieren imaging of more industry-relevant consumables, such as solid wire with 80% Ar / 20% CO_2 shield gas, and flux-cored wire with 86% Ar / 12% CO_2 / 2% O_2 shielding gases. Gas-shielded, flux-cored arc welding (FCAW-G) is a GMAW-like process that is commonly employed in industry but there are no reports of schlieren imaging or of a systematic study of the minimum shield gas levels required for this process.

3.1. Experimental setup

Fig. 16 shows a schematic of the optical setup that used Toepler's double parabolic mirror arrangement in order to minimise optical aberrations [79]. Two 150 mm diameter, parabolic field mirrors with a focal length of 1.27 m, M1 and M2, were located approximately two focal lengths apart. Aligned in a Z-type arrangement, M1 collimated the image formed at the source slit while M2 focused it to a spot. Ideally the included 'Z' angles should be less than 3^0 in order to reduce the separation of the tangential and sagittal focus planes of M2. However, in order to incorporate the welding torch between the mirrors, whilst keeping the distance between the mirrors within the confines of the welding bay, it was necessary to increase the 'Z' angles of the mirrors to approximately 6°. The result was a small amount of astigmatism in the recorded images.

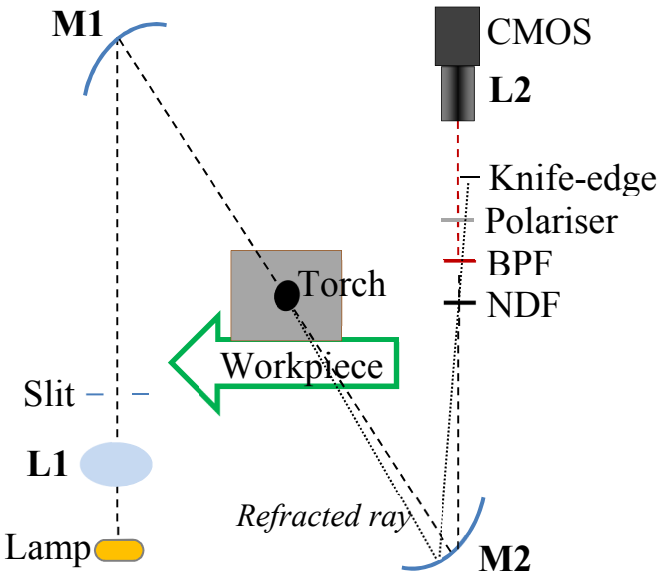

Fig. 16 Schematic of Z-type schlieren and GMAW setup. The optical system comprised of a 200 W tungsten filament lamp, parabolic mirrors, a combination of filters and a CMOS camera.

Illumination was through a composite source comprised of a 200 W tungsten filament lamp, two plano-convex aspheric lenses (D = 75 mm, f = 50 mm) mounted together to form (L1) and a rectangular slit. The shape and size of the source slit determines the sensitivity and measurement range of the schlieren system [70]. We used a 2 mm × 6 mm rectangular source slit with the long edge vertical, as recommended by Siewert et al. for welding applications [67]. The source slit was positioned at the focus of M1, to produce an image of the source at the focus of M2.

In order to match the image created at the source slit, a vertical knife-edge cut-off was positioned midway between the tangential and sagittal focal (Fourier) planes of M2 using a micrometer precision XY stage. Darker or brighter regions in the initial image are created by introducing the knife edge, through the blocking of rays that deflected from their collimated path due to refraction by flow features. Hence, camera images recorded an intensity proportional to the gradient of the refractive index $\partial n/\partial x$, which in turn is proportional to the density gradient $\partial \rho/\partial x$, where the x-direction is taken to be horizontal. In order to achieve a uniform measurement range, 50% of the image of the source slit was blocked by the knife-edge.

The spectroscopic emission profile of the tungsten-halogen filament imaged through the source slit peaked around 630 nm, whilst GMAW arcs with stainless steel have shown relatively low intensity emission in that region [84]. Therefore a 633 nm ±1 nm full width at half maximum band-pass filter (BPF) was used to reduce light from the arc, a polariser was used to remove glare from the workpiece, and a neutral density filter (NDF) reduced the overall light intensity to an appropriate level for the camera [23].

A monochromatic CMOS camera (Flea 3) recording at 150 frames per second (fps) with a resolution of 1280 × 1024 pixels, fitted with a telephoto lens (L2) (f = 75 − 250 mm) was used. The images captured at this lower frame rate have a longer exposure time than with a high-speed camera, as commonly employed in visualisation studies, which is more suitable for the steady-state welding of long weld seams.

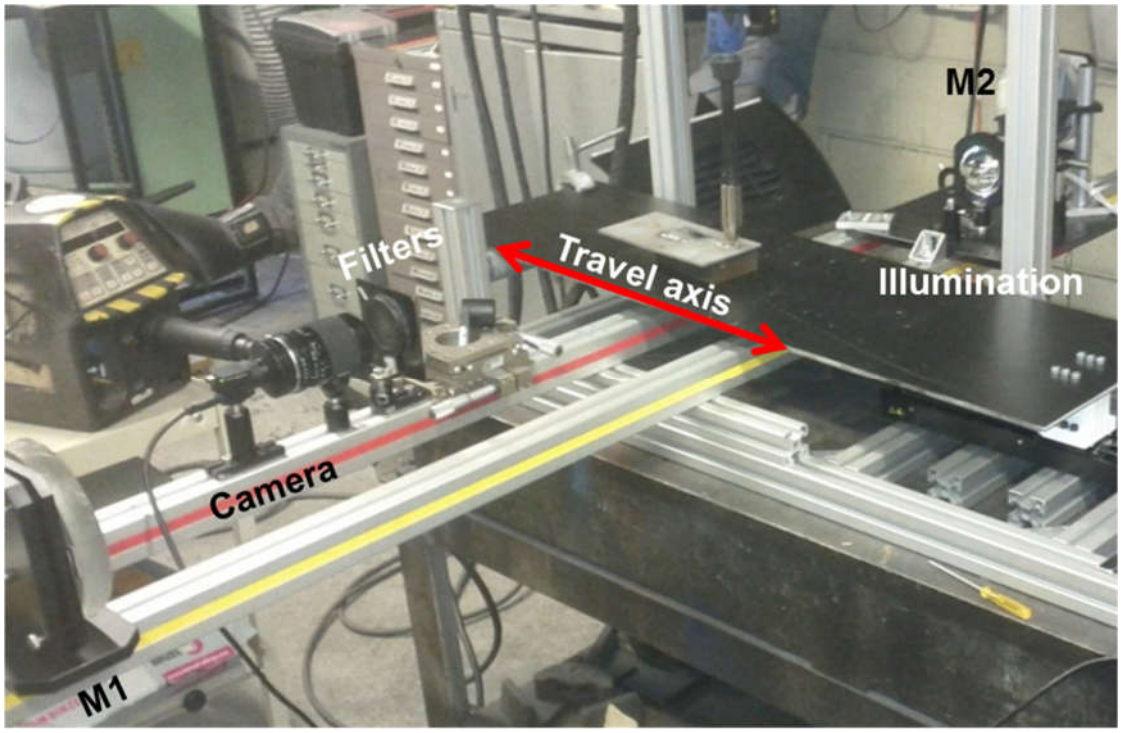

Fig. 17 Optical setup perpendicular to moving plate and stationary torch rig. The yellow rail on the schlieren system comprises the illumination and collimating element, whilst the red rail carries the light collection, filtering and capturing elements.

The automated welding setup, shown on Fig. 17 along with the schlieren system, incorporated a typical shipbuilding production unit, comprising a stationary Binzel straight neck torch with a 16 mm diameter nozzle, connected to a transformer-based Kempii welder and inert gas supply. The welding torch remained stationary whilst the workpiece was moved on a translation stage beneath it, enabling the schlieren system to remain static. The workpieces were 4 mm thick plates of DH36 grade mild steel, which were ground prior to welding to remove primer and expose the surface grain. An 80 mm long weld bead was deposited on to the workpiece that moved with a constant travel speed of 5 mm/s. Other default weld parameters are shown in Table 1. From this default setup, the gas flow was imaged for welds carried out under variation in flow-rate (6 – 15 l/min), nozzle stand-off (10 – 20 mm) and angle (0^{o} – 20^{o}-). An electronic flow meter was used at the nozzle's end, with a measurement accuracy of ±1 l/min. Independent radiographic

examination of a 100 mm length from all welded plates was carried out to determine the presence of porosity.

Table 1 – Welding parameters

Constant voltage V_{set}	28 V	Wire thickness	0.9 mm
Cathode voltage V_c	15.6 V	Workpiece thickness	4 mm
Nozzle stand-off	10 mm	Travel speed	5 mm/s
T_{amb}	300 K	Wire feed speed	9 m/min

3.2. MHD Model

3.2.1. *Geometry and meshing*

As discussed in the introduction, the generic physics governing the MHD effect in welding arcs are well utilised and established. However, appropriate geometric assumptions can be made to simplify and formulate the equations so that they are solved efficiently and accurately using COMSOL multiphysics software. Fig. 19(a) shows the modelled geometry comprising a 2D axisymmetric plane that is rotated about the centre of the filler wire. The lengths corresponding to the labels A-K in Fig. 19(a) are given in Table 2. The geometry was partitioned to form a grid of Lagrangian triangles with varying size. A convergence study showed that a minimum size of the order ~0.1 mm around the arc region provided acceptable accuracy and convergence time. A plot of the normalised difference between different solutions from the convergence study is shown in Fig. 18. The complete mesh comprised ~12,400 domain elements and ~670 boundary elements, yielding a model that required ~5 GB of RAM and converged in ~20 minutes on a Hewlett-Packard Z420 Workstation.

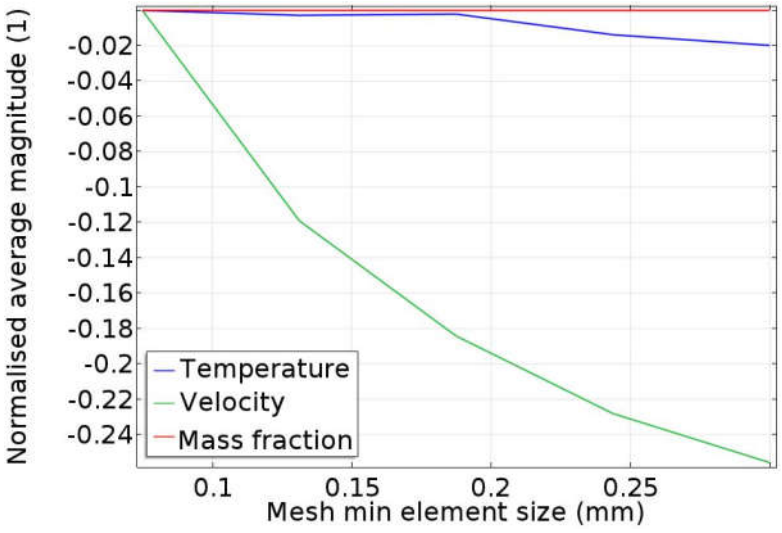

Fig. 18 Mesh convergence study results. Velocity is the most sensitive to mesh variation, with up to 25% difference with the coarsest mesh used. A minimum mesh size of 0.1 mm produced results within 2% of those acquired with the finest tested mesh.

To incorporate variations in the nozzle angle, a 3D half symmetry model was also produced, Fig. 19(b). It comprised ~206,600 domain elements and 12,700 edge elements and required ~45 GB of RAM and ~6 hours to converge. A similar mesh to the 2D case was utilised.

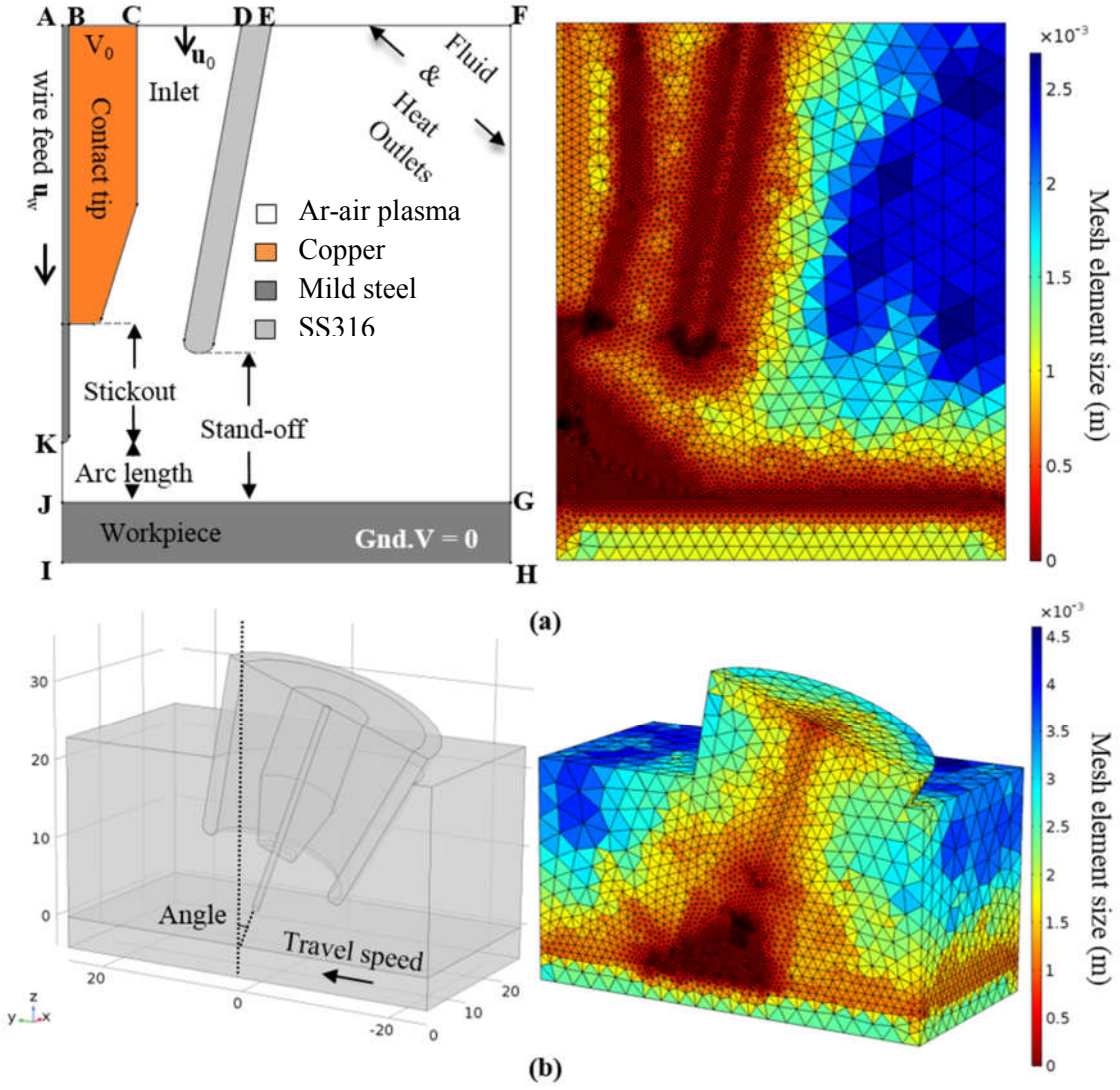

Fig. 19 (a) 2D axi-symmetric model, using COMSOL multiphysics software. Left: Schematic of nozzle end, contact tip, wire and metal plate, and external boundary regions. Right: Typical mesh with locally refined around the arc area with elements sized ~0.1 mm. (b) 3D half-symmetry model at 20° angle and typical mesh at same tilt.

Table 2 – 2D computational domain lengths

Length (mm)	AB	BC	CD	DE	EF	FG	GH	HI	IJ	JK
	0.45	4.55	7	2	16	32	4	30	4	5

It has been shown that the largest turbulence levels in the shield gas coincide with the highest current in the GMAW arc cycle when the Lorentz forces are at their maximum [9], [46]. Therefore, we assume that the largest degree of entrainment of air into the plasma and workpiece occurs at this condition, and used a time-independent formulation

of the conservation equations (described in the following section) corresponding to a steady-state flow at the maximum current and voltage condition. An arc length of 5 mm was used, which is representative of the high current and voltage phase of the arc cycle. The melt pool was excluded from the models on the assumption that the shape of its molten surface has a relatively small effect on the shield gas flow.

The effect of Fe vapour in the plasma was not included in our models. Fe vapour has a noticeable effect on the plasma, typically reducing its temperature from ~20,000 K to ~16,000 K. As a consequence of overestimating the plasma temperature, our models will overestimate the conductivity and hence overestimate the current and Lorenz force. An increased Lorenz force increases air entrainment into the plasma and therefore provides an underestimate of the shielding condition achieved. A conservative estimate of the shielding condition aligns with the aim of this systematic study to minimize shield gas usage.

The models assumed a filler wire made of mild steel and shielding of pure Ar surrounded by air of a standard composition (20.95% O_2). A copper contact tip and stainless steel nozzle, with geometries modelled to match those used experimentally, were included in the computational domain. The material properties for mild, stainless steel and copper were taken from [57], [93], [94]. The plasma, treated as a multicomponent gas with a distributed mass fraction, was assumed to be in local thermodynamic equilibrium (LTE), indicating that electrons have the same temperature with heavy particles. This is a widely accepted and experimentally validated assumption [24] that enables the use of a single temperature variable for all species in the gas mixture. Consequently, the plasma's thermophysical properties (density, heat capacity, viscosity, thermal and electrical conductivity) were expressed as a function of temperature for the range of 300 – 30,000 K as well as the mass fraction of air. Such data have been generated through the Chapman-Enskog method [95], but including some recently updated collision integrals for the Ar and N species, as presented in [28] and [27], respectively.

3.2.2. *Governing equations and boundary conditions*

The MHD equations for conservation of mass, momentum, energy, current, magnetic potential and species, described in detail in chapter 2 and [96] were numerically solved using COMSOL multiphysics software. Despite its shortcomings in fully resolving the energy dissipation across all different length scales within the flow, the two equation RANS k-ε turbulence model was used due to its numerical stability and robustness. A

turbulence model was useful in enhancing the predictive capability of the model through the use of an additional diffusion coefficient, as discussed in chapter 2. The governing equations were solved using a combination of the double dogleg and Newton – Raphson solvers. The input values used in the model were the default welding parameters shown in Table 1.

The conditions applied to the external boundaries of the geometry (labelled in Fig. 19a) are summarised in Table 3. Radiation losses were prescribed on all metal surfaces, as per eqn. (11), At the rounded wire tip and workpiece surfaces, Neumann conditions were imposed on the heat transfer equation as per equations 23 and 24. A convective heat transfer h = 50 W/m^2 was used on the boundaries exposed to ambient convection.

Table 3 – External boundary conditions

	Fluid flow	**Temperature**	**Electric field**	**Species Transport**
AB	n/a	$T = T_{amb}$	$-\mathbf{n} \cdot \sigma\nabla V = 0$	n/a
BC	n/a	$T = T_{amb}$	V = 13 V	n/a
CD	$\mathbf{u} = -\mathbf{n}\cdot u_0 = Q_0/A_{inlet}$	$T = T_{amb}$	$-\mathbf{n} \cdot \sigma\nabla V = 0$	$\omega_2 = 0.0001$
DE	n/a	$T = T_{amb}$	$-\mathbf{n} \cdot \sigma\nabla V = 0$	n/a
EF	p = 0	$-\mathbf{n} \cdot \mathbf{q} = -h(T_{amb} - T)$	$-\mathbf{n} \cdot \sigma\nabla V = 0$	$\omega_2 = 0.99066$
FG	p = 0	$-\mathbf{n} \cdot \mathbf{q} = -h(T_{amb} - T)$	$-\mathbf{n} \cdot \sigma\nabla V = 0$	$-\mathbf{n} \cdot \rho D_2^o \nabla\omega_2 = 0$
GH	n/a	$-\mathbf{n} \cdot \mathbf{q} = -h(T_{amb} - T)$	$-\mathbf{n} \cdot \sigma\nabla V = 0$	n/a
HI	n/a	$-k\nabla T = 0$	V = 0	n/a
IA	Axial symmetry	Axial symmetry	Axial symmetry	Axial symmetry

Additionally, to aid convergence at low temperatures, the thin layer method [57] was used at the wire tip boundary to model enhanced heat transfer due to local charge accumulation. A layer thickness of 0.1 mm was specified, over which the minimum thermal conductivity $k_{min}$was that of ionised Ar, defined as

$$k_{min} = \begin{cases} k(T_0, \omega_1), & k(T, \omega_1) \leq k(T_0, \omega_1) \\ k(T, \omega_1), & k(T, \omega_1) > k(T_0, \omega_1) \end{cases} \quad (29)$$

Giving a rough measure of the energy available within the plasma sheath, T_0 = 10,000 K was used. At the inlet, the prescribed turbulent intensity I_{t0} and length scale L_{t0} were defined as

$$I_{t0} = 0.16Re^{-1/8} \tag{30}$$

$$L_{t0} = 0.07D \tag{31}$$

D is the hydraulic diameter of the nozzle at the height of the contact tip, which was also used as the characteristic length of the Reynolds number in (17). Finally, all the magnetic field vectors were set to 0 across all boundaries by imposing

$$\mathbf{n} \times \mathbf{A} = 0. \tag{32}$$

3.3. Results

3.3.1. *Variation of shielding gas flowrate*

Keeping all other welding parameters as shown in Table 1, the shielding gas flow-rate was varied in the range Q_0 = 6 – 15 l/min. Fig. 20 shows the refractive index gradients in the horizontal direction $\partial n/\partial r$ recorded by schlieren imaging for the two extreme flow-rates. These images are taken from videos which are available online for all the flow-rates tested (6, 9, 12 and 15 l/min) in the additional material accompanying [96]. The refractive index gradients are primarily due to variations in temperature, pressure and gas concentration averaged through the measurement region. Although the interdependence of these three parameters makes it difficult to draw quantitative data directly from the schlieren images, they reveal a great deal of qualitative information regarding the flow. The steady state vortex (marked V in the images) is established further behind the torch at higher flow-rates due to the increased momentum of the shielding gas from the nozzle. A dark, bell-shaped line marked T is visible in both images, primarily due to steep temperature gradients around the arc. Below the nozzle sidewalls, vertical lines marked C indicate the concentration and temperature gradients at the interface between the shielding gas and the surrounding air. An increase in air mass fraction under the nozzle, and hence poorer shielding performance, is indicated for 6 l/min by the blurriness and recessed position of the C lines due to a greater degree of gas intermixing and the increased separation of the T line from the plate surface.

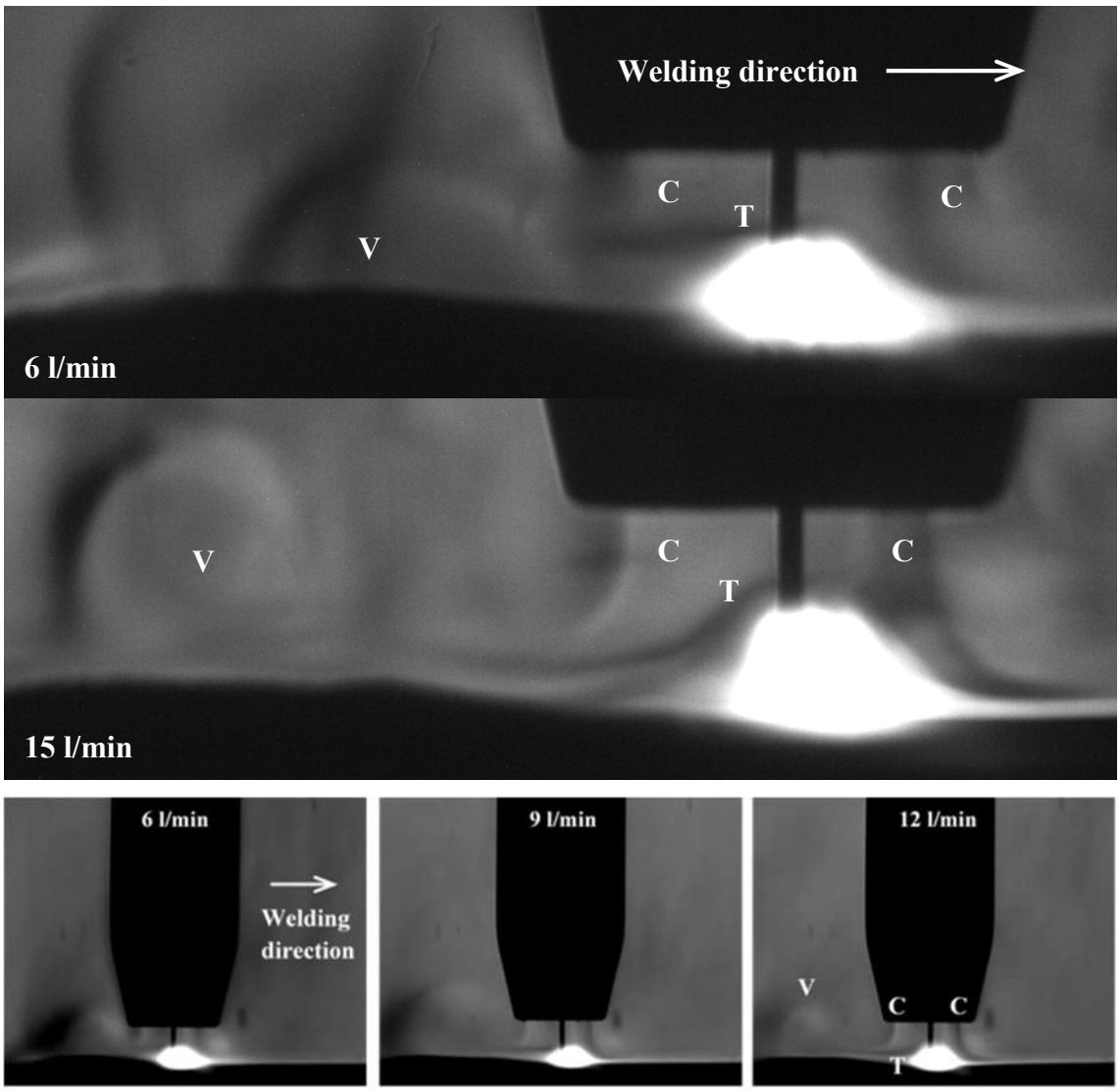

Fig. 20 Schlieren frames under low (top) and high (middle) shielding gas flow-rates. The steady state vortex (V) behind the torch, a bell-shaped line (T) primarily due to steep temperature gradients around the arc, and vertical lines below the nozzle sidewalls (C) due to concentration and temperature gradients at the interface between the shielding gas and the surrounding air, are visible in both cases. (Bottom) Time-averaged schlieren images (250 frames), with steady-state flow features.

The DH36 bead-on-plate samples produced at each flow-rate were inspected in order to determine the weld quality. Fig. 21 shows that a 6 l/min shield resulted in clear porosity in the cross-section (top row), x-ray image of a 20 mm length (middle row) and visual inspection of the weld seam (bottom row). Flow rates of 9 l/min consistently produced welds which satisfied specification requirements for presence of porosity. In effect the welds were free of porosity. Weld hardness measurements showed no significant differences from welds produced under higher gas flow conditions.

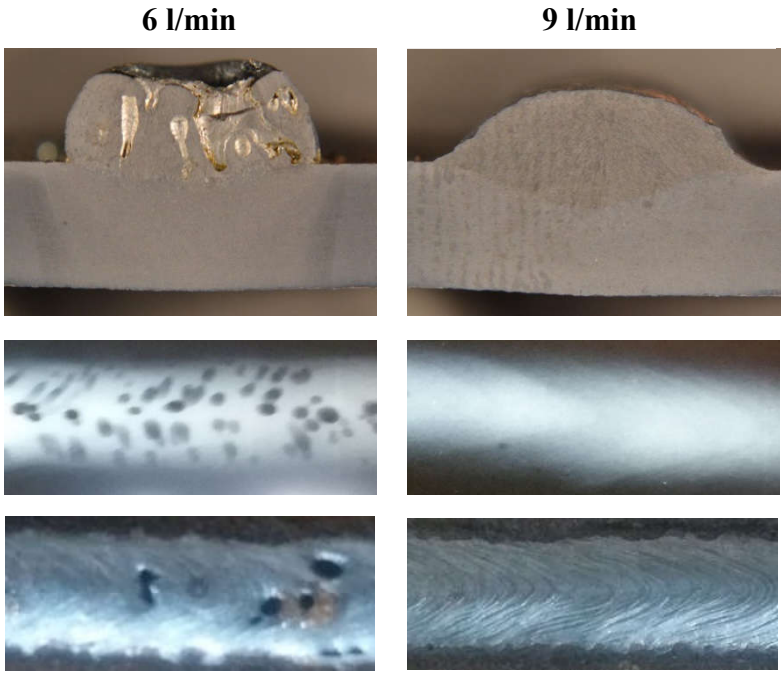

Fig. 21 Inspection of bead-on-plate DH36 samples, made using 0.9 mm mild steel wire and pure Ar shielding with different shielding gas flow-rates. Weld macrographs (top), radiographic imaging (middle row) and weld seam visual inspection (bottom row) all show cluster porosity at 6 l/min (left hand column). All flow-rates at 9 l/min (right hand column) or greater produced acceptable porosity.

Although it is difficult to extract the temperature, pressure and gas concentration quantitatively from the schlieren images, it is straightforward to use the values calculated from the numerical model and to plot the $\partial\rho/\partial r$ density gradient to produce an "artificial schlieren" image.

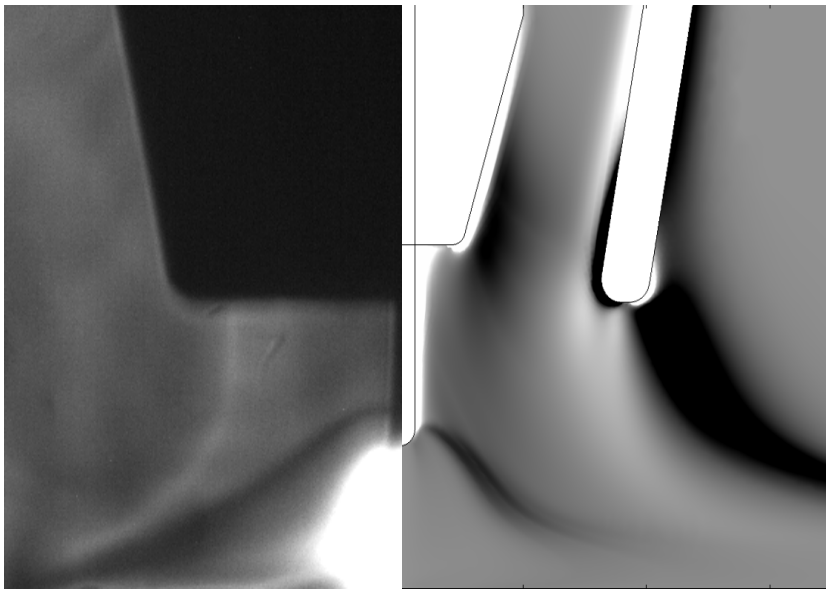

Fig. 22 Comparison between shielding gas visualisation through an experimental schlieren image (left hand side) and numerically calculated density gradient plot (right hand side), at 12 l/min flow-rate.

Fig. 22 shows a direct comparison between an experimental and an artificial schlieren image. The model successfully portrays the observed $\partial n/\partial r$ features, which indicates that the underlying temperature, pressure and concentration gradients are computed with acceptable accuracy to describe the main features of the flow. Discrepancies in the far

field of the flow are visible between the two images, which can be attributed to transient effects which are averaged out in the steady-state model.

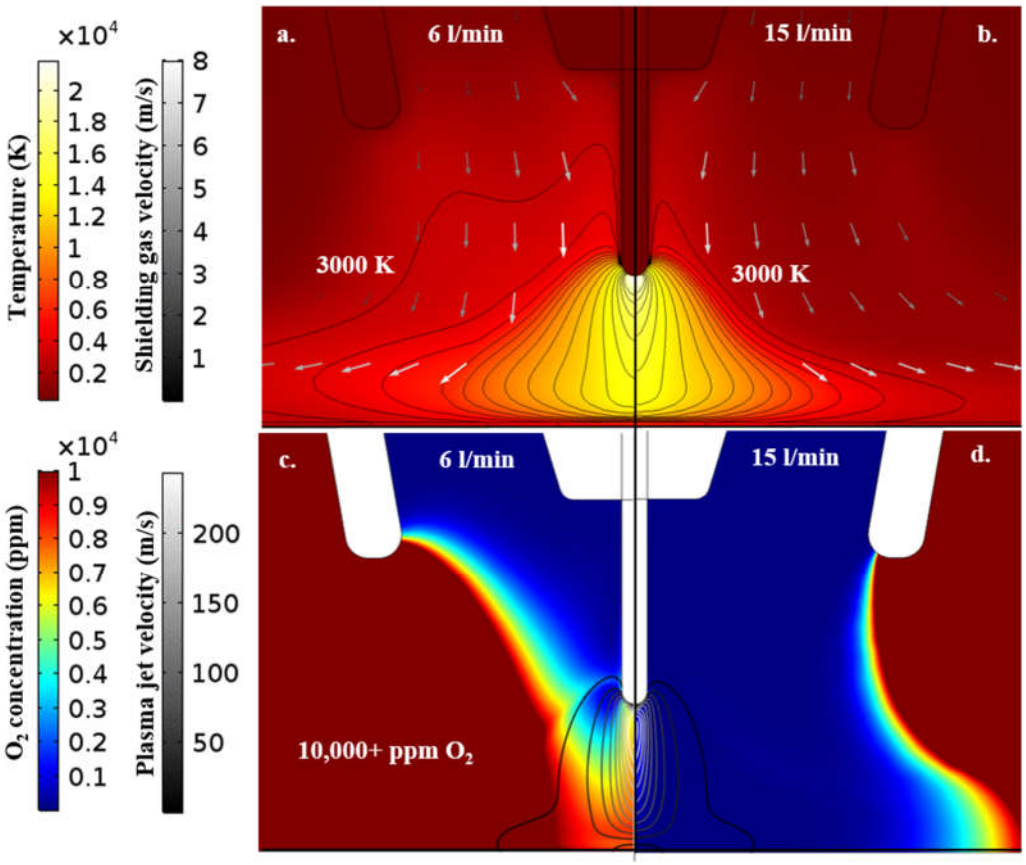

Fig. 23 Simulated temperatures (top) and O2 concentration profiles (bottom) for a 195 A arc. The low velocity gas shield is visualised by arrows (top) while the high velocity plasma jet area is indicated by grayscaled contours (bottom).

The top row of Fig. 23 compares the temperature calculated from the numerical model at the two extreme shielding gas flow-rates. The characteristic bell shape of the GMAW arc is clearly seen. Superimposed on the plots are isothermal contours plotted in 1000 K intervals, and vectors that are coloured and scaled proportionally to the fluid's velocity, but truncated to 8 m/s to show the relatively low velocities characteristic of the shielding gas flow. Increasing the flow of gas from the nozzle has a mild cooling effect in the atmosphere under the nozzle: the 6 l/min case results in higher temperatures than those with 15 l/min. For the 6 l/min case, the fluid has lower momentum when exiting the nozzle, indicated by ~50% lower bulk flow velocities compared to the 15 l/min case. The convective heat transfer at 6 l/min is therefore weaker, as shown by the higher position of the 3000 K isotherm, which is indicated in the figure for both flow-rates. Conversely, the higher velocities at 15 l/min suggest that a larger fraction of the heat around the arc is convected downwards, adding more heat to the workpiece. This effect is seen in the cross-sections of Fig. 21, where penetration is deeper and the heat affected zone is wider

(boundaries out of image) at 9 l/min compared to 6 l/min. These observations suggest that distortion can be reduced at lower shielding gas flow rates.

The bottom row of Fig. 23 shows contours of the fluid velocities above 10 m/s, which are characteristic of the high velocity plasma jet. The fluid is accelerated inwards towards the regions of higher current and magnetic field at the wire tip due to Lorentz forces (the pinch effect). The difference in the plasma jet velocity between the two shielding gas flow-rates is negligible. The bottom row of Fig. 23 also shows the O_2 concentration in parts per million (ppm) with the scale truncated at 10,000 ppm, which corresponds to the ~5% of O_2 found in atmospheric air. It can be seen that air entrainment is severe in the 6 l/min case as a large mass fraction of O_2 is present in that area under the nozzle. In contrast, 15 l/min provides an inert atmosphere with only trace amounts of O_2. The reduced downwards momentum of the flow at 6 l/min compromises the flow's capability to resist the inwards pull effect of the pinch effect. These numerical results show that as the total momentum of Ar exiting the nozzle increases, the net outwards flow is stronger, while the pinch of the arc remains the same. As a result, the boundary after which O_2 content increases exponentially is pushed outwards, away from the filler wire and melt pool. Consequently, resistance to air entrainment and coverage area increase with input flowrate.

The effect of the total momentum carried by the flow contributing to resist air entrainment can be quantified by determining the area over which O_2 levels are low. For the range of input flow-rates of interest, the calculated O_2 concentration at the surface of the workpiece was plotted against radial distance, r, from the centre of the filler wire, Fig. 24. The concentrations at $r < 4$ mm at the edge of the weld seam are indicative of the amount of O_2 available to react with the molten metal. Fig. 24 shows that flow-rates greater than 12 l/min effectively resulted in the same coverage, while for 9 l/min the quality was only somewhat diminished. It is clear that for 6 l/min the O_2 levels are disproportionately elevated, suggesting an air-rich atmosphere, as seen already in Fig. 23(c). The weld seam inspection of Fig. 21 showed that all welds at 9 l/min were of acceptable quality, indicating that an O_2 concentration in the range of approximately 2,000 – 13,000 ppm at the edge of the weld seam might be used as an estimate of the threshold for sufficient shielding in other configurations of the model.

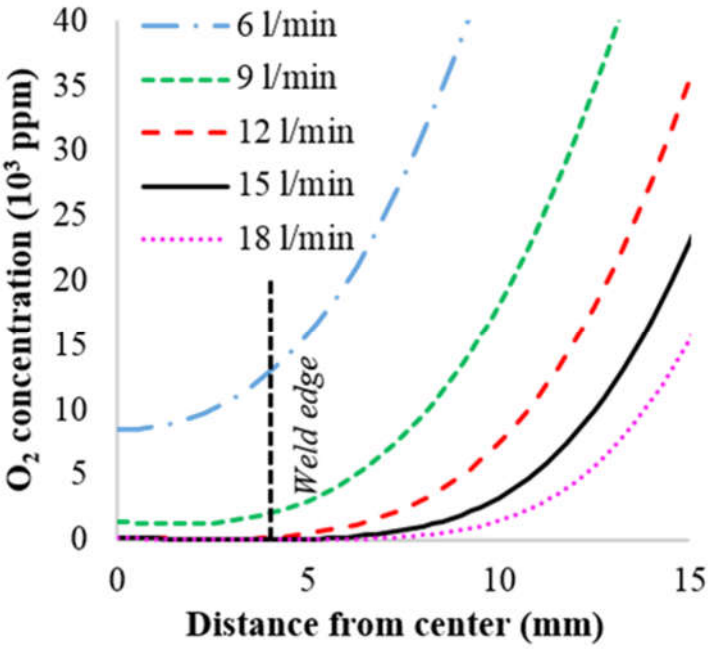

Fig. 24 Calculated O_2 concentration at workpiece surface for 10 mm stand-off and at different shielding gas flow-rates.

3.3.2. *Torch standoff variation*

Fig. 25 shows time-averaged schlieren images made from the image sequences at increasing nozzle stand-distances. Each image was produced by averaging 250 frames (equivalent to an exposure of 1.2 s), taken after the arc had stabilised. This process emphasizes the stationary flow features around the torch and is consistent with the time-independent numerical model. These videos are available in the supplementary material. As the stand-off increased, an inward contraction in the gas shield was noted due to loss of momentum in the flow as the distance travelled increases, but there was no decrease in the visibility of the schlieren gradients at the nozzle edges.

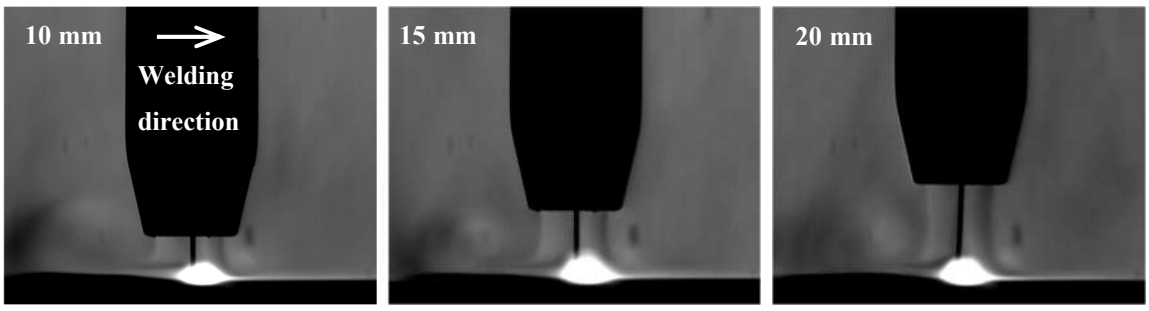

Fig. 25 Time-average schlieren images at different nozzle stand-off distances and 9 l/min flow-rate.

These results indicate that the shielding performance was maintained with increased stand-off and that the important parameter was the shield gas flow-rate. This observation was confirmed with radiography measurements on the welds: all the welds at 9+ l/min were acceptable while all the welds at 6 l/min were again unacceptable. Increased nozzle

stand-off had no effect on the weld seam porosity for the range of stand-off distances tested.

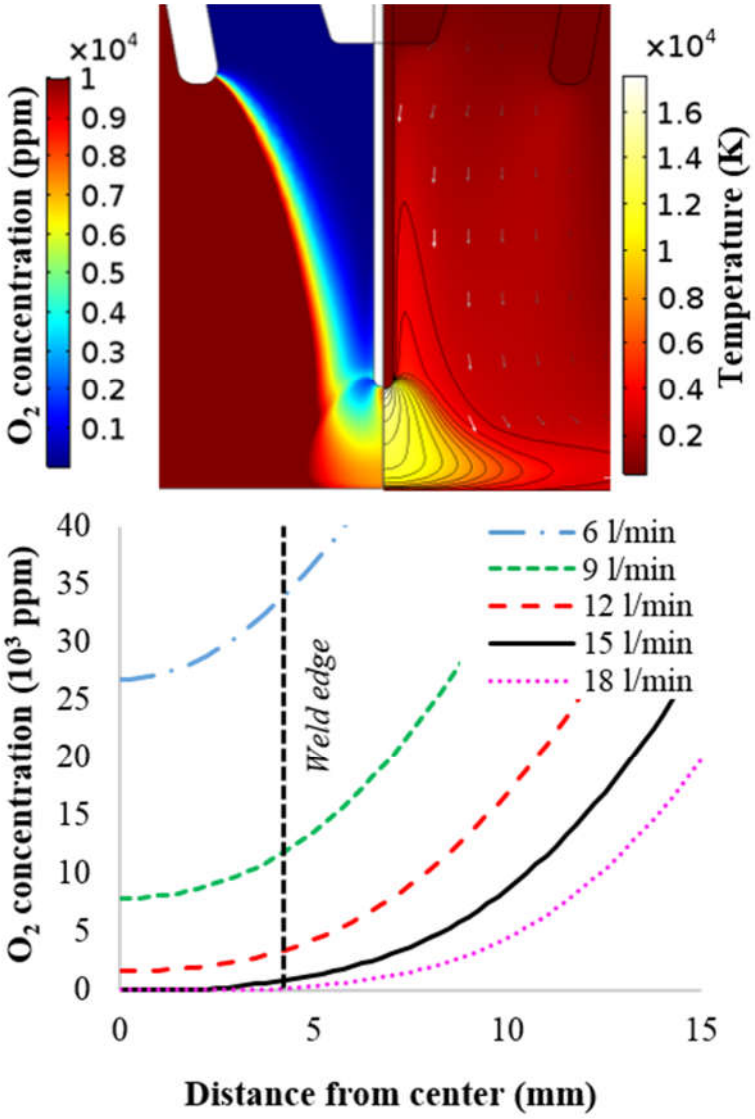

Fig. 26 Numerical results for 20 mm stand-off and a 9 l/min flow-rate. (top) O_2 concentration and the temperature distribution and low flow velocities associated with the shielding gas (arrows scaled as in Fig. 6). (bottom) Calculated O_2 concentration at workpiece surface at different shielding gas flow-rates.

Fig. 26 (top) shows the calculated O_2 concentration and the temperature distribution and low flow velocities associated with the shielding gas, respectively for a 9 l/min flow-rate and at 20 mm stand-off. In practice, it is well known that holding the torch further away from the workpiece results in reduced penetration due to a lower arc current [3], a trend we observed experimentally and in the model. This reduced current at increased stand-off produces a lower peak temperature which reduces the inward pull of the surrounding atmosphere due to the arc. Through this effect, an increase of up to 200% in stand-off was found to be "auto-compensated" in terms of the shielding gas coverage. Fig. 26 (bottom) shows the calculated O_2 concentration at the workpiece surface for each shield gas flow-rate at 20 mm stand-off. Comparing the O_2 concentrations at the edge of the weld seam

for the 9 and 6 l/min cases (good and bad welds respectively) indicates that the estimate of the threshold for sufficient shielding for the model is in the range 11,000 – 33,000 ppm.

3.3.3. *Variation in torch angle*

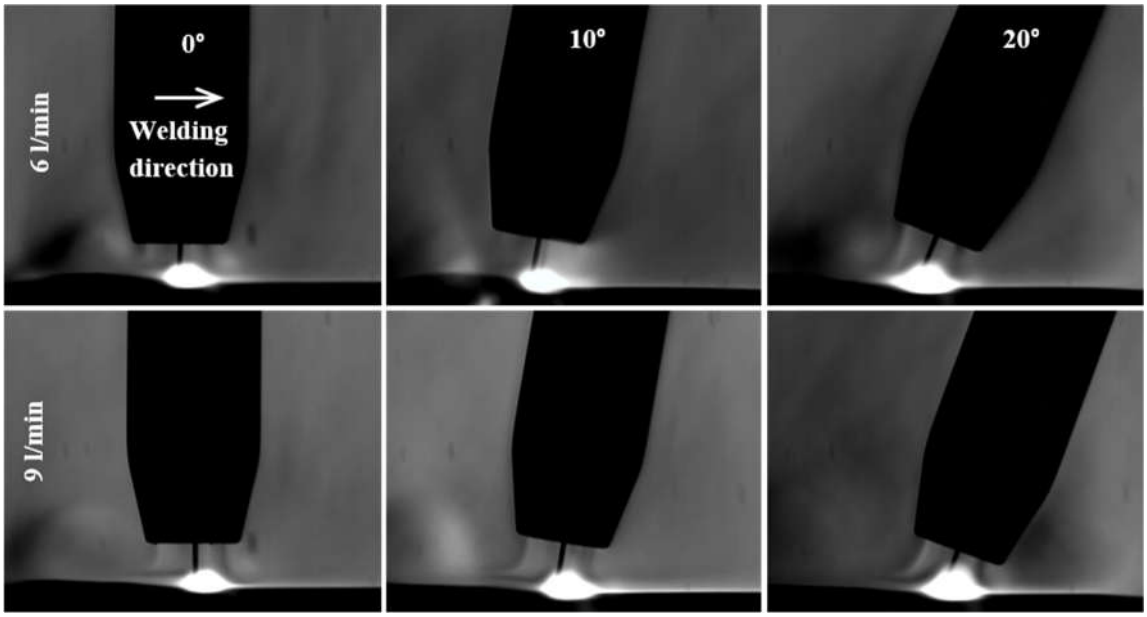

Fig. 27 Time-average schlieren images different nozzle angles and shielding gas flow-rates.

Fig. 27 shows time-averaged images recorded from the schlieren video sequences at increasing nozzle angles to the vertical for the lowest shielding gas flow-rates tested (6 and 9 l/min). The standard stand-off of 10 mm was maintained at the centre of the nozzle. These videos are available in the supplementary material. As the angle increased there is an obvious asymmetry in the shield gas coverage, but there was no decrease in the visibility of the schlieren gradients at the nozzle edges. However, a clear decrease in visibility of the schlieren lines was again noted at 6 l/min. These results indicate that the shielding performance was maintained with increased angle and that the important parameter was again the shield gas flow-rate. This observation was confirmed with radiography measurements on the welds: all the welds at 9 l/min were acceptable while all the welds 6 l/min were again unacceptable. Increased nozzle angle had no effect on the weld seam porosity for the range of angles tested.

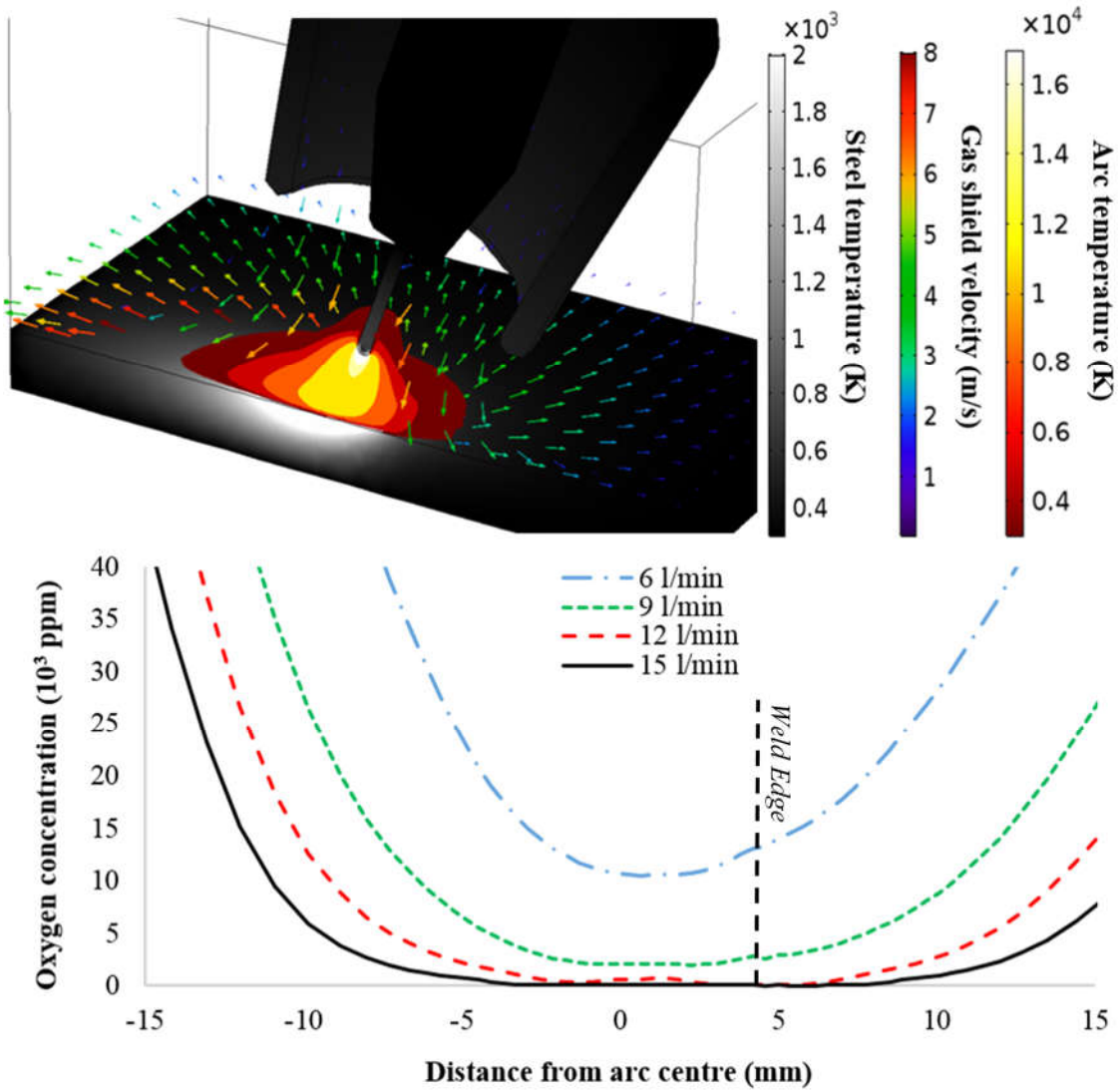

Fig. 28 3D simulation results, with torch tilted at 20°: (Top) arc temperature, gas shield velocity vectors and workpiece/wire temperatures for a 190 A, 28 V GMAW arc. (Bottom) Calculated O_2 concentration at workpiece surface at different shielding gas flow-rates.

Changes in nozzle angle break the 2D axial symmetry and require the 3D numerical model to examine the O_2 concentration. Fig. 28 (top) shows a composite result from the 3D model for the arc and steel temperature distributions and the low flow velocities associated with the shielding gas for a 15 l/min flow-rate and a nozzle angle of 20°. Fig. 28 (bottom) shows the calculated O_2 concentration at the workpiece surface for each shield gas flow-rate at the 20° nozzle angle. The zero position is taken at the intersection of the centre of the filler wire with the workpiece surface. Comparing the O_2 concentrations at 4 mm behind this position for the 9 and 6 l/min cases (good and bad welds respectively) indicates an estimate of the threshold for sufficient shielding for the model of approximately 5,000 – 19,000 ppm. The 4 mm distance was chosen for consistency with the 2D model. The O_2 threshold was higher behind the weld than in front of it; it was also higher behind the weld than the threshold observed at the weld edges.

3.3.4. *Metallurgical analysis of welded samples*

Following x-ray radiography, the DH36 samples produced with solid wire were sectioned and etched to expose the grain. Apart from weld macrographs, shown in Fig. 21, micrographs of the weld bead were produced using a light microscope with a 200x total magnification. The images were converted to grayscale and contrast stretched so that 0.1% of the pixels were saturated. This process facilitates analysis by eliminating slight inconsistencies with the conditions under which the images were taken, due to the proportional expansion of the pixel range over the entire 8-bit colourmap (0-255).

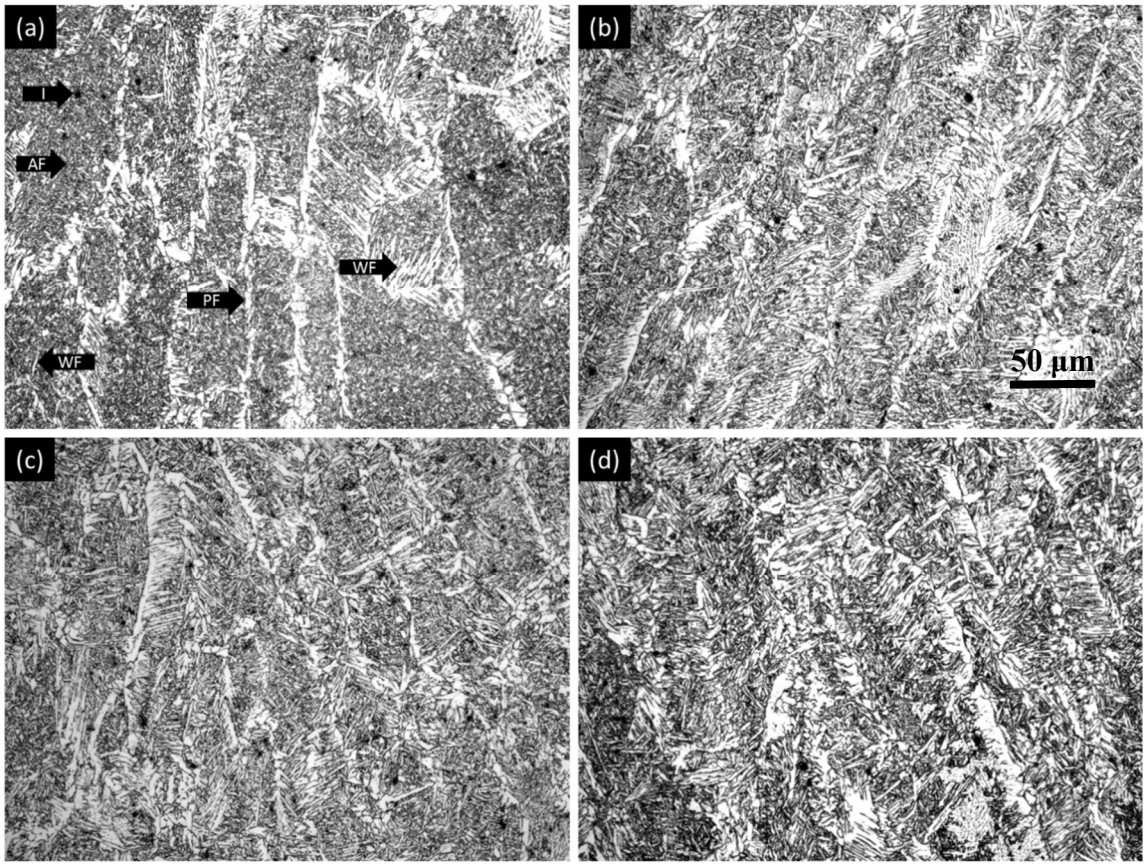

Fig. 29 Weld bead microstructures (a)-(d), from samples produced with Q_0 = 6 – 15 l/min.

Fig. 29 (a)-(d) shows the microstructure for the samples produced with 6 – 15 l/min Ar gas flow, respectively. In all cases, the microstructure is mainly comprised of fine grain acicular ferrite (AF), due to the low alloy content of DH36 steel. Primary ferrite (PF), both idiomorphic and allotriomorphic, can be seen on the prior-γ grains and boundaries, respectively. Two types of Widmanstätten ferrite (WF) are observed: intragranular, originating from idiomorphic polygonal ferrites, and secondary, formed from allotriomorphic ferrite on the prior-γ boundaries. A small number of inclusions (I) are also observable, a typical feature in mild steel GMAW morphologies.

In order to help quantify the observed features, histograms of the microstructure images are shown in Fig. 30. In the histogram of every image, the pixel colour is on the x-axis, ranging from black (0) to white (255), while the total number of pixels with a given colour appears on the y-axis. From the phases identified above, (AF) mostly has grey pixels, the (PF) are mainly white and (WF) contribute pixels of all colours. (I) appear as dark spots, increasing the dark pixel count.

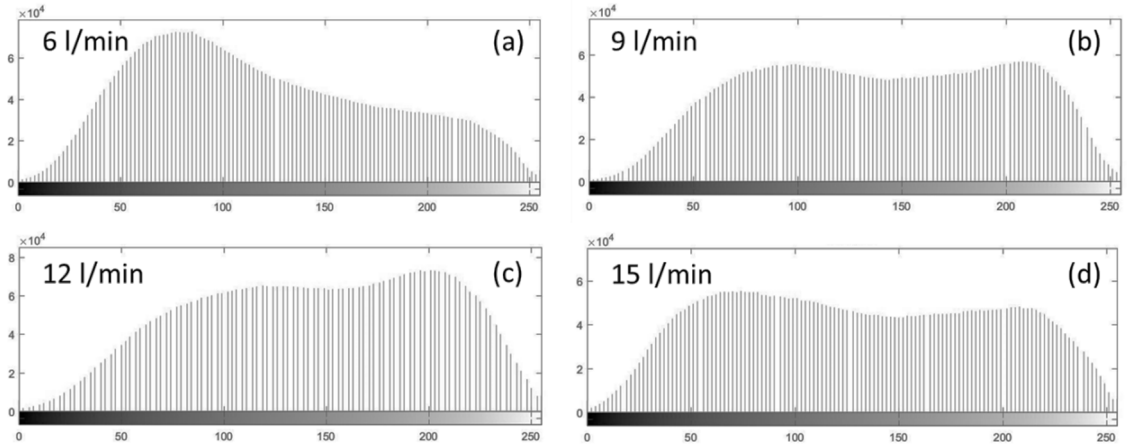

Fig. 30 Histograms of sample macrographs, following image processing. A higher dark and lower white pixel count is observed for 6 l/min.

For the flowrate range 9 −15 l/min, the histograms follow a similar pattern and there is a balance between black and white pixels. However, a significantly smaller fraction of white pixels is present in the 6 l/min case, suggesting that a smaller fraction of (WF) and (PF) is present. Indeed, the comparison of Fig. 29 shows that much larger fractions of (AF) and less (PF) are present for the 6 l/min weld. This can be explained by the increased number of inclusions in the weld, which serve as nucleation sites for the formation of acicular ferrite [97]. The extra inclusions are due to reactions of Fe, C and other elements in the steel with the oxygen-rich environment, a consequence of poor shielding. The microstructures with increasing gas flowrate show that the amount of (AF) in the welds is similar. The increased dark pixel count for the 15 l/min case is attributed to changes in image contrast due to slightly inconsistent sample etching, rather than microstructural differences.

The microstructure of samples produced under different angles and standoff, at 9 l/min were also analysed in the same manner. The microstructures appeared similar, with no significant variability in the observed features.

These results suggest that the input gas flow rate can be used as a tool for manipulation of the microstructure. Although (AF) is a desired microstructure that results in higher

structural properties for the bulk material, the introduction of inclusions is associated with reduced fatigue life and toughness. Such discontinuities serve as crack initiation sites, due to localised stress concentrations [1], contributing to ductile and brittle fracture mechanisms [97]. It is therefore an important design feature to keep the optimal levels of inclusions to promote (AC) formation, but without compromise to the material properties.

3.4. Discussion

Schlieren imaging was used to understand the shielding gas coverage at different stand-off distances and nozzle angles for a range of gas flow-rates. The visibility of the schlieren C lines associated with the flow from the nozzle was significantly reduced at 6 l/min, which corresponded to unacceptable weld porosity. At flow-rates of 9 l/min and above, these schlieren lines had increased visibility and the weld porosity was acceptable irrespective of the nozzle stand-off or angle in the range tested. However, it was not feasible to quantify the shielding using the schlieren images alone because these lines are formed due to both concentration and temperature gradients. The difference in refractive index between pure Ar and air at ambient temperature is of the order of 10^{-4} which would require a very sensitive schlieren measurement to resolve. The schlieren system was configured for low sensitivity and a large measuring range [67], [70], indicating locally elevated temperatures at the flow edges. This behaviour was also observed from the numerical model due to the convective cooling effect from the bulk flow: at lower shielding gas flow-rates the temperature gradients were smaller which contributed to the reduced visibility and blurring of the schlieren lines.

The power of the combined approach lies in using the schlieren imaging to visualize and understand the shielding gas flow and to validate the numerical model, and using the model to gain insight into the effect of various physical parameters on the process. The 2D and 3D models of the flow-rates, nozzle stand-off and nozzle angle provided a satisfyingly consistent result. Radiography measurements indicated that all the welds at 6 l/min were unacceptable while all the welds at 9 l/min or above were acceptable, irrespective of the nozzle stand-off or angle in the range tested. The O_2 concentration ranges predicted by the model for 6 and 9 l/min at r = 4 mm from the nozzle centre was consistent between the three cases, indicating that the main features of the interaction between the shielding gas and plasma jet flows was successfully captured by the time-independent model. Furthermore, the highest concentration at 6 l/min of 11,000 ppm (for stand-off of 20 mm) and the lowest concentration at 9 l/min of 13,000 ppm (for 10 mm stand-off) indicates an approximate threshold of 12,000 ppm can be used in the model.

Clearly this value is not absolute for physical welding due to the necessary assumptions and simplifications used in the model. Besides, it is not possible to measure the absolute value accurately during physical welding and the tolerance to porosity will depend on the particular application of the welded component. However, the important point is that this threshold is pragmatic and related to failure criteria in ship building, rather than 50 ppm [46] which is a limit more usually used for material processing in a sealed chamber. It is consistent with other studies in a welding context where a few thousand ppm has been shown to leave minimal porosity [98].

3.4.1. *Schlieren imaging of FCAW-G*

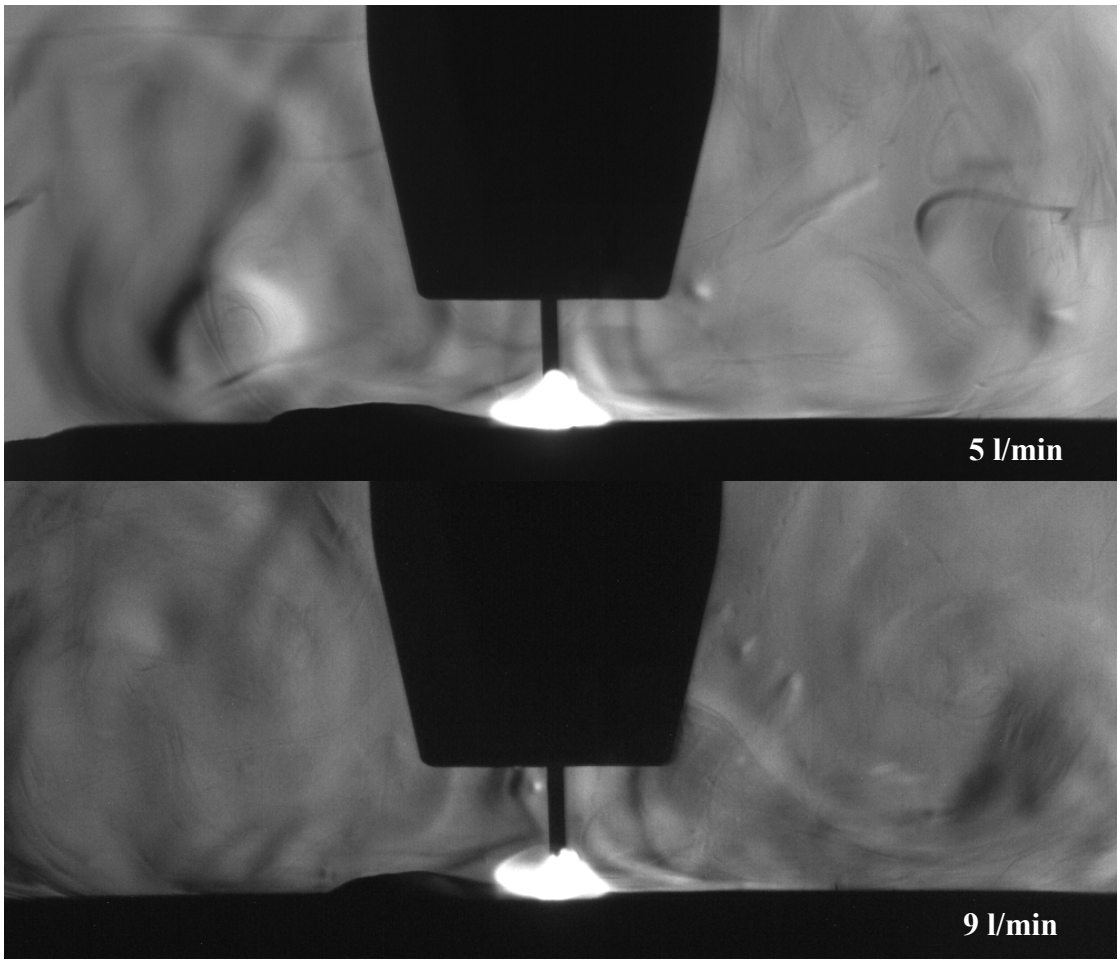

Fig. 31 Schlieren images of FCAW-G using 1.2 mm flux core wire and 86%Ar/12%CO2/2%O2 gas mixture, stand-off 10 mm.

For the application of interest in this paper, namely minimising the shielding gas flow-rate in GMAW, the results indicate that adequate shielding can be accomplished with flow-rates as low as 9 l/min in the absence of cross-drafts. Further experiments were undertaken on other filler wires and shield gases that are of industrial interest. These included: mild steel filler wire with (a) 80% Ar / 20% CO_2 shielding gas and (b) flux core

filler wire with 86% Ar / 12% CO_2 / 2% O_2 shielding gas. These cases were not modelled due to the added complexity and change in properties associated with the inclusion of flux and multicomponent gas mixtures in the simulation. However, the schlieren imaging proved extremely useful in these more complex cases. Fig. 31 shows typical results for flux core filler wire with 12% CO_2/2% O_2 case which we believe to be the first reported schlieren imaging for gas shielded, flux cored arc welding (FCAW-G).

As seen previously, the bulk flow gradients are blurrier for 5 l/min compared to those of 9 l/min, suggesting less intermixing in the latter case. The gradient over the arc appears flatter and the arc itself was consistently shorter and wider. Increased fume levels were observed compared to the pure Ar GMAW videos. Radiography revealed acceptable quality of the FCAW-G welds, even down to 5 l/min for the full range of nozzle stand-offs and nozzle angles used previously. The improved shielding is due to reactions between elements contained in the flux and the remaining O_2 and N from the environment that were not excluded by the shield gas, before they could be absorbed by the steel.

Inspection of the welds with solid wire and 80% Ar /20% CO_2 indicated that they were also acceptable down to 6 l/min for the full range of nozzle stand-offs and nozzle angles used previously. Compared to pure Ar, the extra CO_2 content helps to prevent porosity due to differences in surface chemistry [47], [91]. Using such shielding gas mixtures generally increases the “effective absorptive capacity” of the system, enhancing the tolerance for excess N and O_2.

Based on the findings of this study and including a safety factor, 12 l/min of pure Ar would be the recommended nominal gas flow rate for GMAW of mild steel. An additional factor of safety can be added by changing solid wire to flux-cored wire and including up to 20% CO_2 in the shielding gas. These results supported the introduction of flow controllers set at 12 l/min in production welding units at BAE Systems Govan shipyard, with no compromise in the weld quality. Due to the large volumes of welds in shipbuilding, they represent a considerable reduction in cost, reduce the carbon footprint whilst maintaining the required weld integrity.

3.4.2. *Arc length variation*

In a similar way, the model can be used to investigate the effect of varying physical parameters that are difficult or too time-consuming to implement experimentally. As noted above, the fluctuations in the arc’s length, voltage and current throughout the phases

of the arc [3], [99] are not captured in the steady state model. An arc length l_{arc} = 5 mm was used throughout section 3.3, representative of the high current and voltage phase when the Lorentz forces (and thus turbulence levels and entrainment) are at their maximum. However, the arc length of each phase depends on the inductance regulation of the power supply, resulting in large variability between different settings.

The two main constituents of an electric arc, the voltage and current determine the total energy supplied per unit time. Variation in arc length ultimately results in changes to the electric field distribution and therefore the resulting current density [60]. This leads to a characteristic set of power curves which vary with a given welding configuration, conceptually shown in Fig. 32.

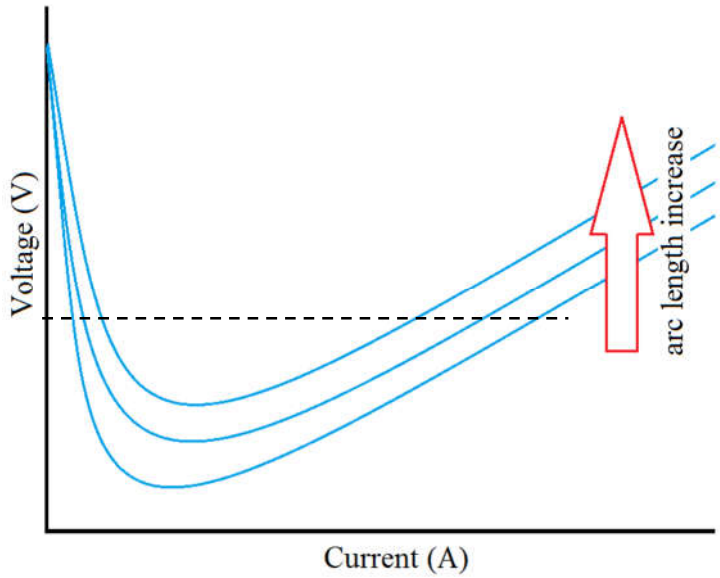

Fig. 32 Arc characteristic variation with arc length. A shorter length will result in a higher power arc, as indicated by the equipotential line and implied by Ohm's law.

To characterise the effect of such dynamics on the resulting entrainment of air, the steady state O_2 concentration profiles with increasing arc current at 5 mm and 3 mm arc length are plotted on Fig. 33. This theoretical approach allowed to study the effects of arc length, voltage and current independently while keeping the wire feed speed constant, therefore decoupling some of the physical boundaries inevitably imposed experimentally. The O_2 concentration plots show the profound effect of arc current on air entrainment. At low currents, a small centralised air vortex retains a few thousands of ppm of entrained air at most, which dissipate before reaching the workpiece. Fig. 10 shows that the reduced arc length does not significantly increase the entrainment of air, despite the associated 30 A current increase. The inwards electromagnetic pinch of the shield gas intensifies with increasing arc current, shown by the body force vectors, and progressively higher air mass

fractions are present in the plasma jet and bulk flow. The ~5000 ppm predicted at 260 A is under the 12,000 ppm threshold established in section 4, indicating sound welds may be produced at the reduced flowrates even with relatively higher currents and spray transfer. However, the model predicted that a rise in current by 33% incurred an increase in the total air stagnating at the workpiece by 250%. This suggests that when operating at very high currents with specialised waveforms, a small increase in the shielding gas flow rate might be warranted to compensate for the stronger electromagnetic pinch.

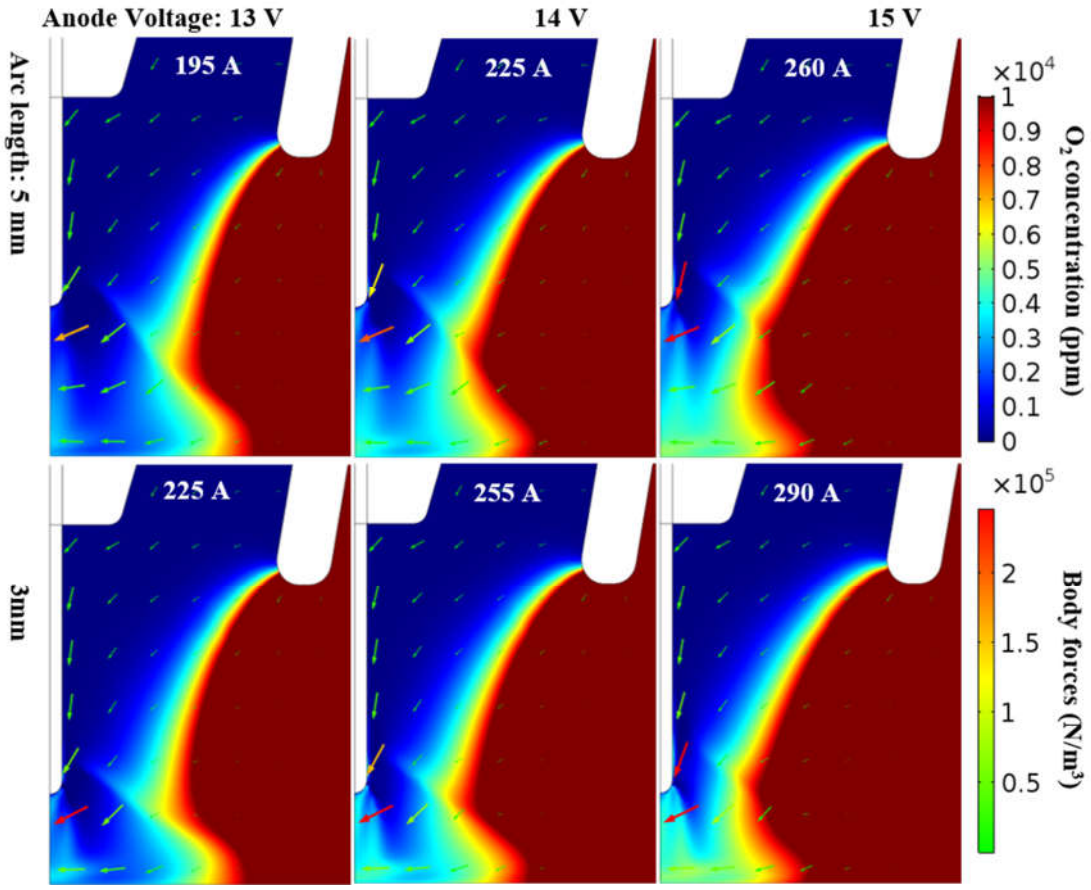

Fig. 33 O_2 concentration with body force vectors (sized on logarithmic scale, 3 orders of magnitude) for various currents, determined from the anode voltage and arc length, 10 mm stand-off and 9 l/min flow-rate.

3.5. Conclusions

A detailed experimental and computational analysis of the GMAW process allowed characterisation of the Ar gas flow under which a weld was adequately shielded. It was shown that, in the absence of cross-drafts, 9 l/min or greater provided sufficient coverage irrespective of increases in the nozzle stand-off to 20 mm and nozzle angle to 20°. An MHD model was validated against the schlieren images and shown to calculate the underlying temperature, pressure and concentration gradients with acceptable accuracy to describe the main features of the flow. The key features of the model were the

interaction of the plasma jet with the low velocity nozzle flow, and the introduction of the diffusion of air into the plasma in to a GMAW context. The model provided physical insight into the welding behaviour observed, for example the autocompensation of incressed stand-off by reduced current, and the benefit of operating at lower arc lengths and currents. A pragmatic O_2 concentration threshold of ~12,000 ppm in the model for DH36 mild steel was found consistently for the range of shield gas flow rates and nozzle stand-off and angles investigated. Micrographs of the samples indicated that optimal microstructures can be achieved by increasing O_2 content to the levels where acicular ferrite formation is promoted (9 and 12 l/min showed the highest (AF) content), while still operating under the threshold for porosity.

These results supported the introduction of flow controllers pre-set at 12 l/min in production welding, with no compromise in the weld quality. Additional experiments with flux core filler wire and 86% Ar/ 12% CO_2 / 2% O_2 shield gas indicate that further shield gas savings could be achieved for gas shielded, flux cored arc welding (FCAW-G). In this case, it was possible to deposit large bead-on-plate welds with flow-rates as low as 6 l/min, yielding cost savings and a reduced carbon footprint whilst maintaining weld integrity, in terms of mechanical properties, hardness and freedom from weld defects.

4. Analyses on the efficient use of shielding gas during welding

The development of the MHD model and optical diagnostic setup allowed analyses to be carried out for a variety of welding-related applications. This chapter is therefore comprised of two self-contained, independent studies. Although the process used in each one (MIG for section 4.1 and pulsed TIG for section 4.2) differs, they are grouped together in one chapter due to the similarity in their scope: understanding of the flow features and physical phenomena involved, therefore enabling the optimal use of shielding gases.

4.1. Imaging and 3D simulation of gas flows in MIG fillet welds

Current industrial practice in shipbuilding involves the deposition of hundreds of km of welds, the majority of which are fillet welds, where two metal plates are welded at 90º to each other. In this case, the torch is tilted in two dimensions to compensate for the effect of gravity, and the surface area of the plates constrains the flow further, as shown in Fig. 35. Extrapolation of the flow effects presented in the previous chapter to the different geometry is not apparent, as heat and momentum are distributed asymmetrically. Finally, the direction of travel relative to the angle of the torch results in the weld bead being deposited in a different orientation (pushing or pulling), therefore altering the geometry which must be protected by the gas flow.

Numerical models in the literature have been employed to characterise the heat transfer related to fillet welds and therefore the residual stress fields [100], or coupled with hydrodynamic modelling of the flow of molten metal, to predict the final weld geometry [101]. No studies have been carried out to date that model or visualise the coverage from the shielding gas flow in this context.

In this study, the systematic approach taken previously for bead-on-plate welds is extended onto fillet welds. MHD flow modelling of the GMAW process for a 3D, fully asymmetric case is reported. In addition, the schlieren system presented in the previous chapter was modified to image shielding gas coverage in fillet welds using GMAW and FCAW-G under a range of flowrates.

4.1.1. *Experimental setup*

The automatic welding rig presented in the previous chapter was modified so that fillet weld samples could be manufactured under any torch angle. Similarly, the schlieren setup

was setup parallel to the motion of movement so that the process could be imaged, Fig. 34. The challenge associated with this change was that to include the entire welding area within the middle part of the Z without interfering with the collection and illumination components. Additionally, the angles of the mirrors were to remain under 6° to limit astigmatism in the images. This was accomplished in the optical setup by increasing the length of the middle part of the Z while keeping the mirror angles constant (therefore creating a greater clearing between the two arms), resulting in a diagonal length of ~5.5 m. An enclosure was made for the camera, lens and filter assembly to protect them from spatter and stray light.

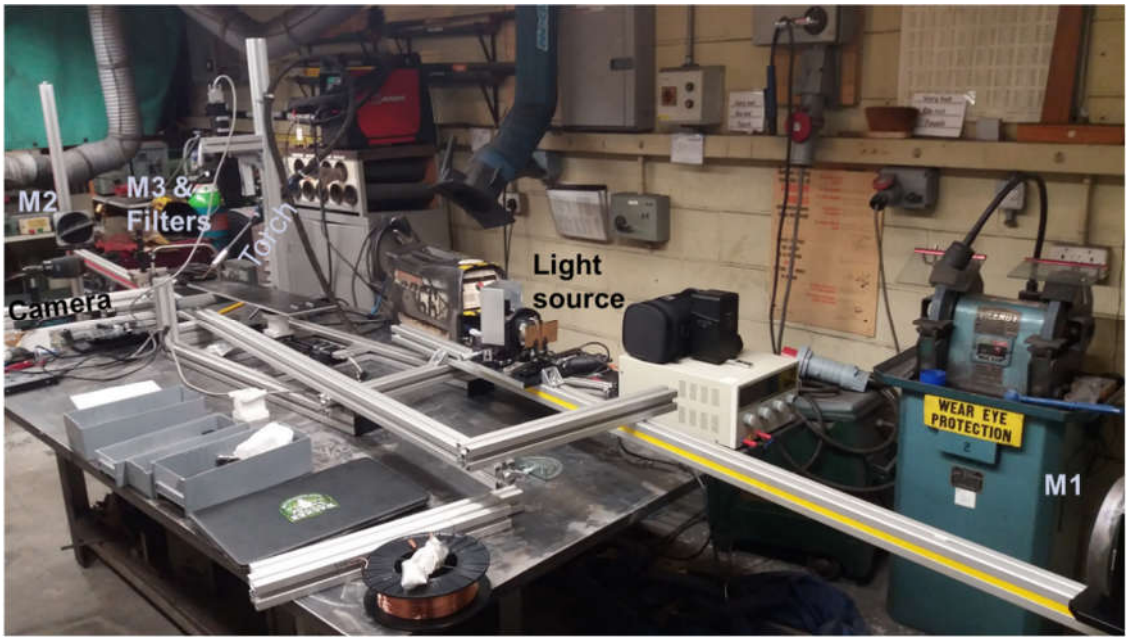

Fig. 34 Modified schlieren setup for fillet weld visualisation. A ~5.5 m collimated path was required to maintain low astigmatism while incorporating the welding setup. Additionally, after filtering at the Fourier plane, the light was steered by 90° by an additional flat mirror, M3.

Two sets of tests were carried out, one using pure Ar and solid, mild steel wire and a set using 80% Ar/20% CO_2 mixture and flux-cored wire. For the solid wire set, the gas flowrate was varied between 6 and 15 l/min, while for the flux cored wire set, the flowrate was tested in the 3 − 15 l/min, in addition to 0 l/min (no shielding gas). For both sets, the experiments were carried out using a positive and negative travel angle (pushing and pulling). This was accomplished with the stationary torch setup by changing the travel direction of the moving workpiece. Other experimental parameters used in each set can be found in Table 4. In order to maintain consistency between the tested wire and gas configurations, the wire feed speed was kept constant and the voltage was increased slightly for the flux cored wire set. This resulted in higher current and thus higher heat

input to the weld. To rectify that, the travel speed was increased by ~40% for the flux cored wire set, resulting in constant line energy, therefore constant heat input.

Table 4 – Experimental parameters for fillet weld visualisation study.

Nozzle stand-off	15 mm	Workpiece thickness	6 mm
T_{amb}	300 K	Travel angle (push/pull)	±30º
Torch angle	47º		
Solid wire, pure Ar shielding gas			
Constant voltage	27 V	Wire thickness	0.9 mm
Current	185 A	Travel speed	6.5 mm/s
Wire feed speed	10 m/min	Line energy	0.74 kJ/mm
Flux cored wire, 20% CO_2 shielding gas			
Constant voltage	28.5 V	Wire thickness	1.2 mm
Current	235 A	Travel speed	9 mm/s
Wire feed speed	10 m/min	Line energy	0.74 kJ/mm

4.1.2. *Numerical model setup*

The fully asymmetric 3D geometry, generated in COMSOL multiphysics software, is shown in Fig. 35. As the same torch was used for this set of experiments as in chapter 2, its geometry was identical to the 2D profile of Fig. 19(a), revolved 360º and tilted according to the travel and torch angles specified in Table 4. The arc root was kept at (0,0,0) and the torch standoff was adjusted to match the schlieren images. The remaining geometry was a 120 x 50 x 50 mm rectangular block, divided into solid and fluid domains. In order to avoid clipping problems during the meshing and discretisation of the fluid domain, the nozzle was extended at the back end through a cylinder (not shown in Fig. 17) long enough for any angle to be prescribable. This extra domain only served as a means to get a well-defined conic section in the fluid domain, and no equations were solved within it. A no slip wall condition was specified in the fluid's surfaces that arose from the conic section.

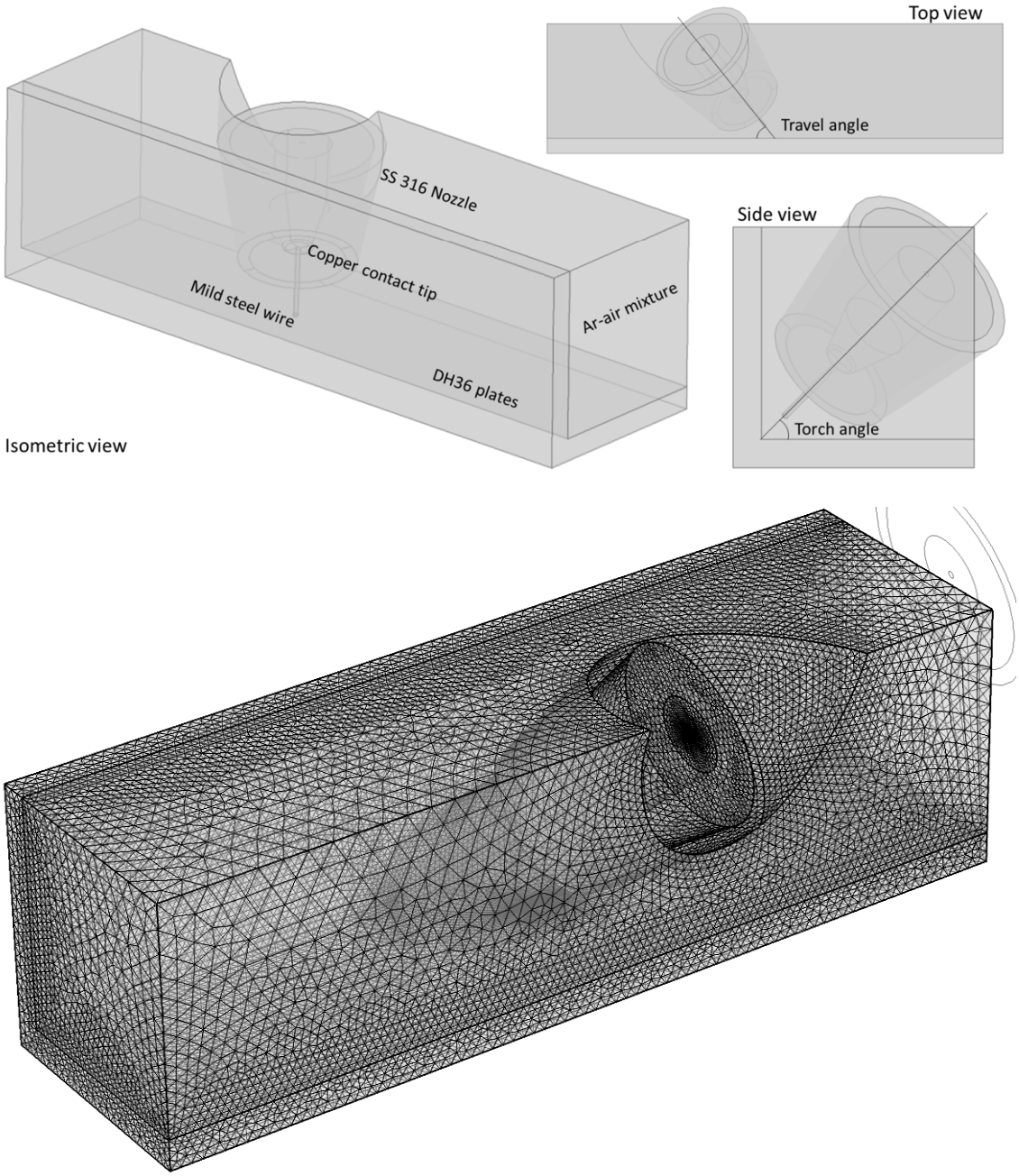

Fig. 35 (Top) Generated fillet weld geometry, in isometric and two orthographic views. Materials for each computational domain and key torch positioning angles are annotated. (Bottom) Meshed configuration.

In terms of governing equations, the set of equations described in chapter 2 was used in the same manner for this model, with one exception. The large size of this model posed a significant obstacle in its numerical solution: the solution of a curl-curl problem as per Ampere's law (eqn. 14) in a large fluid domain requires exorbitant amounts of RAM and CPU power. To counteract that, a suitable control volume over which the self-induced magnetic field decayed to near zero was investigated. It was found by the models presented in chapter 3 that the magnetic field is of the order of a few mT around the wire but decays relatively quickly along the x-direction, and after 5 mm it had decayed to negligible magnitudes. A cylinder was therefore prescribed at the inner diameter of the

nozzle, extending to the top surface of the workpiece. The effective domain in which Ampere's law was solved in therefore extended from the inlet at the nozzle's top, up to the workpiece. Eqn. 14 was only solved within that volume, implying that Lorentz body forces were also only applied within it. The previous models showed that the total body forces exerted on the fluid outside of the control volume were more than four orders of magnitude smaller, Fig. 33, verifying the validity of the approach. This was treated as a continuous internal boundary for all other equation sets, while the condition $\mathbf{n} \times \mathbf{A} = 0$ was prescribed for eqn. 14.

The material properties used for the geometry, also shown in Fig. 35, were the same as those described in chapter 3. The generated mesh consisted of standard Lagrangian tetrahedral elements and was locally refined around the wire tip and workpiece surface to a size of ~0.1 mm, as per the convergence study in chapter 2. The element growth rate was set to 10% for the fluid domain with a maximum of 3.5 mm, and to 15% for the solid domains with a maximum of 2 mm. The final mesh consisted of 1,232,004 domain elements, 56,319 boundary elements, and 1,978 edge elements. Using the double dogleg solver, each parameter set required ~70 GB of RAM and about 8.5 hours using 18 Xeon v5@2.3 GHz cores.

4.1.3. *Flowrate variation during fillet GMAW*

To aid in depicting the information contained in the several hundreds of images collected for each flowrate, time-averaged (250 frames, ~1.7 s) schlieren images of the flow patterns were generated, using the same procedure as in chapter 2. Following the averaging, the images were contrast stretched so that 0.5% of the pixels were saturated. In this manner, image intensity occupied the entire colourmap, enhancing feature visibility. The results for the flowrate range 6 – 15 l/min are shown in Fig. 36 (a) – (d) for a pushing angle, and in Fig. 36 (e) – (h) with a pulling angle.

The schlieren features for fillet welds bear both similarities and differences with the ones formed during bead on plate welds, Fig. 20. Above the arc, there is a dark, arc-shaped gradient, associated with the high local temperature gradient. However, the shape of this gradient is not as well defined, suggesting smaller temperature gradients in the region. This can be attributed to the higher heat transfer under the nozzle area due to the added vertical boundary. High vorticity was observed in the flow, especially on the lower nozzle side, although no steady-state vortices are formed in the time-averaged images. As the flow is bounded on the upper nozzle side, the shielding gas gradient (characteristic of the

coverage) only appears on the lower edge of the nozzle. An upwards flow between the nozzle's upper side and the vertical wall is present under all conditions. The brighter features of the flow on this boundary suggest that a hotter gas plume is directed upwards. This flow directionality can be attributed mainly to buoyancy forces, as shown in Fig. 37.

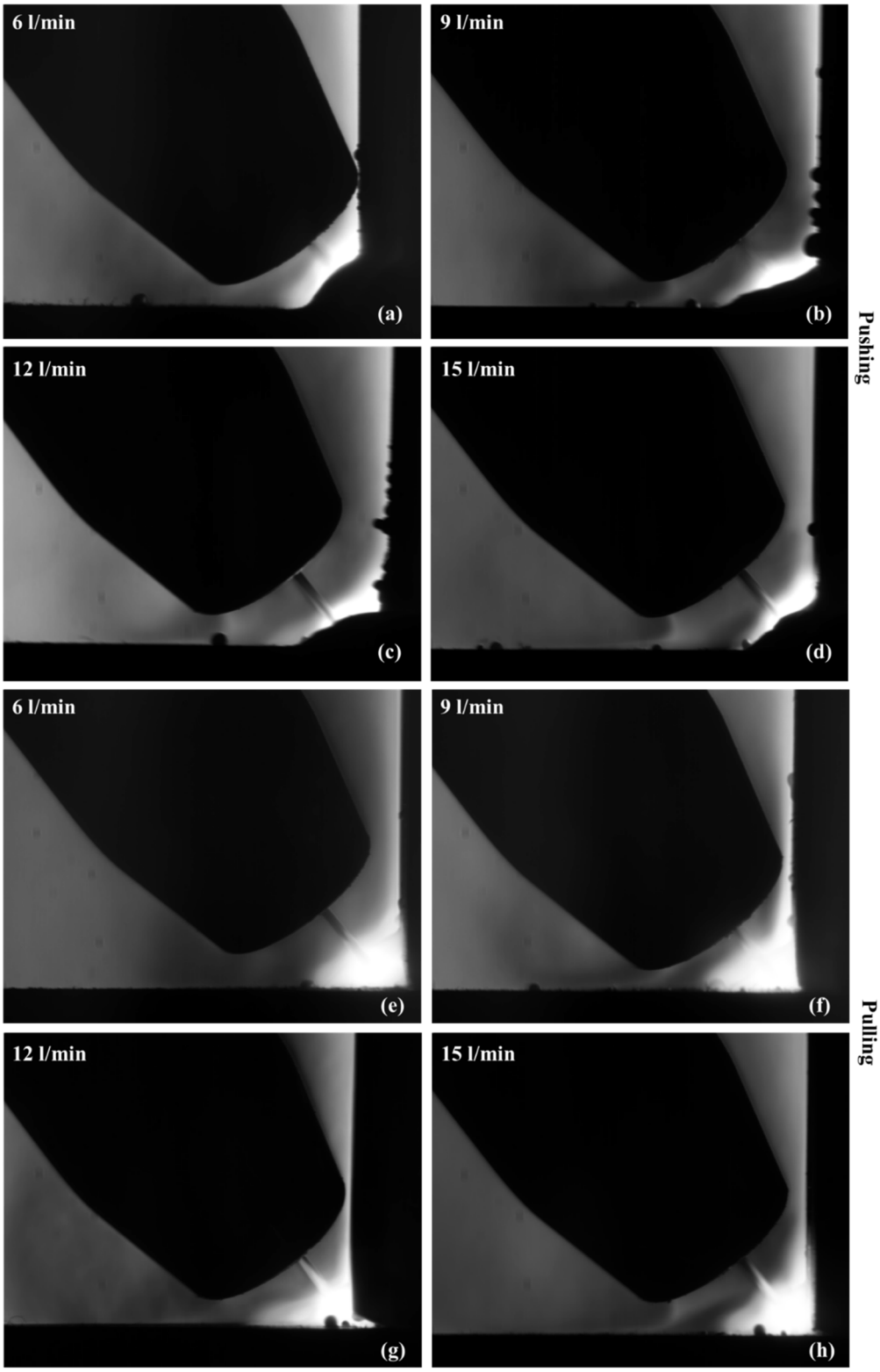

Fig. 36 Time averaged schlieren images of GMAW fillet welds at varying flowrate whilst pushing (a) – (d) and pulling (e) – (h). Consistently with the analysis for bead on plate welds in chapter 3, the gradients associated with the shielding gas flow are only visible for Q ≥ 9 l/min.

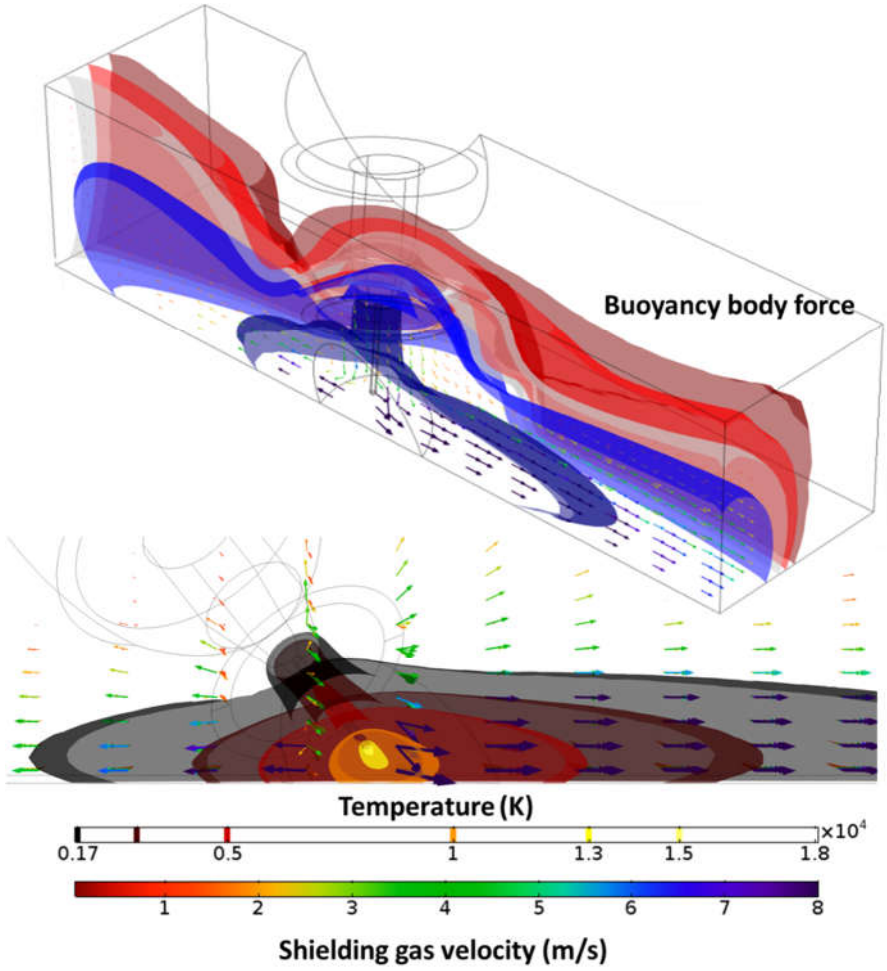

Fig. 37 (Top) Predicted buoyancy body force iso-surface plot for 15 l/min flowrate in 3D model. (Bottom) Temperature and bulk velocity distributions under the same conditions.

Under a 6 l/min flowrate, the steady-state shielding gas flow gradient under the nozzle's lower side (associated mainly with concentration gradients) is not observable. The lack of refractive index gradients suggests locally elevated air mass fractions, with a greater amount of Ar-air intermixing. This is not the case for the welds with 9 l/min or greater, which supports the notion that the flow has enough momentum to limit air entrainment, therefore establishing the gradient. The decrease in flow momentum at lower flowrates is also indicated by the darker region appearing close to the nozzle, as heated gas (which appears darker) remains closer to the nozzle. Finally, more process instability with more frequent arc short circuiting was present for 6 l/min.

Due to a decrease in the frequency of wire bursts, the main mechanism for spatter generation in GMAW, smoother processing was achieved through pulling. Conversely, the welds made with a pushing angle resulted in a marked increase in spatter formation. No notable differences were observed in the flow patterns between pushing and pulling,

both in the schlieren and simulations. The similarity of the flow patterns confirms the assumption made in the previous chapter, where the effects of travel speed were neglected due to orders of magnitude difference between it and the average shielding gas velocity at the nozzle outlets. Similarly, gas directed mostly towards the heated bead geometry whilst pulling or mostly towards the colder plate during pushing did not seem to influence the process significantly. Due to this similarity and improved visibility of the arc whilst pulling, results for pushing have been omitted for the remainder of this results section.

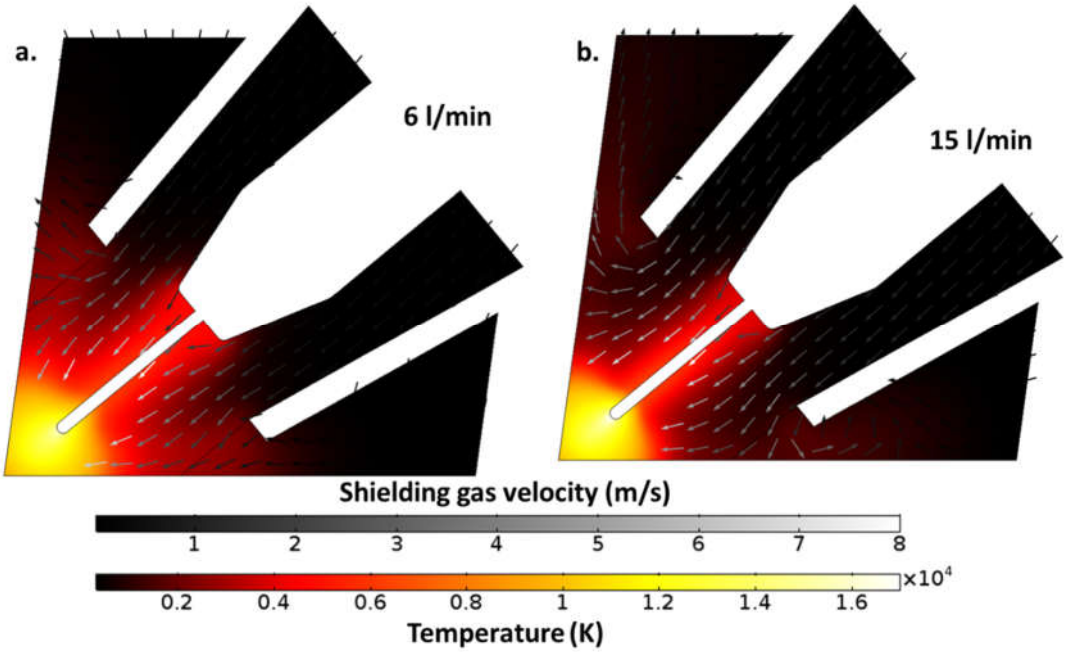

Fig. 38 Heat and momentum transfer at different input flowrates. Higher temperature and lower velocity is calculated under the nozzle region for 6 l/min.

The observed features can be compared to calculated fields for the highest and lowest flowrate, as shown in Fig. 38. An inclined 2D plane was defined in the 3D domain, such that the torch geometry was precisely sectioned in half. The low shielding gas velocity profiles below the nozzle walls in Fig. 38 (a) – (b) indicate that at 6 l/min, not enough downwards momentum is carried by the gas, allowing air to enter close to the arc. Conversely, a clear, outwards flow is shown at 15 l/min. Similarly with the results presented in Chapter 3, the temperatures in the regions below the nozzle walls and above the plasma are higher for the 6 l/min flowrate. This is due to two reasons: the increased conductivity of the air-rich mixture and the reduced convective cooling effect due to a slower gas stream exiting the nozzle.

Fig. 39 (a) – (b) show the momentum transfer in the high-speed plasma jet for the two input flowrates. Here, the non-inclusion of the weld bead in the calculation leads to the underestimation of velocity. Nevertheless, 40 % higher peak velocity is calculated for 15

l/min, suggesting higher outwards momentum is imparted in the shield gas after stagnation at the arc root. The O_2 concentration plots of Fig. 39(c) – (d) show a higher degree of air entrainment for the 6 l/min case compared to 15 l/min.

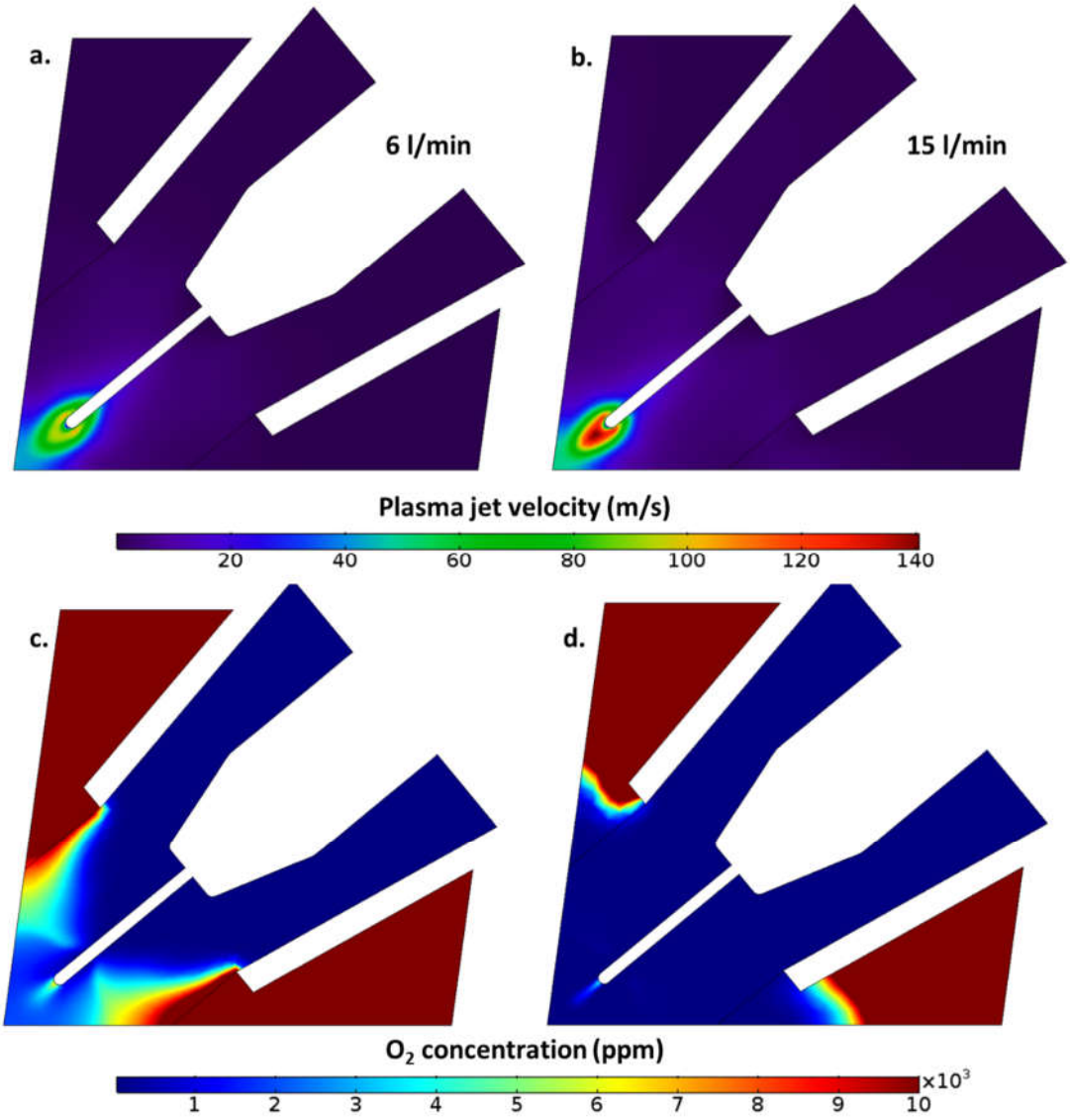

Fig. 39 Momentum and species transfer in Ar-air mixture. High air entrainment is noted due to lower momentum in the shield gas flow at 6 l/min. Good coverage is observed at 15 l/min.

As the schlieren technique can only see a 2D image of the total refractive index gradients within the field of view of the system, the model can also help to understand the directionality of the observed features in 3D space. Fig. 40 shows the shielding gas velocity on the surface of the plates (arrow length normalised). The velocity magnitude has been truncated to 8 m/s, so that the behaviour of the relatively low velocity shielding gas stream can be examined. As expected, the area over which the flow is faster than 8 m/s increases with input flowrate, as higher momentum is given to the gas at the inlet. The flow is generally directed outwards from the arc root, where the high velocity jet stagnates (marked JS). Past this stagnation point, where velocity is 0 and pressure is

maximum, the flow is split into two streams; they are both flowing outwards and parallel to the plate but on opposite directions. It can be observed that the directionality of the momentum imparted to the shielding gas by the plasma jet is strongly affected by nozzle tilt. In Fig. 40, this is shown through the stronger flow towards the left-hand side, a consequence of the 45° travel angle. Stagnation points also occur when the shielding gas streams reach the plate (marked SgS). For the 15 l/min case, enough momentum is carried by the shielding gas so that the flow past the stagnation point is still directed outwards, while at 6 l/min the flow extends roughly until the stagnation point and the non-zero velocity components are mostly pointed inwards. The reduced velocity should be indicative of weaker Ar transport from the nozzle inlet across the plate.

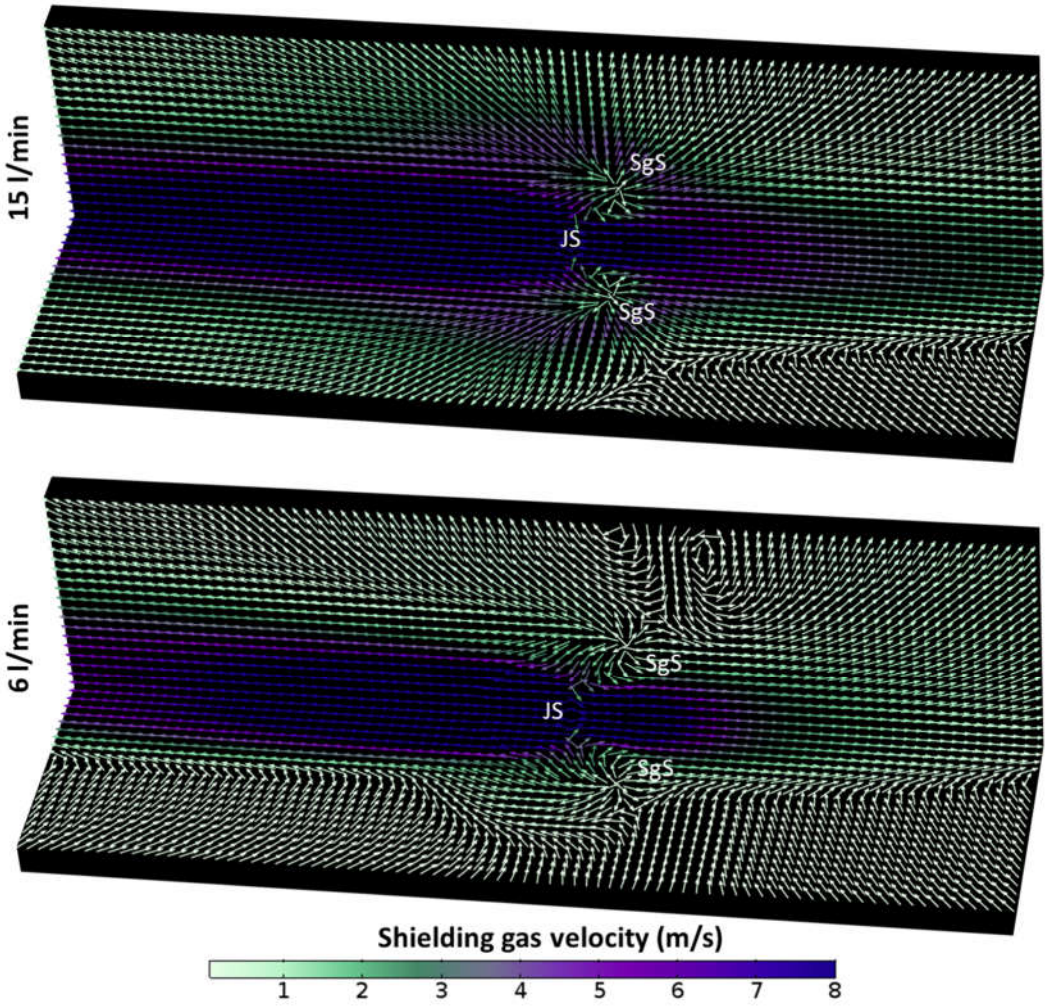

Fig. 40 Shielding gas flow velocity profiles on fillet surface at (top) 6 l/min and (bottom) 15 l/min. The points were the plasma jet and shielding gas streams stagnate have been marked JS and SgS, respectively.

Similarly to Chapter 3, the total coverage on the fillet surface can be characterised in terms of O_2 concentration. A composite 'unwrapped' image, where the two surfaces have been set next to each other at 0° is shown in Fig. 41. A minimum of ~3000 ppm O_2 concentration is calculated at the vicinity of the melt pool at 6 l/min, while for 9 l/min or

higher the minimum is ~50 ppm. Additionally, the covered area decreases in small increments for the flowrates at 15 – 9 l/min, while at 6 l/min the decrease is disproportionally large. This suggests that 6 l/min produce very limited coverage compared to the higher flowrates.

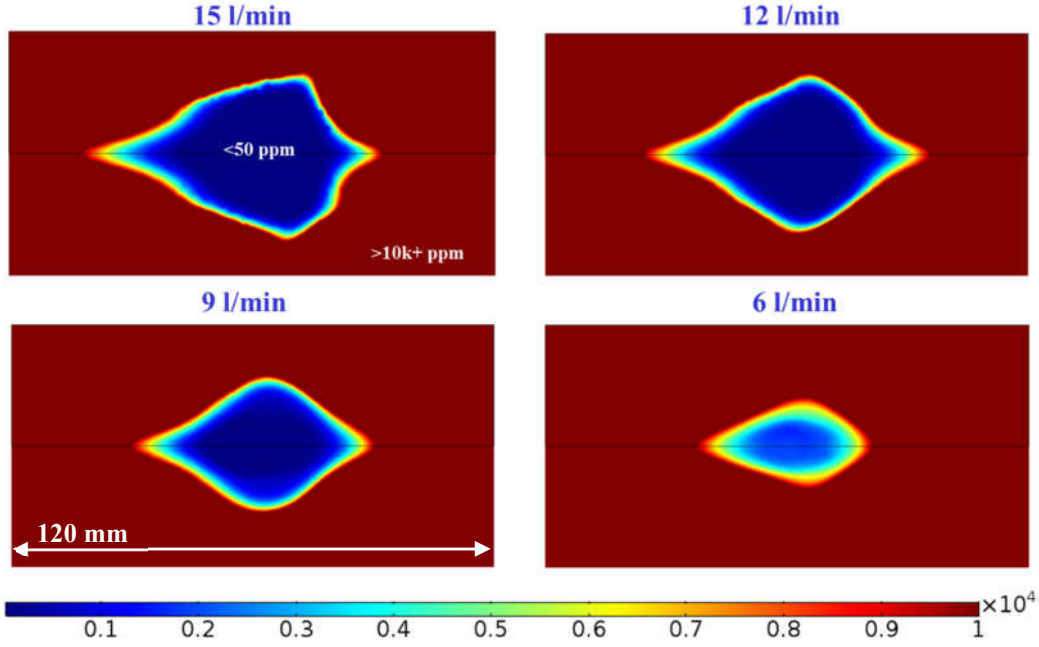

Fig. 41 O_2 concentration plot over 'unwrapped' fillet surfaces at varying flowrate, showing good quality coverage is generated when the flowrate is 9 l/min or higher.

The welds carried out experimentally during the imaging can also be examined to correlate with the diagnostics. Fig. 42 shows the welds produced during the imaging shown in Fig. 36 (e) – (h), using a pull angle. The result at 6 l/min confirms the notion that insufficient shielding gas coverage leads to oxygen entrainment, which in turn leads to gas pores in the solidified material. Similar results were recorded when using a pushing motion.

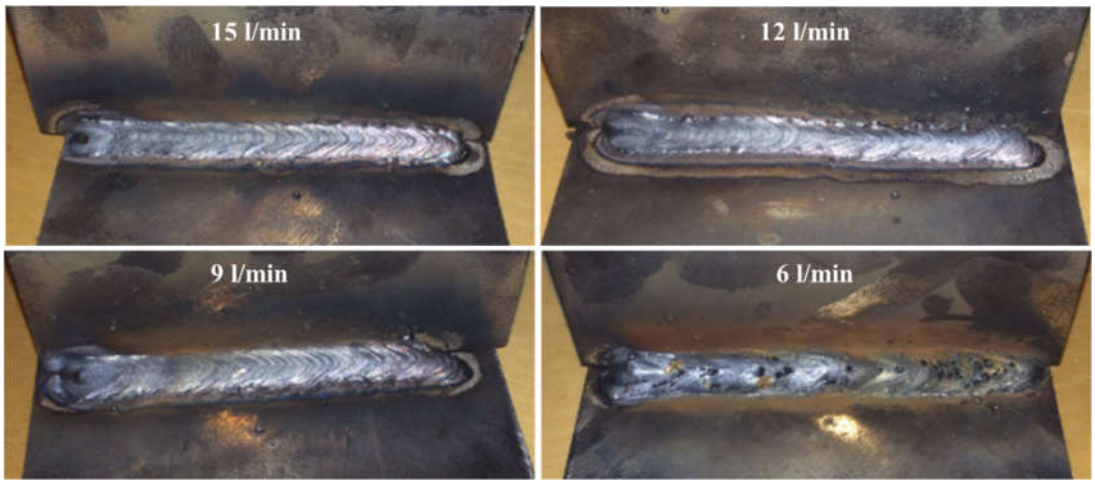

Fig. 42 GMAW fillet weld samples, produced using pure Ar and solid wire at varying flowrates. Porosity is present only for the 6 l/min case, due to insufficient coverage.

4.1.4. *Flowrate variation during fillet FCAW-G*

Following the GMAW experiments, the wire consumable was changed from plain 0.9 mm diameter mild steel to 1.2 mm flux-cored wire and the gas mixture was changed to 20% CO_2/80% Ar. The steady-state images from the visualisation experiments are shown in Fig. 43. As above, the images were time-averaged over 250 frames. Their intensity levels were then stretched so that they occupied the entire 256 grayscale colourmap and 0.5% of the pixels were saturated.

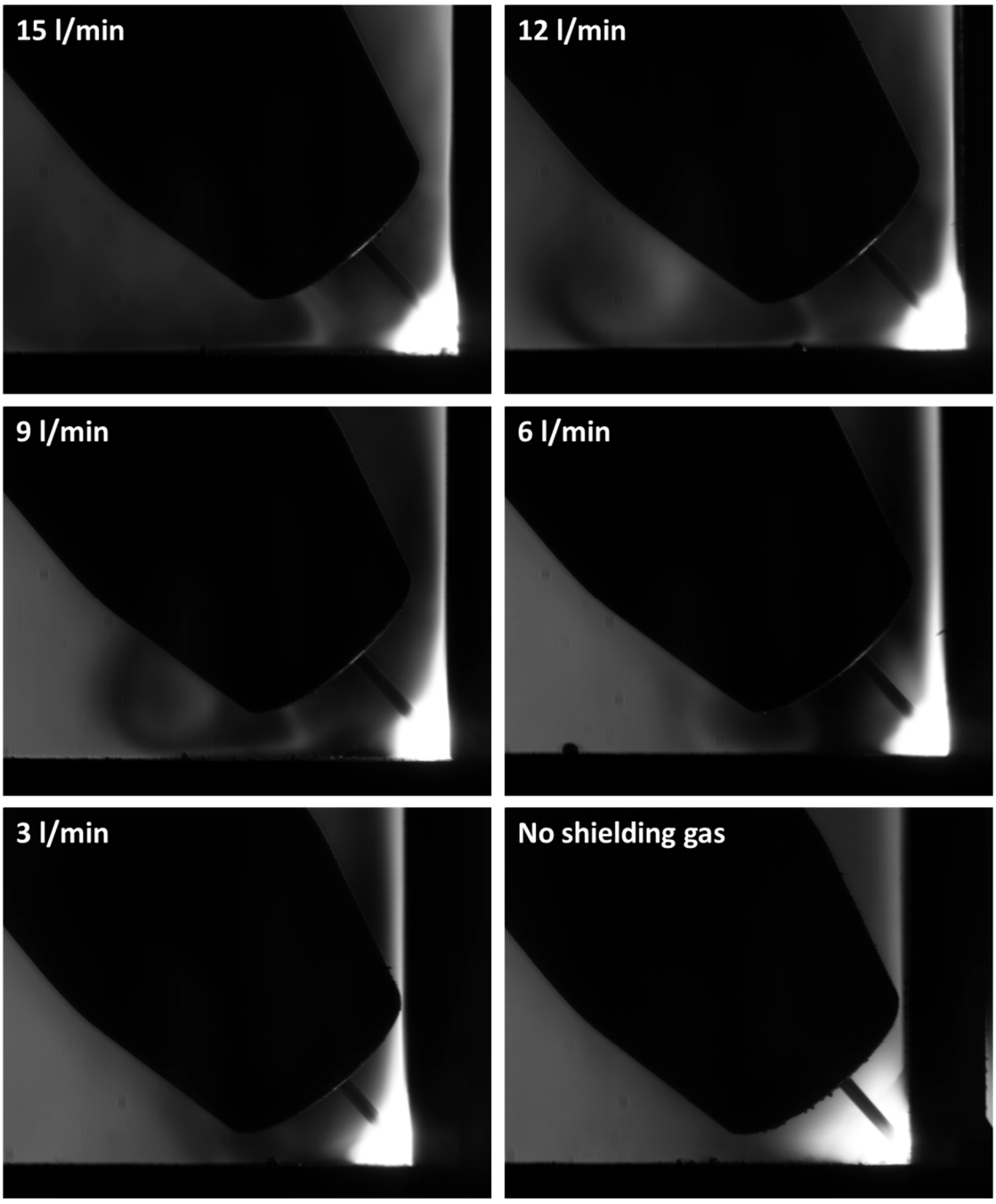

Fig. 43 Input flowrate variation for FCAW-G with 20%CO_2 shielding gas. The reduced momentum in the gas shield is indicated by the receding left hand gradients and vortex.

The images of Fig. 43 closely resemble those of Fig. 36, suggesting that the physical phenomena affecting the flow in GMAW are similar during FCAW-G. Starting from the 15 l/min flowrate, it is clear that enough momentum is imparted to the gas so that the shield gas gradient is formed under the nozzle's left-hand side. The dark region is due to a horizontal flow of the gas exiting the nozzle, mixed with faster stream along the plate's surface, originating from the arc's stagnation point. As the input flowrate decreases, a steady state vortex establishes at some distance away from the arc. At 6 l/min or less, the contrast of the gas shield gradient is low, suggesting higher air content reaches the arc.

Additionally, with decreasing input flowrate, the size of the bright regions around the arc and buoyancy plume root increases. This is attributed to the higher temperatures under the nozzle with decreasing flowrate, as discussed in the previous section. When the shielding gas is entirely removed, the arc functions purely by air entrainment, and the only outwards momentum in the induced atmospheric air flow is due to arc stagnation.

Following removal of the slag, the fillet welds produced whilst imaging are shown in Fig. 44. Visual inspection of the samples suggests that porosity-free welds can be produced down to 3 l/min with this FCAW-G configuration. When shielding gas was not provided, the slag did not surface and remained amalgamated with the weld metal after solidification, producing an unacceptable weld.

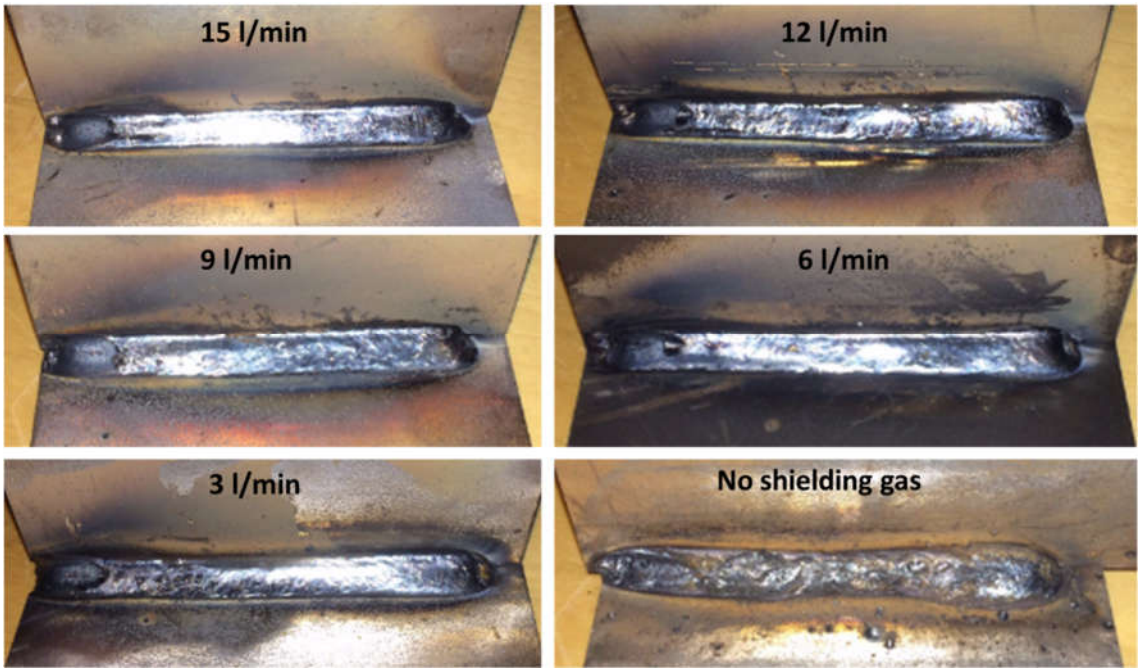

Fig. 44 FCAW-G fillet weld samples produced at varying input flowrate. Good welds were achieved even with 3 l/min.

Although, according to the diagnostics, air entrainment is elevated at the lower flowrates, the potential for the absorption of O_2 by the system is different due to the presence of the flux. The difference between these samples and those produced with solid wire is that with the addition of Si and other elements contained in the slag preferentially react with the O_2 in the environment. As a result, the amount of gaseous CO mixing with the liquid metal is reduced, and thus pore formation during solidification is inhibited despite the elevated O_2 levels.

4.1.5. *Discussion*

The observed schlieren features were consistent with the outputs from the 3D simulations, providing good synergy to analyse the gas flow during GMAW fillet joint production. The image sequences produced at different flowrates showed that sharper refractive index gradients formed under the nozzle walls when the shielding gas input was higher. The predicted temperature, velocity and O_2 concentration showed that, with an increase in shielding gas input, larger concentration and temperature gradients arise in these areas.

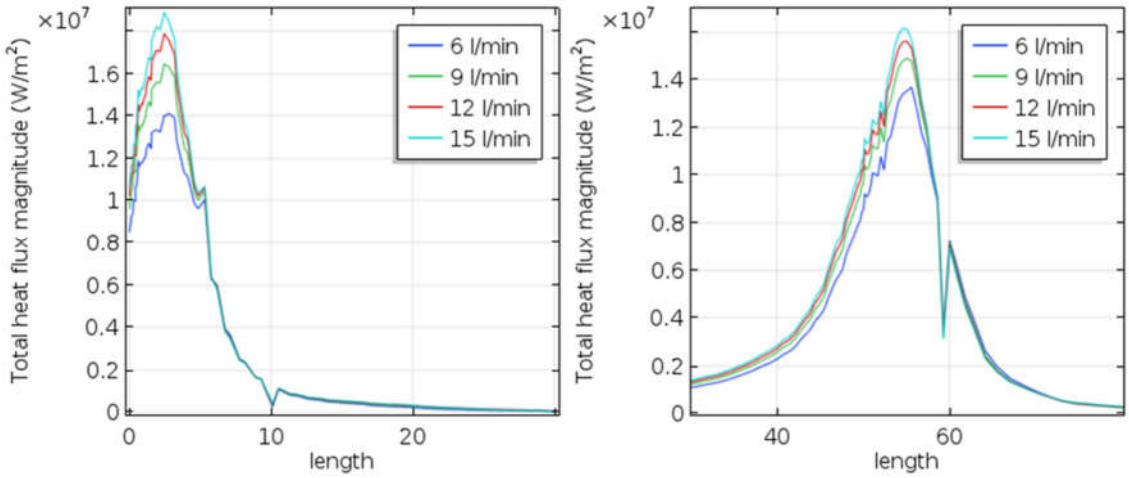

Fig. 45 Total heat flux towards the workpiece: (left) from arc root to the top of vertical wall, (right) along T joint intersection.

To understand how these effects relate to the heat transfer towards the workpiece and weld, the total heat flux from the arc root along the top wall and across the T joint's intersection is plotted in Fig. 45. Both graphs show that reduced heat transfer to the workpiece occurs as gas input is decreased. This can be attributed to a decrease in convective heat transfer at the surface of the workpiece due to the reduced momentum in the flow. Moreover, as air is more heat conductive than Ar, an increased air content in the gas mixture suggests that more heat escapes in the gas/plasma flow before reaching the workpiece. These results suggest that adjusting the flowrate can influence the heat input into the weld. However, comparison of the HAZ in the samples welded under varying gas flowrates did not show any significant differences, suggesting that any change in heat input is small.

Experimental samples showed that 9 l/min of Ar or higher were required to adequately protect GMAW fillet welds. Despite the changes in joint geometry and associated flow patterns, the model's results and visualisations followed similar trends with those for bead-on-plate welds, as in Chapter 3. However, predicted O_2 levels were lower for fillet welds than for bead on plate welds at low gas flow rates. In fact, based on the pragmatic

threshold identified in Chapter 3, fillet welds at 6 l/min should be of acceptable quality, as a maximum of ~4,000 ppm was calculated in the model. This discrepancy can be attributed to a combination of the following factors:

- Deviations between the modelled geometry and experimental setup, especially regarding wire stickout and nozzle-to-workpiece distance.
- Additional protection from air entrainment arising from the fillet weld geometry.
- Omission of the bead shape, which is more important in the fillet geometry than in the bead on plate configuration, due to the flow directionality and different arc length arising in the gap between plates.

Regardless of this inconsistency, the fillet weld model allowed characterisation of observed flow phenomena such as buoyancy-driven upwards flow, atmospheric heat accumulation and air entrainment under the nozzle area. Identification of such features in the flow aided in the interpretation of the FCAW-G visualisations. No significant differences were observed in the shielding gas flow behaviour, suggesting that predicted oxygen levels were present due to entrainment mechanisms. Porosity-free FCAW-G fillet welds produced whilst imaging, even with as little as 3 l/min shielding gas, indicated that the "dual shielding" effect of the flux-cored wire limits the amount of CO formed in the melt pool. Furthermore, the reduction in porosity can also be attributed to the addition of CO_2 in the gas, which has been shown to decrease O absorption in the weld metal [47].

4.2. TIG welding using an alternating gas supply as a pulsing method

Although the standard inert gas for any shielding application is pure argon, a variety of argon-based gas mixtures are used in industrial practice. By adding gases such as He, CO_2 or O_2, the thermophysical properties of the plasma can be controlled, resulting in improvements in heat transfer, arc formation, gas coverage or material weldability.

Pulsing the shielding gas to achieve dynamic in-process changes to arc power was first proposed by Cunningham [102] in 1967 for welding and cutting, in which pulses of a second shield gas, such as helium, were incorporated into the main argon flow via a modified torch design. Subsequently, a valve-regulated gas delivery system that alternated the shielding gases in the same feed line to the welding nozzle was used for the same purpose in Novikov et al. [103]. Variations in the arc conductivity were noted, and it was suggested that these produced a higher total power and caused a varying pressure and effective diameter of the arc. The pulsed gas delivery method has been used in both gas metal arc welding (GMAW) and gas tungsten arc welding (GTAW) of aluminium alloys [103]–[105], as well as of carbon [106]–[108] and stainless [109], [110] steels. Several benefits were reported, such as improved distortion control and re-work reduction [108], [111] or refinement of weld structure and thus better mechanical properties of the weld [103], [109]. The pulsing frequency was shown to influence the dynamics of the melt pool [110] and final geometry of the solidified weld [109], [111].

Such results therefore imply that using this process has potential for an increase in productivity or shielding gas efficiency due to improved heat and momentum transfer towards the weld pool. However, the uptake of the process has been slow because the economic and technical benefits claimed are based on mechanisms which have not been completely understood and quantified. The effect of gas mixing and pre-mixing on the shielding gas flow have not been analysed, and no imaging of the shielding gas flow has been reported.

In this section, pure and alternating Ar and He shielding gas flow are visualised during GTAW with high-speed schlieren imaging. The effect that changes in the pulsing frequency and flow rate have on the flow and arc characteristics are analyzed, and contrasted with imaging sequences of pure and premixed flows. Also, the effect of pre-mixing of the shielding gases in the delivery pipe to the welding nozzle is established analytically through axial dispersion calculations. It is shown that low pulse rates and high flow rates make more efficient use of the He, because it is held in the weld region

by the denser argon from the preceding pulse, whereas high pulse rates and low flow rates result in the shielding gases being delivered premixed. Macrographs of the weld section show that alternating the gases increased the weld penetration by 13% on average compared to using them pre-mixed.

4.2.1. *Experimental setup*

The imaging setup in this study, Fig. 46, was an earlier version to the one outlined in section 3.1. The concave mirrors used in this version of the setup, were 100 mm diameter in diameter with f = 1.27 m. The light source was a 10,000 lm warm white LED, with an intensity spectrum peaking at approximately 630 nm. The light was collected by two condenser lenses, L1 and L2, with focal lengths of 120 mm and 60mm respectively, in a telescope arrangement to reduce the LED's spot size at the source slit and to maximise the light collection efficiency. The shape and size of the source slit determines the sensitivity and measurement range of the schlieren system [70]. We used a 2 mm × 6 mm rectangular source slit with the long edge vertical, as recommended by Siewert et al. for welding applications [67]. The source slit was positioned at the focus of M1, to produce an image of the source at the focus of M2.

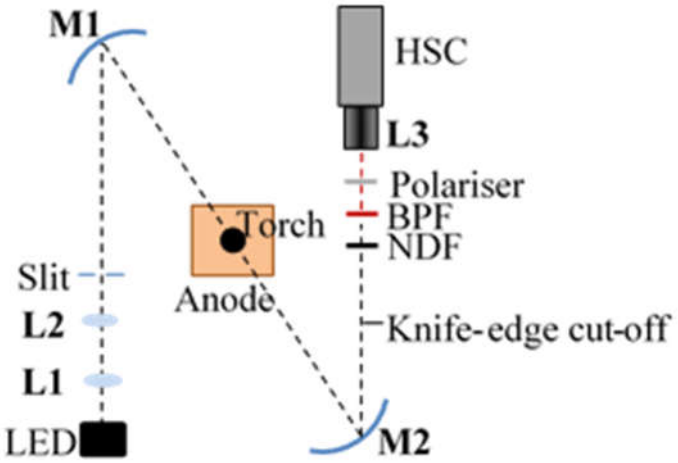

Fig. 46 Schematic of Z-type schlieren and alternating gas GTAW setup. The optical system comprised a high intensity light emitting diode (LED) source, parabolic mirrors, a combination of filters and a high-speed camera (HSC).

Images were recorded at a resolution of 256 × 256 pixels using a Kodak Ektapro high-speed camera, with a variable focus macro lens (L3). The exposure time was varied based on the level of radiation from the object by adjusting the frame-rate of the camera. Gas flows without welding were imaged at 4,500 frames per second (fps) and there was no need for additional optical filters between the knife-edge cut-off filter and the high-speed camera. For GTAW welding, filters were added between the knife-edge and the camera in order to reduce the bright light emitted from the plasma. Spectroscopic analyses of GTAW Ar arcs have shown that no strong lines are present in the region around 630 nm

[84]. Furthermore, He radiation is very low at 633 nm [65], as shown in Fig. 8. Thus a 633 nm ±10 nm full-width-half-maximum band-pass filter (BPF) was used to eliminate as much arc light as possible. Narrower band pass filters at 633 ±1 nm and ±3 nm were also tested but reduced the source light to a level below the sensitivity of the camera. A polariser was used to remove glare from the workpiece. Finally a neutral density filter (NDF) was included and the high-speed camera frame rate was reduced to 750 fps to record images.

The welding setup consisted of a stationary welding torch, located between the mirrors M1 and M2, and a water-cooled copper anodic plate to prevent melting. A 2.4 mm diameter, 2% thoriated tungsten electrode was used throughout, with a 45° vertex angle. A 12.2 mm internal diameter nozzle with a 5 mm stand-off distance was used to direct the shielding gas flow.

In order to alternate the shield gas flow, a dedicated electronic gas control unit was designed, allowing the two shielding gas supplies to be connected to the welding torch. The unit utilises two timing circuits, which regulate the flow of each gas independently by giving a control signal to a solenoid valve on each gas line. The volumetric flow rate of both gases was set to be equal but supplied to the main hose at inverse time intervals of equal duration within the period of one shielding gas switching cycle, i.e. a 50% duty cycle between the two gases. A schematic diagram of the shielding gas control system is shown in Fig. 47.

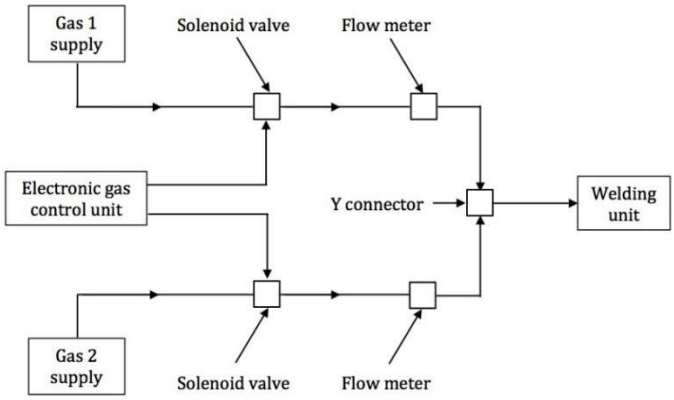

Fig. 47 Schematic diagram of the control system used for alternating the shield gases. The argon and helium gas cylinders were connected to the welding torch through solenoid valves, controlling the gas cycling over time.

In order to maintain consistency in the results, all trials were performed using DC electrode negative with a constant welding current of 100 A. However, due to the difference in their ionization potentials, a higher arc voltage was required to maintain an arc for helium (~19 V) than for argon (~13 V), resulting in lower total power for argon.

Welds were carried out using the pure gases to establish the upper and lower bounds of the available heat input. When alternating the shield gases, the current was again held constant at 100 A and the voltage was observed on the welding power supply to fluctuate at the pulsing frequency between these extremes, according to the shield gas composition and flow conditions. Such fluctuations in voltage are well-known in alternating shielding gas flows with GTAW and typical waveforms are shown in Traidia et al. [8]. Therefore, the amount of energy put into a given weld is associated with how efficiently the available helium is utilised, and the effect of varying flow conditions on the resulting welds was thus directly comparable by keeping the volumetric mass fractions constant.

4.2.2. *GTAW visualisation using pure Ar*

In order to analyse the motion and identify the ambient properties of the gases used during the GTAW process, 'cold' flow imaging of the shielding gas flow without an arc was carried out to supplement 'hot' flows where the arc plasma was present. To provide a comprehensive reference, flow rates of 5 and 10 l/min for argon, helium, and alternating shielding gases at frequencies of 2 and 8 Hz were imaged.

The flow visualisations of Ar are shown in Fig. 48. The difference in refractive index between the surrounding air and the shielding gas determines the amount of refraction and hence the visibility of flow features [70], [73]. Analysis of the light passing through an idealised gas column at the same temperature as the surrounding air shows that argon refracts by an order of magnitude less than helium [69], [73]. Therefore the visualisation of the 'cold' argon flow showed weak refractive index gradients and rather poor visibility in the schlieren image. The schlieren sensitivity was increased for the 'cold' argon flow only by reducing the slit width to 3.2 mm; fluid motion and mixing of argon with air is just discernible in Fig. 48, although it was more observable in the high-speed video sequences. A laminar stream of argon exits the welding nozzle and spreads out over the workpiece surface due to the stagnation pressure, preventing environmental contamination near the weld bead. In the radial direction, the flow was mildly turbulent for the 10 l/min case with eddies forming away from the weld region, where the gas mixed with the surrounding air. It should be noted that the three distinct vertical, black lines (one just to the left of the tungsten electrode, one beneath and the other just to the right of the nozzle) are due to mirror scratches. These mirror defects can be seen in all subsequent images to some degree.

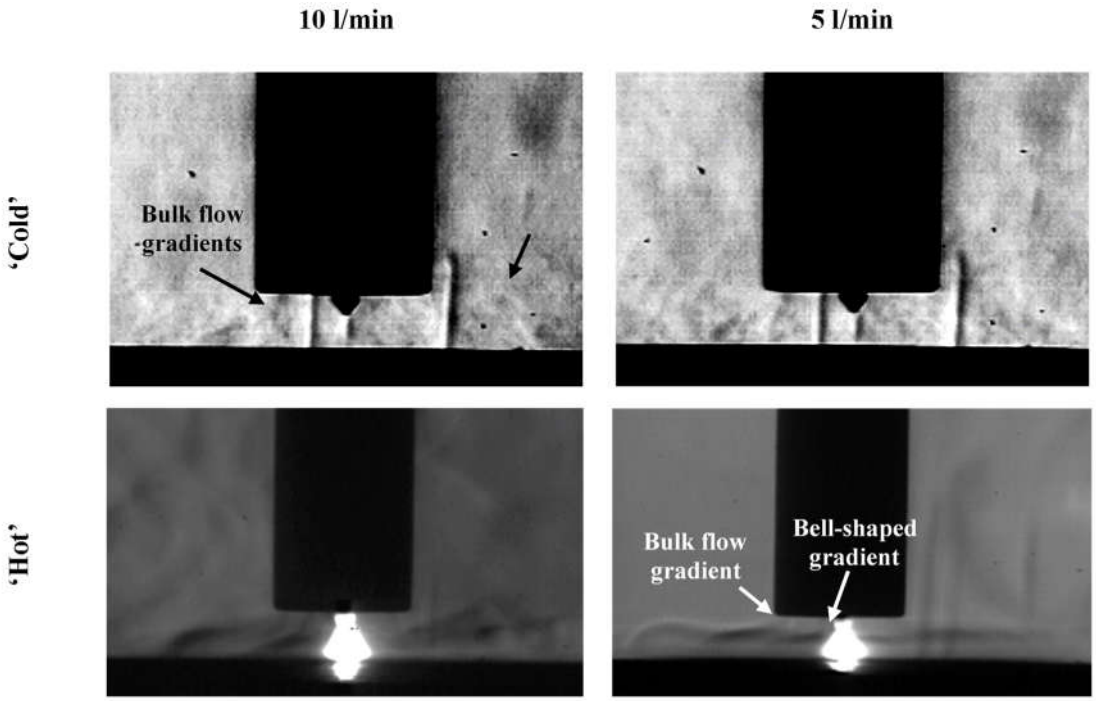

Fig. 48 Steady state schlieren images of Ar gas flows showing density gradients observed during 'cold' and 'hot' flows. The three vertical black lines in the 'cold' images are due to scratches in the parabolic mirrors, as discussed in the text.

Fig. 48 also shows the case for the 'hot' argon visualisations recorded during GTAW welding. The intense self-luminance of the argon plasma was brighter than the source despite the band pass filter, obscuring any axial flow features immediately below the tungsten electrode. However, the heated shielding gas increased the refractive index gradients elsewhere in the image enabling two distinct flow features to be seen in the figure. The first feature is a bell-shaped density gradient around the arc that was not visible in the 'cold' flow. This feature is characteristic of the downwards plasma jet: resistive, thermoelectric and thermionic heating cause the ionisation of gas particles which are accelerated due to Lorentz forces in the inter-electrode region [3], [48]. The second feature in the images is the bulk flow of the shielding gas, closer to the nozzle edges, which does not interact heavily with the arc. Within this secondary flow, the mean velocity is much lower than that of the plasma jet [48]. The form of this feature is similar to that seen on the 'cold' flow images, including mixing at the interface with the environment. Buoyant mixing also occurs at the boundary, with the surrounding air as the heated argon rises up due to its reduced density and mixes with air. At 5 l/min there was a strong horizontal density gradient, suggesting a local equilibrium at the argon-air interphase. At 10 l/min, the mixing became more turbulent and no steady-state density gradient was observed.

4.2.3. *GTAW visualisation using pure He*

The use of pure helium as a shielding gas in GTAW is not a common choice, mainly due to the prohibitive cost but also because arc initiation is harder and arc stability is limited [83]. However, in order to establish a benchmark of its characteristics, its flow was visualised as shown in Fig. 49. The nozzle has been delineated in the first frame to distinguish it from a large dark region in the schlieren image. The net emission coefficient of helium is an order of magnitude lower than that of argon [112]. Furthermore, He emits relatively little radiation around the 633 nm spectral range [65]. Therefore, in the 'hot' flow visualisations for helium, light from the bell-shaped plasma beneath the tungsten electrode was eliminated by the band pass and neutral density filters.

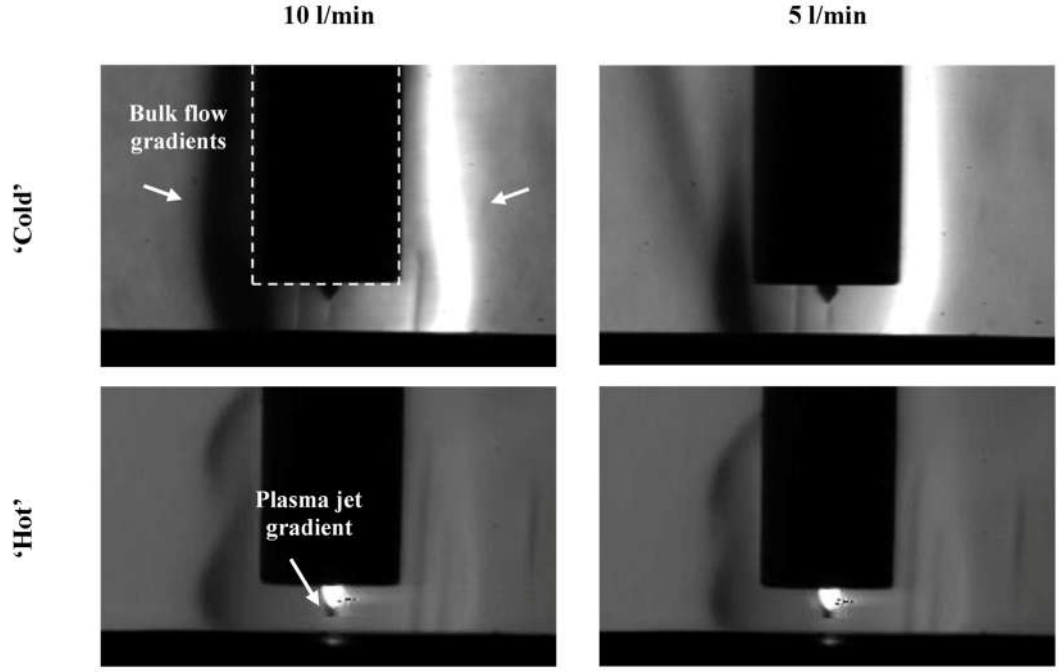

Fig. 49 Steady state schlieren images of helium gas flows showing density gradients observed during 'cold' and 'hot' flows.

The 'cold' visualisations for helium show a smoother flow than those for argon. The bulk flow gradients show buoyancy forces carry the gas upwards, creating a 'bulb' shaped plume, as internal viscous forces quickly eliminate any vortices and a steady state flow is reached. Comparison of the steady state flows between 5 and 10 l/min showed that the coverage on the workpiece was increased in diameter when using the higher flow rate.

In the 'hot' images of Fig. 49, a short cylindrical refractive index gradient feature can be seen immediately below the electrode due to the plasma jet. This cylindrical feature does not extend fully to the anode and extends only slightly beyond the electrode, suggesting that a body force is acting heavily on the flow close to the anode. Based on numerical magneto-hydrodynamic models [24,26,27], the plasma jet is indeed expected to

decelerate, as the axial Lorentz forces are expected to change magnitude and direction locally due to increased electromagnetic activity close to the anode. This observation is also supported by previous measurements which show that helium produces a lower arc stagnation pressure than argon [114]. The predicted local decrease in flow vectors is validated by the lack of a strong horizontal jet parallel to the workpiece. Such a horizontal flow feature is characteristic of a higher velocity stream with increased momentum, as encountered in the argon visualisations, Fig. 48. Instead for helium, a 'bulb' shaped helium column rises up from the nozzle sides, mostly due to the difference in density with air. The black spots close to the arc in the 'hot' images are due to saturation of the CCD from excess arc radiation.

4.2.4. *GTAW visualisation using alternating Ar and He gases*

As noted above, a 50% duty cycle was used for all alternating shielding gas tests, i.e. the argon and helium were switched on for equal times within the period of one shielding gas switching cycle. Fig. 50 shows the visualisation for a 10 l/m flow with alternating shielding gases within one cycle. Two switching frequencies are shown, 2 and 8 Hz, and the time of each image is indicated. In order to compare these two frequencies directly, the cycle period is indicated on the left-hand side of the figure: 0% and 100% of the cycle period correspond to the mid-point of the argon-dominated flow, while 50% corresponds to the mid-point of the helium-dominated flow. When using the alternating shielding gas technique, the shielding gas flow rapidly transitioned from one with the characteristics of pure argon, to one with the characteristics of helium. However, subtle differences were present as the mass fractions of each constituent varied, forming distinct, transient features over time.

The arc at 0% and 100% of Fig. 50 is typical of the argon flow of Fig. 48 and the arc at 50% is typical of the helium flow of Fig. 49. However, the arc in the 50% image at 8 Hz is brighter than at 2Hz, suggesting that more argon was present. Ideally the mixture of the two gas flows exiting the nozzle would be equal at the two frequencies, but in practice the maximum fraction of helium comprising the arc during any given pulse was affected by flow and pre-flow conditions. The most significant contribution to this effect was the amount of premixing between the gases in the combined delivery pipe to the nozzle.

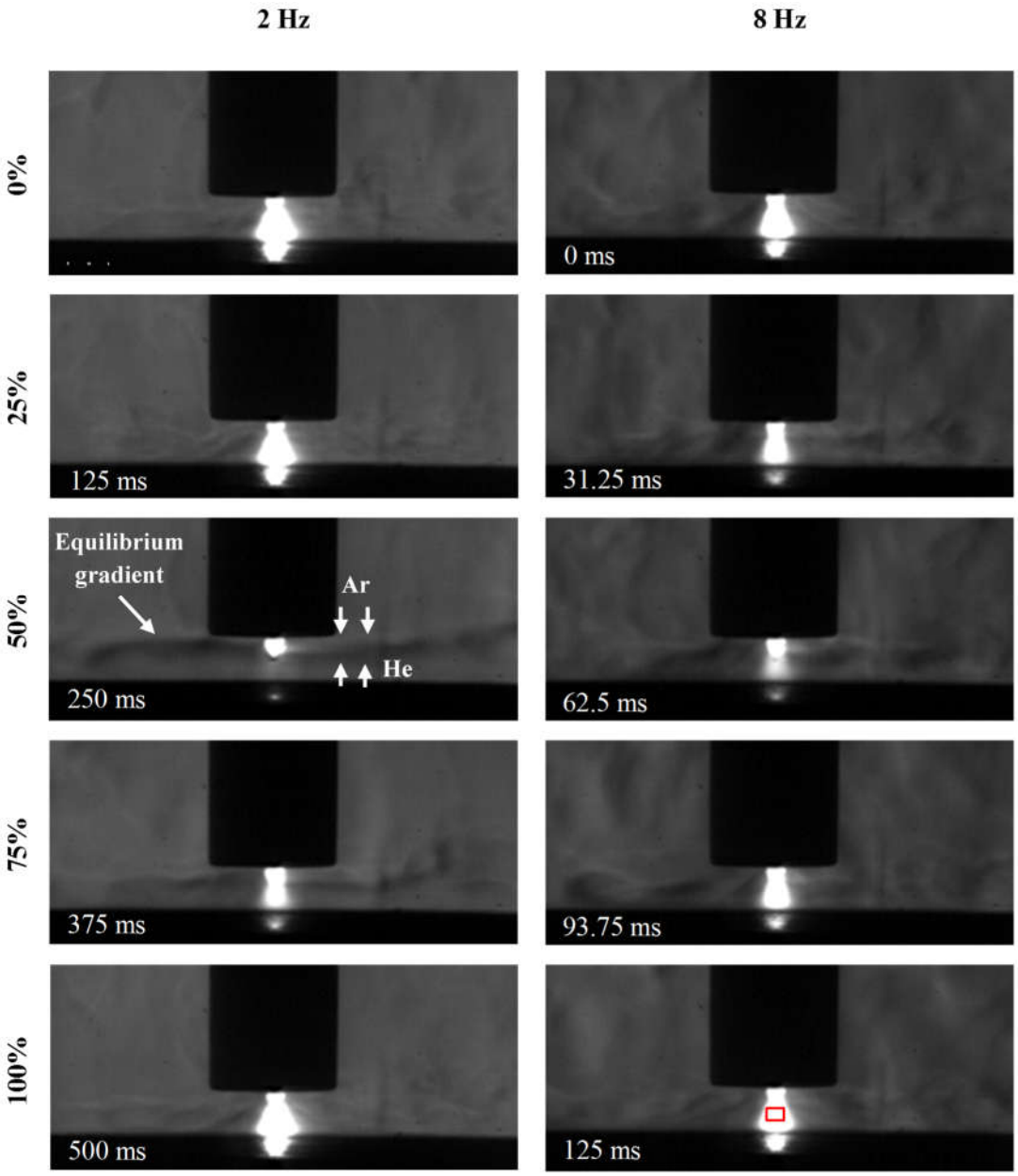

Fig. 50 Visualisation of 10 l/m flow with alternating shielding gases at different times within one shield gas switching cycle. 0% corresponds to argon dominated, 50% to helium dominated and 100% returning to argon dominated again. The typical arc radiation measurement area (see text) is shown in bottom right image.

In order to characterise this pre-mixing, a theoretical analysis of axial dispersion in the gas line leading to the torch was conducted. It is assumed that the alternating cycle begins with a pulse of argon followed by a pulse of helium, both of equal lengths, flowing laminarly along the delivery pipe. The pipe has a circular cross-section with a solid inner core, i.e. the power supply to the welding torch. The mixing zone length L, is the length from the original argon-helium boundary to which the two gases are completely mixed, by the time the gas boundary reaches the end of the pipe and is delivered to the torch. It is determined by solving the diffusion equation, and is given by [115]:

$$L = 4\sqrt{Et}$$

where E is the dispersion coefficient and t is the total residence time of the boundary in the pipe. E for a laminar flow comprises contributions from both convection and diffusion, and can be calculated from a formula based on experiment and theory:

$$E = D + \frac{(d\,v)^2}{192D}$$

where d is the pipe's hydraulic diameter, v is the fluid's velocity and D is the binary gas diffusion coefficient which was calculated for argon and helium using the method of Fuller et al. [116]. The fluid velocity v can be calculated from the shielding gas volumetric flow rate and the pipe's hydraulic cross-section, assuming an incompressible flow. Therefore, the mixing zone length can be plotted against the shielding gas flow rate, as shown in Fig. 51. In the figure, the mixing zone length has been expressed as a percentage of the length of the original argon pulse. Hence a mixing length ratio of 100% indicates that the argon and helium pulses have completely mixed within the delivery pipe. Fig. 51 shows that that the relative mixing of a pulse decreases as the flow rate increases. Conversely, the relative mixing of a pulse increases as the alternating frequency increases.

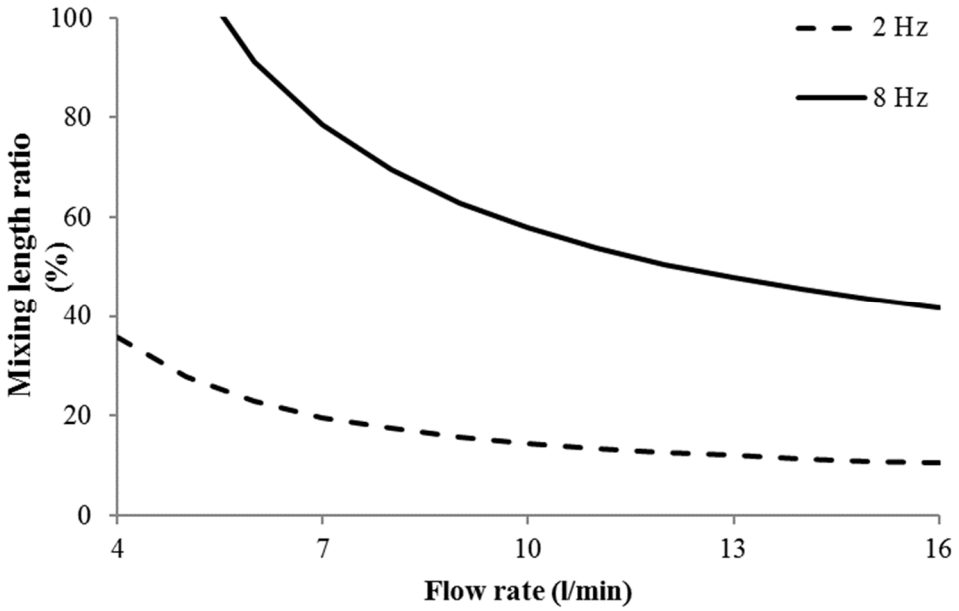

Fig. 51 Axial dispersion of a helium pulse within a 5m GTAW gas delivery system. The gases will be mixed completely before reaching the torch if pulsed at high frequency and the flow rate is low.

Fig. 51 can be related to the previous images for the 10 l/min alternating shielding gas flow. For the 2 Hz alternating frequency, mixing occurs over approximately 15% of each argon pulse, whilst at 8 Hz it increases to approximately 60% as the duration of the gas pulses is four times smaller. The greater pre-mixing of the two shielding gas pulses at

8Hz explains the brighter arc seen at 50% pulse position in Fig. 50. The dispersion calculation shows that for a 5 l/min shielding gas flow rate, pre-mixing is stronger than at 10 l/min: 30% ratio at 2 Hz and >100% at 8 Hz. The mixing ratio approximately doubles because the actual mixing zone length is similar in going from 10 to 5 l/min but the pulse length halves. A mixing length ratio of more than 100% of the argon pulse indicates that the pulses mix almost completely within the delivery pipe. These effects can be observed experimentally: Fig. 52 shows visualisations of the shielding gas alternating at 2 and 8 Hz for the 5 l/min flow rates. At 2 Hz the result is similar to Fig. 50, but at 8 Hz the arc intensity did not vary at different times through the 'pulse' cycle due to complete mixing of the two gases within the delivery pipe.

In order to estimate the composition of the arc plasma at any instant, an estimate of the total arc radiative flux for the wavelengths of 633±10 nm was made from the image sequences, for a 1 x 1.5 mm rectangular cross-sectional area below the cathode, indicated in Fig. 50. The emission characteristics already seen for pure argon and pure helium in Fig. 48 and Fig. 49 indicate that the brightest points correspond to an arc mainly comprised of argon, while the local minima in intensity correspond to an arc mainly comprised of helium.

Clearly the transition between these two arc types does not follow the square-wave with 50% duty cycle applied to the shielding gas switching valve. This is attributed to pre-mixing of the gases in the delivery pipe prior to the torch, in addition to turbulence in the weld region and transient flow vectors from electromagnetic field cycling. The extreme case is 5 l/min at 8 Hz where a constant arc intensity was observed in Fig. 52, due to the 100% pre-mixing of the shield gases prior to delivery. As discussed above, increasing the flow rate to 10 l/min at 8 Hz reduces pre-mixing to approximately 30%, although Fig. 53 shows that the time spent during each cycle at the minimum intensity is somewhat shorter than that. It could be observed from the associated video sequence of Fig. 50 that at 8Hz the turbulence in the shielding gas flow reduced as helium entered the weld region, due to its lower viscosity. Indeed, during the helium pulse a horizontal intensity gradient (indicated in the figure) started to establish itself, but did not have sufficient time to form completely before the next argon pulse.

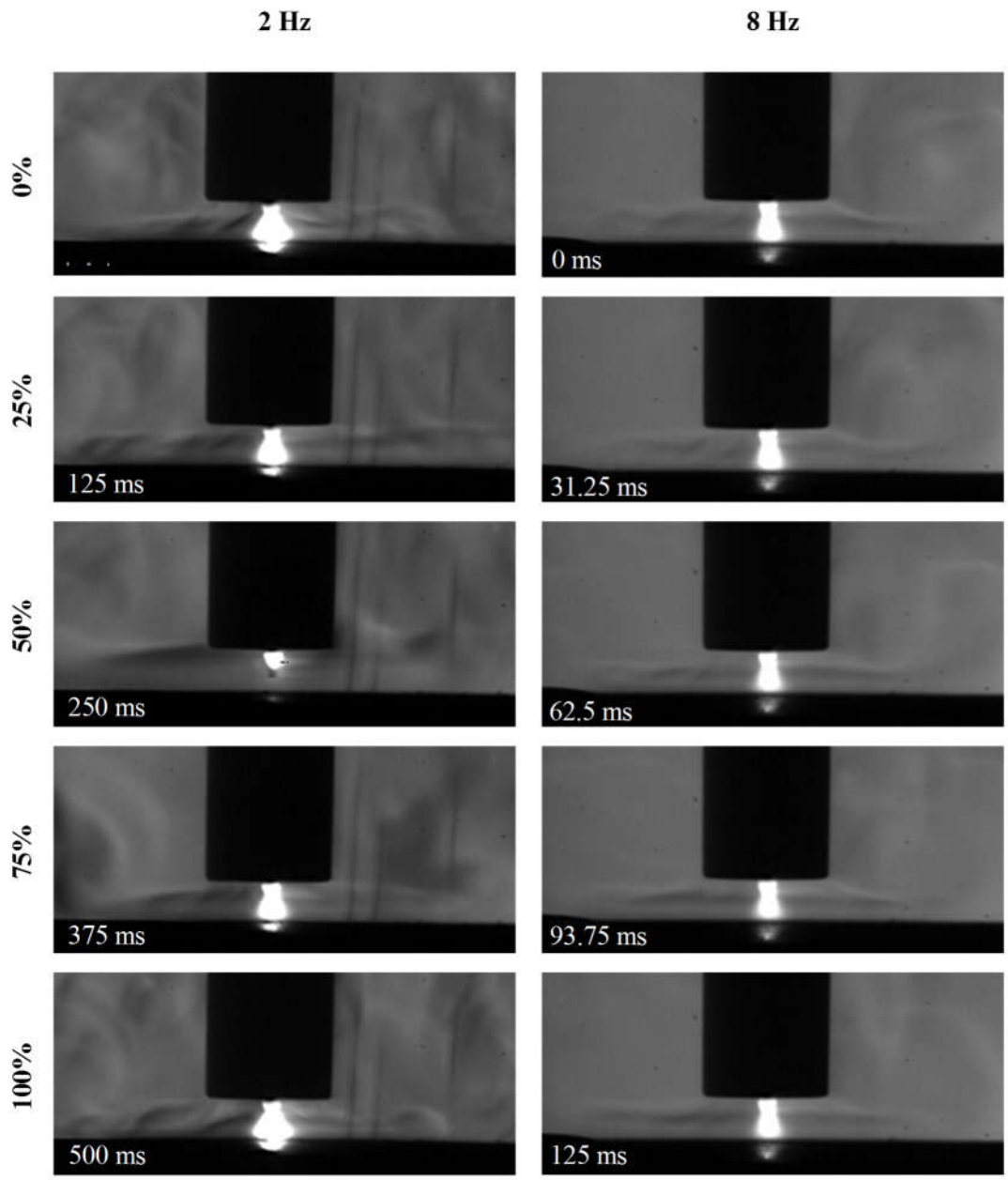

Fig. 52 Visualisation of 5 l/m flow with alternating gases at 2 and 8 Hz frequencies. The 2 Hz cycle shows transient arc characteristics, while for 8 Hz the process is almost steady state because the two gases have mixed fully in the delivery pipe.

Fig. 53 shows lower minima when alternating at 2 Hz for both the 5 l/min and 10 l/min flows: overall a higher average fraction of helium exists in the arc due to reduced pre-mixing in the delivery pipe and the shielding gas has less vorticity due to the longer cycling times. Indeed, the associated video sequences of Fig. 50 and Fig. 52 at 2Hz show the formation of a large horizontal density gradient extending from the top of the nozzle towards the edge of the image, indicating that equilibrium in gas concentration and partial pressures was reached during the helium pulse. This feature persisted throughout the helium phases, replacing the 'bulb' shaped buoyant plume observed in the steady state helium images, Fig. 49. The helium is restricted from flowing upwards, due to the heavier argon-air mixture acting to constrict it. The duration of the local minima in radiation

intensity during the 2 Hz cycles shown in Fig. 53 was again somewhat less than the 50% duty cycle applied to the alternating shielding gas supply.

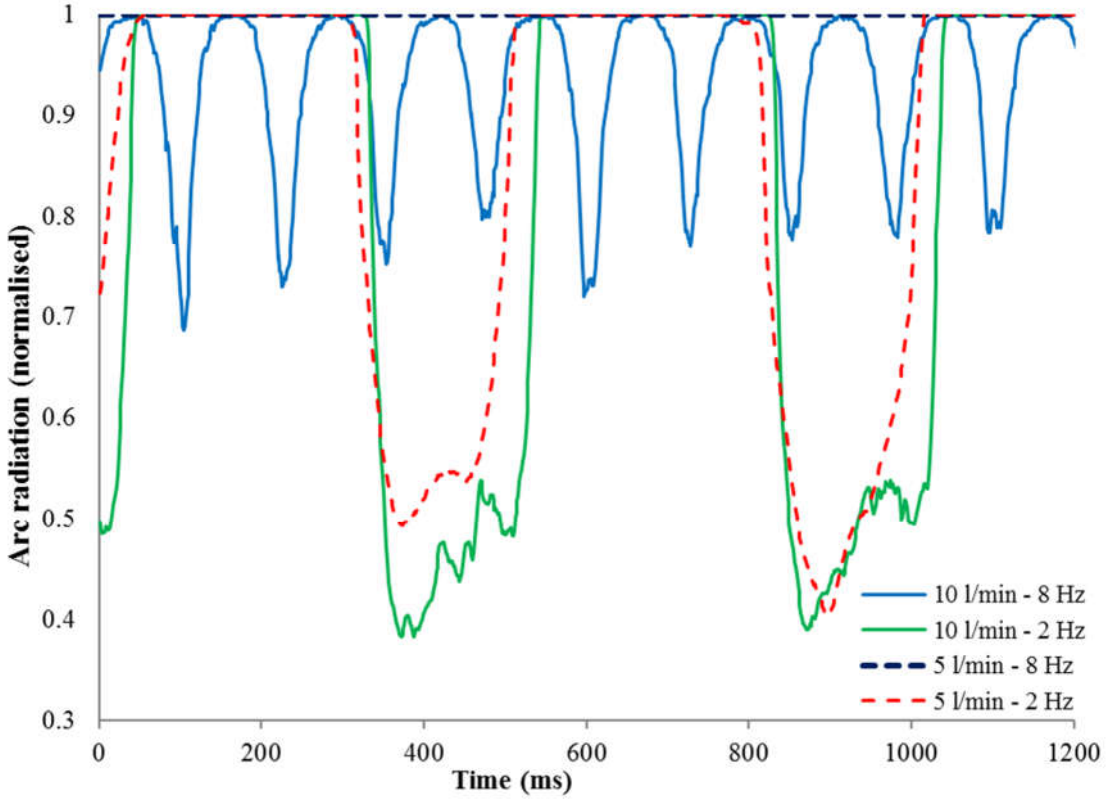

Fig. 53 Normalised arc radiation measurements obtained through image processing of the visualisations. The intensity of radiation is directly related with the fraction of ionised argon in the arc plasma, since helium emissions are much lower for the wavelengths allowed by the 633nm band pass filter.

4.2.5. *Discussion*

The results presented in the previous section serve to characterise the flow at any given phase of the alternating shielding gas cycle. For the steady state flow during spot GTAW on a cooled copper plate, the argon flow was seen to be mildly turbulent with large eddies, whereas that of helium was smoother with buoyancy forces carrying the gas upwards to form a bulb shaped feature. When utilising the alternating shielding gas technique, the choice of pulsing frequency and flow rate determined the stability of a relatively stable horizontal region of helium shielding that formed in the weld region, maintained in position by the denser argon from the preceding pulse. It might be supposed that lower turbulence entrains less argon into the weld region and thus increases heat transfer into the workpiece, affecting weld size and penetration. In order to test this idea, GTAW welds were performed directly on to 6 mm thick, DH36 grade steel plate under the same conditions as the previous tests on the cooled copper plate.

The macrographs of the weld geometry produced for the shielding gas configurations used previously are shown in Fig. 54. As expected, the weld produced using pure helium resulted in a considerably larger weld size and penetration compared to the other shielding gas configurations. Due to 100% pre-mixing in the delivery pipe, the alternating flow at 5 l/min and 8 Hz provides a useful reference for a standard 50/50 (by volume) pre-mixed argon/helium shielding gas cylinder. Compared to this reference case, the weld width for the three cases where the flow was alternated increased by 3% on average, while the depth of penetration increased by 13% on average. The welds made using the non-premixed flows were almost identical regardless of the flow rate used, establishing the 2Hz, 5 l/min case as the most economical option.

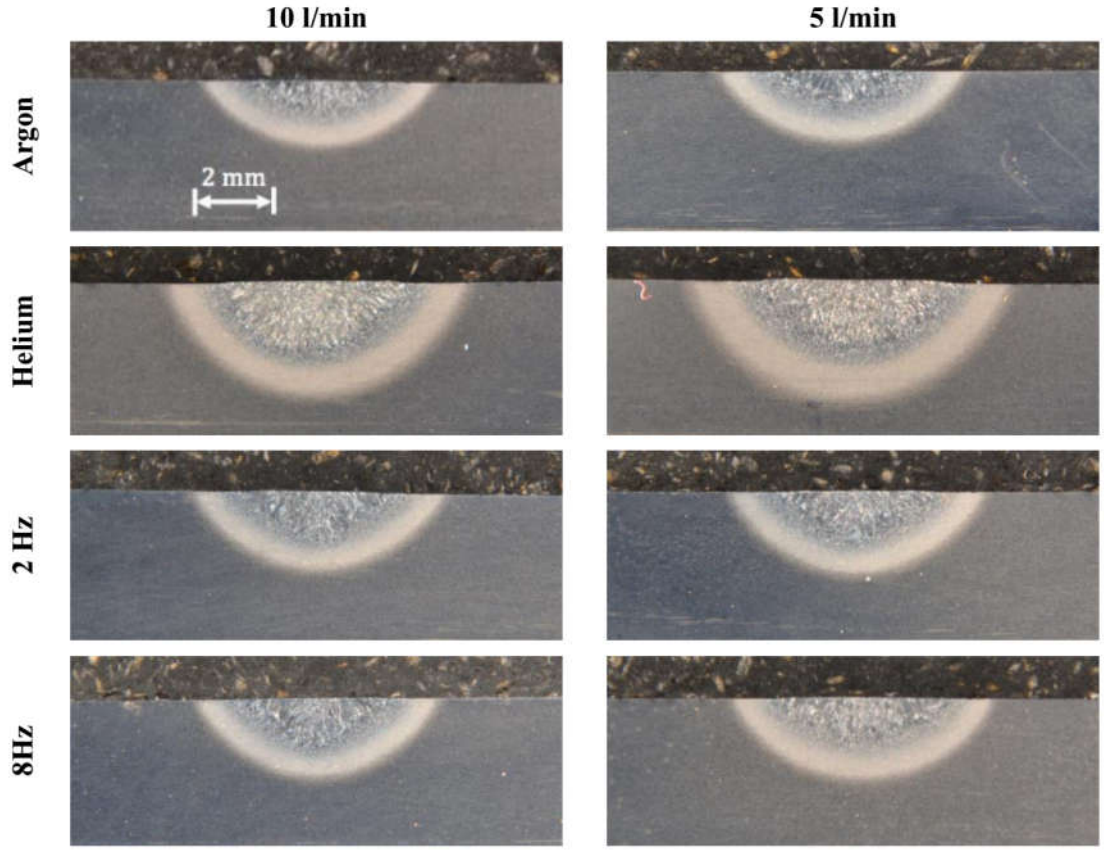

Fig. 54 Weld macrographs showing effect of shielding gas configuration. Due to pre-mixing, the alternating flow at 5 l/min and 8 Hz provides a useful reference for a standard 50/50 (by volume) pre-mixed argon/helium shielding gas cylinder.

The other important function of the shielding gas is to prevent porosity in the weld. The main mechanism for the entrainment of contaminants such as air or nitrogen from the environment into the weld is two-fold. Firstly, air mixes with the bulk flow through convection and diffusion. In the vicinity of the arc, the radial component of the flow is generally turned inwards and perpendicular to current's path in the plasma, accelerating gas through the shielding gas flow and towards the electrode [3]. Consequently, the

degree to which the shielding gas flow mixes with the surrounding air close to the nozzle predominantly dictates the extent of contamination in the weld.

Through inspection of the image sequences under flow rates of 5 and 10 l/min, it was found that the coverage area would be larger than the weld pool regardless of the shielding gas composition or supply method, provided no cross drafts were present. With this condition satisfied, the gas would be expected to have shielded the weld adequately at all times in both cases. Still, these results are specific to the welding setup used, and the stand-off distance or indeed nozzle diameter would influence the degree of porosity or microporosity in the weld. At the same time, a general trend in gas behaviour was observed, which can be expected of most GTAW setups provided a reasonable combination of welding parameters are implemented.

Radiographic examination was performed on each experimental weld in order to detect discontinuities through the thickness of the weld. All the shielding gas configurations reported produced welds free from undesirable imperfections, which would pass industrial testing. The defect level, i.e. the percentage of the x-ray image that exhibited a shade contrast to that of the bulk material, is used to characterise the level of micro-porosity, metallic and non-metallic inclusions. Its distribution was found to be consistent throughout the range of shielding gas parameters (composition and flow rate) investigated, and therefore all configurations produced welds in which the imperfections present would not be detrimental to the overall weld integrity.

4.3. Conclusions

The first study in this chapter was an analysis of the flow characteristics during the production of fillet welds using GMAW and FCAW-G. Results from a fully 3D MHD model were compared with visualisations of the gas flow in the fillet configuration. It was found that the shielding gas flow is asymmetric with regards to the torch axis due to buoyancy effects along the vertical plate of the fillet. No significant flow differences were observed when changing the torch angle relative to the direction of travel (“pushing” or “pulling”), although less spatter was observed when pulling. In both cases, air entrainment was minimal for welds carried out with 9 l/min or greater shielding gas flows. Welds produced with 6 l/min Ar resulted in unacceptable porosity for GMAW, whilst acceptable quality welds were produced even at 3 l/min using FCAW-G. A reduction in the shielding gas flow was associated with reduced heat input into the joint, due to lesser convective heat fluxes. As long as the penetration of a given weld is according to

specifications, a reduced heat input is desirable due to increased structural properties and reduced distortion. These results therefore suggest that porosity-free welds with minimal heat input can be achieved when using FCAW-G with shielding gas flowrates much lower than current industry standards.

The second study presented in this chapter visualised the flow of an alternating supply of argon and helium shielding gas during GTAW. In all cases, a 50% duty cycle between the two gases was applied, although in practice the duration of the arc associated with the helium pulse was less than the 50%, and more than 50% for the argon pulse, due to premixing between the gases in the combined delivery pipe to the nozzle and shield flow conditions after the nozzle. By choosing an appropriate pulsing frequency and flow rate, a stable horizontal region of helium was observed in the weld region, maintained in position by the denser argon from the preceding pulse. A 13% increase in weld penetration was observed with the alternating shielding gas method compared to the 'pre-mixed' case, suggesting that the helium is used more efficiently with the alternating shielding gas method. The understanding of this mechanism can be applied to other shielding gas mixtures and welding geometries in order to optimize performance.

5. Local shielding diagnostics during WAAM

5.1. Introduction

One of the challenges often associated with the welding of metallic alloys is to provide adequate shielding, not only for the molten pool, but also for the long reactive metal surface that follows it. For Ti-6Al-4V, it has been shown that increased levels of oxidation, a direct consequence of air contamination, result in reduced structural properties, especially ductility [117], [118]. Although this can be improved by manufacturing within an inert enclosure, operating thusly can be impractical and resource-intensive for the metre-scale part production capabilities of WAAM. Instead, local shielding is preferred to protect the part during the printing process without restricting the printing area.

A "trailing shield" device is usually employed to provide an inert gas flow locally, complementing the limited shielding capability of a MIG, TIG or PAW torch. Optimisation of the individual components of the torch, shielding device as well as the combined system is therefore crucial to maintain process reliability. The torch's manoeuvrability and ability of depositing complex shapes must not be compromised, limiting the available options for protecting the desired region. Moreover, long deposition times can carry increased production costs through inefficient gas use. Based on these principles, the inert gas supply along a given length from the torch and the way in which a diffuse, laminar flow can be engineered must be examined. To achieve this, several designs have been developed; the main considerations are the design of the inlet, which introduces a concentrated gas flow, and that of the setting chamber in which the gas expands and diffuses before reaching the shielded surface.

Following previous work, Ding et al. [92] investigated the level of contamination that can be tolerated for acceptable quality Ti-6Al-4V parts. They found that ~4000 ppm oxygen or less in the atmosphere were sufficiently low, although a large portion of the total oxygen content in the part was attributed to the composition of the wire. The coverage achieved when introducing a trailing shield with multiple inlets and a composite chamber configuration, as shown in Fig. 55, was compared with that of a simpler design. In the improved layout, comprised of a combination of straighteners, diffusive and mesh elements, a level of 2000 ppm oxygen or less was measured over the target surface, compared to an average of 5000 ppm without improvements. Finally, it was shown through experiment and a simple CFD model that standoff and input flowrate are critical

factors in the resulting gas shield. More efficient coverage at long standoffs due to Ar jetting was suggested as a benefit of the enhanced design.

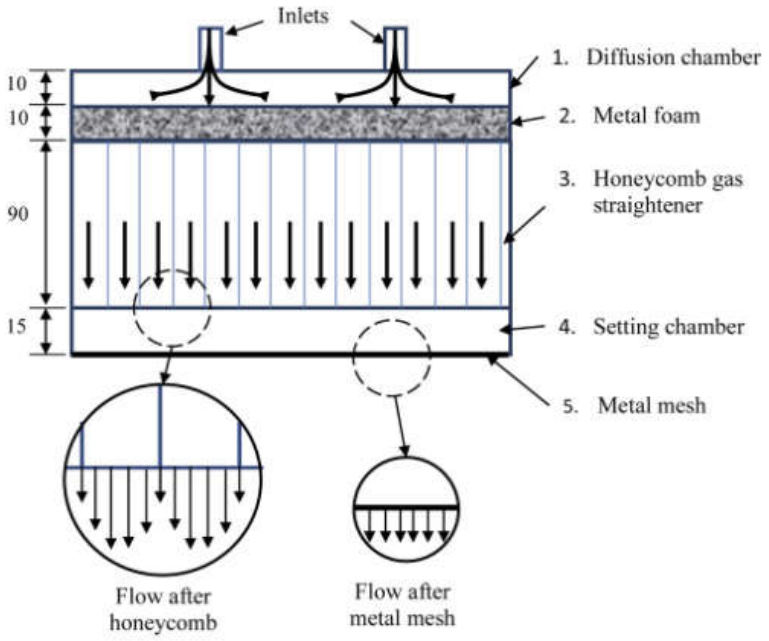

Fig. 55 Trailing shield layout, consisting of multiple inlets and composite chamber to deliver a laminar flow of shielding gas. [92]

Jäckel et al. [119] utilised an MHD model to theoretically analyse the mechanisms with which contamination occurs in TIG torch-trail shield configurations. The analysis identified that two main sources of entrainment: direct intake of air near the torch and turbulence generated within the device, both due to arc-driven gas acceleration. For the case of direct introduction of air in the shielding device, the effect of the arc's Lorentz forces was considered; separation of the box's outlet from that of the torch nozzle through an element such as a mesh at the bottom of the device was shown to ameliorate this effect. To counteract the indirect entrainment due to eddy formation, an increased number of inlets with a dedicated Ar supply along with the insert at the bottom were suggested.

Beyond the analyses above, the effect that differences in geometry or process parameters have on the gas coverage during WAAM has not been characterised in the literature. Additionally, to the best of our knowledge, no visualisations of gas flows in this context have been published prior to this thesis. As the flow conditions can only be qualitatively analysed through schlieren imaging, numerical modelling "grounded" in the observations can help overcome that disadvantage. Thus, a FEM model of the PAW torch gas flow was developed in COMSOL multiphysics. Using the combination of schlieren and MHD simulations, the conditions under which defects are likely to occur can be identified, so that shielding can be improved or preventative measures can be taken during process planning.

5.2. Flow visualisation from WAAM components

In this section a two-fold analysis is presented, beginning with the flow from a trailing shield alone, without the arc. Following that, the flow from a PAW torch is visualised in the context of multilayer Ti-6Al-4V deposition. Finally, the flow from the combined shielding system is examined, using the previous information from individual components to build understanding of the complex flow structures encountered during the process.

5.2.1. *Investigation of trailing shield effectiveness*

The schlieren system, as described in the previous chapters, was used to visualise the refractive index gradients of the flow. A scaled-up version of the highly engineered trailing shield presented in Ding et al. [92] was utilised for these experiments, which was attached to the gantry-based high value engineering (HiVE) printer at Cranfield university (Fig. 56).

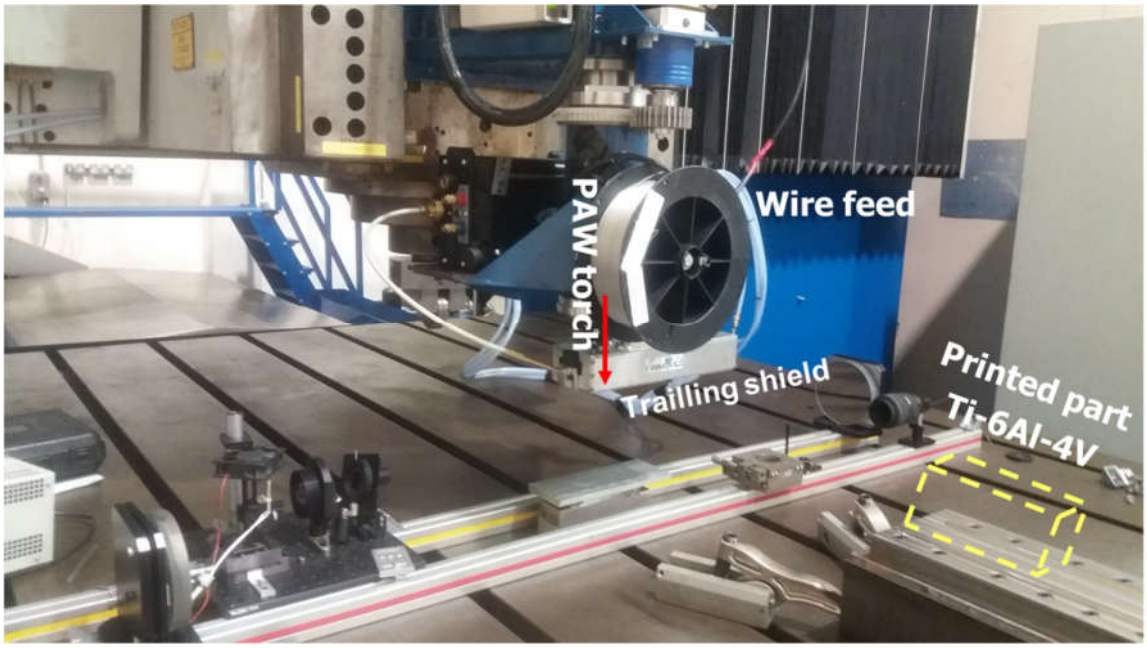

Fig. 56 Z-type schlieren system and trailing shield device setup in HiVE.

In the schlieren setup, 50 % of the light was cutoff at the Fourier plane to evenly capture positive and negative gradients. Due to the small difference between the refractive indices of Ar and air, discussed in section 4.2, the source slit area was reduced, to increase the sensitivity of the system. Apart from a polariser used to remove glare due to surface reflections (not shown in Fig. 56), no further filtering was required for the imaging of cold flows. A Flea 3 CMOS camera with a 250 mm telephoto lens was used to image at 150 fps.

Firstly, the flow onto a flat plate was imaged at different standoffs, ranging from 50 mm to 15 mm. Due its large size, a total flowrate of 195 l/min was provided to the trailing shield by two independent inlets. Despite the high mass flowrate, the observed turbulence intensity was small under all conditions. As shown in Fig. 57, two large symmetric gradients appear at the flow's edges, marking the transition from a steady, laminar Ar flow to the ambient air. The flow is driven by the pressure at the outlet of the device, accelerated downwards by gravity.

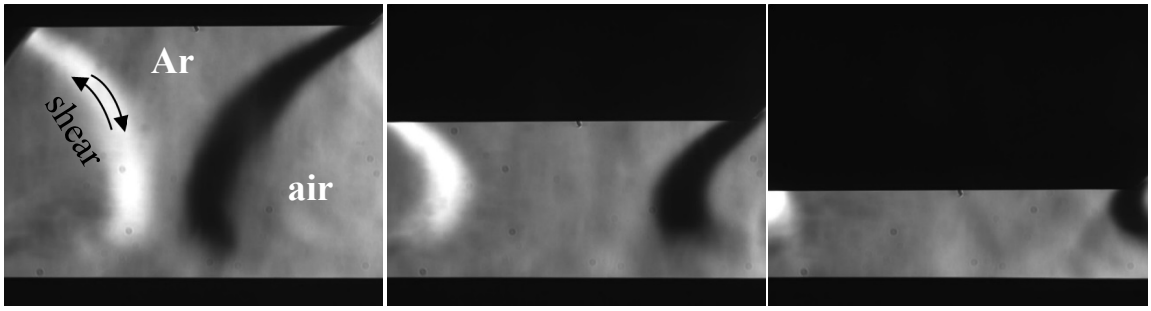

Fig. 57 Steady-state density gradients from trailing device cold flow under standoff distances of 50-15 mm.

Due to shear stresses developing at the flow edges, the gradients are converging inwards. At the maximum standoff, a neck is developed over the 50 mm length before the fluid stagnates on top of the plate. Mixing occurs at the surface, due to the relatively low momentum of the fluid. As the standoff decreases, the cross-sectional area of the neck increases and the gradients start to diverge outwards, and a stronger lateral flow develops on the plate. At the minimum tested standoff, the curvature of the gradients is changed completely, and only divergence is observed. The flow reaching the plate at lower standoff experiences fewer losses and carries higher outwards momentum, providing wider and more effective coverage.

Following the flat plate geometry, printed samples of varying wall thickness, shown in Fig. 58, were used to understand what is the limit in thickness that can be adequately shielded. The standoff from the top of the walls to the shield was kept at ~3 mm, as specified for deposition. The images show that only the top part of the 64 mm thickness wall was shielded, while the thinner samples were covered entirely. No gradients were observable at the walls, suggesting that Ar stagnation on the part does not produce a strong pressure gradient. Only a mild disturbance to the gradients was observed by the resulting outwards flow on the top flat area of the walls.

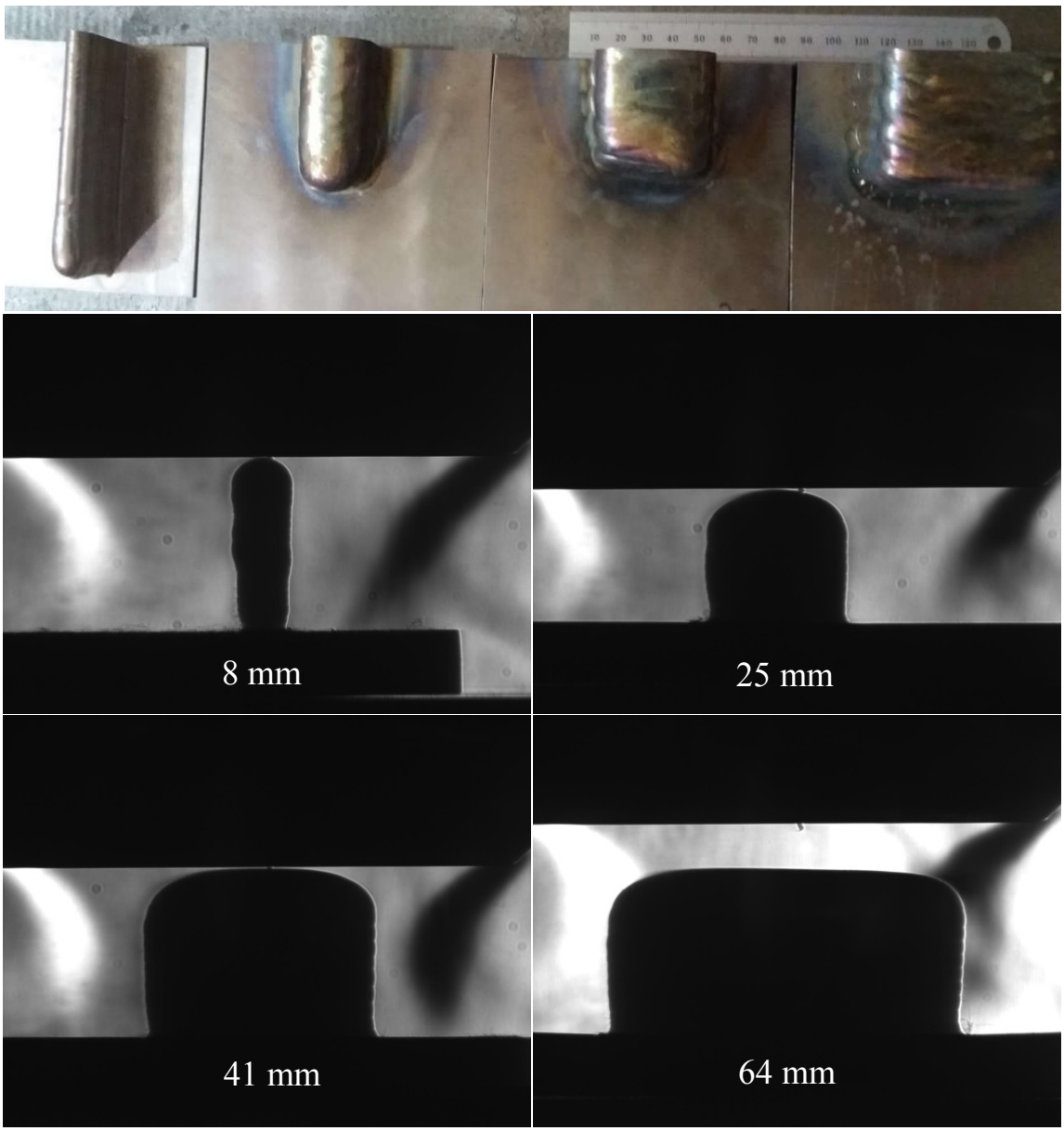

Fig. 58 Thin and thick wall Ti-6Al-4V samples used during cold flow trailing shield visualisation.

Due to the increasingly larger standoff between the trailing shield and the substrate during deposition of several layers, the gradients are converging towards the wall. Through this inwards motion of the Ar-air boundary, more air becomes available close to the wall and some fraction of it is inevitably transported in the shielded area by convection-diffusion. Therefore, combined with the results of Fig. 57, it can be inferred that as the height of the shielded wall increases, the coverage quality will decrease overall, even if its width is small compared to that of the trailing shield.

Having established the level of coverage that can be provided with 195 l/min, the experiments were repeated for a flowrate of 150 l/min. Fig. 59 shows the gradients which develop in both cases, for a 41 mm thickness sample. At the lower flowrate, the overall downwards momentum is less, hence the coverage area decreases. Consequently, the

inertia posed by the Ar flow against an inwards air flow is lowered. Indeed, air entrainment is expected to be more severe for the 150 l/min case, as air can be transported in from the flow's edges which are closer to the wall.

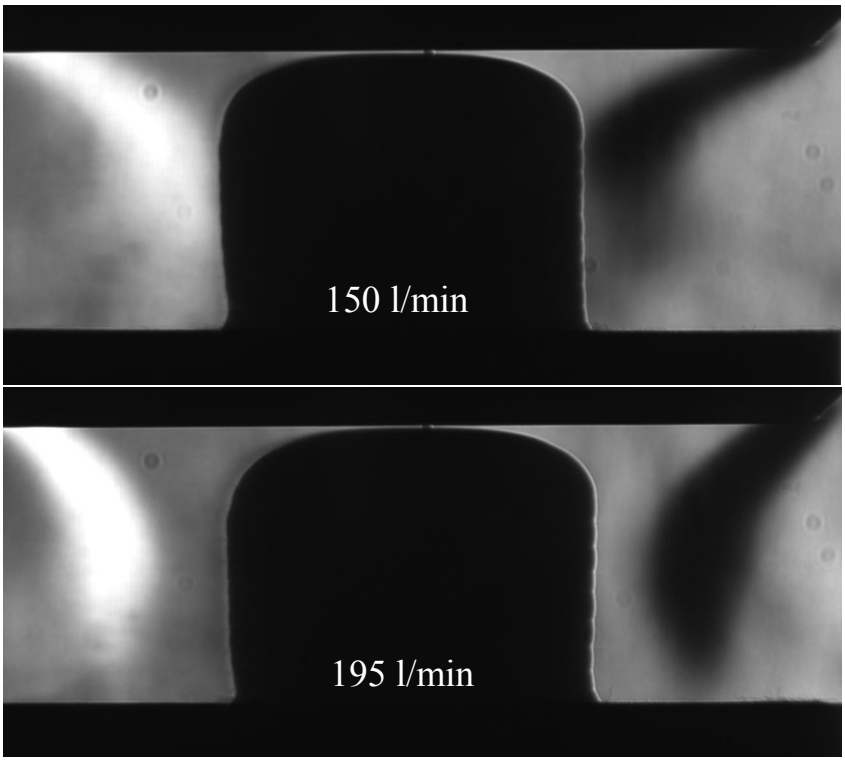

Fig. 59 Comparison of cold flow conditions from trailing shield under flowrate variation

5.2.2. *Analysis of flow patterns from plasma arc welding torch*

The most central part of the WAAM process is the heat source, which enables the deposition of material. The flow patterns which arise due to the operation of the PAW torch carry information about the physical effects in place during this type of AM. Their visualisation and analysis is therefore an important "stepping stone" to understanding the process.

The difference between a TIG and a PAW torch is that in the latter, a nozzle is fitted that separates the gas flow into two different streams. The nozzle contains a small channel close to the electrode which delivers the so-called plasma gas flow, named thusly as it becomes the medium for the arc plasma. The arc is constricted by the lower part of the nozzle, focusing a high velocity jet onto the workpiece. Shielding gas is independently directed to the sides of the arc through a different channel to protect the reactive material. However, due to the high sensitivity of the plasma jet to the design of the nozzle, which is usually purpose-built and non-standardised, it is difficult to predict optimal operating parameters without extensive experimentation.

For this set of experiments, the PAW torch was used without a trailing shield attachment (see section 5.3 for a detailed figure of the geometry of the torch's lower end). A large rectangular Ti-6Al-4V block was used as the workpiece, to emulate the manufacture of a wall feature and dissipate the heat from the torch. No material deposition occurred during torch visualisation, giving focus to the features of the MHD flow alone. The torch was moved along the length of the workpiece with a constant velocity of 0.2 m/min. The direction of travel was parallel to the test area (middle part of the "Z") of the schlieren system. To prevent over-ranging of the system, the source slit size was increased to a 2 mm x 6 mm rectangle, reducing the sensitivity to levels appropriate to the large gradients of welding processes.

To start the arc, first a pilot high frequency arc is struck within the torch, using only the plasma gas flow (0.2 l/min), illustrated below. The plasma gas flow does not occur in this way during processing, as this flow within the inner channel of the nozzle "feeds" the plasma jet and is therefore subject to thermal ionisation and the arc's electromagnetic pinch. While imaging the pilot arc does not directly relate to the model, it is of interest as one of the characteristics associated with nozzle design, affecting arc ignition.

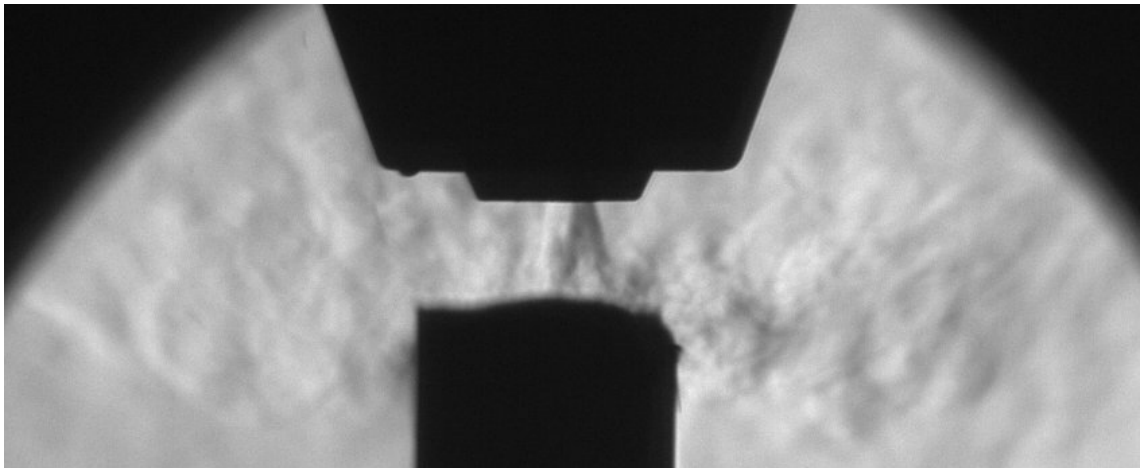

Fig. 60 Plasma gas flow of 0.2 l/min from PAW torch, moments before main arc initiation.

Following the main arc's initiation, the shielding gas flow starts and the torch is rapidly raised to the desired standoff, kept constant at 5 mm for all experiments. The gradients which develop during the early seconds of the process are shown in Fig. 61. As expected, the features are symmetric, with the axis passing from the centre of the arc. For clarity, a dashed line was inserted at the arc's left edge based on the arc's symmetry, to distinguish between the arc and the white schlieren gradient.

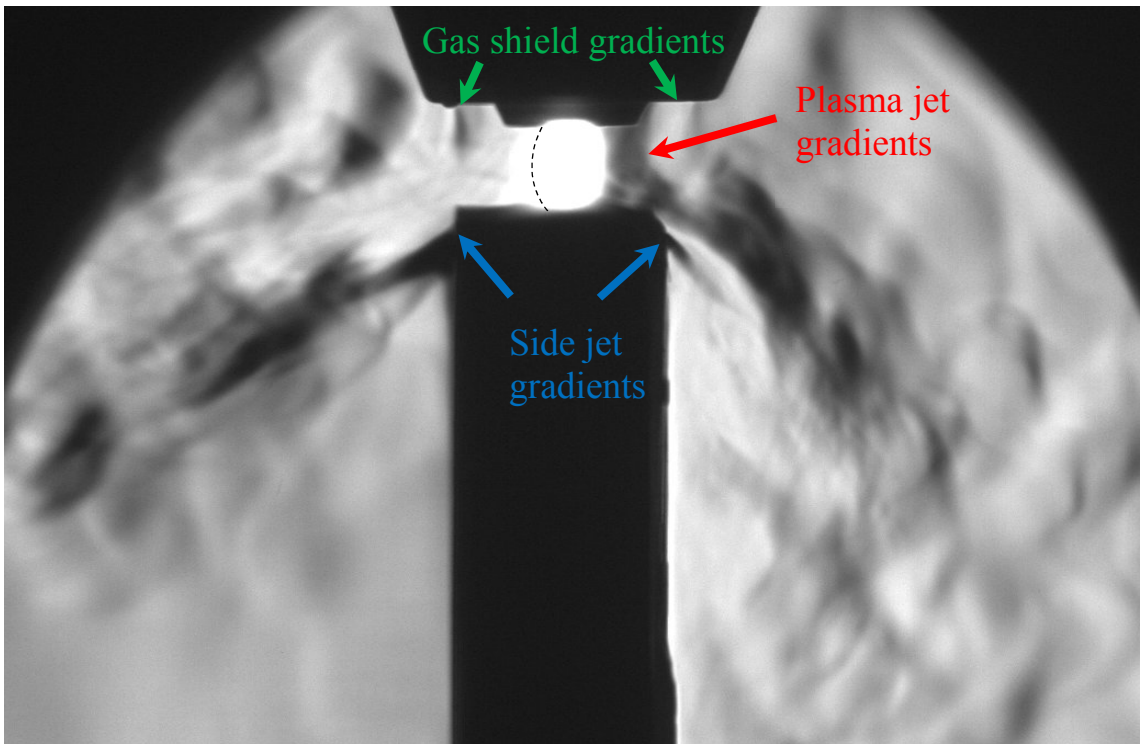

Fig. 61 Torch gradients of 100 A PAW arc on Ti-6Al-4V block, with 12 l/min shielding gas flowrate and 0.2 l/min plasma gas flowrate. Frame taken 0.6 s after arc ignition.

The bright part in the middle is arc radiation, obscuring any gradients which occur close or within the structure of the plasma jet. At the arc's edges, the plasma jet gradients can be observed. Their formation can be attributed mainly to the large thermal gradient between the plasma and the shielding gas. Beyond these, a set of vertical features establishes at the torch's edges, denoting the edges of the shielding gas flow. These are attributed to differences in both the concentration and temperature of the Ar-air medium at either end. Overall the flow is highly turbulent, due to the MHD acceleration of the plasma jet. At the bottom of the plasma jet, a high pressure region develops due to the jet's stagnation. Thus, a fast outwards flow is formed, which separates from the substrate after only a short length and breaks into turbulence, as indicated by the two side jets.

Due to a small misalignment between the workpiece placement and the gantry's axis of motion, the torch position relative to the edge of the plate varied while traversing the workpiece's length. As a result, the tilt of the side jets changed as the torch moved, yielding more insight into the process: the distance between plasma jet and the edge of the workpiece or even the curvature of the surface plays a role in the interaction between the shielding gases, stagnating side jet and ambient air. Generally, it was observed that as the arc moved closer to the edge of the wall, the turbulent jet was downwards-tilted. This could be attributed to a separation of the boundary layer occurring further down the length of the wall.

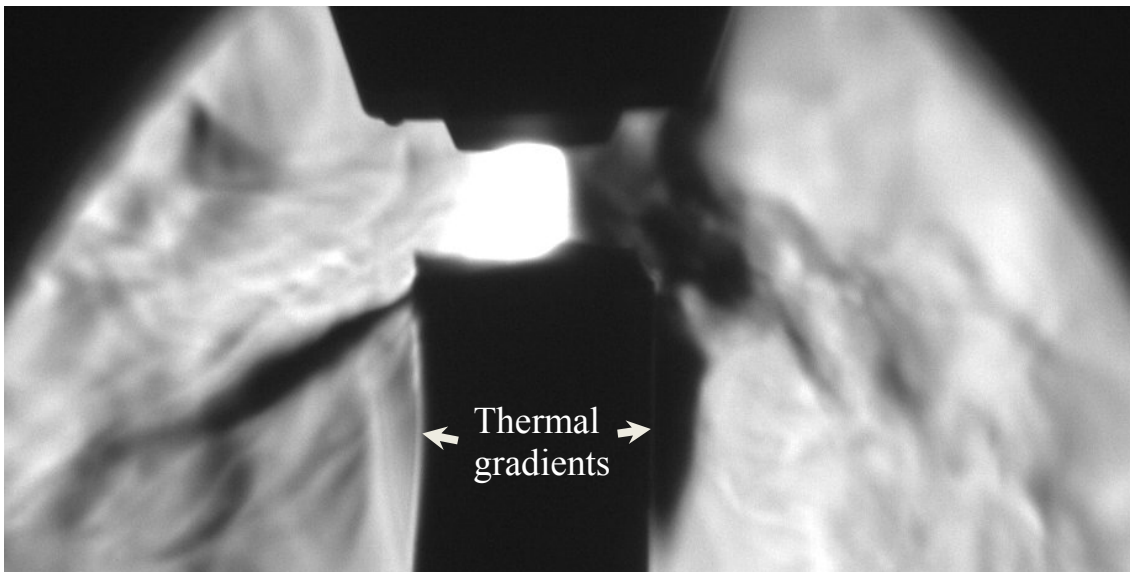

Fig. 62 Thermal gradient formation due to heat build-up in part during PAW, 25 s after arc initiation.

As the processing continued for several seconds, the torch advanced along the workpiece applying a continuous thermal load. Another set of gradients forms at the wall's upper part, Fig. 62. These can be attributed to local heat transfer between the top part of the titanium block and the ambient medium. The length and width of these thermal gradients increases over time, as more heat is input into the workpiece. As buoyancy can be observed, it can be inferred that the density of the gas is lowered locally due to the higher temperature. This buoyancy plume interacts with the other gradients, contributing to changes in the imaged flow patterns over time, as evident by examination of Fig. 62 and Fig. 63.

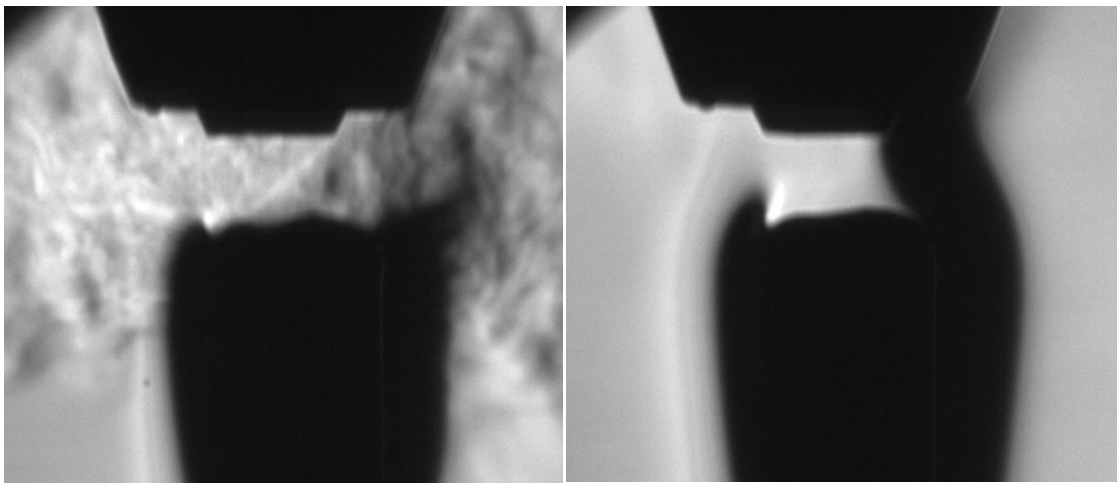

Fig. 63 Gradients after arc extinction. (Left) a short post flow period ensures contamination does not occur while the metal cools. (Right) Buoyancy plume rising due to heat left in workpiece.

5.2.3. *Schlieren imaging of shielding conditions during WAAM*

A third set of experiments was carried out to analyse the behaviour of the complete PAW torch and trailing shield system used for AM on the HiVE. As the main driver of heat and momentum transfer in the process, input currents of 100 A and 200 A were tested. Further, to understand the effects of the gantry's motion on the achieved coverage, a travel speed of both 0.2 and 0.4 m/min were used for each current. The gas flowrates were kept constant, as specified in the sections above. Metal deposition did not take place, to maintain a constant workpiece geometry. The experiments were carried out for two substrates; one tall and one short Ti-6Al-4V block, to draw further conclusions on how increasing the build height affects air contamination.

Beginning with the case of a short wall, a characteristic image (half-cropped to focus on one side) is shown in Fig. 64. Following arc ignition, the plasma and side jet gradients are established, discussed in section 5.2.2 and labelled "torch gradients" here. It is easily observed that the direction in which these are established is diagonal with respect to the workpiece. One can therefore infer that the momentum they carry is split in three dimensions: outwards, downwards and backwards (with respect to the travel direction). They are a key driver for the effects observed, through their interaction with the bulk, downwards flow of 195 l/min from the trailing shield.

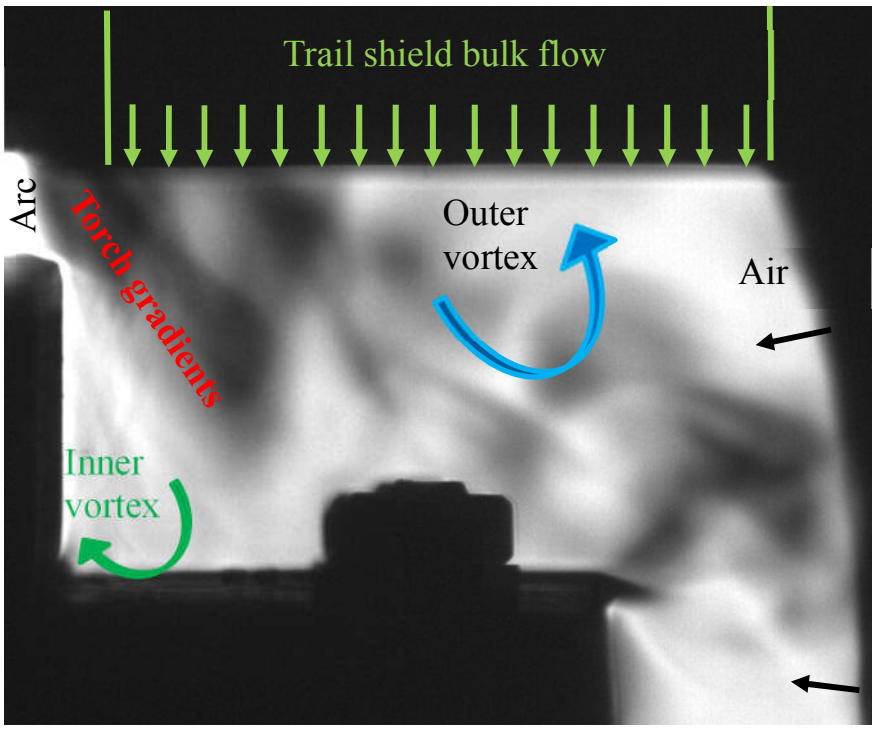

Fig. 64 Local shielding gradients developing during PAW-WAAM short wall deposition (100 A arc, 0.2 m/min travel speed).

A set of large eddies is created due to the disruption of the downwards flow of the trail shield by the side jets. These outer vortices promote mixing with the ambient air, potentially diluting the inert Ar atmosphere that eventually reaches the arc through the usual entrainment mechanisms, if the gas flow rate of the trailing shield is not high enough. Additionally, as the torch gradients stagnate on the substrate, a fast surface flow develops on either side of the stagnation point. This leads to a gas recirculation between the torch gradients and inner wall, labelled "inner vortex" in Fig. 64. Upwards flow along the wall through momentum accumulated in this inner vortex could constitute another mechanism through which air is transported closer to the arc and by extension, the reactive surface area of the Ti anode.

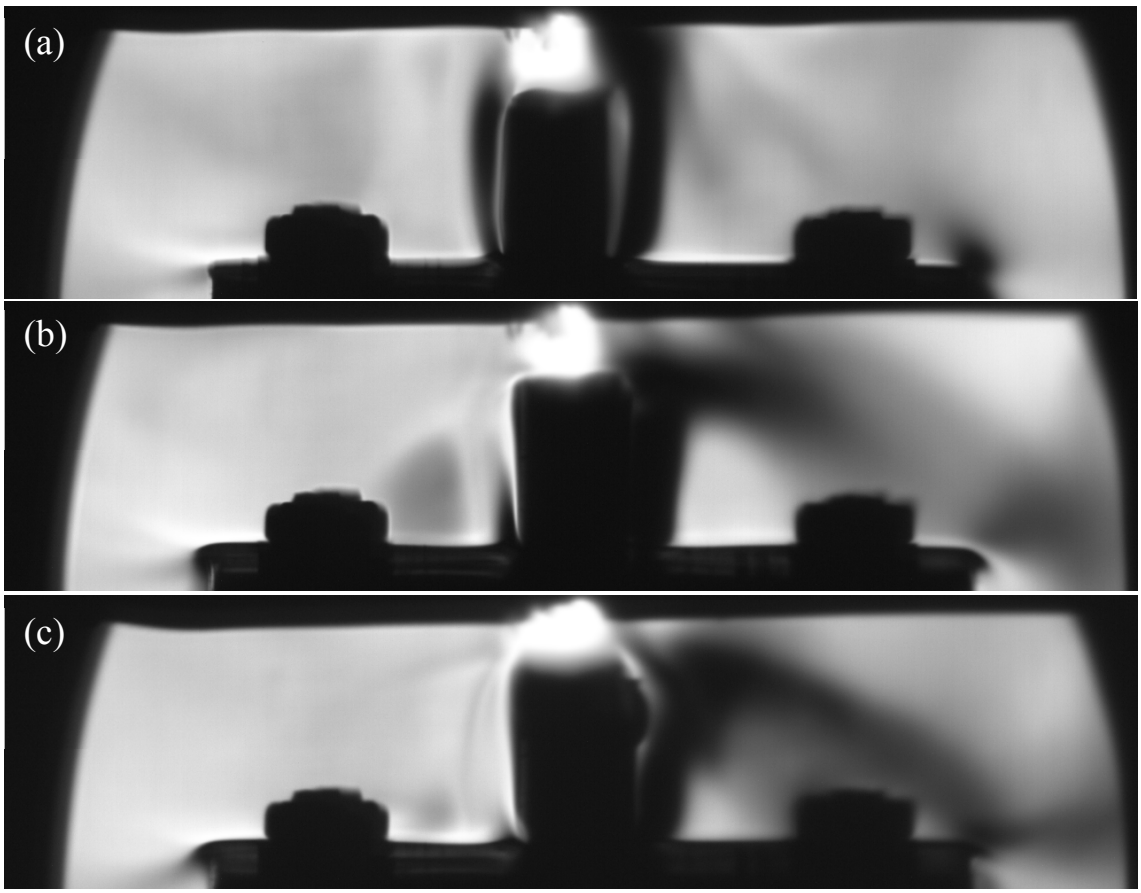

Fig. 65 Time averaged images over 1000 frames, with different process parameters (a) 100 A, 0.4 m/min, (b) 100 A, 0.2 m/min and (c) 200 A, 0.2 m/min.

To show the changes in the flow patterns with travel speed more clearly and remove some of the transient variability, average images were produced, as shown on Fig. 65. To ensure a fair comparison, both images were averaged over 1000 frames (~ 6.7 s), starting when the torch was midway through the total travel length. Variation of the travel speed affects the gas flow in two interconnected ways. Firstly, the energy input per unit length onto the workpiece is doubled when the travel speed is halved. Consequently, twice as much

thermal energy is stored in the deposited wall of Fig. 65(b) compared to (a). The buoyancy forces around the wall are stronger, as indicated by the stronger thermal gradient of Fig. 65(b). Secondly, according to Newton's first law, the forwards momentum carried by the torch/shield assembly generates a constant backwards acceleration for the jets. This motion, which is proportional to the travel speed, in combination with the outwards momentum of the jets creates a "wake" field along the sides of the walls as the torch passes. Thus, in the case of Fig. 65(a) the wake field is more pronounced than in (b) due to the higher backwards momentum.

Frame by frame analysis of the image sequences showed greater outwards momentum and greater overall turbulence levels with higher current. When the current was increased to 200 A, Fig. 65(c), flow changes occurred due to the much higher energy in the arc. The torch gradients were more intense, suggesting a greater temperature in the region near the arc. Additionally, the gradients were longer compared to Fig. 65(b), suggesting higher outwards side jet velocities. The extra momentum and higher turbulence levels in the gas result in overall stronger convective mixing behaviour. It is therefore likely that a higher air content is transported to the reactive metal when operating at higher currents.

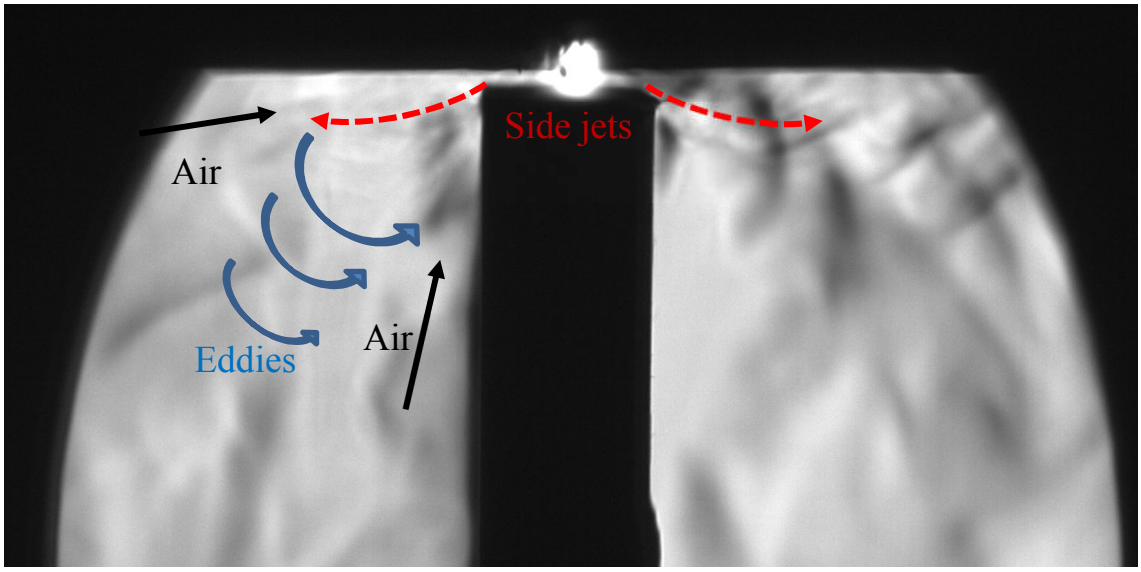

Fig. 66 100 A, PAW arc and trail shield flow on tall Ti-6Al-4V wall. Air entrainment mechanisms are more prevalent due to the increase in exposed area and lack of closed vortices.

For the case of a tall substrate, the same entrainment mechanisms are observable, as shown in Fig. 66. The difference here is that, as the physical constraint of the bottom substrate is no longer present, the side jets do not stagnate there. The top flow is under-constrained so the outer vortex is significantly stretched, reducing the overall effectiveness with which air is pushed outwards. Further, the area where the inner vortex

previously established is now exposed. Due to this "double front" of entrainment, the overall level of contamination is expected to increase significantly as soon as the standoff distance exceeds a given height.

5.3. Numerical modelling of PAW during WAAM

It has been shown that using PAW as the heat source with this 3D printing technology offers higher deposition rates and allows better control over the process due to the independent setting of current and wire feed speed [120]. However, air contamination is more prevalent in this approach compared to GTAW, due to significantly higher plasma jet speeds, in addition to the higher temperatures involved, which would increase oxidation rates. Furthermore, due to the part geometry which results from the printing process, shielding conditions can vary significantly during the build process. The need therefore arises to study the interaction between the arc, shielding/ambient gases and part to understand the main drivers for air entrainment.

5.3.1. *Numerical PAW arc models: a brief literature survey*

Due to the increased cost and complexity of using PAW for welding applications, relatively few studies have been carried out studying the process numerically. Such simulations are mostly focused on the behaviour of the metal and only even fewer include the arc in the calculations. The relative results are summarised below, to provide additional context for the theoretical work presented in this section.

Schnick et al. [121] used an MHD model of the PAW arc to study the changes in heat and momentum transfer to the workpiece due to variation in process parameters. To validate the model, the pressure on a copper cooled anode from a PAW torch was measured through a pressure transducer. Measurements showed that torch standoff and nozzle orifice diameter have a large impact on the recorded pressure. The numerical results, which were validated by the experiments, showed that the pressure applied on the anode surface increased proportionally with the supplied plasma gas flowrate and current. This stagnation pressure is the result of a higher velocity plasma jet, indicative of increased air entrainment due to higher turbulence. Similarly, heat transfer to the workpiece was predicted to increase almost linearly for currents up to 120 A and plasma gas flowrates up to 3 l/min. At these maximum settings, a peak temperature of 28 kK and a stagnation pressure of 12 kPa was reported, using a 1.5 mm diameter nozzle and 5 mm arc length.

Using the same approach for the arc but combined with a more comprehensive treatment of the weld pool deformation, a unified model has been employed to analyse keyhole formation during PAW in 2D [122] and 3D [123]. A transient analysis on the deforming weld surface showed that while heat input can decrease by more than 300% within 1.5 s due to the keyhole depression, the predicted pressure distribution remained constant over the same time interval. Additionally, while the current density at the workpiece changed drastically as the keyhole formed, the peak current density near the cathode (a key driver for entrainment due to the contribution to the Lorentz force) remained constant.

Pan et al. carried out pressure and temperature measurements to validate a unified 2D axisymmetric PAW model [124]. The pressure was measured with a piezoelectric sensor similar to [121], while the temperature was inferred by measuring the relative intensity of five known Ar II lines and curve fitting. Excellent agreement was shown between the MHD model and the experiments, with peak measured temperatures of 25 ± 2.5 kK and peak pressures in the 1.7 kPa range (4 mm inner nozzle diameter, 8 mm arc length).

5.3.2. *Model setup: geometry, mesh, material properties and physics*

An accurate representation of the nozzle, electrode and shroud used in the imaging experiments was generated in a 2D axisymmetric layout, as shown in Fig. 67. The assembly results in two orifices, one channelling the so-called plasma gas flow (because this stream is fed towards the electrode, it will become ionised) and a wider one for a shielding gas flow. Use of the axisymmetric assumption for this application implies that the modelled wall feature is a cylinder rather than a straight wall. The results in this section are therefore only partly describing the full complexity of the actual process. Nevertheless, as the focus of these results is the behaviour of the plasma jet and its interaction with the surrounding gas and substrate, the major details of the flow can be captured through an axisymmetric model.

To adequately resolve the wall distance as required by the SST turbulence model (see below), 10 boundary layers were specified near walls, spanning a total thickness of ~0.1 mm. However, the length over which ambipolar diffusion effects are significant near the electrode sheaths in welding plasma applications is also approximately 0.1 mm [40]. To avoid introducing mesh points in regions where the LTE assumption leads to inaccuracies, no boundary mesh was generated around the tungsten electrode, with the minimum mesh size being kept equal to the diffusion length.

In the approach taken throughout this thesis, focus was given to the treatment of the Ar-air plasma and the mixing with ambient air, while mass transport and weld shape were not calculated as they are not deciding factors in determining coverage and entrainment. Thus, rather than producing a computationally expensive unified model as in Pan et al. [124], three different workpiece geometries were investigated, representative of cases occurring during WAAM. Wide and narrow non-deformable walls on a substrate, in addition to a flat substrate alone, were used to explore the resulting variability in flow patterns, as shown in Fig. 68. In all cases, the distance between the electrode and the top surface of the workpiece (arc length) was kept constant at 5 mm for consistency with the literature.

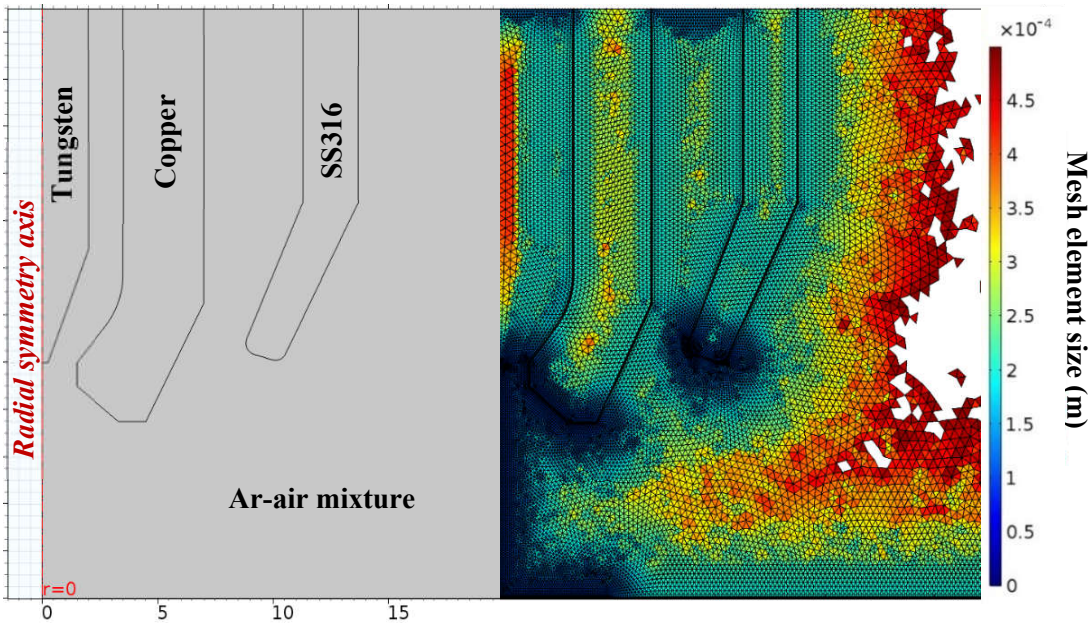

Fig. 67 Torch geometry with material allocation (left) and locally refined mesh (right) of electrode, nozzle and gas shroud assembly. Elements sized over 0.5 mm were excluded to highlight variation.

The material properties used for the different domains were taken from the literature, either as a function of temperature or as constants. For the electrode, temperature-dependent tungsten properties were taken from [55]. The nozzle was given constant properties for copper [94], while the shroud was given the properties of stainless steel by Kim [93]. The treatment of the Ar-air mixture was the same as in chapter 3, using the thermophysical properties of Murphy [26]. The temperature-dependent properties of Ti-6Al-4V were taken from [125].

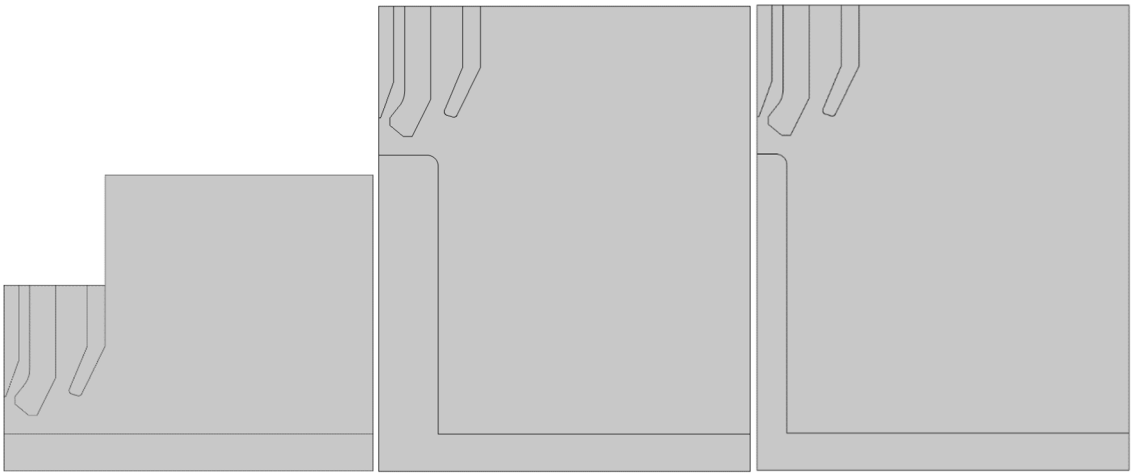

Fig. 68 Representative workpiece geometries used for PAW WAAM study.

The continuum mechanic equations commonly used to describe the MHD phenomena in PAW are the same with MIG and TIG, described in detail in section 2.1. Due to polarity used in PAW and the tungsten thermionic cathode, equations (18) – (22) were used to describe thermionic effects at the electrode sheaths (see section 2.2). For this study, the flow effects near the walls are of importance, and therefore the SST turbulence model was preferred instead of the k-ε model, due to the improved predictive capability near walls. The turbulence enhancements to the diffusion coefficient were implemented using the outputs from the SST model instead. Flowrates of Q_p = 0.8 l/min and Q_s = 15 l/min were specified at the plasma gas and shielding gas inlets, respectively. The boundary conditions for the equations of state used in the model were otherwise the same as in Chapter 3.

5.3.3. *Flow during the 1st layer*

To provide a basis for comparison with deposition at the n^{th} layer, the case of a flat substrate is considered first. Fig. 69 and Fig. 70 show the temperature, velocity and pressure distributions which occur under 100 A and 200 A arcs. The peak temperatures are in the 24kK and 30kK range respectively, distributed in the characteristic bell shape. The nozzle constricts the top part of the arc, where the peak temperatures are observed. Due to the diverging geometry of the nozzle, the temperature distribution widens 1 mm downstream of the cathode, generating a more diffuse flux towards the workpiece. In both cases, the high temperatures at the arc's centre reduce quickly with an increase in r, showing a large thermal gradient, which is consistent with the observed "plasma jet gradient" of section 5.2.2.

Due to the steady state and axisymmetric nature of the simulations, the calculated temperature distributions on the workpiece are only qualitatively indicative of the ones encountered during deposition conditions. As expected, comparison between the low and high current cases shows a wider distribution with a higher peak temperature for the 200 A melt pool. Due to the lack of current flow, heat transfer to the nozzle and shroud occurs mainly by conduction and therefore no significant heat build-up is observed there.

The full range of calculated velocities in the jet and surrounding gas is shown in Fig. 70 (top). As a result of the high Lorentz forces that develop in the jet, gas in the vicinity is accelerated towards the arc. While the entirety of the 0.8 l/min flow in the first orifice is channelled in the jet, there is an interplay between the arc and the 15 l/min shielding gas flow from the second orifice, as part of the stream is also pinched by the jet, as indicated by the low velocity arrows of Fig. 69. In addition, due to the stagnation of the main plasma jet on the workpiece, a fast, outwards convective flow is generated there. This fast stream joins the slower one from the shielding, forming a flow parallel to the anode. These motions combined result in the formation of an inner vortex, between the two orifices. At 200 A, this vortex is more pronounced and closer to the arc, due to the stronger pinch associated with the higher current.

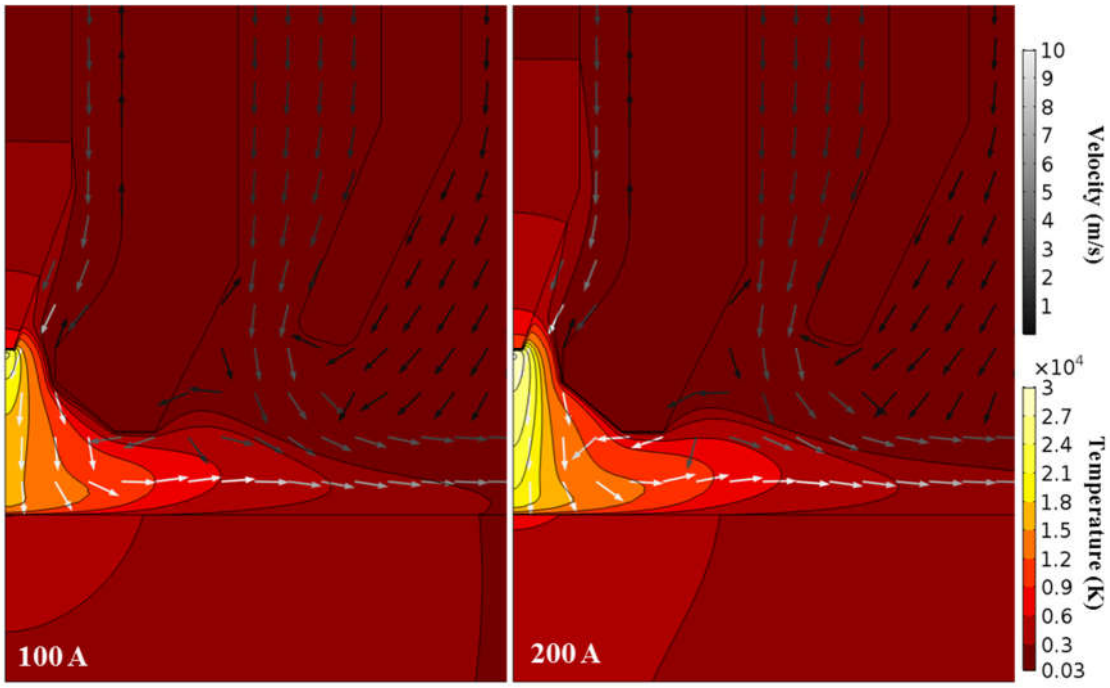

Fig. 69 Arc temperature and velocity distributions in PAW. The velocity vectors' length was normalised and they were coloured in grayscale to highlight the relatively low magnitudes of velocity.

The bottom row plots of Fig. 70 show that at 100 A, the pressure generated at the anode surface is roughly equal to that directly under the cathode. By taking into consideration the calculated velocity fields, the interplay between pressure and velocity is clear. Gas is

rapidly accelerated near the tungsten electrode, reaching maximum velocity halfway between cathode and anode, before decelerating and stagnating at the anodic surface. When the current increases to 200 A, the maximum pressure is increased by a factor of four, located at the anode, while the pressure at the cathode is roughly doubled. As the maximum is now located at the anodic surface, suggesting that the higher temperatures, shown in Fig. 69, change the thermophysical properties of the jet sufficiently to promote much larger Lorentz forces and therefore greater acceleration in the plasma along the length of the arc.

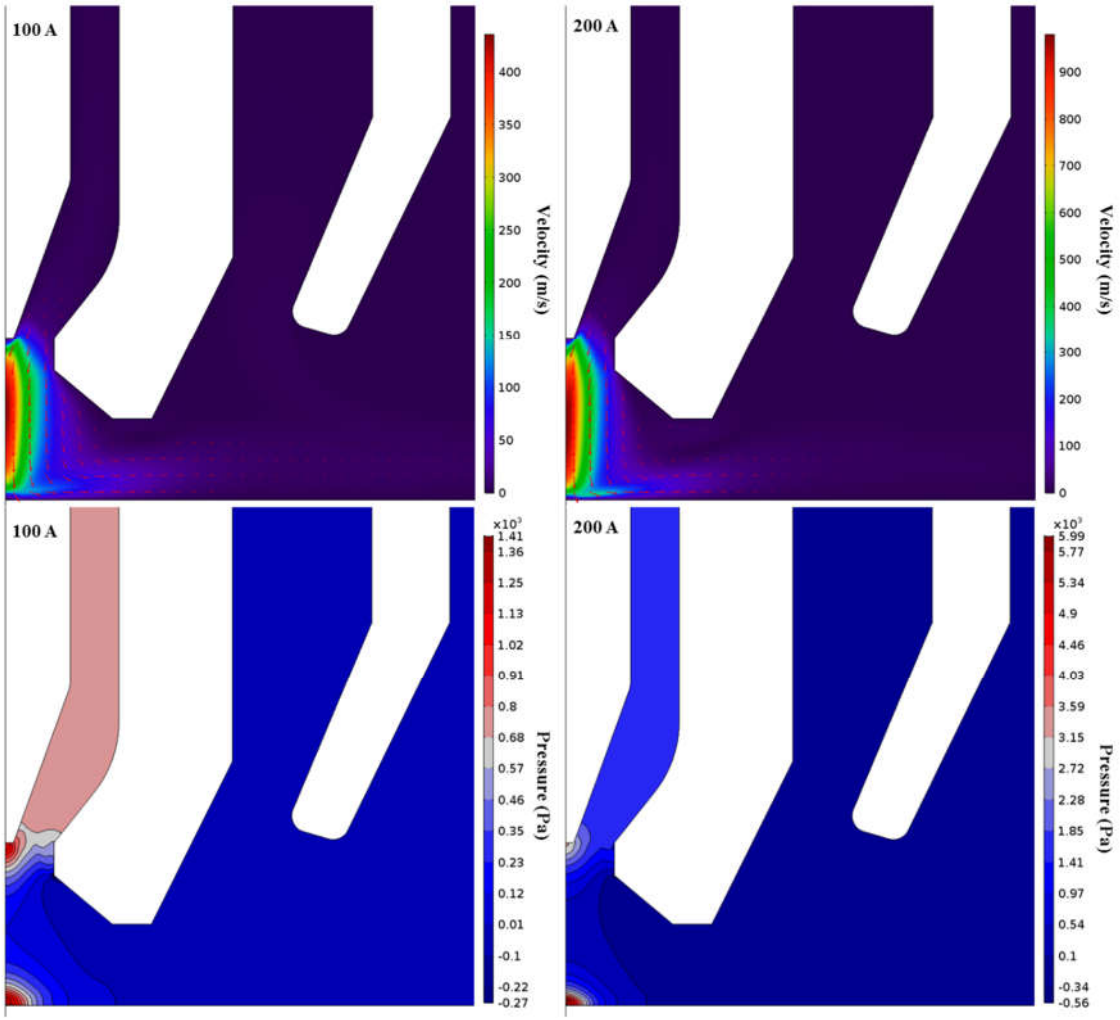

Fig. 70 Calculated velocity (top) and pressure (bottom) distributions in PAW torch at 100 A (left) and 200 A (right) with a flat substrate.

The pinch of the arc and resulting inner vortex has implications for the entrainment of air into the plasma jet, as a fraction of the ambient air, which is in contact with the shielding gas flow, is mixed with Ar and transported towards the jet, as shown in Fig. 71. Due to this action, there is stagnation of air in the divergent part of the nozzle, which feeds a steady entrainment into the plasma jet. Although around ~10,000 ppm of oxygen are calculated in the nozzle stagnation region, much less reach the workpiece due to the fast

convective action in the interelectrode region. Larger body forces develop near the jet for the 200 A case, showing a greater degree of air entrainment and suggesting a more intense swirling motion. On the workpiece surface, a local maximum of ~4000 ppm of oxygen is observed ~4 mm away from the arc root. This quantity of oxygen is seemingly constrained between the stagnation points of the plasma jet and local shielding stream and could potentially react with the melt pool.

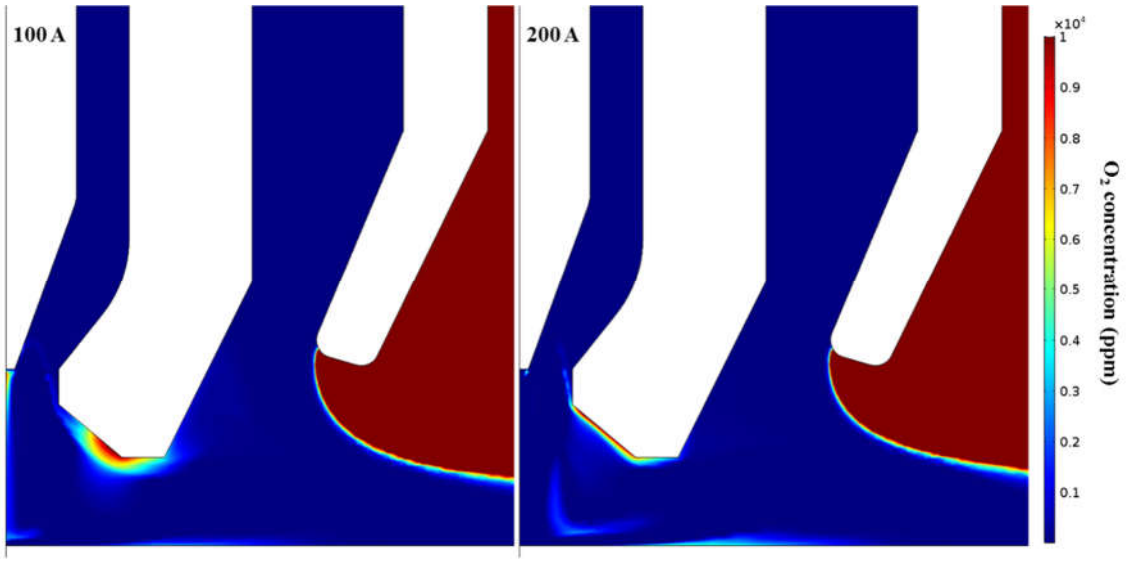

Fig. 71 Oxygen concentration at 100 A and 200 A arcs, showing a larger degree of air entrainment close to the substrate at higher current.

5.3.4. *Flow during the n^{th} layer*

Having established how the physical phenomena in the torch interact to shape the MHD flow on a flat surface, the changes in flow patterns after several layers have been deposited can be contrasted. The major difference between the thick (8 mm half-width) and thin (4 mm half-width) wall profiles in this study is that the latter ends just under the nozzle, while the former is longer to the extent that the shielding gas flow is also allowed to stagnate on top of the wall. Fig. 72 shows the calculated temperature and velocity profiles for both cases, at 100 and 200 A. It can be seen from the calculated temperature that the heat in the arc does not change with wall thickness. However, due to the smaller anodic surface area, the flow pattern beyond the plasma jet changes significantly. For the thin wall case, enough momentum is imparted by the arc so that the horizontal flow generated by the jet's stagnation on the substrate is not separated from the wall. The flow follows the outline of the wall with relatively high velocity, especially at 200 A. In contrast, in the thick wall scenario, most of the downwards momentum is counteracted by the wall and the horizontal flow extends further. At the outer edge of the wall, flow separation occurs resulting in an inclined side jet which does not follow the wall's outline.

A flow recirculation appears in this case, with a weak upwards flow establishing along the wall's vertical boundary. This result is consistent with the 'inner vortex' observed in the schlieren images, Fig. 61.

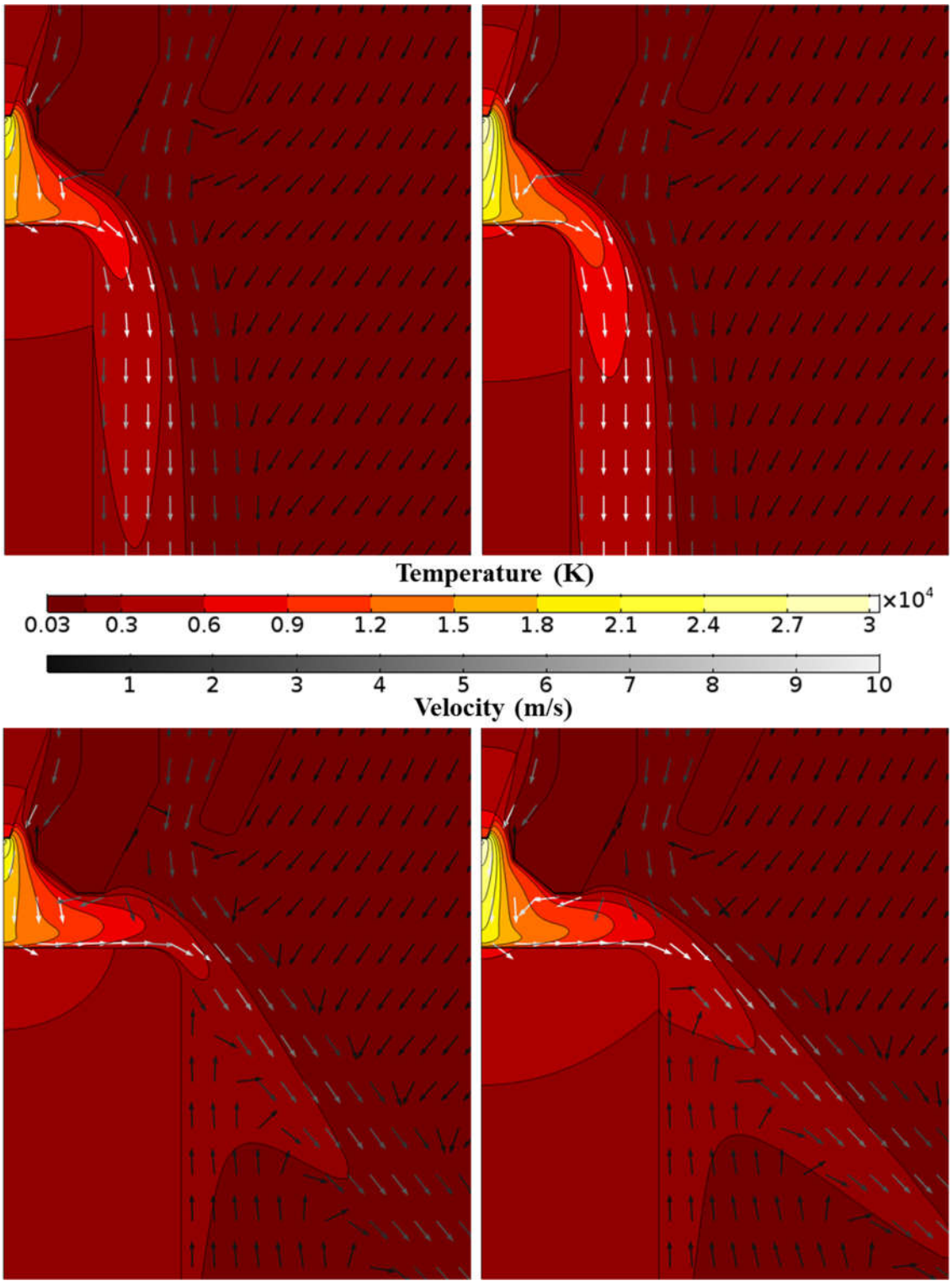

Fig. 72 Temperature and low velocity profiles during deposition of (top) thin and (bottom) thick wall at (left) 100 A and (right) 200 A. Side jet inclination changes with wall thickness, altering the heat input and flow dynamics of the process.

Buoyancy forces are induced in the flow, due to heat transfer from the wall towards the fluid. In both cases, the heat build-up on the wall profile is significant, spanning several layers. This effect is also shown by the thermal gradient formed at the sides of the wall after long interaction times in the schlieren images. Due to the larger mass and higher thermal inertia of the thicker wall, the high temperature zone is significantly smaller, as expected.

Another aspect of the model which is of interest is the Ar coverage generated in each case. Fig. 73 shows plots of O_2 concentration at 100 A over the entire computational domain. Near the arc region, similar O_2 levels were found in both cases, which were also similar with the entrainment levels of the flat substrate. A maximum O_2 content of ~4000 ppm was predicted over the molten material for both geometries, regardless of current. A significant difference in coverage is shown along the height of the thin and thick wall geometries. For the thick wall, the side jet directs a stream of Ar into the bulk of the air atmosphere, and as a result, the side of the structure remains exposed to the environment. Conversely, the laminar Ar shielding gas stream from the nozzle does not stagnate on the thin wall, creating an Ar-rich environment along its height.

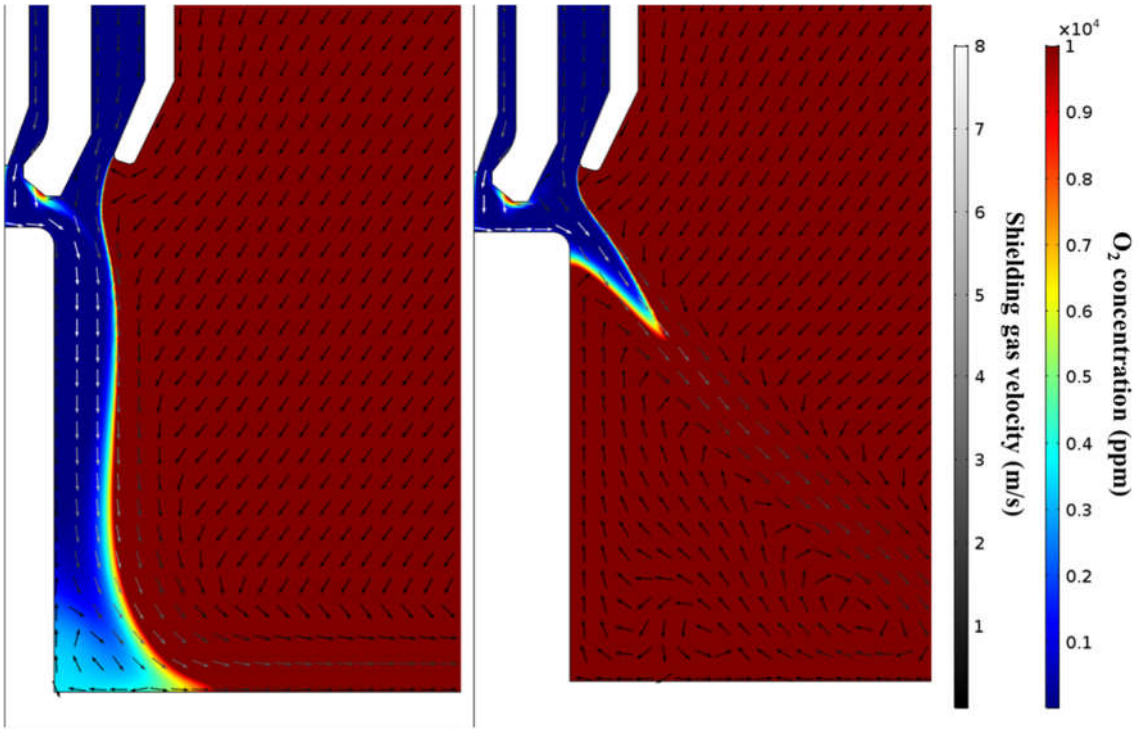

Fig. 73 O_2 concentration and gas velocity vectors for thin and thick wall features, 100 A.

5.4. Conclusions

A study of shielding gas flows and their interaction with the arc during WAAM using the schlieren technique was presented in the first part of this chapter. Imaging of the Ar flow from a purpose-built trailing shield device without the arc revealed that the covered area decreased non-linearly with standoff distance from the workpiece. Additionally, the imaged refractive index gradients suggested that shear Ar flow components that resisted air entrainment were weaker with increasing standoff. Experiments carried out at reduced Ar flowrate suggested that inadequate shielding may occur if the input Ar is reduced without redesign of the device. Visualisation of the flow showed that entrainment of air in the process region occurs from the sides and, if the deposited wall is sufficiently high, from under the side jets. Trailing shield designs for WAAM could potentially benefit from directing flow not only downwards but radially around the process region and along the wall's height. This could possibly be accomplished with tilted jet streams along the device's edges. An automated tilting system with a circular outlet design could be implemented to accommodate thick wall builds.

The flow from the PAW torch was also visualised, with and without trailing shield. Experiments with the torch alone showed that gradients appear around the arc region (temperature gradients), at the fringes of the shielding gas streams (concentration gradients) and at the edges of deposited walls (side jets). Additionally, thermal gradients due to buoyant plume formation around the heated part of the wall were visible. Their intensity was proportional to heat input to the material. When combined with a trailing shield, it was shown that the stagnation of the side jets onto the substrate generated inner and outer vortices within the shielded atmosphere. Adequate shielding conditions were found under such flow dynamics, irrespective of current and associated turbulence levels. However, air entrainment increased when the deposited wall was high enough to prevent vortex formation. The ability to image these features underlines the capability of the schlieren technique as a tool for the visualisation of a wide range of transport phenomena.

The interpretation of the image sequences was facilitated and complemented by the simulations. Through comparison of their results, a good agreement was shown between the imaged gradients and predicted flow fields in the MHD model. The heat and momentum transfer to the workpiece increased exponentially with input current. Additionally, it was found that the width of the workpiece surface and/or proximity of the torch to the edge of a build influences heat input and coverage on the deposited feature. As the distribution of heat input and available air varied with wall geometry, it can be

inferred that microstructural differences and variability to stress/strain distributions can be expected in features of varying widths and heights. The simulation of a wide variety of cases can lead to further control over the optimisation of deposition strategies, where heat input and contamination levels must be held within limits. A calculated maximum of 4000 ppm of O_2 close to the melt pool was calculated when using only the local shielding from the PAW torch. This result confirms the notion that a local shielding device is essential to minimising entrainment and oxidation.

6. Gas flows during metallic laser-powder bed fusion AM

6.1. Introduction

The most broadly commercialised contemporary AM technique is laser powder bed fusion (LPBF), also known as selective laser melting (SLM), with applications across most industry sectors. In parts manufactured with LPBF, each layer is built using a laser beam to melt continuous tracks in metallic powder, finely spread over a metal substrate (or over the previous built-up part as processing continues). This is carried out within a processing chamber filled with Ar, and preferably with a crossflow of shielding gas sufficiently high above the bed so as not to disturb the powder. Numerous experimental and theoretical studies have been carried out to characterise, monitor and improve it [126]–[128]. Despite the wide adoption and academic interest, fundamental interactions between the laser, powder and molten surface are not yet fully understood. Unacceptable levels of porosity and inclusions in the as-built parts are common, as further process understanding is needed for stable regimes to be identified, leading to greater control and prevention of defects.

Imaging of the LPBF process is one approach being used to achieve this improved understanding. Imaging of the melt pool in a representative powder layer was reported by Matthews et al. [129], who investigated the depletion of metal powder particles in the zone immediately surrounding the solidified track (denudation), which can affect porosity and surface roughness. It was proposed that denudation at ambient pressure is caused by the intense evaporation of metal vapour from the melt pool, which produces an inward flow of the ambient gas towards the melt track. The inward flow of the ambient gas is sufficient to entrain powder particles, which can become incorporated into the melt pool or ejected with the metal vapour. Imaging of the melt pool with an optical resolution of ~5 μm per pixel enabled this particle motion to be observed, with particles ejected backwards with respect to the scan direction [129] or vertically upwards [130], depending on the process setting. Gunenthiram et al. [131] noted the complexity of performing diagnostics during the LPBF build process and so recorded single track images in a similar system to [129] but with a powder layer that moved on a translation stage below the laser. Motion of powder particles towards the melt pool due to the metal vapour was again observed. Zhao et al. [132] used synchrotron radiation to image the interaction of 1 ms laser pulses with a powder layer at 50,000 fps. Vapour-driven particle motion was again observed and, additionally, the dynamic keyhole development beneath the powder

bed could be seen. In this case, the powder bed was only 450 μm wide to enable transmission of the x-rays and a single laser spot was illuminated.

To satisfy the demand for parts with optimal quality, several models have been developed based on thermodynamic analyses of LPBF [126]. Across the scientific literature, the computed temperature fields are used either to predict thermal stresses and distortion on part-level simulations [133]–[136], or they are coupled with hydrodynamic equations to help understand melt pool behaviour [137], [138], [129], thereby increasing the accuracy of process-level models. In melt pool models, the recoil pressure generated by the evaporated gas is calculated by the Clausius-Clapeyron equation [139] and used as a contribution to the momentum in the liquid metal. Approximate calculations in Ly et al. [130] based on the model in Khairallah et al.[138] estimated the vapour ejection velocity at ~700 m/s.

During laser scanning with high intensities (typically 100 W – 1 kW for LPBF) and small beam sizes (50 – 100 μm), predicted temperatures in the melt pool often far exceed the vaporisation point of the metal, resulting in the recoil of gas and the formation of plasma [140], which is supported by the physical observation of light emission from the laser plume as well as the imaged particle entrainment. Most state of the art models such as [129], [135] take into account the energy losses due to vaporisation, however the hydrodynamics of the vapour/gas/plasma phases are not explicitly included in the simulations, and therefore the gas-particle interactions observed experimentally cannot be analysed.

Indeed, very limited work has been carried out regarding the numerical modelling of such phenomena in an SLM context. In the case of stainless steel, a stream of Fe vapour is ejected from the melt pool, which mixes with the ambient Ar atmosphere. Masmoudi et al. [141] investigated Fe vapour generation from the powder bed within an Ar atmosphere using a meso-scale finite volume model. However, the laser plume was not modelled: instead an assumed mass fraction from elements that exceeded the vaporization temperature of the metal was used as vapour input to the gas phase. Their analysis showed that a greater degree of vaporisation occurred with a decrease in ambient pressure. Estimated flow velocities for a 100 W, 68 μm beam ranged from 300 m/s at 1 mbar to under 50 m/s at 1 bar, which is insufficient to account for the particle motion observed experimentally. Furthermore, convective and diffusive species transport incorporating the physical properties for a multicomponent Ar/Fe mixture were not included.

In this chapter, detailed high-speed imaging of the interaction of the laser with the powder bed is presented at a range of laser powers and scan speeds. A pragmatic FE model for the powder bed and observed fluid dynamics is presented, including a hydrodynamic treatment of the laser-induced plume and atmospheric flow. The literature concerning evaporative and plasma phenomena occurring in arc welding, laser welding and laser ablation studies, such as [142]–[145], is used as a basis for the analysis in the context of LPBF. High-speed schlieren imaging for gas flow visualization of the density gradients in the gas flow, not attempted for LPBF previously, is used both to elucidate aspects of the physical phenomena involved and to validate the FE model. The modelling and schlieren imaging support the direct, high-speed imaging observations of gas flow-induced powder particle motion in the LPBF process.

6.2. Experimental rig and imaging setup

An in-house, open architecture LPBF system, as described in Bidare et al. [146], was used to carry out the material processing. The system was fitted with observation windows for direct imaging, made from infra-red absorbing KG glass as well as windows to allow schlieren imaging, made from Zerodur glass flats of diameter 75 mm, polished to $\lambda/4$ on both surfaces. For the schlieren experiments only, the spreader block assembly was used to spread a powder layer on the coupon and was then carefully removed.

All the experiments were undertaken with gas-atomized stainless steel 316L powder (Renishaw PLC) with particle diameters in the range 15 to 45 μm and a mean diameter of 30 μm [147]. Powder layers were melted on to 80 × 40 mm^2 stainless steel 304L build plates (coupons) of thickness 2 mm, using a single mode fibre laser (SPI 400 W continuous wave, 1070 nm) which was scanned over the powder surface (Raylase MS-II-14 scanner with 163 mm focal length f-theta lens). Light from the laser was focussed to a spot with a Gaussian beam profile and $4D\sigma$ diameter of 50 μm in both the x- and y-directions, measured with an Ophir Spiricon SP928 beam profiling camera. The shielding chamber was purged with argon until the measured oxygen concentration was <0.1%. The pressure in the chamber was maintained just above 1 atm.

A Photron Fastcam Mini UX100 monochrome camera was used for high-speed imaging. The direct imaging experiments reported here were recorded at 8,000 fps and 1,280 × 616 pixels. The camera was fitted with a C-mount QiOptiq Optem Fusion lens, configured to provide a zoom of 7:1 and a working distance of 135 mm. At this working distance, the

region of interest could be varied between approximately 14 × 11 mm^2 (depth of field 2 mm) and 2 × 1.5 mm^2 (0.2 mm). Illumination was provided by a 300 W tungsten filament lamp that was focussed through the top of the Perspex shielding chamber on to the powder bed in a rectangle of approximately 15 × 5 mm^2. The illumination was switched on for a few seconds during imaging and produced negligible heating of the powder bed.

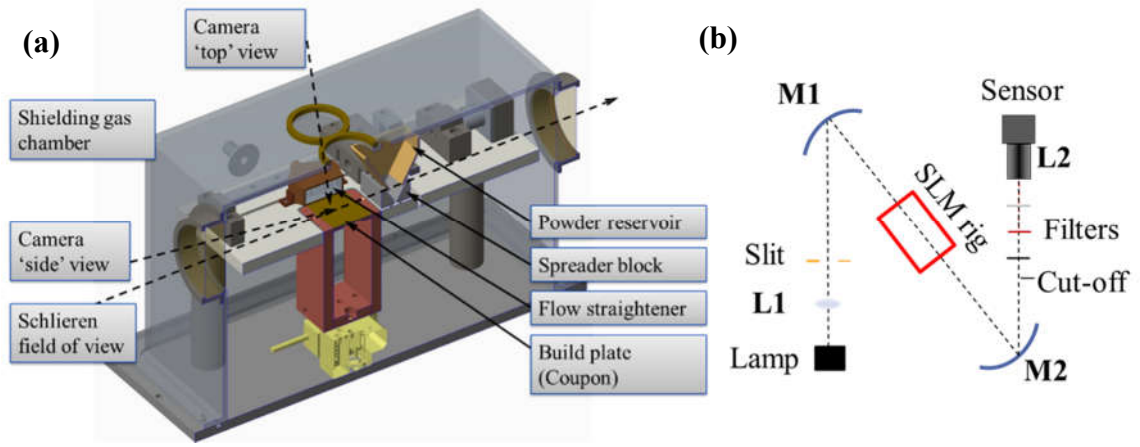

Fig. 74 (a) Schematic of the open architecture PBF system with modifications for high speed imaging and schlieren imaging. (b) Schlieren system setup across rig.

The portable z-type schlieren system was setup across the PBF system with minimum modifications. The 300 W tungsten lamp was focussed on to a 2 × 5 mm^2 rectangular source slit with its long edge vertical. The slit was placed at the focus of the first schlieren mirror (focal length 1.27 m) to produce a collimated beam that passed across the powder bed via the windows in the side of the Perspex shielding chamber, Fig. 74. The knife-edge filter was positioned with a micrometer to block 50% of the image of the source slit in the horizontal (x) direction, producing images with a uniform measurement range in which the intensity was proportional to the gradient of the refractive index $\partial n/\partial x$. Schlieren images were recorded with the Photron Fastcam high-speed camera at 16,000 fps and 1,280 × 312 pixels, in addition to a Flea 3 camera at 200 fps and 800 x 700 pixels. A variable focus telephoto lens (f = 75 – 300 mm) was used. An infra-red absorbing filter, and a polariser to remove glare, were placed in front of the camera lens. Due to the long exposure times for the experiments at 200 fps, the infra-red absorbing filter was replaced with a band pass filter at 633 ± 10 nm to reduce the light from the plume and hot metal.

6.3. Direct and schlieren imaging of fluid and particle dynamics in LPBF

The experimental results in the following sections examine phenomena across single laser scans as well as multilayer builds. In order to focus attention on the gas movement due to the laser's interaction with the powder bed, these experiments were conducted without a

flow of shielding gas across the powder bed. The effect of an additional flow of shielding gas across the powder bed is discussed in section 6.3.2. Additionally, the difference in laser plume characteristics under an atmosphere of He as well as Ar is examined.

6.3.1. *High speed imaging of the 1st powder layer: laser line scans*

Fig. 75 shows high-speed imaging for side and top views of the powder bed during laser scans of single lines. Three different laser power and scan speed combinations are shown: 50 W and 0.1 m/s, 100 W and 0.5 m/s, and 200 W and 1 m/s. It is interesting to note that the two latter parameter sets have the same line energy (laser power divided by scan speed) at 200 J/m, while the first one has a line energy of 500 J/m. These results are for the first powder layer spread on the coupon, which had a thickness of 50 µm.

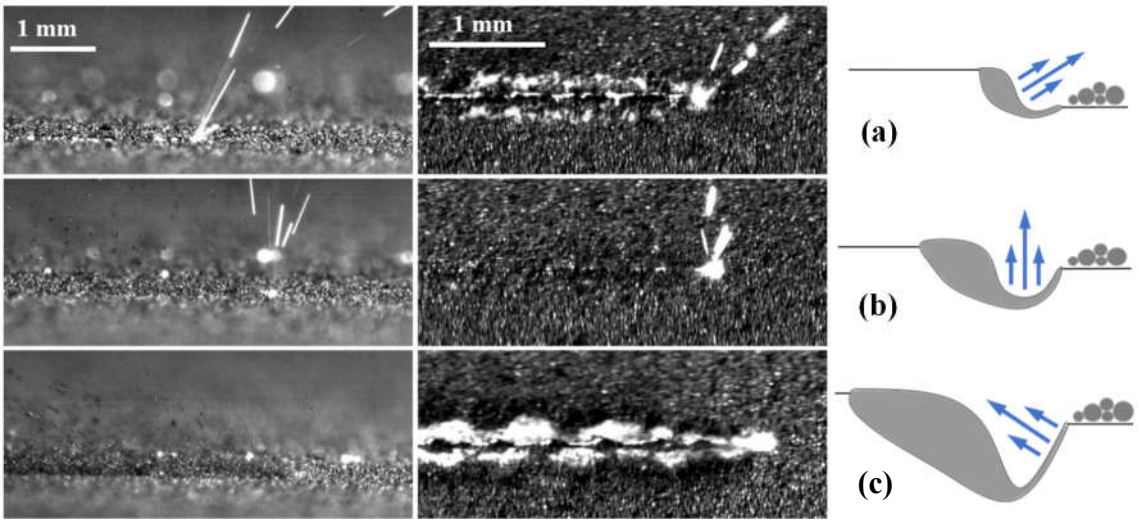

Fig. 75 High-speed images for side and top views when scanning single tracks (left to right laser movement) with laser power and scan speeds of (a) 50 W and 0.1 m/s; (b) 100 W and 0.5 m/s and (c) 200 W and 1 m/s. Inset is a schematic of the melt pool shape, which determines the spatter direction.

The results show that the direction of spatter changes with process parameters, creating a different denudation pattern on the powder bed. At the 50 W condition, the plasma and spatter are in the upper forward direction with respect to the laser scan direction. The induced flow of the ambient gas entrains powder particles in towards the melt pool from all directions on the powder bed. Particles behind the melt pool are lifted off the powder bed, as seen in the side view Fig. 75(a). Entrained particles are unlikely to be consolidated into the track and are mostly ejected by the laser plasma and gas flow. At the 100 W condition, the plasma and spatter are directed predominantly vertically upwards, resulting in less momentum in the shield gas flow at the powder level and consequently less denudation. At the 200 W condition, the plasma and spatter are directed backwards with respect to the scan direction. The induced gas flow is at a sufficiently low angle that it

impinges on the powder bed and causes denudation by blowing particles away from the track.

High-speed schlieren imaging was used to visualise the flow which caused the observed particle motion at the same parameters across the powder bed, Fig. 76. Refractive index gradients around hot particles expelled by the laser plume are visible. Ejection of entrained particles occurs according to the direction of the laser plume with respect to the laser scan direction and the process parameters, consistently with Fig. 75.

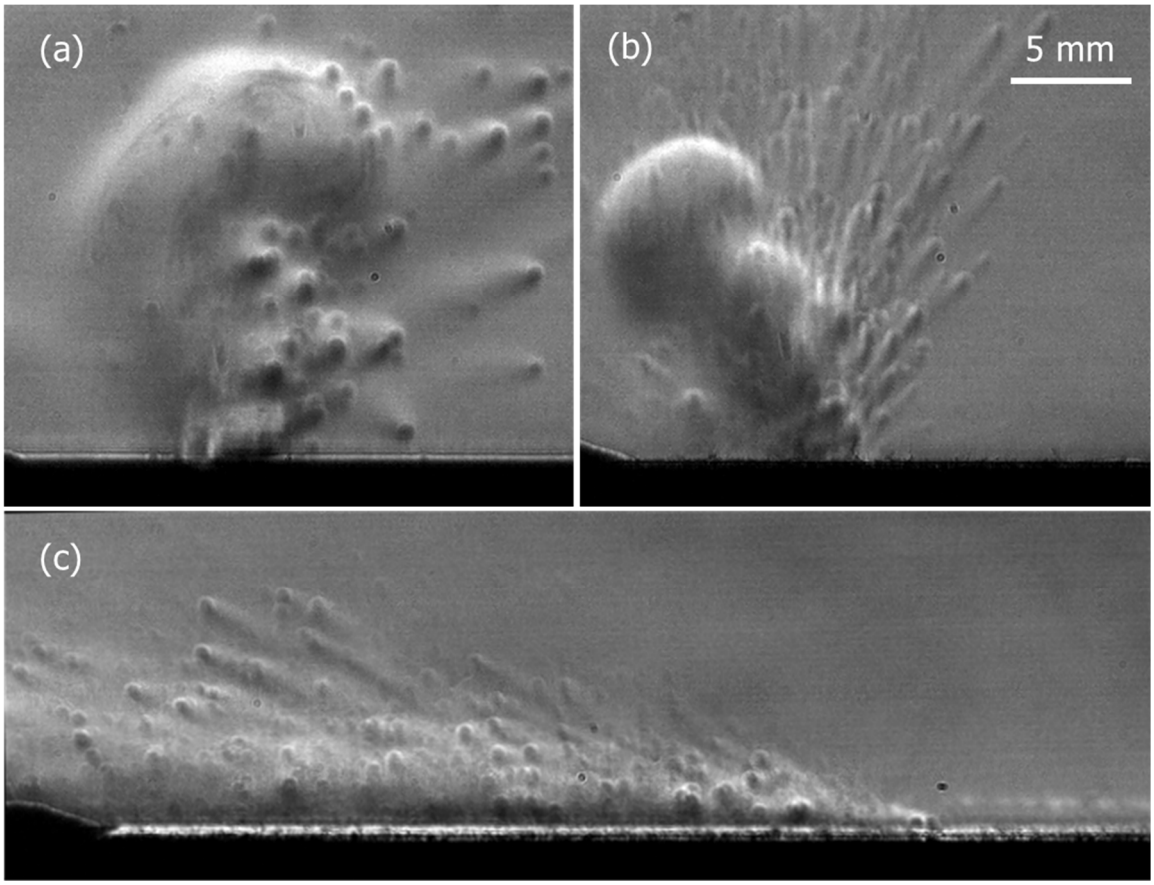

Fig. 76 Schlieren images during left to right line scans at (a) 50 W and 0.1 m/s, (b) 100 W and 0.5 m/s, (c) 200 W and 1 m/s. The characteristic refractive index gradients due to the plume are visible in (a) and (b) but not present in (c) due to backwards tilt of the laser plume. Entrained Fe vapour is visible behind the convection front in (a). Due to the system's resolution, diffraction blur occurs around the larger individual powder particles and across the powder layer.

At the 50 W condition, the low scan speed combined with the forward plasma ejection causes the laser beam to traverse a considerable distance of heated gas, metal vapour and plasma before it reaches the powder bed surface. It is not possible to separate the relative contribution due to temperature, pressure and metal vapour concentration on the measured refractive index gradient from the images. However, these refractive index gradients are undesirable as they can contribute to process instability through defocus and lateral wander of the laser spot. At the 100 W condition, the laser beam is apparently just in front of the region of high refractive index gradients once the large convection plume

from the initial laser incidence on the powder bed has been cleared. Circular plumes of vapour can be seen when vertically ejected particles are vaporized by the laser beam. For the 200 W condition, interaction between the laser beam and the heated gas, metal vapour and plasma is not an issue due to the high laser scan speed, although these conditions were previously seen to produce a balled track.

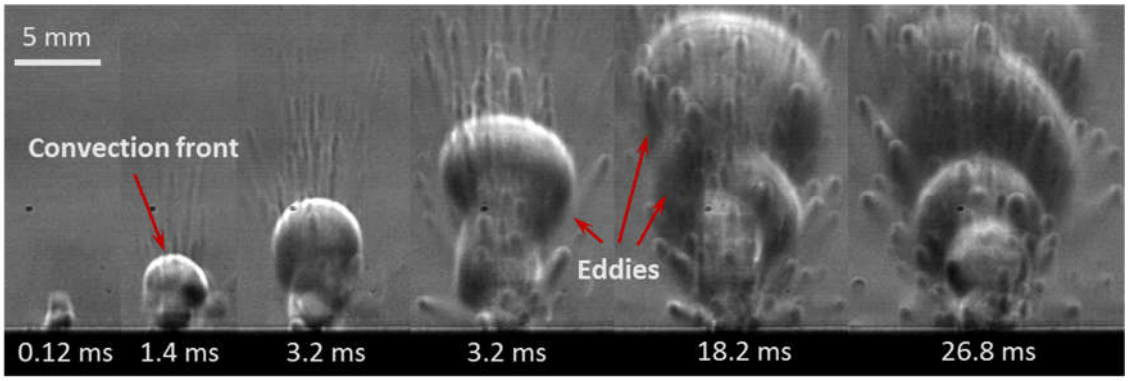

Fig. 77 Composite image of the plume of heated gas rising due to convection at the times indicated at power 100 W and scan speed 0.5 m/s towards the direction of view. Radial momentum is imparted to the atmosphere by the eddies trailing the convection fronts.

Fig. 77 shows an image sequence at the times indicated during a single laser line scan across the powder bed, towards the camera. Upwards momentum carried by the plume is imparted to the surroundings, as indicated by the observed convection front while radial gas motion is induced by the eddies trailing it. Drag is exerted to powder particles in a radius proportional to the plume's intensity. Dark lines in the initial convection front are particularly clear, and are due to entrained iron vapour. The plume of heated gas continues to be fed by the laser plume: intermittent bursts of gas and vapour could be caused by LSC to LSD transitions although the spatial and temporal resolution of these measurements is insufficient to resolve directly the shock front associated with those events.

6.3.2. *Visualisation of LPBF plumes, including the effect of cross-flows*

Atmospheric gradients are undesirable and can cause variations in the laser position and focus. In a commercial system, these hot fluids should be cleared by a flow of shield gas across the powder bed during the process, which can also serve to extract 'airborne' particles and prevent them from landing back on the powder bed. All the results presented so far have excluded this cross-flow, in order to focus on the effects of the plume-induced flow. These cross-flows are typically of the order of a few m/s, and therefore do not interfere with the plasma flow; they do however intact with the induced flow. It is instructive to observe the interaction of the laser-plume induced flow with a laminar cross-flow of 10 l/min across the powder bed from a flow-straightener.

To ensure that the flow delivered was laminar and homogeneous, the design of the straightener was numerically analysed in COMSOL. The fluid flow equations (1) and (2) were solved along with the k – ε turbulence model on a representative 2D slice of the straightener and immediate Ar atmosphere. Fig. 78 shows the calculated velocity profiles from two potential designs, one using a honeycomb design alone, and the second also incorporating an inverted cone diffuser.

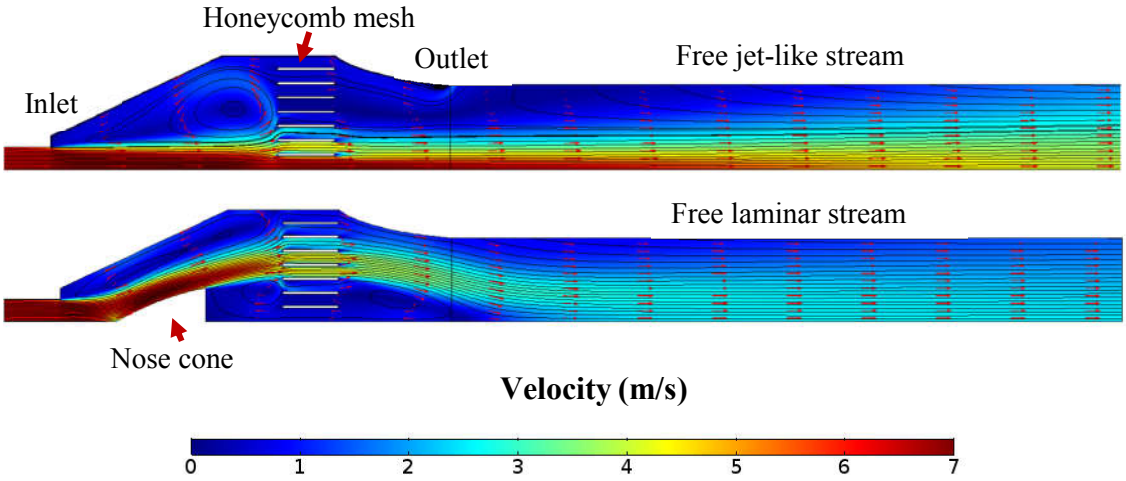

Fig. 78 Velocity profiles of 10 l/min flow through flow straightener with (a) "honeycomb" diffuser, (b) inverted cone element plus diffuser. The centralised maximum is avoided by "breaking" the flow through the central cone.

Clearly, the inverted cone element helps in delivering a more homogeneous flow across the bed. Following the simulation, the flow straightener with the nose cone and honeycomb design was printed in ABS plastic using fused deposition modelling (FDM) and fitted a few mm above the bed as shown in Fig. 74(a).

Due to the relatively low velocities in the flow above the powder bed, a lower imaging frame rate was more suitable for this application. The high-speed camera was thus replaced with the flea 3 camera, operating at 200 fps. An additional 633 nm ±1 nm full width at half maximum band-pass filter was included to eliminate incandescence and plasma light from the melt pool. Fig. 79(a) shows the Ar plume with no cross draft. Fig. 79(b) and (c) show the introduction of an Ar cross-draft for laser powers of 100 and 200 W respectively, which indicate the need to match the cross draft to process setting if the plume and particles are to be removed effectively. Another interesting observation is that ejected particles carry enough upwards momentum so as not to be affected by the cross-flow initially, but are swept to the side upon re-entry to the stream after free-falling. It is difficult to separate the relative contribution due to temperature, pressure and metal vapour concentration on the measured refractive index gradient from these images.

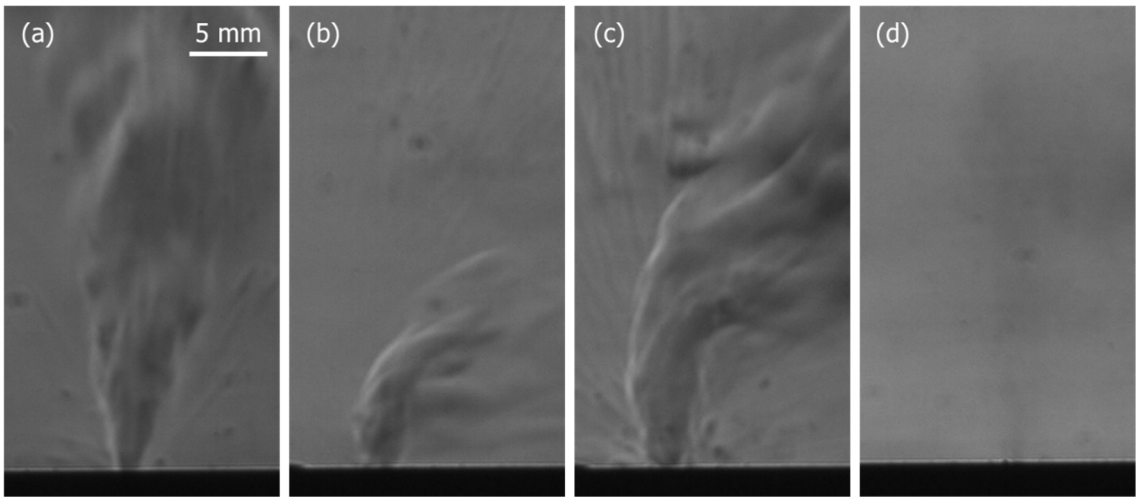

Fig. 79 Long exposure (5 ms) schlieren images. (a) 100 W laser power, (b) 100 W laser power with 10 l/min cross-flow, (c) 200 W laser power with 10 l/min cross-flow, (d) vapour stream in He atmosphere -He refractive index gradients not visible with schlieren sensitivity tuned for Ar flow.

However, Fig. 79(d) shows the effect of introducing a helium inert atmosphere at 200 W. Regardless of laser power, the total observed refractive index gradient was much less intense in He than in Ar, due to differences in their thermophysical properties and ionisation potentials. The lack of gradients suggests that no interference occurs to the laser beam by the atmosphere. Additionally, the metal vapour jet can be distinguished from the background flow features. A systematic study of LPBF under a He atmosphere is beyond the scope of this thesis, as discussed in the further work section.

6.4. Numerical modelling of laser-induced gas flows during LPBF

The scientific literature concerning evaporative and plasma phenomena that occur in laser welding and laser ablation studies was used as a basis for numerical analyses in the context of LPBF. During LPBF, incident radiation fluxes can exceed 10^7 W/cm^2, mainly due to the small laser beam diameter. In the irradiance range of 10^5 – 10^7 W/cm^2, the laser-material interaction produces a plume that comprises an upwards flow of metal vapour and plasma, potentially amplified by laser-supported combustion (LSC) waves [148]. The energy provided by the laser to the material is sufficient to cause evaporation and also the ionisation of vaporized atoms. For fluxes > 10^7 W/cm^2, laser supported detonation (LSD) waves can occur [148], characterised by increased absorption of the laser beam by the metal vapour and plasma,. The intensity of these LSC and LSD waves depends primarily on the laser intensity and wavelength [149] and their frequency and duration can vary accordingly. For modelling, these phenomena are grouped together with general evaporation mechanisms and analysed by hydrodynamic modelling of the lased-induced plume that comprises metal vapour and plasma [142]–[145]. In such models, the Knudsen layer approach is commonly used to model the plume (combined

vapour and plasma) flow into the atmosphere through a contact discontinuity at the substrate-gas interface. The plume velocity is represented as the speed of sound in the gas at its elevated temperature, with a local Mach number reaching 1 for even moderate laser powers.

6.4.1. *Model geometry, materials and mesh*

An approximation commonly employed in the study of laser-materials interaction is to consider that the geometry of the system can be described by a 2D axisymmetric plane, rotated around the centre axis of the laser beam, Fig. 80. Additionally, a time independent formulation of the equations is well suited for CW laser scanning of several seconds, as is the case with most LPBF processes. This allows the use of small mesh sizes without the prohibitive computational costs typically involved with models of this process.

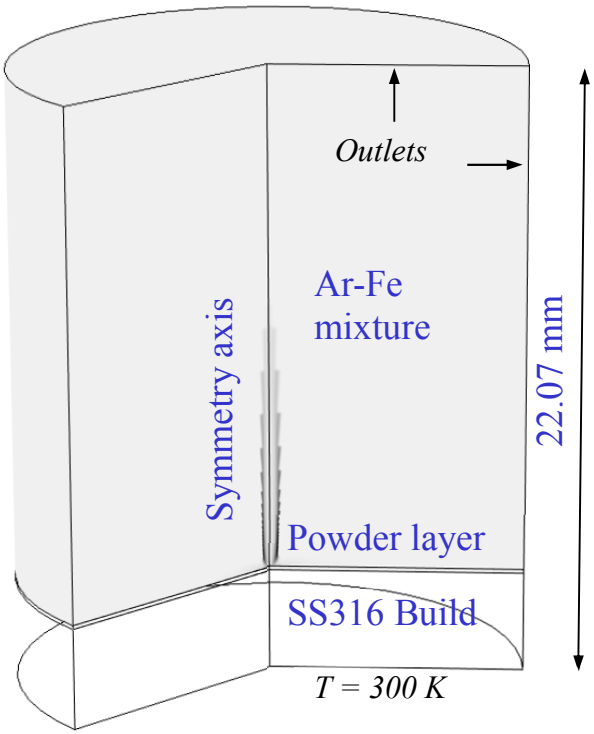

Fig. 80 2D axisymmetric geometry used in LPBF model, comprised of three domains: solid, powder and fluid.

The mesh was locally refined at the innermost edge of the powder bed so that at least 30 elements were generated along its depth, resulting in minimum element sizes of ~1.5 µm for a 70 µm layer. Standard Lagrangian elements were used across all domains, only allowing a 2.5% growth rate, up to a maximum of 12 µm in the powder layer and 0.25 mm elsewhere.

For the substrate and powder layer, the thermophysical properties of grade 304 and 316 stainless steel respectively were input as a function of temperature [93]. In modelling the powder layer, a volume-averaged approach was used for temperatures below melting,

after [141]. For an average packing density ϕ = 0.6 in the powder layer, the equivalent thermophysical properties were written as:

$$\xi_{powder} = \phi\xi_{steel} + (1 - \phi)\xi_{Argon} \quad (33)$$

Although the thermal conductivity of the powder might be exaggerated in this manner at relatively low temperatures, the fluid dynamic phenomena of interest to this study occur at much higher temperatures, where the material properties are representative of the liquid and gas phase. Therefore, the use of volume averaged properties does not undermine the accuracy of the prediction for evaporation phenomena. Using actual powder thermophysical properties is however essential for simulations investigating the melt pool size or residual stress development.

The properties used in the fluid domain were those of an Ar-Fe plasma, calculated Cressault et al. [150] using the Chapman-Enskog method, and given as a function of temperature and Fe mass fraction. The plasma was assumed to be optically thin, and the net radiative coefficient required to characterise the lost radiation per unit volume was taken from Menart and Malik [22]. Based on the literature [145], [151] as well as in-house numerical solutions of the Saha equation, inverse bremsstrahlung absorption for the 1070 nm laser wavelength used in the experiments and temperatures under 10 kK is negligible and therefore was not included in the model.

6.4.2. *Governing equations and boundary conditions*

The partial differential equations (PDEs) used in the model are given below using vector notation. Vectors are represented in bold while constitutive properties used as a function of temperature and Fe mass fraction are in italics. For fluid flow, the compressible Navier-Stokes equations for momentum and mass conservation were used, (eqn. 1 and eqn. 2). In order to better capture the turbulence due to the plasma jet but also to expand the stable solution space of the model, the RANS SST turbulence model was utilised. An additional conservation equation was added to model the convective and diffusive modes of transport of the vapourised Fe during the process, as per eqn. 5 and eqn. 6. For the process thermodynamics, an energy balance was used to account for conductive, convective and radiative heat transfer, eqn. 7. The net radiative coefficient method was used within the gas/plasma domain to account for the net radiation losses, where the coefficient ε_N was input as a function of both temperature and Fe mass fraction. For the substrate and powder layer, no convection term was used as the melt pool motion was omitted for this study

and translational motion cannot be conveyed in axisymmetric models. Graybody radiative energy losses were prescribed for all solid surfaces, including the powder-substrate boundary. The temperature at the outer boundaries of the powder and substrate was set at 300 K. To account for ambient convection, the total losses at the gas/plasma outer boundaries were prescribed as:

$$\mathrm{q} = -\mathrm{h}(T_{amb} - T) \tag{34}$$

A convective heat transfer coefficient of h = 50 W/m^2 was used. The laser radiation reaching the powder layer was modelled as a gaussian heat source with intensity

$$\mathrm{I} = \frac{2\mathrm{AP}}{\pi \mathrm{R}^2} \exp\left(\frac{-2\mathrm{r}^2}{\mathrm{R}^2}\right) \tag{35}$$

Where A = 0.6 is the absorption of the powder layer, P is the laser power and R is the beam radius. The heat lost from the metal surface due to evaporation is given by

$$\mathrm{q} = -\dot{m}_{vap} L_{vap} \tag{36}$$

where L_{vap} is the heat of vapourisation and $\dot{m}_{vap}$ is the Fe vapour mass flowrate, based on the vapour pressure P_{vap} and temperature, written as [57], [93]:

$$\log\left(\dot{m}_{vap}\right) = 2.52 + \log\left(P_{vap}\right) - 0.5\log(T) \tag{37}$$

$$\log\left(P_{vap}\right) = 6.121 + \frac{18836}{T} \tag{38}$$

Using the Knudsen layer approach, the velocity at the powder bed surface was set based on the local sound speed

$$\mathrm{u} = \mathrm{M}\sqrt{\frac{\gamma K T}{\omega_1 m_{Ar} + \omega_2 m_{Fe}}} \tag{39}$$

Where M is the Mach number, γ = 5/3 is the heat capacity ratio for a monoatomic gas, K is the Boltzmann constant and m_{Ar}, m_{Fe} are the atomic masses of Ar and Fe, respectively. The Mach number was assumed to vary linearly based on the incident laser radiation [148], from M = 0.01 at an intensity of 10^5 W/cm^2, to M = 1 for a flux of 10^7 W/cm^2. An outlet condition with p = 0 was set at the outer flow boundaries.

The Fe mass fraction at the powder surface may be defined based on the vapour pressure and molar masses of Ar and Fe as [48]:

$$\omega_2 = \frac{P_{ev} M_{Fe}}{P_{ev} M_{Fe} + (P_{atm} - P_{ev}) M_{Ar}} \tag{40}$$

On the outer flow boundaries, an outflow condition was specified by setting the normal diffusive flux equal to 0.

6.4.3. *Results*

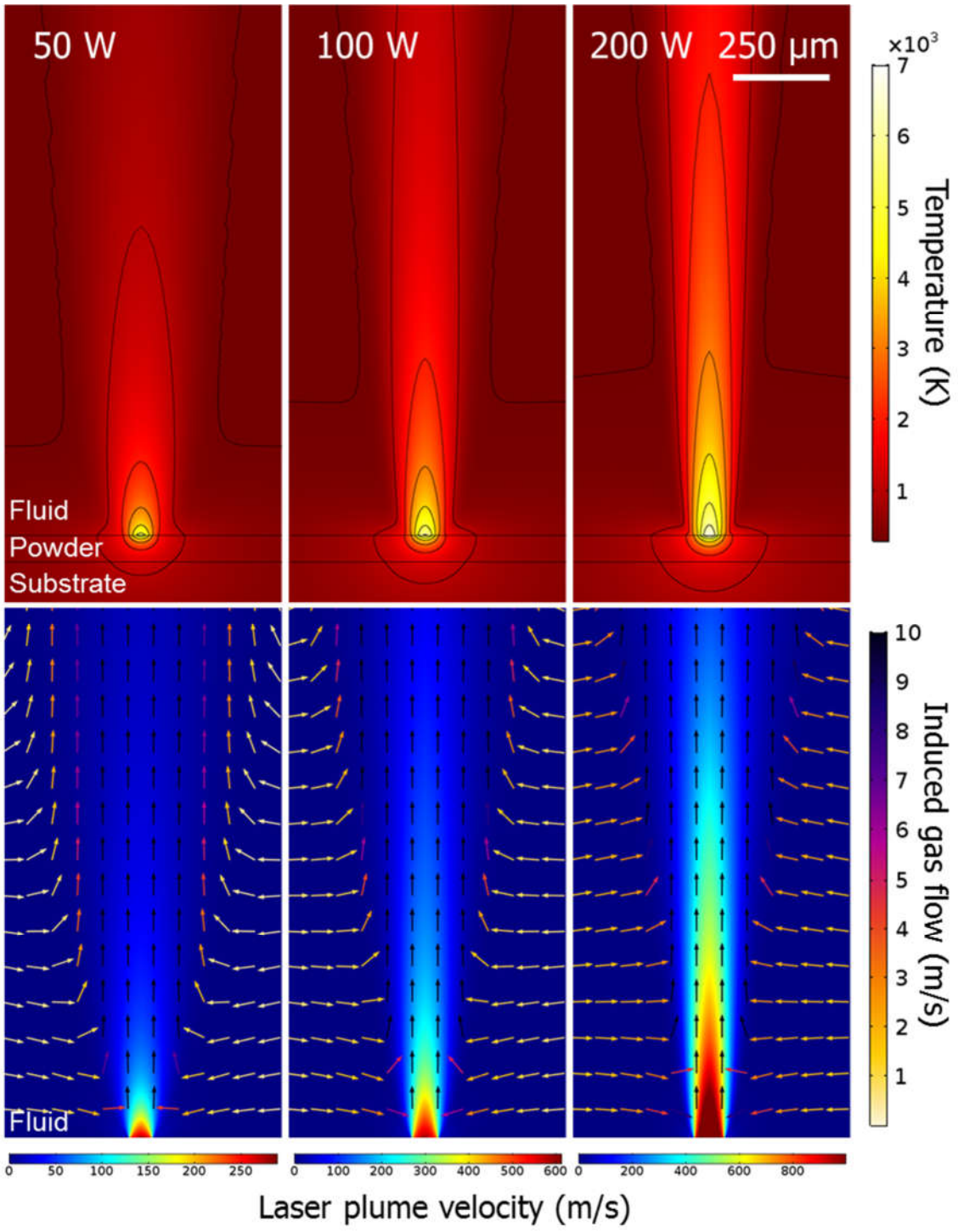

Fig. 81 (Top) Calculated temperature fields for 50, 100 and 200 W laser power. (Bottom) Velocity surface plot of fast plume, with arrows showing the slower, radial atmospheric gas flow.

Fig. 81 (top) shows temperature distributions for 50 - 200 W laser-induced plumes. The maximum predicted temperature, located at the plume's centre, ranges from ~5000 K at 50 W to ~7,000 K at 200 W. The temperature is predicted to be higher than the

evaporation point over a radius of 33 – 44 μm, suggesting vapour is generated over an area roughly 1.5 – 2 times that of the laser spot's. For all cases, the temperature drops to under 500 K within ~0.3 mm in the r direction. In the vertical direction of the fluid domain, the temperature decreases to under 500 K after 3, 8 and 16 mm for 50, 100 and 200 W respectively. This rapid decrease is a consequence of the high upwards convective heat transfer in the laser plume which increases with power and results in a characteristic oval-shaped distribution. In the powder layer and substrate, the high temperatures at the boundary drop sharply and the computed field is similar to FE results in the literature. However, due to the lack of convective motion in the powder and substrate, the lack of free surface deformation and keyhole formation, and an effective radiative absorption coefficient in the z- direction in the powder layer [152], the penetration into the substrate is underestimated.

The bottom row of Fig. 81 shows velocities in the fluid domain. The colour distribution shows the high velocities associated with the laser plume due to the evaporation in the Knudsen layer. The magnitude of the plume's velocity scales linearly with power, ranging from approximately 300 m/s at 50 W to 1200 m/s at 200 W. However, the jet decelerates exponentially in the z direction, reaching ~100 m/s over an upwards distance of 0.15 mm for 50 W, 1.1 mm for 100 W and 2.2 mm for the 200 W case. The arrows in each case indicate the much lower velocities of the Ar atmosphere that are induced by the laser plume. As dictated by momentum conservation, a radial flow field is generated in the Ar atmosphere. Upwards momentum carried by the plume is imparted to the surroundings, while radial gas motion is induced via momentum conservation, consistently with the mechanism observed in the schlieren images, Fig. 77. The radial flow exerts drag forces on particles in the powder layer, resulting in a net particle motion towards the laser and denudation observed experimentally.

Fig. 82 (a) shows a plot of this radial component of the flow of the Ar atmosphere at 100 W and at different z heights above the top of the powder layer. The velocity is highest closer to the bed and decreases with height, due to the maximum momentum being located at the Knudsen layer. The variation of the velocity with height suggests that a swirl is imparted in the particles, which is consistent with the observed motions of particle agglomerates. At all z heights, the radial plume-induced flow of the Ar gas is mainly inwards towards the laser, i.e. negative values. Its effect extends to ~0.2 mm from the centre of the laser beam, which is consistent with the extent of the denudation observed experimentally. A short region of flow reversal is predicted between approximately 25 –

50 µm from the centre of the laser beam, i.e. approximately between the edge of the laser spot and the edge of the melt pool. The flow reversal is mainly due to a pressure gradient which develops at the edges of the fast laser plume, caused by flow stagnation and associated with the jet's wake. Additionally, the change in density from a Fe rich mixture to mostly Ar accentuates this effect, Fig. 82(b). This suggests that a radial deceleration is experienced by entrained particles approaching the melt pool, promoting upwards ejection. Additionally, particles caught in the wake with no prior momentum are ejected upwards and outwards. Fig. 82 (b) plots the Fe concentration at the powder bed surface against radial distance from the centre of the laser spot. Vapour generation scales almost linearly with laser power in the range simulated, and is concentrated almost entirely within the laser spot radius where temperatures exceed the vaporisation point.

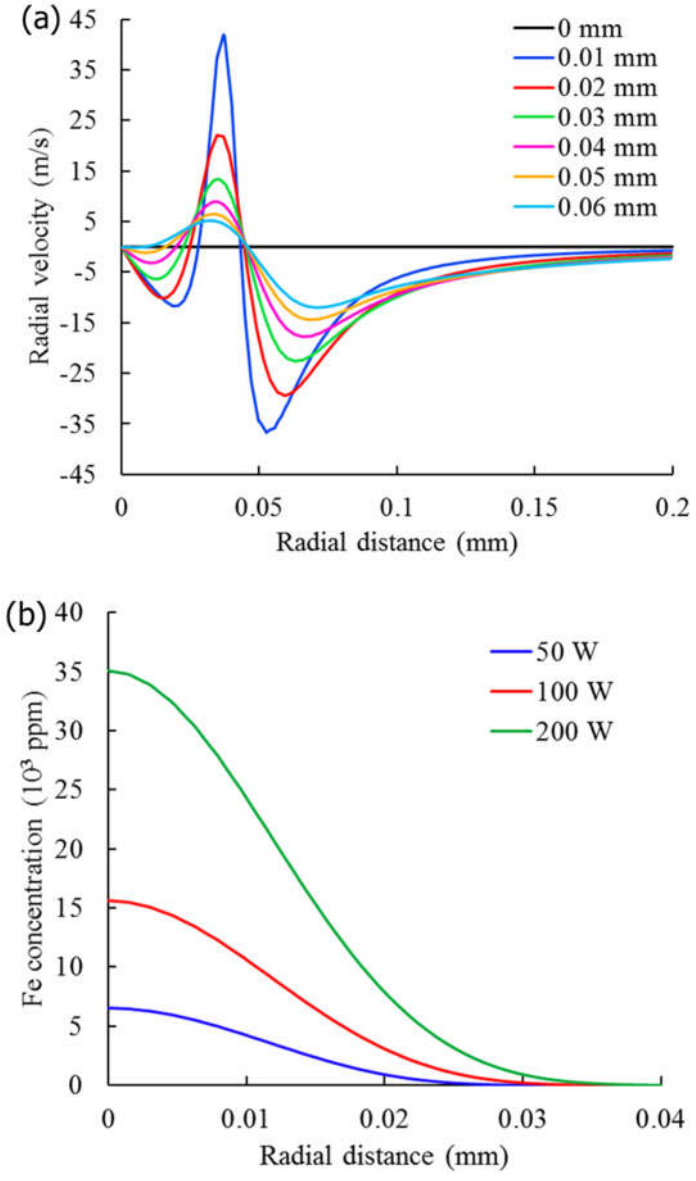

Fig. 82 (a) Radial velocity component at different z-heights above the powder bed. The denuding flow is faster closer to the Knudsen layer, and carries less momentum with increasing height. A brief flow reversal occurs due to Fe concentration and pressure gradients at the plume's fringes (b) Fe concentration plot at the Knudsen layer for different laser powers.

Fig. 83 (a) shows the upwards transport of the vaporized Fe stream at 100 W, which is similar to that observed experimentally. It has a steep concentration gradient, reducing to under 1000 ppm within 1 mm in the z-direction, suggesting that despite the high velocity ejection, the majority of vaporized Fe remains close to the powder bed. The net radiative emission of light across all visible wavelengths from the plasma can be calculated, Fig. Fig. 83 (b), and shows the characteristic shape of the laser plume. Additionally, a plot of the density gradient $\partial\rho/\partial x$ is proportional to refractive index variations $\partial n/\partial x$. The good match between the resulting 'artificial' schlieren image, Fig. 83 (c), and the experimental observations, Fig. 79, indicate that the calculated gradients of temperature, pressure and composition are representative.

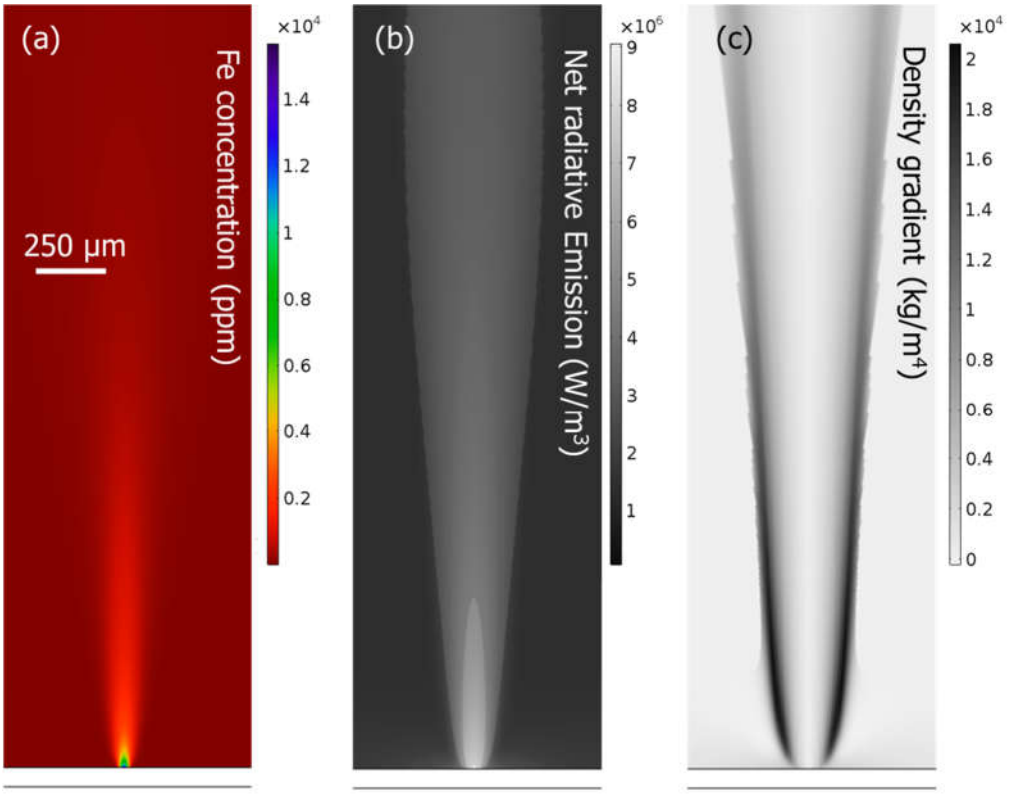

Fig. 83 Simulation outputs at 100 W. (a) Fe concentration plot, showing localised dissipation of generated vapour, (b) Plot of the net radiative emission coefficient term $4\pi\varepsilon_N$, (c) artificial schlieren, generated by plotting the $\partial\rho/\partial r$ density gradient. Comparison of (b) with Fig. 11(a) and (c) with Fig. 9(a) shows qualitative agreement between observations and model.

6.5. Discussion

This chapter shows the importance of including the laser plume and ambient atmosphere for a full understanding of the PBF process, and in the numerical models used to describe it, because of the influence on denudation especially but also on the production and subsequent transport of debris. In this section, the effect that the observed phenomena have on the process is discussed.

6.5.1. *Species ionisation*

Based on the calculated temperatures above 5 kK, but also on spectroscopic measurements from similar CW radiant fluxes on flat substrates [148], the laser-induced plume includes Fe vapour and plasma. It is therefore of interest to characterise the plasma generation of the process, to determine whether it directly interacts with the laser beam. While phenomena such as laser-supported absorption waves have been reported for CO_2 lasers in laser welding, for example by Kim et al. [142], no studies have been reported in the context of LPBF, where Nd:Yag-based fibre lasers are typically used. For the calculation of inverse bremsstrahlung absorption, the main cause of energy transfer between the laser and the plume, the electron density must first be known.

The Saha equation can be used to determine the degree of ionisation in an LTE plasma, based on the temperature of the fluid, as discussed in Zhang et al. [157] and Han [158] for laser welding. For the first ionisation of a given species, it is given by:

$$\frac{n_e n_i}{n_0} = \frac{1}{\Lambda^3}\frac{g_i g_e}{g_0}\exp\left(-\frac{\Delta E}{k_B T}\right) \tag{41}$$

Here n_e, n_i and n_0 is the number density of electrons, ions and neutral atoms of the gas, while g_i, g_e and g_0 are the degeneracy constants for ions, electrons and neutrals and ΔE is the difference in energy between the neutral and first ionisation stage. Λ is the thermal deBroglie wavelength, given by

$$\Lambda = \sqrt{\frac{h^2}{2\pi m_e k_B T}} \tag{42}$$

Where h is Planck's constant and m_e is the electron mass. Numerical solution of a system of Saha equations for singly ionised Fe and Ar species, allowed the calculation of electron density. By imposing quasi-neutrality, $n_e = n_i$ and applying mass conservation, the total number of atoms is $n = n_0 + 2n_e$. By treating the Ar-Fe mixture as a mass-averaged ideal gas, ie the average atomic mass is $\bar{m} = \omega_1 m_{Ar} + \omega_2 m_{Fe}$, the total number of atoms can be estimated by

$$n = \frac{N_A \rho}{\bar{m}} \tag{43}$$

Where N_A is Avogadro's number and ρ is the local calculated temperature and mass fraction-dependent density. The number density of Ar and Fe is then given simply by $n_{Ar} = n\omega_1$, $n_{Fe} = n\omega_2$. The degree of ionisation in the plasma (total ratio between

neutral species and electrons) is then $y = y_{Ar}\omega_1 + y_{Fe}\omega_2 = (n_{eFe} + n_{eAr})/n$. Equation 41 can then be re-written for Ar and Fe in a more numerically stable manner as

$$y_{Ar}{}^2 - \frac{A_1}{n_{Ar}} T^{\frac{3}{2}} \exp\left(-\frac{\mathrm{B}_1}{\mathrm{T}}\right) = 0 \tag{44}$$

$$y_{Fe}{}^2 - \frac{A_2}{n_{Fe}} T^{\frac{3}{2}} \exp\left(-\frac{\mathrm{B}_2}{\mathrm{T}}\right) = 0 \tag{45}$$

Where A and B are the characteristic constants for each gas. COMSOL multiphysics software was used to solve equations 44 and 45 for y_{Ar} and y_{Fe}, based on the computed 2D temperature (Fig. 81a) and mass fraction fields.

The total degree of ionisation y is plotted for the 50 - 200 W range in Fig. 84. Due to the difference in ionisation potential in Fe and Ar, electron density peaked at Fe-rich regions at T > ~5kK. At 50 W almost no ionisation occurs, but with increasing power, y increases non-linearly with ~2% of the fluid in the plasma state at 200 W. Due to the relatively low degree of ionisation and low absorptivity at 1070 nm, inverse Bremsstrahlung absorption in the plume was found to be negligible, based on the coefficients in [145], [154], [155]. Laser energy is therefore delivered onto the powder bed with minimal losses.

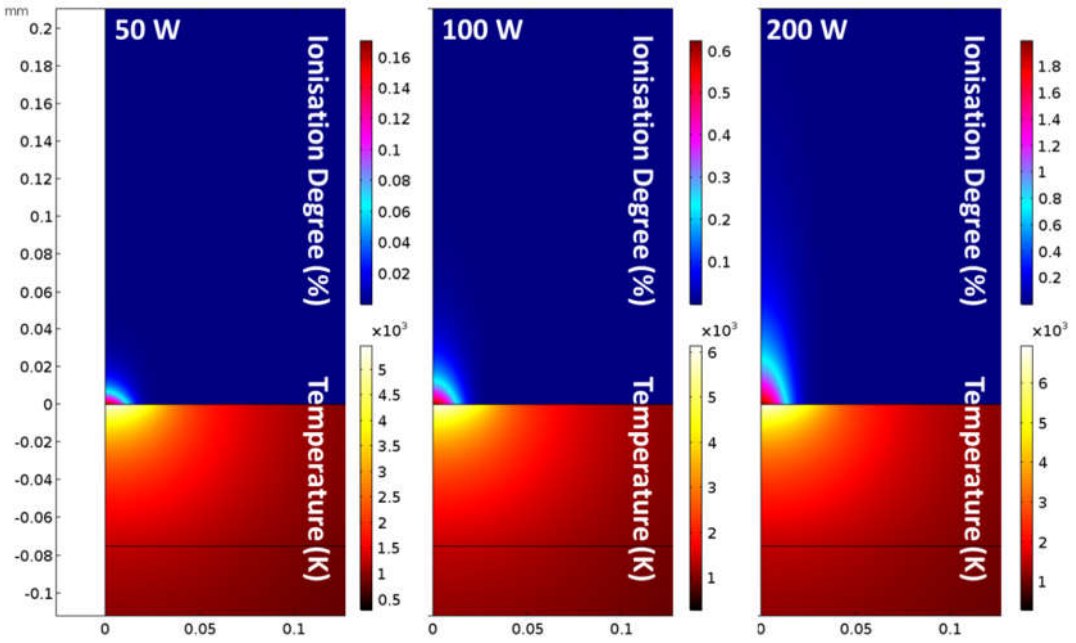

Fig. 84 Degree of ionisation y = n_e/n in the plasma plume, and temperature of substrate/powder bed. Maximum electron density appears at the high temperature, high Fe concentration region.

The intensity of the laser beam during the imaged experiments varied from 2.5 x 10^6 W/cm^2 at 50 W to 10^7 W/cm^2 at 200 W, suggesting that enough energy was locally available to induce LSC and possibly LSD waves. Although the timescales associated with such phenomena are of the order of ns, multiple of these events could be taking place

during the continuous irradiance by the laser. The LSC to LSD transition might be the cause of the discontinuous feeding of the convective plume observed in the high-speed schlieren footage, where variation of the propagating convection fronts' velocity and intensity was observed over time. Depending on the intensity, the electron density at the interaction point could be fluctuating around (or constantly over) a threshold value, increasing the prevalence of such waves. Visualisation at higher temporal resolution is required to further understand these effects and their relative impact on the process.

The fluid temperature calculations indicate that sufficient heat is available to cause local vaporization and ionization around particles which reach the inner layers of the plume. It can be inferred that such particles will be enveloped in hot gas due to the Leidenfrost effect, which is consistent with the radiation emitted by the particles in the direct imaging experiments and by the refractive index gradients observed in the schlieren images. The gas envelope around these particles and relatively low calculated local flow velocities suggest that such particles are more likely to be ejected than incorporated into the melt track. However, if they are incorporated, the likelihood of local porosity is increased due to this surrounding gas and surface oxides coating such particles [156].

6.5.2. *Plume hydrodynamics and effect on particles*

The plume velocity is of the order of several hundred m/s and scales with laser power. The laser plume induces an inwards flow in the surrounding atmosphere that reaches velocities of the order of tens of m/s. This flow exerts a significant drag on powder particles and agglomerates in the proximity of the melt pool, altering the local particle distribution and powder availability.

Agglomerates can also be affected by the laser plume-induced flow: they can be drawn back into the melted track, presumably with an increased likelihood of producing porosity, or ejected into the atmosphere and produce large molten beads if they interact sufficiently with the hot gas or laser beam. Particles that are "heat-treated" and ejected by the plume act as an inclusion if reincorporated into the build at a later time, due to microstructure mismatch and oxide layer formation, as shown by previous studies for maraging steels [157], Stainless steel, Al-Si10-Mg, and Ti-6Al-4V [156] and Ni-based superalloys [158]. These entrained powder particles, agglomerates and larger solidified beads are also routinely found in the filters of commercial PBF systems, which is explained by these results.

The motion of particles entrained in the flow of the inert atmosphere produced by the high-speed jet from the melt pool has been observed previously [129], [131], [132]. The description of the jet as a laser plume recognizes that it contains plasma in addition to metal vapour, which is consistent with the presented hydrodynamic modelling of the fluids above the powder bed. Entrained particle motion has been proposed as a mechanism for denudation [129], but the results presented here are the first direct observation of this denudation process. Entrained particles are generally drawn towards the melt pool, but denudation arising due to particles being blown away from the melt pool was also observed. The diameter of the induced flow increases with distance from the melt pool, and for the laser scan conditions in Fig. 76(c), the flow was angled backwards sufficiently to impinge directly on the powder bed and blow particles away. It is perhaps worth emphasizing that denudation due to particle motion away from the melt track was inferred by Matthews et al. [129], but that was at very low ambient pressures and was therefore solely due to ejection of Fe vapour and plasma.

The evolution of vertical to backwards ejection of material from the melt pool as the laser scan speed decreases has been observed in laser welding [159] and PBF [129], [130]: the ejection direction is taken to be normal to the surface of the melt pool under the laser spot which varies due to a complex interaction of the laser plume recoil pressure and the liquid metal, as indicated by the schematics in Fig. 76 (a-c). Hence, the denudation pattern transitions from a forwards or upwards plume, pulling powder inwards towards the track as in Fig. 76(a), through to a plume tilted sufficiently far backwards that the flow impinges on the bed and blows away from the track, Fig. 76(c). Through variation in the melt pool shape due to the interplay of surface forces, gradual transition in plume tilt from vertically upwards to backwards can be inferred. The onset of Plateau-Rayleigh instability (balling) may be related to the drag forces exerted by the plume to the liquid surface, as in Fig. 76(c), however the numerical characterisation of this interaction requires a unified model of the melt pool and plume.

Vertical ejection could be investigated further as a favourable process setting, both with respect to reduced denudation and uniform direction of spatter within the build chamber. However, imaging of raster scans at 100 W showed that the laser plume tilts away from the adjacent track, which we again attribute to the modified shape of the melt pool. Hence spatter, entrained particles and agglomerates are ejected away from the build towards fresh powder in the bed. The interaction of particles and agglomerates above the powder bed is entirely dependent on the scan pattern of the laser within the island. Particles

carried by the flow can be dragged towards the scan line without being sintered or ejected upwards by the flow and can interact with the beam at a later time. This effect becomes more prevalent as the layer number increases and more powder is available in the build area. A detailed analysis of the particle velocities was not undertaken, because only its component in the image plane is available; furthermore, the particles are of different diameters and the force acting on them varies with distance from the melt pool making any inferences rather speculative. Nevertheless, cold particles raised off powder bed typically move at ~2 m/s, and the maximum length of image streaks from the ejection of hot particles corresponds to ~6 m/s. These speeds are in agreement with the simulated velocity of the induced flow.

6.6. Conclusions

The results presented in this work elucidate the dynamic phenomena which arise from the complex interaction between the laser and the molten metal during PBF, which are related to the quality of the manufactured part. The open architecture design of the system enabled detailed high-speed imaging to be performed for single tracks and multiple layer builds, as well as schlieren imaging for flow visualisation. It was shown that the Fe vapour, plasma and induced Ar gas flow determine the pattern in which powder is denuded from the vicinity of the melt pool. Single line scans showed that the direction of particle ejection with regards to the scanned direction changes from forwards to backwards with increasing laser power and scan speed. When the scan speed and power were relatively high, the plume was pointed fully backwards and towards the powder layer, which was heavily disrupted as a result. Upward ejection resulted mostly in particles being pulled towards the laser spot due to the aerodynamic drag. Particles that approached the plume were either sintered or melted and subsequently ejected according to their accumulated heat and momentum. The high temperatures of the plume promoted the formation and ejection of agglomerates (particles sintered together) and large spherical beads (particles fused together) which may result in defects and inclusions if reincorporated into the build after landing.

Schlieren imaging enabled the visualisation of the plume, facilitating flow characterisation. It was observed that convection fronts originating from the melt pool propagate in the atmosphere above the powder bed. Momentum was conveyed radially with respect to the plume axis through transient eddies trailing the convection fronts. The jet of vapourised material becomes entrained in the hot gas, accentuating the refractive index gradient presented to the laser. Refractive index gradients were observed around

ejected particles, confirming that both heat and momentum is transferred from the plume. High speed observation of the convection patterns in the atmosphere correlated well with the denudation effect observed through the direct imaging. Vapour jet visibility was enhanced in a He atmosphere, due to weaker refractive index gradients. This difference suggests that heat and mass transfer in the plume can vary significantly with a change in ambient gas. A full study of the effect of He atmosphere are beyond the scope of this thesis. However, this study highlighted the importance of fluid and particle dynamics on the cross-draft requirements in commercial systems and in the usefulness of schlieren imaging to determine the effectiveness of the extraction system during builds.

The proposed multiphysics treatment of the plume and induced atmospheric gas flow using a multicomponent plasma approach allowed theoretical analysis of the process's fluid dynamic effects. It was shown that the denuding flow is of the order of a few tens of m/s and acts over a radius roughly ten times that of the laser's. This radial Ar flow is caused by a fast, upwards ejection of Fe vapour and Fe ions with velocities of the order of several hundreds of m/s which rapidly decelerates within a few mm of travel in the Ar atmosphere. The temperatures in the plume were found to be higher than 3,500 K, causing melting and vaporisation of entrained particles that reach the proximity of the melt pool. Fe concentrations of up to 35,000 ppm were predicted in the ambient atmosphere at 10^7 W/cm^2 laser intensity.

The combined results showed that the inert atmosphere and laser plume are integral to the heat, mass and momentum transfer of the process. Their inclusion in numerical models is critical to process optimisation, to identify parameter sets which result in reduced denudation. Observation of plume and particle behaviour under cross-flow emphasised the importance of uniform extraction streams above the bed, carrying enough momentum to prevent contamination of the bed from ejected particles. Taking hydrodynamic phenomena into account during process planning can improve the overall build quality and limit the adverse effects of ejected vapour and particles.

7. Concluding summary and remarks

The work in this thesis is a collection of results concerning a variety of materials processing techniques. Common amongst all of them was the use of an inert gas to protect the high temperature metallic surfaces from oxidation, resulting in complex, non-

isothermal flows. The approach taken throughout this work was to use hydrodynamic modelling in order to better understand the physical phenomena which affected the gas flow in each case. Additionally, schlieren visualisation was used to validate the results of the model, but also to give additional information on flow dynamics that could not be modelled. This proved to be a powerful approach, as the simulations helped the interpretation of the imaged features but also the images portrayed the real effects that had to be modelled. The combined use of the developed diagnostic tools allowed the flexibility to model cases where several repetitive experiments were required or conversely, to image cases where modelling was not possible. The insight gained was used to identify the best possible operating conditions to improve the process.

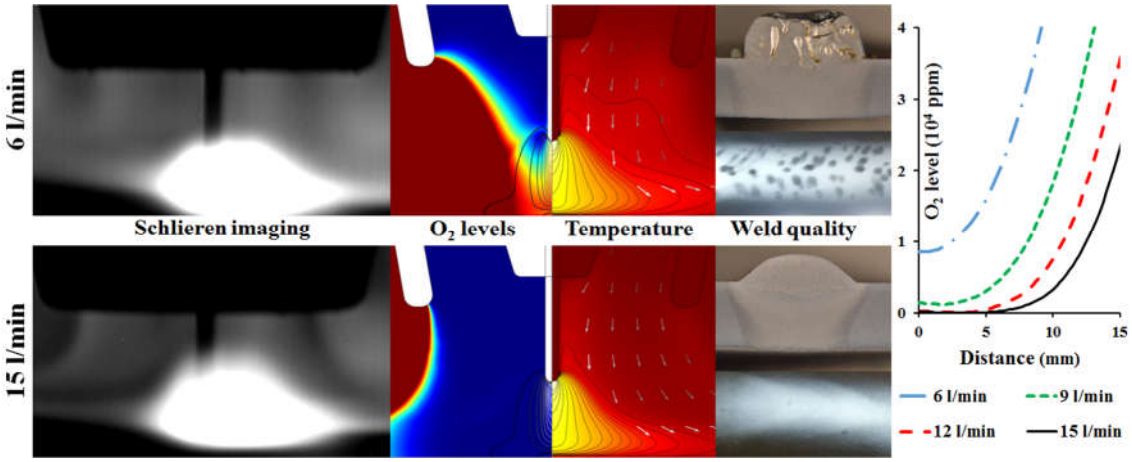

Fig. 85 Summary of GMAW visualisation study results

For GMAW, MHD modelling showed that the current and self-induced magnetic field generate strong, inwards Lorentz forces under the nozzle area. These forces resulted in the entrainment of air, leading to unacceptable O_2 levels if not counteracted by a sufficiently strong shielding gas stream. The simulations and experiments were in excellent agreement, allowing the characterisation of shielding effectiveness with varying process settings. Schlieren imaging showed that the refractive index gradients associated with the change in air concentration at the edges of the shielded zone were blurred when coverage was poor. Higher mass fractions of air over the weld area were computed under the same conditions in the model. Independent non-destructive testing, using x-ray radiography, allowed to assess the porosity levels in the produced samples in order to establish pragmatic limits for the allowed O_2 levels. It was found that 9 l/min of Ar were sufficient to produce samples that passed the inspection, which is roughly half of what is currently recommended in industrial practice. Additional imaging and simulations showed that this reduced limit applied consistently, regardless of changes in torch

standoff, angle, travel direction (push or pull) or joint geometry (bead-on-plate or fillet weld).

Due to the added complexities associated with the introduction of flux in the interelectrode area and use of multicomponent gas mixtures, MHD modelling of the FCAW-G process is beyond the current state of the art. However, when carrying out the same experiments as with GMAW, flow visualisation showed that the similar gradients were present. Extrapolation of the information gained from GMAW allowed interpretation of the imaged features, showing that similar entrainment dynamics were in place. Examination of the produced samples showed that the presence of flux dramatically increased the potential for O_2 absorption from the atmosphere without excess gaseous CO formation in the melt pool. This resulted in porosity-free welds produced at much lower flowrates, with a minimum input of 3 l/min. These results suggest that significant reductions on the input flowrates can be implemented in welding practice, with no compromise to weld quality.

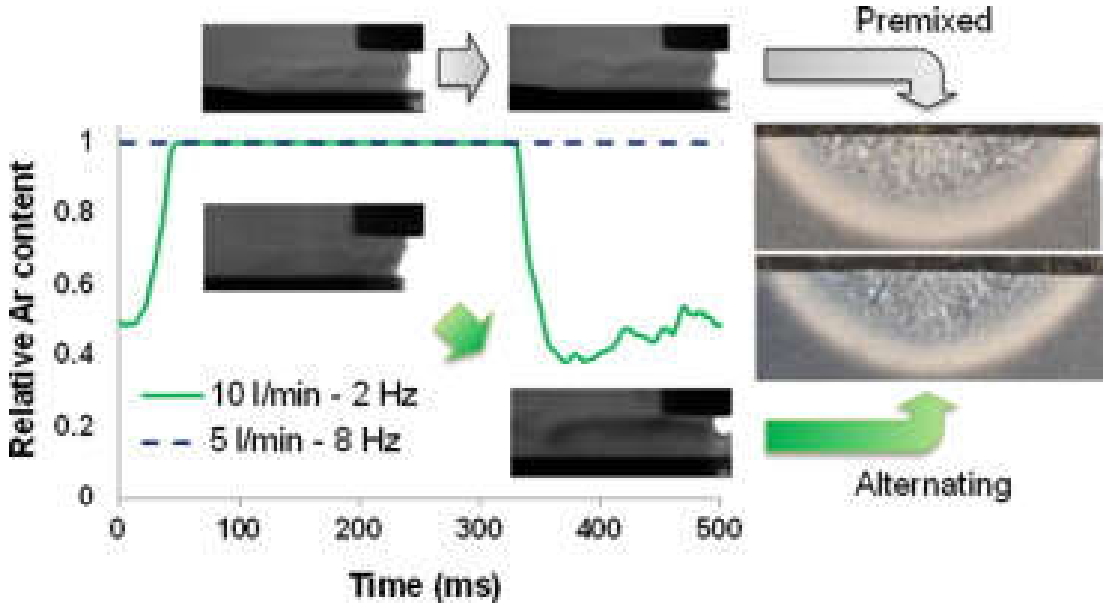

Fig. 86 Summary of GTAW alternating gas visualisation study.

Another application was for GTAW, where the flow patterns occurring with an Ar, He and pulsed Ar/He supply were visualised. Ar shield gas flow was more turbulent and mainly established parallel to the anode, while that of He was more laminar and buoyancy-driven. When the gases were pulsed, the flow features were different from those of pure gases, and transitioned between a turbulent and more laminar state, with flow always parallel to the anode. When pulsing occurred, a stable horizontal region of helium was observed near the weld region, maintained in position by the denser argon from the preceding pulse. Axial dispersion analysis suggested that the flowrate, pulsing

frequency and pipe length determined the degree of premixing in the gas flow before reaching the torch. It was found that a higher than average mass fraction of helium was present when applying the shielding gases alternately, compared to a premixed gas with the same volume of argon and helium. Pulsing in this manner resulted in more efficient use of the available He, increasing the weld penetration by 13% on average compared to pre-mixed. By increasing the travel speed, this improvement in heat transfer can be utilised as an increase in productivity compared to conventional steady-state GTAW.

For WAAM, the diagnostics revealed the flow structures that occurred under common deposition conditions. Visualisations of the flow from the trailing shield device alone showed that good coverage can be achieved, albeit at a high Ar throughput. The increase in standoff, inevitably incurred when printing tall structures, was found to diminish its shielding effectiveness and covered area. Imaging of the PAW torch without the shield showed that temperature, concentration and pressure gradients form due to the plasma jet and shielding gas stream. Side jets appeared due to the plasma jet's stagnation on the wall, running parallel or perpendicular to it, depending on torch position relative to the wall's edge. Whilst imaging the combined effects of torch and trailing shield, it was shown that the side jets interacted with the flow from the trailing shield, splitting the shielded area into an outer and inner vortex. Adequate shielding was achieved in this manner, regardless of input current or travel speed. However, when the deposited surface was significantly higher from the substrate and the double vortex structure could not be established, higher air entrainment occurred. MHD simulations verified that deposition without a trailing shield leads to unacceptable contamination levels for Ti-6Al-4V, with predicted O_2 levels at ~4000 ppm, regardless of input current. Additionally, heat transfer to the workpiece was shown to be influenced by the geometry of the deposited feature, due to changes in the convection patterns.

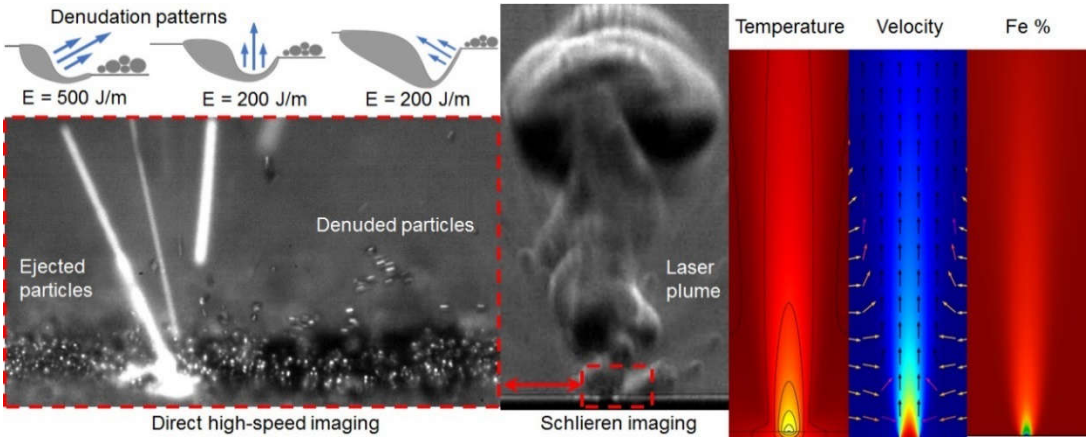

Fig. 87 Summary of LPBF study results

The final chapter of this thesis was an analysis on the fluid dynamic phenomena during LPBF, and the interaction between laser, powder particles and gas flow. High speed video showed that a flow was induced in the Ar atmosphere, exerting drag forces on powder particles. The powder denudation pattern on the bed varied with laser power and scan speed, according to the inclination of the area over which the Fe vapour jet was established. For cases where the surface depression was deep (200 W power with 1 m/s scan speed), the plume was tilted at an oblique angle, blowing powder away from the track. Conversely, when the plume was pointed upwards, powder motion was towards the melt pool. Direct imaging of island scans over several layers beyond the first showed that the prevalence of denudation decreased due to the greater amount of powder available around the laser path, as well as due to the increased surface roughness from the previous layers. Schlieren imaging allowed the visualisation of the laser plume, and the induced flow due to the laser-material interaction. It was shown that eddies form at the edges of the plume, inducing a lateral gas flow due to the Kelvin-Helmholtz instability. Fe vapour entrainment on the convection fronts generated by the plume was observed. Hydrodynamic modelling allowed the quantification of the gas flow velocity, temperature and Fe concentrations in the atmosphere above the bed. The computed velocity fields were in agreement with the observed particle motion; their estimated velocities from the image sequences were consistent with what would be expected due to drag from the induced Ar flow. These results highlighted the importance of taking into account the heat, mass and momentum transfer in the atmosphere during LPBF, in order to minimise defects in manufactured parts.

7.1. Further work

7.1.1. *GMAW and FCAW-G*

The model used in this thesis was focused on the fluid dynamic behaviour of the plasma jet and shielding gas flow. One limitation in the capabilities of the model was the omission of the melt pool from the calculations. By including the flow of molten metal and free surface deformation, more conclusions can be drawn about the characteristics of the weld bead under the tested conditions. The surface deformation can also be linked to the entrainment levels, by including a temperature and oxygen-dependent surface tension coefficient in the calculations for the Marangoni flow. Moreover, the modified shape of the workpiece surface when mass would be added to it could improve the accuracy of predictions for fluid dynamic phenomena. The simulations could be further improved through the comprehensive modelling of the effects of flux. This would require

modifications to the "standard" melt pool model, so that the flow effects of a mixture of Fe and Si could be resolved.

7.1.2. *GTAW, PAW and WAAM*

The good agreement between the simulated outputs and imaged features was the first qualitative validation of the model. Quantitative validation through the measurement of pressure, current density or temperature and comparison with predicted values is required to establish the model's accuracy. The computed O_2 concentration in the 2D axisymmetric simplification were only indicative of the fully 3D case of the moving torch with attached trailing shield device. Fluid dynamics analyses in 3D are therefore required to capture all aspects of the deposition system as used in current industrial practice for WAAM.

The model enables the functional optimisation of the tools used during WAAM through quantitative comparison of outputs such as temperature, pressure or O_2 concentration. Similarly, process inputs such as the current variation presented in this thesis can be used to estimate heat and momentum transfer to the melt pool. A unified model of the torch, arc and melt pool could be used to facilitate operating parameter selection.

7.1.3. *LPBF*

The FE model provided a pragmatic first introduction of laser plume hydrodynamics and the atmosphere to the PBF process. Clearly it will be possible to extend this approach in the future, to a time-dependent model incorporating the melt pool. In a similar fashion, existing particle level models could be extended to include the laser plume hydrodynamics. The considerable powder movement we observed in the powder bed can be interpreted as a dynamic powder packing density, which could be incorporated into other common modelling approaches. These include optical ray-tracing for laser energy coupling into the powder bed, the values of powder bed properties which are generally inferred from the properties of a static powder bed and discrete element modelling (DEM) of the particle distribution in a spread powder layer which will be disturbed as the laser spot reaches it.

7.1.4. *Schlieren imaging system*

The z-type system used throughout this thesis is one of the most accurate and widely used schlieren setups. If properly aligned, then the only source of "error" is due to the astigmatism incurred by the angle of the two parabolic mirrors. However, this type of setup is not without its limitations. Firstly, the quality of any transmissive element that is

introduced in the system must be impeccable, as even the smallest refractive index gradient is picked up by the system. Moreover, large focal length mirrors must be used for accurate measurements, increasing the overall length of the system to several meters. This makes it hard to use the system by imaging through the windows of processing chambers in commercial AM systems. Secondly, the size of the imaged area is limited by the diameter of the mirrors, which is restrictive for some applications. Thirdly, a composite 2D image is sent to the detector, characteristic of the interaction between the light beam and all gradients along its path; this leads to loss of 3D information. One way of overcoming these limitations is through the use of a "lens and grid" schlieren system, where the light source is superimposed by a grid. By focusing the light through a large format lens and filtering at the Fourier plane using the inverse grid of that used for the light source, the instrument response is similar to a series of schlieren measurements. While it is much harder to setup and trade-offs are required between field of view size, depth and resolution, the advantage of this method is that information is only picked up from a limited region of the test area. A better sense of depth is conveyed in this manner, in addition to the benefit that imperfect surfaces introduced in the system have little effect to the measurement if they are far enough from the region of interest.

Another limitation of the schlieren method is the lack of quantitative flow information. The use of quantitative methods is restricted in materials processing, due to the variation of the refractive index of inert gases at the typical pressure and temperature levels. Consequently, the Gladstone-Dale relationship which relates refractive index and density cannot be reliably used as no values for the constant involved have been published as a function of pressure and temperature. Plasma emission spectroscopic methods are therefore more suited for the quantitative measurement of high temperature gas flows.

References

[1] S. Kou, *Welding Metallurgy*. J. Wiley & Sons, 2003.

[2] P. G. Jönsson, T. W. Eagar, and J. Szekely, "Heat and metal transfer in gas metal arc welding using argon and helium," *Metall. Mater. Trans. B*, vol. 26, no. 2, pp. 383–395, Apr. 1995.

[3] J. Lancaster, *The Physics of Welding*. International Institute of Welding, 1986.

[4] A. B. Murphy, M. Tanaka, K. Yamamoto, S. Tashiro, T. Sato, and J. J. Lowke, "Modelling of thermal plasmas for arc welding: the role of the shielding gas properties and of metal vapour," *J. Phys. Appl. Phys.*, vol. 42, no. 19, Oct. 2009.

[5] M. Suban and J. Tušek, "Dependence of melting rate in MIG/MAG welding on the type of shielding gas used," *J. Mater. Process. Technol.*, vol. 119, no. 1, pp. 185–192, 2001.

[6] K. C. Hsu, K. Etemadi, and E. Pfender, "Study of the free-burning high-intensity argon arc," *J. Appl. Phys.*, vol. 54, no. 3, p. 1293, 1983.

[7] J. Hu and H. L. Tsai, "Heat and mass transfer in gas metal arc welding. Part I: The arc," *Int. J. Heat Mass Transf.*, vol. 50, no. 5–6, pp. 833–846, Mar. 2007.

[8] A. Traidia and F. Roger, "A transient unified model of arc-weld pool couplings during pulsed spot gas tungsten arc welding," in *Excerpt from the Proceedings of the COMSOL Conference*, 2010.

[9] M. Dreher, U. Füssel, M. Schnick, and M. Hertel, "Numerical simulation of the shielding gas flow with GMA welding and options of validation by diagnostics," *Mater Sci Technol*, vol. 2, pp. 39–49, 2009.

[10] C. W. Chang, T. W. Eagar, and J. Szekely, "The Modelling of Gas Velocity Fields in Welding Arcs," *Arc Phys. Weld Pool Behav.*, vol. 381, 1980.

[11] A. Traidia, "Multiphysics modelling and numerical simulation of GTA weld pools," Ph. D. Thesis. Ecole Polytechnique, Palaiseau, France, 2011.

[12] G. J. Gibson, "Gas flow requirements for inert-gas shielded arc welding," *Weld. J.*, vol. 32, no. 4, pp. 128s-208s, 1953.

[13] M. Schnick, M. Dreher, I. J. Zschetzsche, U. Füssel, and A. Spille-Kohoff, "Visualization and optimization of shielding gas flows in arc welding," *Weld. World*, vol. 56, no. 1–2, pp. 54–61, 2012.

[14] I. Bitharas, S. W. Campbell, A. M. Galloway, N. A. McPherson, and A. J. Moore, "Visualisation of alternating shielding gas flow in GTAW," *Mater. Des.*, vol. 91, pp. 424–431, Feb. 2016.

[15] R. L. Williamson, J. R. Fincke, D. M. Crawford, S. C. Snyder, W. D. Swank, and D. C. Haggard, "Entrainment in high-velocity, high-temperature plasma jets. Part II: computational results and comparison to experiment," *Int. J. Heat Mass Transf.*, vol. 46, no. 22, pp. 4215–4228, Oct. 2003.

[16] J. R. Fincke, D. M. Crawford, S. C. Snyder, W. D. Swank, D. C. Haggard, and R. L. Williamson, "Entrainment in high-velocity, high-temperature plasma jets. Part I: experimental results," *Int. J. Heat Mass Transf.*, vol. 46, no. 22, pp. 4201–4213, Oct. 2003.

[17] K. Cheng and X. Chen, "Prediction of the entrainment of ambient air into a turbulent argon plasma jet using a turbulence-enhanced combined-diffusion-coefficient method," *Int. J. Heat Mass Transf.*, vol. 47, no. 23, pp. 5139–5148, Nov. 2004.

[18] M. Shigeta, "Turbulence modelling of thermal plasma flows," *J. Phys. Appl. Phys.*, vol. 49, no. 49, Dec. 2016.

[19] A. B. Murphy, "Calculation and application of combined diffusion coefficients in thermal plasmas," *Sci. Rep.*, vol. 4, Mar. 2014.

[20] I. Boulos, P. Fauchais, and E. Pfender, *Thermal Plasmas*, vol. 1. Springer, 1994.
[21] L. E. Cram, "Statistical evaluation of radiative power losses from thermal plasmas due to spectral lines," *J. Phys. Appl. Phys.*, vol. 18, no. 3, p. 401, 1985.
[22] J. Menart and S. Malik, "Net emission coefficients for argon-iron thermal plasmas," *J. Phys. Appl. Phys.*, vol. 35, no. 9, p. 867, 2002.
[23] M. A. Ramírez, G. Trapaga, and J. McKelliget, "A comparison between two different numerical formulations of welding arc simulation," *Model. Simul. Mater. Sci. Eng.*, vol. 11, no. 4, p. 675, 2003.
[24] F. Valensi *et al.*, "Plasma diagnostics in gas metal arc welding by optical emission spectroscopy," *J. Phys. Appl. Phys.*, vol. 43, no. 43, Nov. 2010.
[25] P. Porytsky *et al.*, "Transport properties of multicomponent thermal plasmas: Grad method versus Chapman-Enskog method," *Phys. Plasmas*, vol. 20, no. 2, p. 023504, Feb. 2013.
[26] A. B. Murphy and C. J. Arundelli, "Transport coefficients of argon, nitrogen, oxygen, argon-nitrogen, and argon-oxygen plasmas," *Plasma Chem. Plasma Process.*, vol. 14, no. 4, pp. 451–490, 1994.
[27] A. B. Murphy, "Transport coefficients of plasmas in mixtures of nitrogen and hydrogen," *Chem. Phys.*, vol. 398, pp. 64–72, Apr. 2012.
[28] A. B. Murphy and E. Tam, "Thermodynamic properties and transport coefficients of arc lamp plasmas: argon, krypton and xenon," *J. Phys. Appl. Phys.*, vol. 47, no. 29, p. 295202, Jul. 2014.
[29] A. Gleizes, J. J. Gonzalez, and P. Freton, "Thermal plasma modelling," *J. Phys. Appl. Phys.*, vol. 38, no. 9, pp. R153–R183, May 2005.
[30] M. Tanaka and J. J. Lowke, "Predictions of weld pool profiles using plasma physics," *J. Phys. Appl. Phys.*, vol. 40, no. 1, pp. R1–R23, Jan. 2007.
[31] L. E. Malvern, *Introduction to the mechanics of a continuous medium*. 1969.
[32] L. A. Jones, P. Mendez, D. Weiss, and T. W. Eagar, "Dynamic Behavior of Gas Metal Arc Welding," presented at the 9th Annual Conference on Iron and Steel Technology, Pohang, Korea, 1997.
[33] J.-M. Bauchire, E. Langlois-Bertrand, C. De Izarra, and others, "Numerical Modelling of a Free-Burning Arc in Argon A Tool for Understanding the Optical Mirage Effect in a TIG Welding Device," in *Excerpt from the Proceedings of the COMSOL Multiphysics User Conference*, 2009.
[34] A. Savaş and V. Ceyhun, "Finite element analysis of GTAW arc under different shielding gases," *Comput. Mater. Sci.*, vol. 51, no. 1, pp. 53–71, Jan. 2012.
[35] J. J. Lowke, P. Kovitya, and H. P. Schmidt, "Theory of free-burning arc columns including the influence of the cathode," *J. Phys. Appl. Phys.*, vol. 25, no. 11, p. 1600, 1992.
[36] P. Zhu, J. J. Lowke, and R. Morrow, "A unified theory of free burning arcs, cathode sheaths and cathodes," *J. Phys. Appl. Phys.*, vol. 25, no. 8, p. 1221, 1992.
[37] P. Zhu, J. J. Lowke, R. Morrow, and J. Haidar, "Prediction of anode temperatures of free burning arcs," *J. Phys. Appl. Phys.*, vol. 28, no. 7, p. 1369, 1995.
[38] L. Sansonnens, J. Haidar, and J. J. Lowke, "Prediction of properties of free burning arcs including effects of ambipolar diffusion," *J. Phys. Appl. Phys.*, vol. 33, no. 2, p. 148, 2000.
[39] J. J. Lowke, R. Morrow, and J. Haidar, "A simplified unified theory of arcs and their electrodes," *J. Phys. Appl. Phys.*, vol. 30, no. 14, p. 2033, 1997.
[40] J. J. Lowke and M. Tanaka, "'LTE-diffusion approximation' for arc calculations," *J. Phys. Appl. Phys.*, vol. 39, no. 16, p. 3634, Aug. 2006.
[41] J. J. Lowke and M. Tanaka, "The physics of non-thermionic cathodes of electric arcs," in *Gas Discharges and Their Applications, 2008. GD 2008. 17th International Conference on*, 2008, pp. 137–140.

[42] Y. Yokomizu, T. Matsumura, W. Y. Sun, and J. J. Lowke, “Electrode sheath voltages for helium arcs between non-thermionic electrodes of iron, copper and titanium,” *J. Phys. Appl. Phys.*, vol. 31, no. 7, p. 880, 1998.
[43] A. B. Murphy, “A self-consistent three-dimensional model of the arc, electrode and weld pool in gas–metal arc welding,” *J. Phys. Appl. Phys.*, vol. 44, no. 19, May 2011.
[44] M. Dreher, U. Füssel, M. Schnick, and M. Hertel, “Numerical simulation of the shielding gas flow with GMA welding and options of validation by diagnostics,” *Mater Sci Technol*, vol. 2, pp. 39–49, 2009.
[45] M. Dreher, U. Füssel, and M. Schnick, “Numerical optimization of gas metal arc welding torches using ANSYS CFX,” in *Proceedings of 63rd Annual Assembly and International Conference of the Int. Institute of Welding, July*, 2010, pp. 11–17.
[46] M. Dreher, U. Füssel, S. Rose, M. Häßler, M. Hertel, and M. Schnick, “Methods and results concerning the shielding gas flow in GMAW,” *Weld. World*, Mar. 2013.
[47] Y. Sato, K. Tomita, and T. Kuwana, “Oxygen absorption by steel weld metal in an Ar-CO_2-O_2 welding atmosphere. 2nd Report: Oxygen absorption during gas metal arc welding,” *Weld. Int.*, vol. 7, no. 5, pp. 358–364, Jan. 1993.
[48] A. B. Murphy, M. Tanaka, K. Yamamoto, S. Tashiro, T. Sato, and J. J. Lowke, “Modelling of thermal plasmas for arc welding: the role of the shielding gas properties and of metal vapour,” *J. Phys. Appl. Phys.*, vol. 42, no. 19, Oct. 2009.
[49] J. Haidar, “The dynamic effects of metal vapour in gas metal arc welding,” *J. Phys. Appl. Phys.*, vol. 43, no. 16, p. 165204, Apr. 2010.
[50] M. Schnick, U. Füssel, M. Hertel, A. Spille-Kohoff, and A. B. Murphy, “Metal vapour causes a central minimum in arc temperature in gas–metal arc welding through increased radiative emission,” *J. Phys. Appl. Phys.*, vol. 43, no. 2, Jan. 2010.
[51] D.-I. M. Hertel, D.-I. S. Rose, D.-I. M. Haessler, A. B. Murphy, and others, “Numerical Investigations of the influence of Metal Vapour in GMA Welding,” *Weld. World*, vol. 55, no. 11–12, pp. 114–120, 2011.
[52] M. Schnick, U. Fuessel, M. Hertel, M. Haessler, A. Spille-Kohoff, and A. B. Murphy, “Modelling of gas–metal arc welding taking into account metal vapour,” *J. Phys. Appl. Phys.*, vol. 43, no. 43, Nov. 2010.
[53] S. Zielińska *et al.*, “Investigations of GMAW plasma by optical emission spectroscopy,” *Plasma Sources Sci. Technol.*, vol. 16, no. 4, pp. 832–838, Nov. 2007.
[54] M. Tanaka, H. Terasaki, M. Ushio, and J. J. Lowke, “A unified numerical modeling of stationary tungsten-inert-gas welding process,” *Metall. Mater. Trans. A*, vol. 33, no. 7, pp. 2043–2052, 2002.
[55] M. Brochard, “Modèle couplé cathode-plasma-pièce en vue de la simulation du procédé de soudage à l’arc TIG,” PhD Thesis, Université de Provence, 2009.
[56] F. L. Zhu, H. L. Tsai, S. P. Marin, and P. C. Wang, “A comprehensive model on the transport phenomena during gas metal arc welding process,” *Prog. Comput. Fluid Dyn. Int. J.*, vol. 4, no. 2, pp. 99–117, Jan. 2004.
[57] J. Hu and H. L. Tsai, “Heat and mass transfer in gas metal arc welding. Part I: The arc,” *Int. J. Heat Mass Transf.*, vol. 50, no. 5–6, pp. 833–846, Mar. 2007.
[58] J. Hu and H. L. Tsai, “Heat and mass transfer in gas metal arc welding. Part II: The metal,” *Int. J. Heat Mass Transf.*, vol. 50, no. 5–6, pp. 808–820, Mar. 2007.
[59] T. Zacharia, S. A. David, J. M. Vitek, and T. DebRoy, “Weld pool development during GTA and laser beam welding of type 304 stainless steel, Part II—experimental correlation,” *Weld. J.*, vol. 68, no. 12, pp. 510s–519s, 1989.
[60] L. M. Gourd, *Principles of Welding Technology*, 3rd ed. H. Arnold, 1980.
[61] B. A. Finlayson and L. E. Scriven, “The method of weighed residuals-A review,” *Appl. Mech. Rev.*, vol. 19, no. 9, pp. 735–748, Sep. 1966.

[62] Z. H. Rao, J. Zhou, and H. L. Tsai, “Determination of equilibrium wire-feed-speeds for stable gas metal arc welding,” *Int. J. Heat Mass Transf.*, vol. 55, no. 23–24, pp. 6651–6664, Nov. 2012.
[63] Y. Ogino and Y. Hirata, “Numerical simulation of metal transfer in argon gas-shielded GMAW,” *Weld. World*, vol. 59, no. 4, pp. 465–473, Jul. 2015.
[64] Y. Ogino, Y. Hirata, and A. B. Murphy, “Numerical simulation of GMAW process using Ar and an Ar–CO2 gas mixture,” *Weld. World*, vol. 60, no. 2, pp. 345–353, Mar. 2016.
[65] Y. Ogawa, “High speed imaging technique Part 1 – high speed imaging of arc welding phenomena,” *Sci. Technol. Weld. Join.*, vol. 16, no. 1, pp. 33–43, Jan. 2011.
[66] S. Subramaniam, D. R. White, D. J. Scholl, and W. H. Weber, “In situ optical measurement of liquid drop surface tension in gas metal arc welding,” *J. Phys. Appl. Phys.*, vol. 31, no. 16, 1998.
[67] E. Siewert *et al.*, “Visualization of Gas Flows in Welding Arcs by the Schlieren Measuring Technique,” *Weld. J.*, vol. 94, pp. 1s-5s, Jan. 2014.
[68] V. Beyer, S. W. Campbell, G. M. Ramsey, A. M. Galloway, A. J. Moore, and N. A. McPherson, “Systematic study of effect of cross-drafts and nozzle diameter on shield gas coverage in MIG welding,” *Sci. Technol. Weld. Join.*, vol. 18, no. 8, pp. 652–660, Nov. 2013.
[69] L. M. Weinstein, “Review and update of lens and grid schlieren and motion camera schlieren,” *Eur. Phys. J. Spec. Top.*, vol. 182, no. 1, pp. 65–95, Apr. 2010.
[70] G. S. Settles, *Schlieren and Shadowgraph Techniques: Visualizing Phenomena in Transparent Media*. Springer, 2001.
[71] E. Hecht, “Hecht optics,” *Addison Wesley*, vol. 997, pp. 213–214, 1998.
[72] C. Allemand, R. Schroeder, D. Ries, and T. Eagar, “A method of filming metal transfer in welding arcs,” *Weld. J.*, vol. 64, no. 1, pp. 45–47, 1985.
[73] T. Okada, H. Yamamoto, and S. Harada, “Observation of the shielding gas flow pattern during arcing by the use of a laser light source,” *Arc Phys. Weld Pool Behav.*, vol. 1, pp. 203–213, 1980.
[74] R. Hou, D. M. Evans, J. C. McClure, A. C. Nunes, and G. Garcia, “Shielding gas and heat transfer efficiency in plasma arc welding,” *Weld. J.- Weld. Res. Suppl.*, vol. 75, no. 10, pp. 305–310, 1996.
[75] V. Beyer, S. W. Campbell, G. M. Ramsey, A. M. Galloway, A. J. Moore, and N. A. McPherson, “Systematic study of effect of cross-drafts and nozzle diameter on shield gas coverage in MIG welding,” *Sci. Technol. Weld. Join.*, vol. 18, no. 8, pp. 652–660, Nov. 2013.
[76] P. Zhu, M. Rados, and S. W. Simpson, “Theoretical predictions of the start-up phase in GMA welding,” *Weld. J.- Weld. Res. Suppl.*, vol. 76, no. 7, p. 269s, 1997.
[77] V. A. Ferraresi, K. M. Figueiredo, and T. H. Ong, “Metal transfer in the aluminum gas metal arc welding,” *J. Braz. Soc. Mech. Sci. Eng.*, vol. 25, no. 3, pp. 229–234, 2003.
[78] M. J. Hargather and G. S. Settles, “Recent developments in schlieren and shadowgraphy,” in *AIAA meeting paper*, 2010, vol. 4206.
[79] H. Shardin, “Toepler’s Schlieren Method: Basic Principles for its Use and Quantitative Evaluation,” *Forsch. Auf Dem Geb. Ingenieurwesens Ausg. B*, vol. 5, no. 367, Aug. 1934.
[80] J. W. Hosch and J. P. Walters, “High spatial resolution Schlieren photography,” *Appl. Opt.*, vol. 16, no. 2, pp. 473–482, 1977.
[81] T. Mey, M. Rein, P. Großmann, and K. Mann, “Brilliance improvement of laser-produced soft x-ray plasma by a barrel shock,” *New J. Phys.*, vol. 14, no. 7, Jul. 2012.
[82] J. M. Desse and R. Deron, “Shadow, Schlieren and Color Interferometry.,” *AerospaceLab*, no. 1, p. p–1, 2009.

[83] W. B. Moen and G. J. Gibson, “Schlieren Analysis of Inert-Gas Arc Shields,” *Weld. J.*, vol. 31, no. 3, pp. 208–213, 1952.
[84] D. Schwass, M. Wittlich, M. Schmitz, and H. Siekmann, “Emission of UV radiation during arc welding,” Institute of Occupational Safety and Health of the German Social Accident Insurance (IFA), Sankt Augustin, Dec. 2011.
[85] S. Rose, M. Schnick, M. Hertel, J. Zschetzsche, and U. Füssel, “Transient simulation of pulsed gas metal arc welding processes and experimental validation,” *Magnetohydrodynamics*, vol. 46, p. 4, 2010.
[86] C. B. Boss and K. J. Fredeen, *Concepts, instrumentation and techniques in inductively coupled plasma optical emission spectrometry*. Perkin Elmer Norwalk, 1999.
[87] S. S. Glickstein, “Temperature measurements in a free burning arc,” *Weld. J.*, vol. 55, no. 8, pp. 222–229, 1976.
[88] G. N. Haddad and A. J. D. Farmer, “Temperature Measurements in Gas Tungsten Arcs,” *Weld. J.*, vol. 24, pp. 339–342, 1985.
[89] N. Konjević, A. Lesage, J. R. Fuhr, and W. L. Wiese, “Experimental Stark widths and shifts for spectral lines of neutral and ionized atoms (a critical review of selected data for the period 1989 through 2000),” *J. Phys. Chem. Ref. Data*, vol. 31, no. 3, pp. 819–927, 2002.
[90] J. Mirapeix, A. Cobo, S. Fernandez, R. Cardoso, and J. M. Lopez-Higuera, “Spectroscopic analysis of the plasma continuum radiation for on-line arc-welding defect detection,” *J. Phys. Appl. Phys.*, vol. 41, no. 13, Jul. 2008.
[91] M. Ebrahimnia, M. Goodarzi, M. Nouri, and M. Sheikhi, “Study of the effect of shielding gas composition on the mechanical weld properties of steel ST 37-2 in gas metal arc welding,” *Mater. Des.*, vol. 30, no. 9, pp. 3891–3895, Oct. 2009.
[92] J. Ding, P. Colegrove, F. Martina, S. Williams, R. Wiktorowicz, and M. R. Palt, “Development of a laminar flow local shielding device for wire+arc additive manufacture,” *J. Mater. Process. Technol.*, vol. 226, pp. 99–105, Dec. 2015.
[93] C. S. Kim, “Thermophysical properties of stainless steels,” Argonne National Lab. (USA), ANL--75-55, 1975.
[94] W. F. Gale and T. C. Totemeier, *Smithells Metals Reference Book*. Butterworth-Heinemann, 2003.
[95] A. B. Murphy, “Transport coefficients of air, argon-air, nitrogen-air, and oxygen-air plasmas,” *Plasma Chem. Plasma Process.*, vol. 15, no. 2, pp. 279–307, Jun. 1995.
[96] I. Bitharas, N. A. McPherson, W. McGhie, D. Roy, and A. J. Moore, “Visualisation and optimisation of shielding gas coverage during gas metal arc welding,” *J. Mater. Process. Technol.*, vol. 255, pp. 451–462, May 2018.
[97] H. Bhadeshia and R. Honeycombe, *Steels: Microstructure and Properties*. Butterworth-Heinemann, 2017.
[98] K. Tamaki, I. Masumoto, and Y. Takahashi, “Some observation of the gas shielding conditions of CO2 arc welding by the application of a television system.pdf,” *J. Jpn. Weld. Soc.*, vol. 47, no. 5, pp. 37–42, 1978.
[99] G. Wilhelm, G. Gött, H. Schöpp, and D. Uhrlandt, “Study of the welding gas influence on a controlled short-arc GMAW process by optical emission spectroscopy,” *J. Phys. Appl. Phys.*, vol. 43, no. 43, Nov. 2010.
[100] L.-E. Lindgren, “Numerical modelling of welding,” *Comput. Methods Appl. Mech. Eng.*, vol. 195, no. 48, pp. 6710–6736, Oct. 2006.
[101] W. Zhang, C.-H. Kim, and T. DebRoy, “Heat and fluid flow in complex joints during gas metal arc welding—Part II: Application to fillet welding of mild steel,” *J. Appl. Phys.*, vol. 95, no. 9, pp. 5220–5229, Apr. 2004.
[102] J. Cunningham, “Pulsed welding and cutting by variation of composition of shielding gas,” US3484575 A, 16-Dec-1969.

[103] O. M. Novikov, A. S. Persidskii, E. P. Rad'ko, A. V. Baranovskii, and B. A. Khasyanov, "Effect of changes in the composition of the gas shielding medium on the properties of arc welded joints in aluminium alloys," *Weld. Int.*, vol. 27, no. 3, pp. 222–225, Mar. 2013.
[104] B. Y. Kang, Y. K. D. V. Prasad, M. J. Kang, H. J. Kim, and I. S. Kim, "Characteristics of alternate supply of shielding gases in aluminum GMA welding," *J. Mater. Process. Technol.*, vol. 209, no. 10, pp. 4716–4721, Jun. 2009.
[105] S. W. Campbell, A. M. Galloway, N. A. McPherson, and A. Gillies, "Evaluation of gas metal arc welding with alternating shielding gases for use on AA6082T6," *Proc. Inst. Mech. Eng. Part B J. Eng. Manuf.*, vol. 226, no. 6, pp. 992–1000, Jun. 2012.
[106] S. Campbell, A. Galloway, and N. McPherson, "Artificial neural network prediction of weld geometry performed using GMAW with alternating shielding gases," *Weld. J.*, vol. 91, no. 6, pp. 174s-181s, Jun. 2012.
[107] R. G. Tazetdinov, O. M. Novikov, A. S. Persidskii, B. A. Khasyanov, E. N. Ivanov, and L. T. Plaksina, "Arc welding in shielding gases with alternate pulsed supply of dissimilar gases," *Weld. Int.*, vol. 27, no. 4, pp. 311–314, Apr. 2013.
[108] F. H. Ley, S. W. Campbell, A. M. Galloway, and N. A. McPherson, "Effect of shielding gas parameters on weld metal thermal properties in gas metal arc welding," *Int. J. Adv. Manuf. Technol.*, pp. 1–9, Apr. 2015.
[109] B. Y. Kang, Y. K. D. V. Prasad, M. J. Kang, H. J. Kim, and I. S. Kim, "The effect of alternate supply of shielding gases in austenite stainless steel GTA welding," *J. Mater. Process. Technol.*, vol. 209, no. 10, pp. 4722–4727, Jun. 2009.
[110] A. Traidia and F. Roger, "A computational investigation of different helium supplying methods for the improvement of GTA welding," *J. Mater. Process. Technol.*, vol. 211, no. 9, pp. 1553–1562, Sep. 2011.
[111] S. W. Campbell, A. M. Galloway, and N. A. McPherson, "Techno-economic evaluation on the effects of alternating shielding gases for advanced joining processes," *Proc. Inst. Mech. Eng. Part B J. Eng. Manuf.*, Aug. 2011.
[112] D. Salem, R. Hannachi, Y. Cressault, P. Teulet, and L. Béji, "Radiative properties of argon–helium–nitrogen–carbon–cobalt–nickel plasmas used in CNT synthesis," *J. Phys. Appl. Phys.*, vol. 48, no. 6, Feb. 2015.
[113] Z. H. Rao, S. M. Liao, and H. L. Tsai, "Effects of shielding gas compositions on arc plasma and metal transfer in gas metal arc welding," *J. Appl. Phys.*, vol. 107, no. 4, 2010.
[114] S. W. Campbell, A. M. Galloway, and N. A. McPherson, "Arc pressure and weld metal fluid flow while using alternating shielding gases. Part 1: arc pressure measurement," *Sci. Technol. Weld. Join.*, vol. 18, no. 7, pp. 591–596, Oct. 2013.
[115] E. L. Cussler, *Diffusion: Mass Transfer in Fluid Systems*. Cambridge University Press, 1997.
[116] E. N. Fuller, P. D. Schettler, and J. C. Giddings, "New method for prediction of binary gas-phase diffusion coefficients," *Ind. Eng. Chem.*, vol. 58, no. 5, pp. 18–27, 1966.
[117] F. Wang, S. Williams, P. Colegrove, and A. A. Antonysamy, "Microstructure and Mechanical Properties of Wire and Arc Additive Manufactured Ti-6Al-4V," *Metall. Mater. Trans. A*, vol. 44, no. 2, pp. 968–977, Feb. 2013.
[118] W. E. Frazier, "Metal Additive Manufacturing: A Review," *J. Mater. Eng. Perform.*, vol. 23, no. 6, pp. 1917–1928, Jun. 2014.
[119] S. Jäckel, M. Hertel, and U. Füssel, "Design of gas trailing shields for TIG-welding of stainless steels," *Weld. World*, vol. 61, no. 1, pp. 117–123, Jan. 2017.

[120] F. Martina, J. Mehnen, S. W. Williams, P. Colegrove, and F. Wang, “Investigation of the benefits of plasma deposition for the additive layer manufacture of Ti–6Al–4V,” *J. Mater. Process. Technol.*, vol. 212, no. 6, pp. 1377–1386, Jun. 2012.
[121] M. Schnick, U. FÜssel, and A. Spille-Kohoff, “Numerical investigations of the influence of design parameters, gas composition and electric current in plasma arc welding (PAW),” *Weld. World*, vol. 54, no. 3–4, pp. R87–R96, 2010.
[122] X. Jian and C. S. Wu, “Numerical analysis of the coupled arc–weld pool–keyhole behaviors in stationary plasma arc welding,” *Int. J. Heat Mass Transf.*, vol. 84, pp. 839–847, May 2015.
[123] X. Jian, C. Wu, G. Zhang, and J. Chen, “A unified 3D model for an interaction mechanism of the plasma arc, weld pool and keyhole in plasma arc welding,” *J. Phys. Appl. Phys.*, vol. 48, no. 46, Nov. 2015.
[124] J. Pan, S. Hu, L. Yang, and S. Chen, “Numerical analysis of the heat transfer and material flow during keyhole plasma arc welding using a fully coupled tungsten–plasma–anode model,” *Acta Mater.*, vol. 118, pp. 221–229, Oct. 2016.
[125] M. Boivineau *et al.*, “Thermophysical Properties of Solid and Liquid Ti-6Al-4V (TA6V) Alloy,” *Int. J. Thermophys.*, vol. 27, no. 2, pp. 507–529, Mar. 2006.
[126] W. E. King *et al.*, “Laser powder bed fusion additive manufacturing of metals; physics, computational, and materials challenges,” *Appl. Phys. Rev.*, vol. 2, no. 4, p. 041304, Dec. 2015.
[127] S. K. Everton, M. Hirsch, P. Stravroulakis, R. K. Leach, and A. T. Clare, “Review of in-situ process monitoring and in-situ metrology for metal additive manufacturing,” *Mater. Des.*, vol. 95, pp. 431–445, Apr. 2016.
[128] J. J. Lewandowski and M. Seifi, “Metal Additive Manufacturing: A Review of Mechanical Properties,” *Annu. Rev. Mater. Res.*, vol. 46, no. 1, pp. 151–186, Jul. 2016.
[129] M. J. Matthews, G. Guss, S. A. Khairallah, A. M. Rubenchik, P. J. Depond, and W. E. King, “Denudation of metal powder layers in laser powder bed fusion processes,” *Acta Mater.*, vol. 114, pp. 33–42, Aug. 2016.
[130] S. Ly, A. M. Rubenchik, S. A. Khairallah, G. Guss, and M. J. Matthews, “Metal vapor micro-jet controls material redistribution in laser powder bed fusion additive manufacturing,” *Sci. Rep.*, vol. 7, no. 1, p. 4085, Jun. 2017.
[131] V. Gunenthiram, P. Peyre, M. Schneider, M. Dal, F. Coste, and R. Fabbro, “Analysis of laser–melt pool–powder bed interaction during the selective laser melting of a stainless steel,” *J. Laser Appl.*, vol. 29, no. 2, May 2017.
[132] C. Zhao *et al.*, “Real-time monitoring of laser powder bed fusion process using high-speed X-ray imaging and diffraction,” *Sci. Rep.*, vol. 7, no. 1, p. 3602, Jun. 2017.
[133] I. A. Roberts, C. J. Wang, R. Esterlein, M. Stanford, and D. J. Mynors, “A three-dimensional finite element analysis of the temperature field during laser melting of metal powders in additive layer manufacturing,” *Int. J. Mach. Tools Manuf.*, vol. 49, no. 12–13, pp. 916–923, Oct. 2009.
[134] A. Hussein, L. Hao, C. Yan, and R. Everson, “Finite element simulation of the temperature and stress fields in single layers built without-support in selective laser melting,” *Mater. Des. 1980-2015*, vol. 52, pp. 638–647, Dec. 2013.
[135] N. E. Hodge, R. M. Ferencz, and J. M. Solberg, “Implementation of a Thermomechanical Model in Diablo for the Simulation of Selective Laser Melting,” Laurence Livermore National Laboratory, LLNL-TR-644936, 2013.
[136] B. Schoinochoritis, D. Chantzis, and K. Salonitis, “Simulation of metallic powder bed additive manufacturing processes with the finite element method: A critical review,” *Proc. Inst. Mech. Eng. Part B J. Eng. Manuf.*, vol. 231, no. 1, pp. 96–117, Jan. 2015.

[137] C. Qiu, C. Panwisawas, M. Ward, H. C. Basoalto, J. W. Brooks, and M. M. Attallah, "On the role of melt flow into the surface structure and porosity development during selective laser melting," *Acta Mater.*, vol. 96, pp. 72–79, Sep. 2015.
[138] S. A. Khairallah, A. T. Anderson, A. Rubenchik, and W. E. King, "Laser powder-bed fusion additive manufacturing: Physics of complex melt flow and formation mechanisms of pores, spatter, and denudation zones," *Acta Mater.*, vol. 108, pp. 36–45, Apr. 2016.
[139] A. B. Murphy, "The effects of metal vapour in arc welding," *J. Phys. Appl. Phys.*, vol. 43, no. 43, p. 434001, Nov. 2010.
[140] J. P. Kruth, L. Froyen, J. Van Vaerenbergh, P. Mercelis, M. Rombouts, and B. Lauwers, "Selective laser melting of iron-based powder," *J. Mater. Process. Technol.*, vol. 149, no. 1–3, pp. 616–622, Jun. 2004.
[141] A. Masmoudi, R. Bolot, and C. Coddet, "Investigation of the laser–powder–atmosphere interaction zone during the selective laser melting process," *J. Mater. Process. Technol.*, vol. 225, pp. 122–132, Nov. 2015.
[142] K. R. Kim and D. F. Farson, "CO2 laser–plume interaction in materials processing," *J. Appl. Phys.*, vol. 89, no. 1, pp. 681–688, Jan. 2001.
[143] T. Mościcki, J. Hoffman, and Z. Szymański, "Modelling of plasma plume induced during laser welding," *J. Phys. Appl. Phys.*, vol. 39, no. 4, pp. 685–692, Feb. 2006.
[144] C. Yan, X. Wen-Jing, W. Yue, S. Da-Wei, and W. Yixiong, "Numerical and experimental study of the effect of groove on plasma plume during high power laser welding," *J. Laser Appl.*, vol. 25, no. 5, Nov. 2013.
[145] N. S. Hosseini Motlagh, P. Parvin, M. Jandaghi, and M. J. Torkamany, "The influence of different volume ratios of He and Ar in shielding gas mixture on the power waste parameters for Nd:YAG and CO2 laser welding," *Opt. Laser Technol.*, vol. 54, pp. 191–198, Dec. 2013.
[146] P. Bidare, R. R. J. Maier, R. J. Beck, J. D. Shephard, and A. J. Moore, "An open-architecture metal powder bed fusion system for in-situ process measurements," *Addit. Manuf.*, vol. 16, pp. 177–185, Aug. 2017.
[147] Renishaw plc, "Data sheet: SS 316L-0407 powder for additive manufacturing." 2017.
[148] T. J. Rockstroh and J. Mazumder, "Spectroscopic studies of plasma during cw laser materials interaction," *J. Appl. Phys.*, vol. 61, no. 3, pp. 917–923, Feb. 1987.
[149] M. von Allmen, *Laser-Beam Interactions with Materials*, vol. 2. Berlin, Heidelberg: Springer Berlin Heidelberg, 1987.
[150] Y. Cressault, A. B. Murphy, P. Teulet, A. Gleizes, and M. Schnick, "Thermal plasma properties for Ar–Cu, Ar–Fe and Ar–Al mixtures used in welding plasmas processes: II. Transport coefficients at atmospheric pressure," *J. Phys. Appl. Phys.*, vol. 46, no. 41, Oct. 2013.
[151] M. Gao, Y. Kawahito, and S. Kajii, "Observation and understanding in laser welding of pure titanium at subatmospheric pressure," *Opt. Express*, vol. 25, no. 12, p. 13539, Jun. 2017.
[152] A. V. Gusarov and I. Smurov, "Modeling the interaction of laser radiation with powder bed at selective laser melting," *Phys. Procedia*, vol. 5, pp. 381–394, 2010.
[153] Z. Zhang, Z.-X. Han, and G. S. Dulikravich, "Numerical simulation of laser induced plasma during pulsed laser deposition," *J. Appl. Phys.*, vol. 90, no. 12, pp. 5889–5897, Dec. 2001.
[154] W. Han, "Computational and experimental investigations of laser drilling and welding for microelectronic packaging," Worcester Polytechnic Institute, 2004.

[155] D. L. Wiggins, C. T. Raynor, and J. A. Johnson, “Evidence of inverse bremsstrahlung in laser enhanced laser-induced plasma,” *Phys. Plasmas*, vol. 17, no. 10, Oct. 2010.
[156] M. Simonelli *et al.*, “A Study on the Laser Spatter and the Oxidation Reactions During Selective Laser Melting of 316L Stainless Steel, Al-Si10-Mg, and Ti-6Al-4V,” *Metall. Mater. Trans. A*, vol. 46, no. 9, pp. 3842–3851, Sep. 2015.
[157] L. Thijs, J. Van Humbeeck, K. Kempen, E. Yasa, J. Kruth, and M. Rombouts, “Investigation on the inclusions in maraging steel produced by Selective Laser Melting,” in *Innovative Developments in Virtual and Physical Prototyping*, CRC Press, 2011, pp. 297–304.
[158] X. Wang, N. Read, L. N. Carter, R. M. Ward, and M. M. Attallah, “Defect Formation and its Mitigation in Selective Laser Melting of High γ′ Ni-Base Superalloys,” in *Superalloys 2016*, John Wiley & Sons, Inc., 2016, pp. 351–358.
[159] R. Fabbro, S. Slimani, I. Doudet, F. Coste, and F. Briand, “Experimental study of the dynamical coupling between the induced vapour plume and the melt pool for Nd–Yag CW laser welding,” *J. Phys. Appl. Phys.*, vol. 39, no. 2, p. 394, 2006.